**Seismic imaging of lithosphere structures of the Western Canada Sedimentary Basin**

by

Yunfeng Chen

A thesis submitted in partial fulfillment of the requirements for the degree of

Doctor of Philosophy

in
Geophysics

Department of Physics
University of Alberta

# Abstract

The Western Canada Sedimentary Basin (WCSB) resides in a transition region from the Precambrian Canadian Shield to the Phanerozoic Cordillera. This broad foreland area has undergone more than three billion years of tectonic evolution from the Paleoproterozoic assembly of the Laurentian craton to the Mesozoic Cordilleran orogenesis along its western margin. This thesis presents updated geophysical imaging results of this tectonically diverse area based on more than a decade (2006-2017) of broadband recordings from dense seismic arrays in western Canada. This unique dataset enables a higher resolution illumination of the 3D seismic structures of the WCSB than previously available, which offers critical constraints on the morphology, composition and evolution history of the lithosphere of the western margin of the North American craton.

The receiver function imaging reveals increased thickness and Vp/Vs ratio in the crust near the Snowbird Tectonic Zone and the Great Falls Tectonic Zone, two Precambrian discontinuities in the WCSB, which provide compelling evidence for Proterozoic collisions along these boundaries. The finite-frequency travel-time tomography provides high-resolution P- and S-wave velocity models reveals distinct high velocities beneath major Precambrian domains. The lithospheric root beneath the Hearne craton extends down to a minimum depth of 300 km,

about 100 km thicker than the surrounding domains. The deep high-velocity root and substantially reduced crustal-shallow mantle velocities beneath the Hearne craton are consistent with earlier tectonic models of the Precambrian assembly. Through an integration of mantle velocity with surface heat flow, isostatic gravity anomaly and kimberlite spatial distribution, this thesis sheds new light on the formation and post-assembly modifications of western Laurentia. Finally, our model reveals a sharp Cordillera-Craton boundary (CCB), which is characterized by large (4.3%) P (7.0% for S) velocity and lithospheric thickness (>200 km) contrasts over a horizontal distance of ~100 km. The CCB dips steeply to the west beneath the southern Rocky Mountain Trench, contrary to a presumed landward-dipping Lithosphere-Asthenosphere boundary. We attribute the CCB to a preserved leading edge of the North American Craton established during its terminal collision with a microcontinent (Cordillera), which provides strong evidence for an upper mantle suture and favors a collisional origin of the southern Canadian Cordillera.

# Preface

This thesis is an original work by Yunfeng Chen. Chapters 4 of this thesis has been published as: *Gu, Y. J., Chen, Y., Dokht, R. M., & Wang, R. (2018). Precambrian tectonic discontinuities in western Laurentia: Broadband seismological perspectives on the Snowbird and Great Falls tectonic zones. Tectonics.* I conducted data analysis and contributed to result interpretation and manuscript drafting. Y. J. Gu was the supervisory author developed the original concept and drafted the manuscript. R. M. Dokht and R. Wang contributed to field data collection and manuscript revision.

Chapter 5 of this thesis has been published as: *Chen, Y., Gu, Y. J., & Hung, S. H. (2017). Finite-frequency P-wave tomography of the Western Canada Sedimentary Basin: Implications for the lithospheric evolution in Western* Laurentia. Tectonophysics, 698, 79-90.

*Chen, Y., Gu, Y. J., & Hung, S. H. (2018). A new appraisal of lithospheric structures of the Cordillera-Craton boundary region in western Canada. Tectonics (accepted).* I was responsible for model development and manuscript composition. Y. J. Gu was the supervisory author and was involved with concept formation and assisted with manuscript preparation. S. H. Hung provided the codes for tomographic imaging and contributed to manuscript revision.

Chapter 6 of this thesis has been submitted as: *Chen, Y., Gu, Y. J., Currie, C. A., Johnston, S. T., Hung, S. H., Schaeffer, A. J., & Audet, P. "Seismic Evidence for a Mantle Suture and Collisional origin for the southern Canadian Cordillera." Nature Communications (submitted).* I was responsible for seismic model

analysis, idea development and manuscript composition. Y. J. Gu was the supervisory author contributed to the concept formation and assisted with manuscript drafting. C. A. Currie conducted the thermal calculation, interpreted the results and assisted with manuscript drafting. S. T. Johnston provided geological background and contributed to the ribbon continent hypothesis. S. H. Hung provided the tomographic codes and contributed to seismic imaging. A. J. Schaeffer and P. Audet contributed to velocity gradient analysis and manuscript revision.

Chapter 7 of this thesis is an original work and is prepared to submit.

# Acknowledgement

During the past six years at the University of Alberta, I would not be where I am without the great cares, supports and helps from my colleges, friends and my families. I would like to thank first and foremost my supervisor, Dr. Yu Jeffrey Gu, for his guidance throughout my MSc and Ph.D. studies. To me, Jeff is not only a great mentor but also a lifetime friend whose passion in life and enthusiasm for scientific research will always inspire me.

I would like to thank Dr. Shu-Huei Hung from the Taiwan National University. It would not be possible for me to complete my thesis research without her help. I also would like to thank Dr. Claire Currie, Dr. Mauricio Sacchi and Dr. Stephen Johnston for their guidance in various scientific aspects at the UofA, which significantly broaden my scientific interests and horizons in terms of geodynamic, geophysics and geology. I also thank Dr. Larry Heaman and Dr. Carl Tape for their advice and input on my Ph.D. thesis, and thank my collaborator Dr. Qinya Liu, Dr. Andrew Schaeffer and Dr. Pascal Audet for their help on my project.

Thanks to all my fellow friends Ramin Dokht, Ruijia Wang, Yuanyin Zhang, Lei Wu, Simon Schneider, Jiayue Shen, Jingchuan Wang, Tianyang Li, Cheng Zhang. It is all of you who make my life at UofA so much enjoyable.

Finally, special thanks to my beloved wife and parents for your loves and supports throughout the peaks and valleys of my life.

# Table of Contents

# List of Figures

# List of Tables

# List of Symbols and Abbreviations

| | |
|---|---|
| $\alpha$ | Damping parameter for smoothing term |
| $\beta$ | Damping parameter for model norm term |
| $\lambda$ | Wavelength for seismic wave |
| $\phi$ | Cross-correlation coefficient |
| $\phi(t, \omega_0)$ | Phase spectrum of filtered analytical signal |
| $\kappa$ | Vp/Vs ratio |
| $\sigma$ | Correlation length |
| $\lambda$ | Constant in the exponential term |
| $\rho$ | Ray path density |
| $\tau_{3D}$ | Crustal travel time in a 3D model |
| $\tau_{1D}$ | Crustal travel time in a 1D model |
| $\tau(\omega_0)$ | Group arrival time for filtered signal |
| $\omega$ | Frequency |

| | |
|---|---|
| $\omega_0$ | Center frequency of Gaussian filter |
| $\delta c$ | Wave-speed perturbation |
| $\delta u$ | Slowness perturbation |
| $\delta t$ | Travel-time perturbation |
| $\delta t_c$ | Crustal correction term |
| $\Delta t$ | Relative arrival time |
| $\Delta T$ | Relative travel time delay between the perturbed and background wavefields |
| $\mathbf{C}$ | Covariance matrix |
| $\mathbf{F}$ | Matrix applying the smoothness constrains to the model |
| $\mathbf{G}$ | Inversion kernel |
| $\mathbf{H}$ | Matrix computing the weighted model normal |
| $\mathbf{Q}$ | Regularization matrix combining **F** and **H** |
| $\mathbf{d}$ | Data vector |
| $\mathbf{m}$ | Model vector |
| $\hat{\mathbf{m}}$ | Least-squares solution of model vector |

| | |
|---|---|
| **r** | Receiver point |
| **s** | source point |
| **x** | Scattering point |
| $A(t)$ | Amplitude of correlation function between the radial- and vertical-component seismograms |
| $A(H,\kappa)$ | Stacking amplitude in the $H$-$\kappa$ domain |
| $\lvert A(t,\omega_0)\rvert$ | Amplitude spectrum of filtered analytical signal |
| $G(\omega-\omega_0)$ | Gaussian filter with center frequency of $\omega_0$ |
| $H$ | Crustal thickness |
| $J$ | Cost function |
| $R(t)$ | Radial-component seismogram |
| $R(\omega)$ | Frequency spectrum of radial-component seismogram |
| $R_s(t)$ | Current estimate of radial-component seismogram |
| $R'(t)$ | New radial-component seismogram |
| $s(t)$ | Surface wave signal |

| | |
|---|---|
| $S(\omega)$ | Frequency spectrum of surface wave |
| $S_a(\omega)$ | Frequency spectrum of analytical signal of surface wave |
| $S(\mathbf{r}_i, \mathbf{r}_j)$ | Function conducting spatial smoothing between points $\mathbf{r}_i$ and $\mathbf{r}_j$ |
| $\mathscr{R}_{rs}$ | Gometrical spreading factor for source-receiver path |
| $\mathscr{R}_{xs}$ | Geometrical spreading factor for scatter-source path |
| $\mathscr{R}_{xr}$ | Geometrical spreading factor for scatter-receiver path |
| $Z(t)$ | Vertical-component seismogram |
| $Z(\omega)$ | Frequency spectrum of vertical-component seismogram |
| $Z^*(\omega)$ | Conjugate of $Z(\omega)$ |
| $c$ | Velocity |
| $c_0$ | Background velocity |
| $c_x$ | Wavespeed at the scattering point |
| $c_r$ | Wavespeed at the source |
| $dl$ | Differential path length |
| $i, j, k$ | Vector/matrix indices |

| | |
|---|---|
| m | Percentage of velocity perturbation |
| $\lvert \dot{m}(\omega) \rvert^2$ | Power spectrum of source-time function |
| $p$ | Ray parameter |
| $r_k$ | Amplitude of *k*-th ray on radial-component seismogram |
| $s(t)$ | Source time function |
| $t_0$ | Time difference between preliminary arrival time and the beginning of correlation window |
| $t_i^p$ | Preliminary arrival time for the *i*-th trace |
| $t_i^{\mathrm{obs}}$ | Observed phase arrival time for the *i*-th trace |
| $\bar{t}^{\mathrm{obs}}$ | Observed average phase arrival time for all stations recording the same earthquake |
| $t_i^{\mathrm{ak135}}$ | Predicted arrival time for the *i*-th trace based on AK135 model |
| $\bar{t}^{\mathrm{ak135}}$ | Predicted average phase arrival time for all stations recording the same earthquake |
| $t_k$ | Arrival time of the *k*-th ray |
| $w_i$ | Weight of phase used in the *H*-$\kappa$ stacking |

| | |
|---|---|
| $z_k$ | Amplitude of *k*-th ray on vertical-component seismogram |
| ANT | Ambient noise tomography |
| AK135 | AK135 reference earth model |
| CANOE | Canadian Northwest Experiment |
| CAT | Central Alberta Transect |
| CCB | Cordillera-Craton boundary |
| CCP | Common conversion points |
| CDF | Cordillera Deformation Front |
| GFTZ | Great Falls Tectonic Zone |
| CRANE | Canadian Rockies and Alberta Network |
| CNSN | Canadian National Seismograph Network |
| FTAN | Frequency Time Analysis |
| Ga | Billions of year |
| HVZ | High velocity zone |
| HVGZ | High velocity gradient zone |

| | |
|---|---|
| LAB | Lithosphere asthenosphere boundary |
| LCL | Lower crust layer |
| Ma | Millions of year |
| MCCC | Multi-channel cross-correlation |
| NCF | Noise correlation function |
| NMO | Normal moveout correction |
| POLARIS | Portable Observatories of Lithospheric Analysis and Research Investigating Seismicity |
| *Pms* | P-to-S converted phase generated at the Moho interface |
| *PpPms* | Reverberated phase with 1 S leg generated at the Moho interface |
| *PpSms*(*PsPms*) | Reverberated phase with 2 S legs generated at the Moho interface |
| PRAISE | Peace River Arch Industry Seismic Experiment |
| RAVEN | Regional Alberta Observatory for Earthquake Studies Network |
| RF | Receiver function |
| RMT | Rocky Mountain Trench |

| | |
|---|---|
| PREM | Preliminary reference Earth model |
| SALT | Southern Alberta Lithospheric Transect |
| SNR | Signal-to-noise ratio |
| STZ | Snowbird Tectonic Zone |
| TD | TransAlta Dam Monitoring Network |
| TF | Tintina Fault |
| VS | Vulcan Structure |
| WCSB | Western Canada Sedimentary Basin |

# Chapter 1 Introduction

## 1.1 Overview

Cratons are ancient cores of continents that have survived secular tectonic evolution since the Precambrian (Jordan, 1975; Pollack, 1986; Hoffman, 1988; King, 2005). Their longevity and stability have been largely attributed to the craton being a thick (~300 km), cold and chemically depleted boundary layer that resists the convective disruption from the surrounding mantle over billions of years (Jordan, 1975, 1978, 1979; Griffin et al., 2003; Carlson et al., 2005; Sleep, 2005). Although the mechanisms for the formation and growth of cratons have been a subject of active debate, existing theories generally favor three possible origins (Lee et al., 2011; Gerya, 2014): hot plume (Boyd, 1989; Griffin et al., 2003; Arndt et al., 2009), slab subduction (Helmstaedt & Schulze, 1989; Hoffman, 1990; Bostock, 1998; Canil, 2004; Pearson & Wittig, 2008; Snyder et al., 2015) and continental collision (Jordan, 1978; Cooper et al., 2006; Gray & Pysklywec, 2010). Since their formation in the Precambrian, the majority of continental cratons have remained relatively stable, although the underlying lithospheric keels may have undergone considerable modification through episodic growth and destruction associated with major tectonic events (Gao et al., 2002; Carlson et al., 2004; Foley, 2008; Lee et al., 2011).

Laurentia, the cratonic core of North America, has witnessed protracted lithospheric accretion (Hoffman, 1988, 1989; Villeneuve et al., 1993; Foster et al., 2006; Whitmeyer & Karlstrom, 2007; Pearson & Wittig, 2008; Corriga et al., 2009; Yuan & Romanowicz, 2010; Darbyshire et al., 2013) and reworking (Ross et al., 1991; Davis et al., 2003; Carlson et al., 2004; Mercier et al., 2009; Frederiksen et al., 2013; Bao & Eaton, 2015; Humphreys et al., 2015; Boyce et al.,

2016; Liu et al., 2016) dating back to ~3 billion years ago (Hoffman, 1988; Hammer et al., 2011). The western margin of this ancient continent, which is currently overlain by the Paleozoic strata in the Western Canada Sedimentary Basin (WCSB), has exhibited evidence of rifting, subduction, continent collision and melting during the Precambrian (Ross et al., 1991; Villeneuve et al., 1993) and the Phanerozoic Cordilleran orogenic periods (Dickinson, 2004; Johnston, 2008; Monger & Price, 2002). These tectonic processes and the associated tectonothermal events may have considerable implications for the stabilization and modification of the cratonic lithosphere beneath this region (Ross et al., 1991; Ross, 2002a).

Geologically, the WCSB is a broad foreland basin that contains sedimentary rock deposits in western Canada. It stretches west-east from eastern British Columbia, through Alberta, Saskatchewan to western Manitoba, and north-south from southern Northwest Territories to the US-Canada border, encompassing a large land area of 1,400,000 $km^2$ (Figure 1.1). The major geological units of the WCSB consist of the eastern Canadian Cordillera, which is recognizable through strongly deformed thrust-and-fold belts, and two primary sedimentary depocenters (i.e., the Williston and Alberta basins; Wright et al., 1994) near the western margin of the ancestral North American craton.

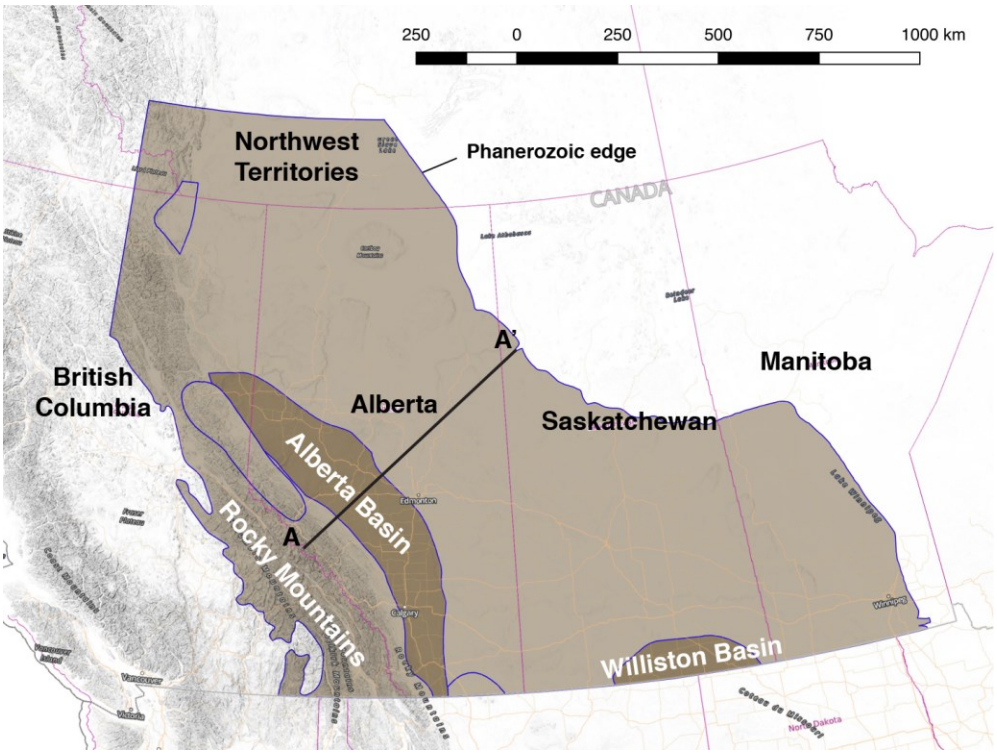


Figure 1.1 Geographic location of the WCSB. Two major depocenters within the WCSB are labeled and shaded in darker colors. The basin outline is obtained from Wright et al. (1994) and is terminated in the northwest and south. The actual area of the WCSB extends further northwestward into Northwest Territories and southward into the US. The black line (A-A') indicates the location of a cross-section across the sedimentary basin shown in Figure 1.2.

As one of the largest reserves of fossil fuel resources in the world, the knowledge of subsurface structure of the WCSB, especially its Alberta portion, has been greatly advanced thanks to development of local oil and gas industries. Tens of thousands of drilling wells and exploration seismic surveys have provided nearly continuous spatial sampling of the sedimentary rocks, outlining a detailed stratification of a thick sedimentary wedge (Figure 1.2). The sedimentary deposits reach a maximum thickness of 5-6 km near the Rocky Mountains foothills and gradually decreases to zero thickness in the exposed Canadian Shield

along an east-tapering ramp of the crystalline basement (see Figures 1.2). These stratigraphic layers have been constantly refined with improved geological constraints from a growing number of industrial wells. For example, a recently released 3D digital geological model of Alberta basin was compiled based on ~620,000 stratigraphic data points, which decomposes the sediments into 32 distinctive layers extending from the surface to the Precambrian basement (Branscombe et al., 2018).

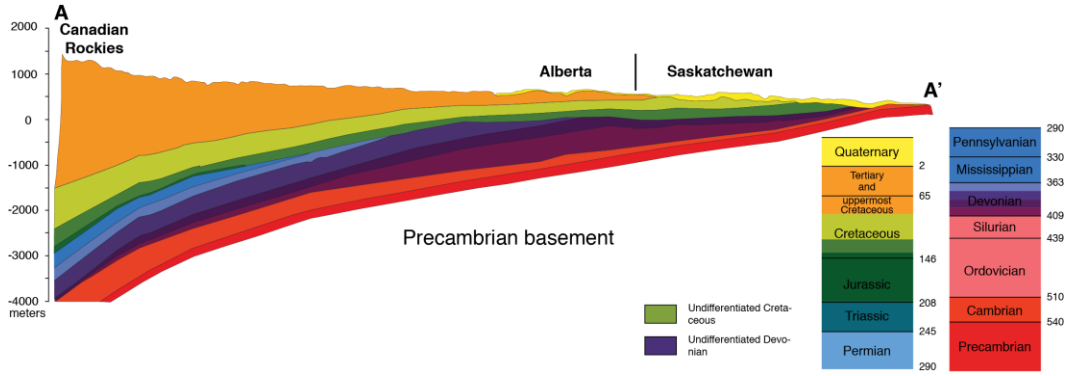


Figure 1.2 A schematic structural cross-section showing the stratigraphy of the WCSB. The profile location is marked by the black line in Figure 1.1. Unconformities and internal deformation (e.g., folds beneath the Canadian Rockies) are not shown for simplicity. Modified after Wright et al. (1994).

Compared to the densely mapped shallow sedimentary strata, the Precambrian basement of the WCSB is less well understood owing to the limited surface exposure and reduced depth sensitivity of exploration seismic surveys. Potential field data and analyses of U-Pb geochronology of drill core samples of the crystalline basement from a few deep wells provided first-order constraints on the configuration of tectonic elements of the WCSB (Ross et al., 1991; Villeneuve et al., 1993) (Figure 1.3). Further refinements to the basement structure were made through multi-disciplinary studies from the Alberta Basement Transects of Lithoprobe (Boerner et al., 2000; Clowes et al., 1995; Clowes et al., 2002; Ross et

al., 1995; Ross et al., 2000; Ross, 2002a), a milestone trans-Canada geophysical experiment (Figure 1.3a). A synopsis of the results from these transects (Bouzidi et al., 2002; Eaton et al., 1999a; Lemieux et al., 2000; Ross et al., 2000) shaped the present-day understanding of the tectonic history of the WCSB, particularly those from the Central Alberta Transect (CAT; Ross et al., 1995, 2000; Eaton & Cassidy, 1996), the Peace River Arch Industry Seismic Experiment (PRAISE) in northern Alberta (Eaton et al., 1999b) and the Southern Alberta Lithospheric Transect (SALT; Eaton et al., 2000; Lemieux et al., 2000; Clowes et al., 2002). A detailed review of the geological findings from these seminal studies will be provided in chapter 2.

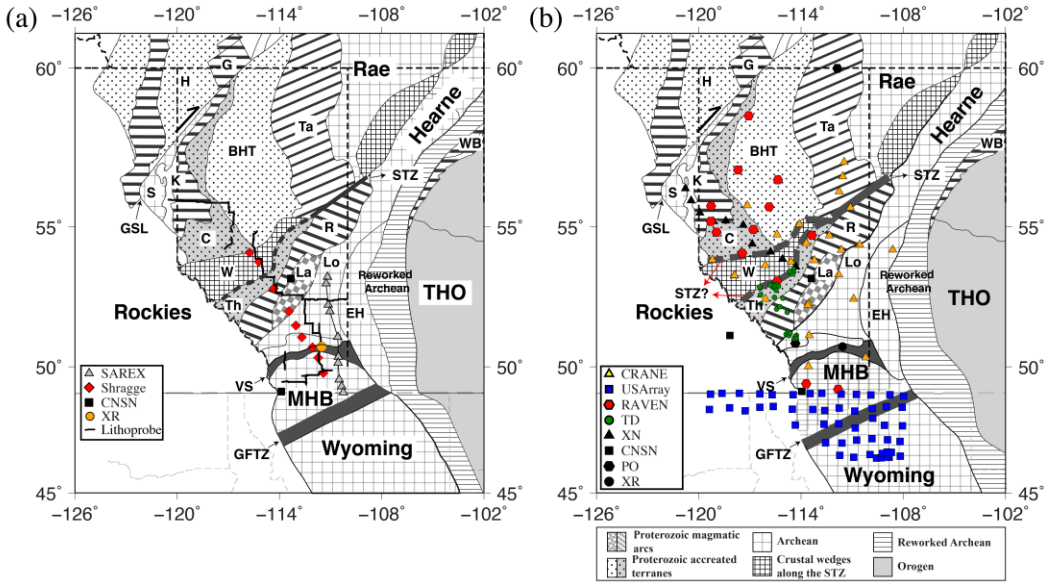


Figure 1.3 The basement domain division of the WCSB derived from the potential field data and drill core analyses (modified after Ross et al., 1991). Symbols superimposed represent geophysical samplings from (a) earlier active/passive source surveys and (b) recently deployed broadband seismic arrays near the WCSB used in this study. See Figure 2.2 for domain definitions.

Complementary to active source experiments, passive seismic surveys provide effective tools with ability to probe the deeper earth structures. Earlier tomographic studies based on sparse stations (see Figure 1.3a) have offered a glimpse of complex lithosphere architectures of the WCSB at continental (Frederiksen et al., 2001) and regional scales (Frederiksen et al., 1998; Shragge et al., 2002). The establishments of broadband seismic arrays enable a more detailed examination of regional mantle lithosphere structures. One notable example is the Canadian Northwest Experiment (CANOE; XN array in Figure 1.3b), a two-year (2003-2005) deployment covering much of northern-central WCSB. The high-quality broadband data led to fruitful scientific outcomes including the discovery of fossil subduction beneath the Slave province (Mercier et al., 2008) and detection of systematic seismic anisotropy (Courtier et al., 2010) and velocity variations (Mercier et al., 2009; Dalton et al., 2011; McLellan et al., 2018) across the Northern Cordilleran Deformation Front (CDF). During the past ten years, the southern-central WCSB has witnessed a period of rapid expansion of broadband seismic networks (Gu et al., 2011; Schultz & Stern, 2015), which opens a new chapter for the seismic imaging of the WCSB (see Figure 1.3b). Recent studies based on passive source data from these newly deployed arrays have unraveled complex evolution history of mantle lithosphere beneath the Precambrian crustal domains (Bao & Eaton 2015; Chen et al. 2015; Gu & Shen 2015; Gu et al. 2015; Bao et al. 2016). The improved structural knowledge from these earlier works and the proliferation of seismic data laid a solid foundation for more accurate, higher resolution imaging of this region.

This thesis aims to conduct high resolution geophysical surveys of the WCSB taking advantage of more than a decade (2006-2017) of seismic data recorded at dense regional arrays. The main target is the Precambrian basement that documents vital tectonic histories of three-quarters of Earth's age. We focus on the integrity and characteristics of continent lithosphere, enabling an updated appraisal of both the existing tectonic framework and the evolutionary history of

the Precambrian western Laurentia and the surrounding Mesozoic Cordilleran orogen. Overall, this study improves the understanding of the assembly and modification of craton, which sheds new light on the growth and development of the North America continent.

## 1.2 Scope of this thesis

This thesis focuses on resolving the subsurface structures of the WCSB at two depth levels, crust and sub-crustal lithospheric mantle, using passive seismic imaging techniques. The crustal studies are conducted using receiver function and ambient noise tomography approaches that provide depth sensitivity down to the crust-mantle boundary (i.e., the Moho). The primary targets are two major crustal discontinuities (Figure 1.3), the Snowbird Tectonic Zone (STZ) and Great Falls Tectonic Zone (GFTZ), respectively reside near the central and southern WCSB, that play significant roles in regional tectonic development. Through detailed examination of seismic reflectivity and velocity variations near these boundaries, we investigate the following major scientific questions.

- What, and how significant, are the crustal and mantle seismic expressions of the STZ?
- Where is the GFTZ based on broadband seismological crustal constraints and if/how is it linked to the proposed underplating event?
- Are they collisional sutures and are there common tectonic processes during the development of these boundaries?

Directly underlying the crustal domains, the structure and dynamics of sub-crustal mantle lithosphere are constrained by P- and S-wave velocities from finite-

frequency travel-time tomography. In this part of the thesis, we seek answers to the following questions.

- How are the crustal domains manifested in the mantle lithosphere?
- How did Precambrian tectonic events initiate and/or modify the intrinsic stability of craton interior?
- What surface expressions (e.g., gravity, heat flow and kimberlites) are attributable to mantle dynamics?
- How was the craton margin modified or reshaped during the Mesozoic orogenesis, and what is its tectonic implication on the nature of the Canadian Cordillera?

## 1.3 Thesis outline

To address the aforementioned questions, this dissertation is organized as follows:

**Chapter 2** provides a general overview of regional tectonics during the Precambrian and Phanerozoic times. Earlier studies based on various geophysical data, particularly those using active/passive seismic recordings, are reviewed.

**Chapter 3** summarizes three main seismic imaging techniques used in this study, which includes 1) receiver function, 2) finite-frequency travel-time tomography and 3) ambient noise analysis. The first section briefly introduces the receiver function processing and focuses more on stacking methods in H-$\kappa$ and time domains. The second section summarizes the finite-frequency wave propagation theory and its application to travel-time tomography. The last part

reviews the extraction of noise correlation functions (NCFs) from ambient noise fields and its application to Rayleigh-wave group velocity inversion.

**Chapter 4**[1] presents the Moho depths and Vp/Vs ratios of the WCSB from receiver function analysis and their geological implications on the nature of two major tectonic discontinuities, the STZ in central Alberta and GFTZ in northern Montana. The nature and locations of these boundaries impose critical constraints on the Precambrian evolution history of western Laurentia.

**Chapter 5**[2,3] provides the first P- (and its update) and S-velocity finite-frequency models of the upper mantle of the WCSB, particularly the cratonic region. The seismic observations are discussed in the framework of the Precambrian tectonics of western Laurentia. Also included are an integrated analysis of seismic velocities with heat flow, gravity and kimberlite data and discussions on the nature (composition and stability) of the craton.

**Chapter 6**[4] focuses on the western margin of the North American craton and provides a detailed analysis of seismic characteristics of the Cordillera-Craton boundary (CCB) and their geological implication on the orogenic style of the Canadian Cordillera.

**Chapter 7** presents a new crustal model from ambient noise tomography and shows the improvement in resolution through comparisons with earlier studies. The new model reveals detailed velocity variation in the crust of the Cordillera

[1] A version of this chapter has been published in Gu et al., 2018. Tectonics.

[2] A version of this chapter has been published in Chen et al., 2017. Tectonophysics.

[3] A version of this chapter has been published in Chen et al., 2018. Tectonics.

[4] A version of this chapter has been submitted to Nature Communications.

foreland, which offers new insight into the Proterozoic and Mesozoic tectonic processes in this region.

**Chapter 8** concludes the observations and interpretations of the crustal and mantle structures in the WCSB. Future work that integrates all existing structural constraints will be discussed at the end of this chapter.

# Chapter 2 Geological and geophysical overview of regional tectonics

The WCSB marks a transition region between the tectonically active Canadian Cordillera and the stable exposed Canadian Shield, covering a broad area extending from the boundary between the Omineca and Intermontane Belts in the southern Canadian Cordillera to the Phanerozoic edge of the exposed craton in the east. The northern limit is defined by the Tathlina high, a Precambrian arch in the Slave province, and, for mapping convenience, the southern boundary coincides with the Canada-US border (Wright et al., 1994; Figure 2.1). Buried beneath the thick Phanerozoic sediment sequence, the crystalline basement of the WCSB has recorded more than three billion years of tectonic evolution of the North American craton, highlighted by a major episode of plate convergence and terrane assembly during the Paleoproterozoic (Hoffman, 1988) and a later-stage Mesozoic Cordilleran orogeny along its western margin. The following sections review these two distinctive periods of tectonic evolutions that formed the present-day WCSB in the context of earlier geological and geophysical studies.

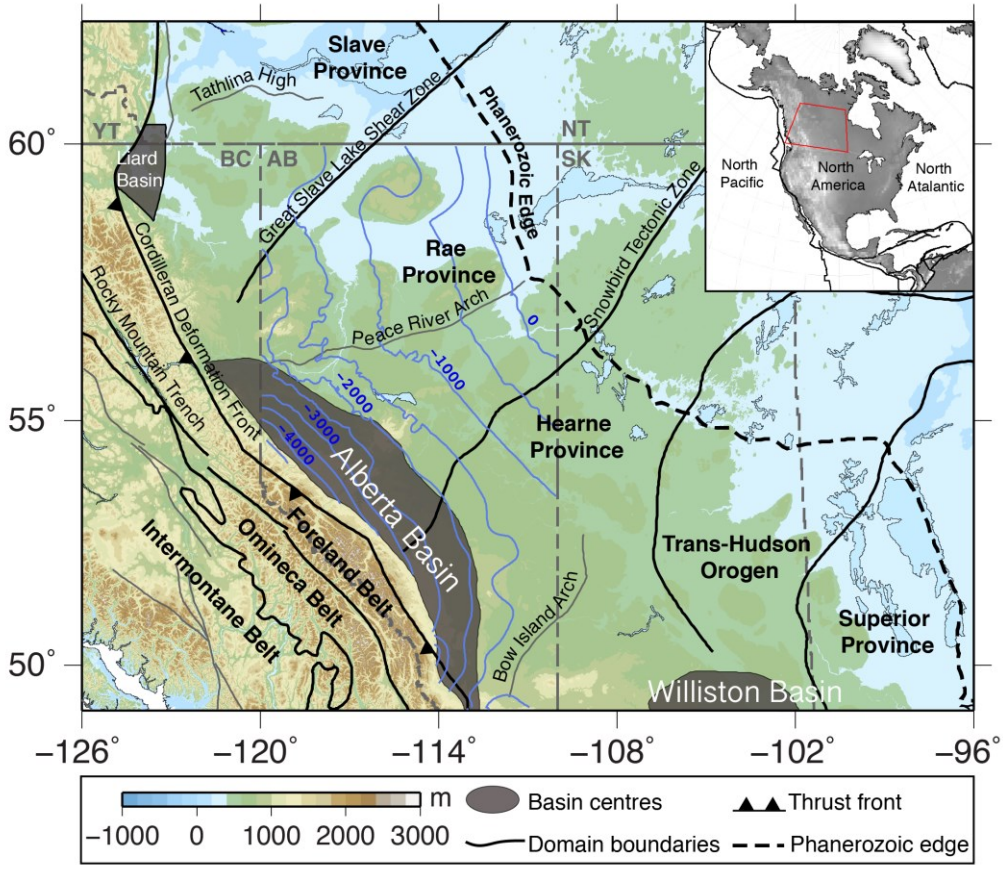


Figure 2.1 Tectonic map of the WCSB. Major domain boundaries are shown by the black solid lines and the Phanerozoic edge is marked by the dashed line. The three topographic highs, Bow island, Peace River Arches and Tathlina high, in the WCSB are indicated by the thin grey lines. The grey shaded regions indicate the deposition centers of the basins (Price, 1994). The Phanerozoic isopach (depth from the surface to the Precambrian basement) of the Alberta basin are indicated by the blue contours (Wright et al., 1994). The enclosed area in the inset marks the location of the study region relative to North America.

## 2.1 Precambrian summary

### 2.1.1 Precambrian domains

The bedrock of region containing the WCSB and northern Montana represents an integral part of the western margin of Laurentia, also known as the North American craton, formed in the early Proterozoic eon during a relatively short (2.0-1.8 Ga) geological period (Hoffman, 1988, 1989). The Precambrian bedrocks are not directly accessible to geological mapping due to thick basin sediment (see Figure 2.1). Therefore the tectonic subdivision of basement structure mainly relies on potential field anomalies, especially the aeromagnetic data. Characterized by banded aeromagnetic signatures in response to magnetite (Figure 2.2a), collisional zones have preserved the protracted deformation histories of the bounding domains during the tectonic assembly of western Laurentia (Ross, 2002a). More detailed age and lithological analyses of bedrocks were achieved from isotopic studies (U-Pb and Sm-Nd data) of 93 igneous rock samples retrieved from exploration drill cores (Ross et al., 1991; Villeneuve et al., 1993). The synthesis of geophysical and geological constraints subdivides the crystalline basement into more than 20 distinctive Precambrian crustal domains (Figure 2.2b) with varying formation age between 3.3 and 1.7 Ga (see Figure 2.2a).

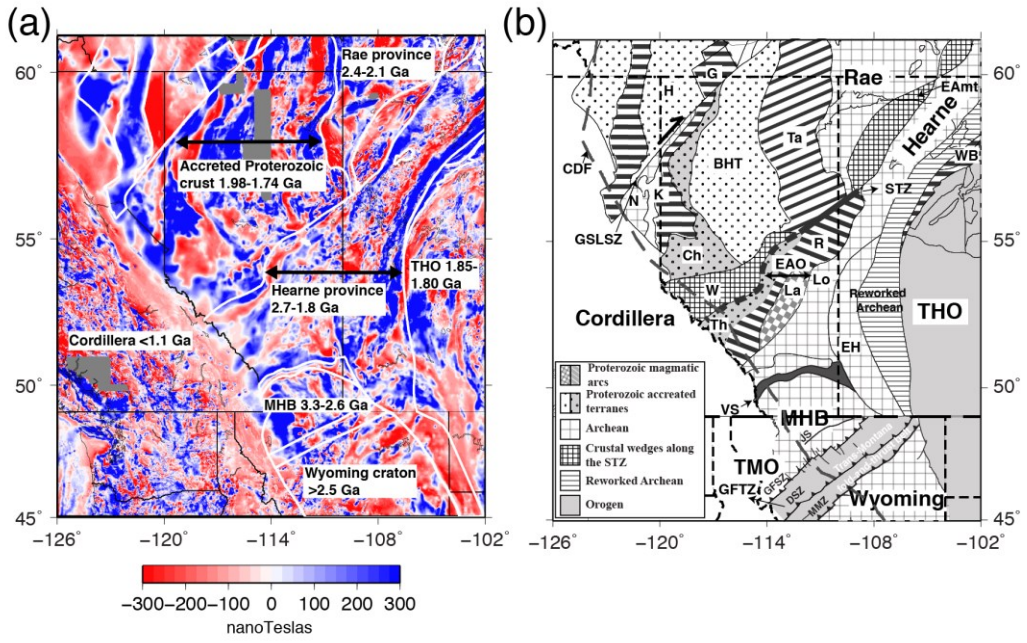


Figure 2.2 (a) Aeromagnetic anomaly map of the WCSB (modified after Ross 2002). The white lines mark major domain boundaries. (b) Tectonic domains of the Precambrian basement. The domain boundaries are determined based on lineation of aeromagnetic anomalies from (a). Major tectonic discontinuities are marked by thick grey lines. Abbreviations: BHT, Buffalo Head Terrane; C, Chinchaga; CDF, Cordilleran Deformation Front; DSZ, Dillon Shear Zone; EAmt, East Athabasca mylonite triangle; EAO, East Alberta Orogen; EH, Eyehill High; G, Great Bear; GFTZ, Greate Falls Tectonic Zone; GFSZ, Great Falls Shear Zone; GSLSZ, Great Slave Lake Shear Zone; H, Hottah; JS, Joplin Structure; K, Ksituan; La, Lacombe; Lo, Loverna block; MHB, Medicine Hat Block; MMZ, Madison Mylonite Zone; N, Nova; R, Rimbey; STZ, Snowbird Tectonic Zone; Ta, Taltson magmatic zone; Th, Thorsby; THO, Trans-Hudson Orogen; VS, Vulcan Structure; W, Wabamun. Modified after Ross et al. (1991).

The major Precambrian domains in the study area encompass the Archean cratons (Hearne, Medicine Hat Block (MHB) and Wyoming) and northern Proterozoic accreted terranes separated by the STZ, a proposed Proterozoic collisional suture of the western Churchill province (Hoffman, 1988; Ross et al.,

1991) (Figure 2.2a). This broad zone is bounded to the east by the Trans-Hudson Orogen (THO), a Himalayan-scale Paleoproterozoic collisional orogenic belt, and to the west by the young (<1.1 Ga) accreted terranes of the Phanerozoic Cordillera that overthrusted onto the western margin of Laurentia after the Jurassic period (Dickinson, 2004). The internal structures of the Precambrian provinces are manifested as a composite assembly of crustal (possibly lithospheric) fragments with diverse tectonic signatures and development histories.

In central Alberta, the East Alberta Orogen, a proposed Proterozoic orogenic belt consists of the STZ, Thorsby, Rimbey and Lacombe domain (see Figure 2.2b), marks a transition region from the underlying Paleoproterozoic crust to the Archean basement of the Hearne province further south (Ross et al., 1995, 2000). The Loverna block, the core of the Archean Hearne province, is characterized by near neutral aeromagnetic anomalies that are superimposed by short-wavelength positive perturbations (see Figure 2.2a; Ross et al., 1991). Sparsely sampled drill cores, which mainly contain magnetite-bearing biotite granite and granitic gneiss with a dominant Archean origin (2.71 Ga), have been subjected to local thermal overprinting at 1.82 Ga and 1.78 Ga (Villeneuve et al., 1993).

The Rimbey domain to the northwest of the Loverna block is a proposed magmatic belt of Paleoproterozoic era (1856-1798 Ma; Villeneuve et al., 1993), presumed to have formed in association with southeastward (current geographic location) subduction of the oceanic basin of the Thorsby domain (Ross et al., 1991). Sandwiched between the Archean Loverna Block and Proterozoic Rimbey domain is the Lacombe domain, which consists largely of low-grade clastic metasedimsentary and felsic metavolcanic rocks (<2.3 Ga; Villeneuve et al., 1993) deposited in either a foreland-foredeep system or a marginal/intra-arc basin flanking the Rimbey arc (Ross et al., 2000). The wedge-shaped Wabamun domain, located to the northwest of the STZ, is an aeromagnetic high with 2.4-2.0 Ga old magmatic rocks (Ross et al., 1991). The nature of this domain is poorly

understood (Boerner et al., 2000) and has been linked to a tectonic escape wedge formed during collisions along the STZ (Ross et al., 1991, 2002a).

The vast regions to the north of the STZ comprise a series of north trending aeromagnetic anomalies in possible connection with the accreted terranes to the Rae province (Ross & Eaton, 2002; see Figure 2.2a). Among the notable domains, the Taltson magmatic zone (2.02-1.91 Ga) constitutes the southern segment of the 2500 km Taltson-Thelon orogen (Hoffman, 1988, 1989) and contains lithologically diverse rock types of granitoids, metasedimentary gneisses, granitic basement gneisses and amphibolites (Chacko et al., 2000). The origin of the Taltson has been debated, either as a product of an eastward subduction of oceanic crust beneath a continental margin (McDonough et al., 2000; Ross et al., 1991; Ross & Eaton, 2002) or, alternatively, a distant hinterland of a convergent plate margin in a continent-interior setting (Chacko et al., 2000; De et al., 2000). To the north, the Talston belt is separated from the Thelon arc, the northern counterpart of the Talton-Thelon orogeny, by the Great Slave Lake Shear Zone (GSLSZ) formed during a dextral-oblique collision between the Slave and Rae cratons (Hoffman, 1989).

To the west of the Taltson, Buffalo Head Terrane (BHT) and Chinchaga domain form the core of the Proterozoic accreted terranes. The southern BHT is intersected by the Peace River Arch (see Figure 2.1), a lineament of topographic high that has been active since the Proterozoic (Eaton et al., 1999b). Mafic sills emplaced from post-collisional magmatism were discovered in the nearby upper crust (Ross & Eaton, 1997; Welford & Clowes, 2006). Three distinctive site of kimberlite magmatism are discovered near the BHT, which collectively defines a northern Alberta kimberlite province. Among them, the Buffalo Hills kimberlites intruded the center of the BHT between 88-86 Ma (Carlson et al., 1999; Aulbach et al., 2004; Davis et al., 2004; Heaman et al., 2004; Banas et al., 2007) whereas the Mountain Lake (~75 Ma; Leckie et al., 1997; Heaman et al., 2004) and Birch

Mountain clusters (78-70 Ma; Heaman et al., 2004) were respectively emplaced to the eastern and western flanks of the BHT.

Despite the earlier geological findings, the tectonic setting of the BHT remains elusive due to episodic overprinting events. The BHT was suggested to have strong chronological affinities to the Taltson based on the similar U-Pb ages and partially overlapped Nd isotopic compositions preserved in the gneiss complex of the Taltson and subsurface rocks of the BHT (McNicoll et al., 2000). The magmatic rocks with ages ranging from 2.32-1.99 Ga potentially document several thermal tectonic events, among which a suite of young granitic rocks (~2.0 Ga) was linked to the intrusion into the basement rocks of the BHT during its collision with the Chinchaga domain to the west (Ross & Eaton, 2002). The drill cores from the latter region revealed mostly metaplutonic rocks with crystallization age of 2.19-2.08 Ga (Villeneuve et al., 1993). With the benefit of improved seismic data coverage surrounding the BHT, our study sheds new light on the enigmatic tectonic history of this region in chapter 5.

The aforementioned tectonic domains form the basic building blocks for the early Proterozoic assembly of western Laurentia, whereas a key geological constraint to decipher this complex evolution period is the collision zone that preserves deformed margins of formerly independent microcontinents. Recognized by prominent quasi-linear features in potential field anomaly, three first-order structural discontinuities have been proposed in the southern WCSB by earlier studies, which, from the north to south, are respectively known as the Snowbird Tectonic Zone (STZ), Vulcan Structure (VS) and Great Falls Tectonic Zone (GFTZ) (see Figure 2.2). The origin and nature of these enigmatic structural lineaments have been subjects of long-standing debate and are the focus of this study. The following sections review existing geological and geophysical constraints of these boundary zones, particularly the STZ and GFTZ, and their

critical roles in the development of western Laurentia, which are the main scientific targets in chapter 4.

### 2.1.2 Snowbird Tectonic Zone (STZ)

The northeast trending STZ is one of the most recognizable geological structures across the North American craton. Originally proposed as an inter-continental suture (Gibb & Walcott, 1971; Hoffman, 1988; Ross et al., 1995, 2000), the nature of the 2,800+ km-long STZ remains a source of contentious debate. Along exposed segments of the STZ west of the Hudson Bay, discoveries of exhumation-related mylonite based on metamorphic and U-Pb zircon data (Hanmer et al., 1995; Mahan & Williams, 2005) and ultra-potassium rocks (Cousens et al., 2001; Hanmer & Relf, 2000) are generally concordant with an Archean tectonic framework. This hypothesis is corroborated by crustal signatures in central STZ (e.g., Legs Lake shear zone), where ultra-potassium rocks exhibit common neo-Archean signatures from both sides and favor an intra-continental origin (Hanmer et al., 1995). However, medium- to high-pressure metamorphic rocks, microdiamonds, local crustal thickening in eastern STZ (1.9 Ga) (MacRae et al., 1996; Berman et al., 2013) and magmatic mafic dikes in central STZ (Heaman & LeCheminant, 1993; Heaman, 1994) are more indicative of Proterozoic subduction (Berman et al., 2007) and/or asthenospheric upwelling-induced incipient rifting (Flowers et al., 2006, 2008).

This thesis mainly focuses on the Alberta segment of the STZ, located in the southwestern part of the east-vergent East Athabasca mylonite triangle (EAmt; Hanmer et al., 1995; see Figure 2.2b). Despite the lack of surface geological exposure, this segment has been widely associated with Paleoproterozoic subduction of the Thorsby domain and the ensuing collision between the Wabamun domain and Hearne province (Berman et al., 2007; Hoffman, 1988, 1989; Ross et al., 1991, 2000; Ross & Eaton, 2002). These collisions are

supported both by the discovery of 2.40 Ga old gabbro beneath the Thorsby domain, which was the proposed ocean basin, and by the presence of 1.78-1.85 Ga granitic rocks beneath the neighboring (southeast of the Thorsby) Rimbey domain (Ross et al., 1991; Villeneuve et al., 1993). This interpretation was largely motivated by aerial magnetic data that exhibit subparallel zones with both negative (Thorsby) and positive (Rimbey) magnetic signatures; Ross et al., 1991; Figure 2.3a). While the direction of slab dip remains debated (e.g., Ross & Eaton, 2002; Whitmeyer & Karlstrom, 2007), an inter-plate origin is favored by an abrupt change of potential field signatures from the Taltson magmatic zone, a key element of the Thelon orogeny (Chacko et al., 2000), to southern central Alberta across the STZ (see Figure 2.2a). Electromagnetic data (Boerner et al., 1995) rendered no recognizable signatures, but elevated levels of electrical conductivity south of the STZ, which was subsequently referred to as the 'Red Deer High', show evidence of graphitic metasedimentary rocks and iron formation within a Proterozoic foredeep sequence (Boerner et al., 1995; Nieuwenhuis et al., 2014). Most of the regional seismological investigations since the early 1990s have been supportive of a collisional tectonic framework. Pronounced upper crustal reflectors known as the 'Winagami reflection sequence' were discovered through reflection surveys to the northwest of the STZ, which may have originated from mafic intrusive sills formed during the syncollisional magmatic events (Ross & Eaton, 1997; Welford & Clowes, 2006). Directly southeast of the STZ, the crust potentially underwent anatectic melting due to plate convergence in the Proterozoic eon (Chen et al., 2015) and was subsequently thinned during an early Proterozoic crustal delamination event (Eaton et al., 1999a; Lemieux et al., 2000), a hypothesis that will be examined by the observations of this thesis in chapter 4.

### 2.1.3 Great Falls Tectonic Zone (GFTZ)

Based largely on the geological mapping of the Salmon-Anaconda tectonic zone in northern Montana, O'Neill & Lopez (1985) extrapolated their observations with extensive fault/dike-swarm systems toward the northeast and proposed a 150-200-km wide, 1500+ km-long GFTZ, extending from eastern Idaho to the southwesternmost Saskatchewan (O'Neill & Lopez, 1985; see Figure 2.2b). This broad zone is cross-cut by a series of northwest trending basement faults (O'Neill, 2007; Sims et al., 2004), extending into the interior of the Wyoming craton (Figure 2.2b). Widespread Mesoproterozoic tectonothermal overprinting and development of basement-controlled structures have been suggested in the region spanning northeastern Idaho batholiths and the cratonic basement of Montana (O'Neill & Berg, 1998; Sims et al., 2004). Similar to the STZ, the GFTZ is also recognizable as a series of northeast trending fabrics in both gravity and magnetic field data in western Montana (Thomas et al., 1987; Ross et al., 1991; Sims et al., 2004; see Figure 2.2a).

The rocks near the GFTZ have preserved records of a complex tectonic evolution history as far back as the Archean eon. Easily recognizable from northeast trending topographic lineaments along mapped high-angle faults and shear zones (O'Neill & Lopez, 1985), this geological structure is truncated in the east by the Proterozoic THO (see Figure 2.2b), which suggests an origin pre-dating the collisional orogen (Boerner et al., 1998). Central GFTZ features exposed basement rocks in the Little Belt Mountains (LBM), where Precambrian (1.86 Ga) calc-alkaline metaigneous assemblages exhibit isotopic signatures characteristic of a convergent environment (Mueller et al., 2002) and is thereby referred to as the 'Little Belt arc' (Foster et al., 2006; Whitmeyer & Karlstrom, 2007; Porritt et al., 2014). In southwestern GFTZ (see Figure 2.2b), Archean gneisses may have experienced a ~1.77 Ga granulite facies metamorphic and

partial melting event (Sims et al., 2005). The westernmost GFTZ terminates between the Archean provinces in southwest Montana and Paleoproterozoic crust in Idaho, though the exact boundary is obscured by later sedimentation and magmatic events (Foster et al., 2006). Immediately north of the GFTZ resides the southern MHB, which was at times incorporated into the southern Hearne (Holm & Schneider, 2002) or Wyoming cratons (Cavell et al., 1993; Henstock et al., 1998), but is more likely to be an independent Archean microcontinent with divergent properties between its eastern and western halves (Ross et al., 1991; Eaton et al., 1999a; Lemieux et al., 2000; Sims et al., 2005). The region south of the GFTZ is occupied by the Wyoming craton that contains Archean aged rocks dating back to 3.5 Ga (Mueller & Frost, 2006). It has been suggested that the Wyoming craton underwent significant modifications by the Laramide (80-55 Ma) deformation (Foster et al., 2006) and impingement of the Yellowstone hotspot (e.g., Schutt et al., 2008; Dave & Li, 2016).

### 2.1.4 Vulcan Structure (VS)

The VS is recognizable from a pair of east-trending gravity and magnetic anomalies (Ross et al., 1991; Villeneuve et al., 1993) sandwiched between Archean-aged Hearne (north) and MHB (south; Hoffman, 1988; Ross et al., 1991; Eaton et al., 1999a) (see Figure 2.2b). While drill core samples suggest an early Proterozoic origin (Villeneuve et al., 1993), which post-dates the granitoids beneath the MHB (2.6-3.2 Ga; Ross et al., 1991; Villeneuve et al., 1993), interpretations of the 350-km-long VS vary broadly in age [i.e., Archean (Hoffman, 1988) versus Paleoproterozoic (i.e., Ross et al., 1991; Eaton et al., 1999a)] and geometry [e.g., northward (Ross et al., 1991) versus southward (Eaton et al., 1999a; Lemieux et al., 2000) dipping]. The nature of this semi-linear geological structure has also been debated among several competing hypotheses involving a failed continental rift (Kanasewich et al., 1969), an

intraplate collision zone (Hoffman, 1990), and a Proterozoic suture separating 1) the Wyoming and Hearne cratons (Thomas et al., 1987; Hoffman, 1988) or 2) the MHB and Hearne craton (Eaton et al., 1999a; Lemieux et al., 2000; Ross, 2002).

## 2.2 Phanerozoic summary

### 2.2.1 Overview

The final stage of the assembly of Canadian Shield completed during the Grenville Orogeny (1 Ga) and led to the formation of super-continent Rodinia (Miall & Blakey, 2008). This Precambrian supercontinent was relatively short-lived (a few 100's of Ma) and the breakup commenced in the Late Proterozoic (800 Ma) (Hoffman, 1991). Laurentia was completely isolated from the surrounding continents during this widespread rifting event and was rimmed by long-standing passive margins (Miall & Blakey, 2008). During this protracted geological period, the western margin underwent a profound evolution from a passive margin established in late Precambrian (Stewart, 1972) or early Paleozoic (~540 Ma; Bond & Kominz 1984) to a convergent margin initiated in Early Jurassic (Coney, 1989; Johnston, 2001; Evenchick, 2007; Dickinson, 2009). On the other hand, the craton interior is suggested to have experienced minimal tectonic modification and remained relatively stable over a long geological time (Yuan & Romanowicz, 2010; Schaeffer & Lebedev, 2014).

The Phanerozoic development of the WCSB is dominated by the Post-Jurassic converging tectonics along the western margin of Laurentia, culminating in the Mesozoic-Cenozoic Cordilleran orogeny that shaped the entire western coast of the North America continent. The basin was developed during a major period of oblique collision between the Cordilleran terranes and North American craton (Beaumont, 1981; Cant & Stockmal, 1989). The maximum subsidence

hence the largest deposition center (i.e., the Alberta basin) was created in front of the Cordilleran Deformation Front (CDF) under the load of the easterly thrust sheets (see Figure 2.1). The sedimentary deposits contain both older (Paleozoic) platformal sequences and younger (Mesozoic-Cenozoic) eroded clastic detritus from the Cordillera, which reflect distinct evolution stages of the WCSB from an Early Paleozoic rifted margin to a foreland region of the Cordillera orogen (Porter et al. 1982; Price 1994)

### 2.2.2 Cordilleran belts

On a continental scale, the North American Cordillera (Hoffman, 1988) is a broad Phanerozoic orogenic belt that extends from Mexico northwards to Alaska. The Canadian portion consists of a series of northwest trending crustal structures, which are divided into five morphogeological belts including, from east to west, the Foreland, Omineca, Intermontane, Coast and Insular belts (Figure 2.3). Each of these belts is an assemblage of unique rock types, metamorphic grade and structural style result from distinct geological processes that collectively form the Cordillera (Monger & Price, 2002).

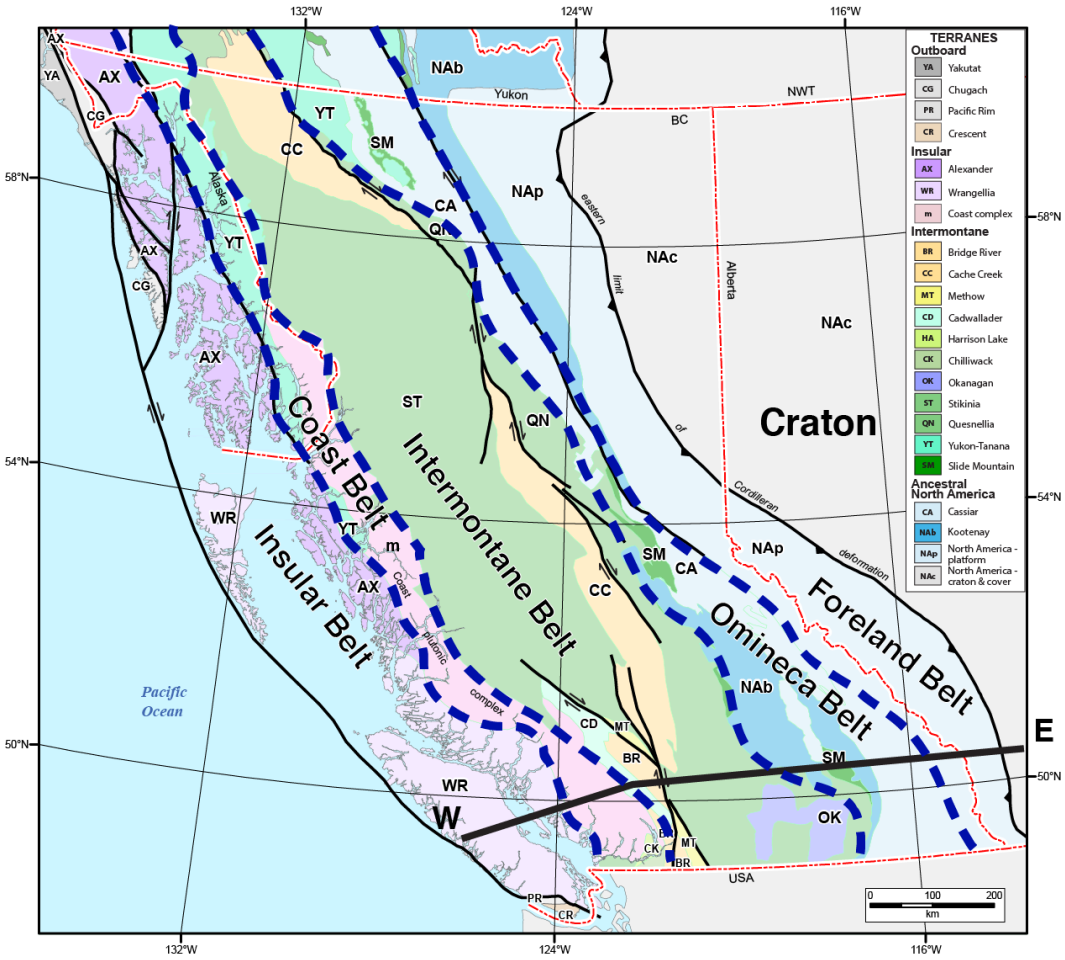


Figure 2.3 Simplified tectonic map of southern Canadian Cordillera. The blue dashed lines represent the domain boundaries between the major Cordilleran morphogeological belts. The thin black lines show the major faults system and the heavy black line marks the location of the cross-section shown in Figure 2.4. Modified after (Colpron & Nelson, 2011)

Among these Cordilleran domains, the Omineca and Coast Belts are composed of high-grade metamorphic and plutonic complexes, which record intense regional deformation and tectonothermal histories (Monger et al., 1982). The formation of these two tectonics welts has been linked to crustal thickening during successive convergences of super-terranes of the Intermontane and Insular belts with the North American craton (Monger et al., 1982). Both super-terranes

are characterized by unmetamorphosed and low-grade metamorphic rocks of sub-greenschist phases, indicating a shallow burial depth of less than 10 km (Monger & Price, 2002). The Foreland Belt comprising the easternmost Cordillera is juxtaposed to the east by the Alberta basin. This region has recorded some of the most intense deformation during the Cordilleran orogenesis as manifested by the east-verging thrust faulting and decollement folding within an easterly-tapering wedge of supracrustal rocks (Price, 1986; Figure 2.4). The continuously northeast translation of the detached supracrustal strata results in a significant shortening up to 200 km in the foreland region and induces subsidence of the basin (Percival et al., 2012).

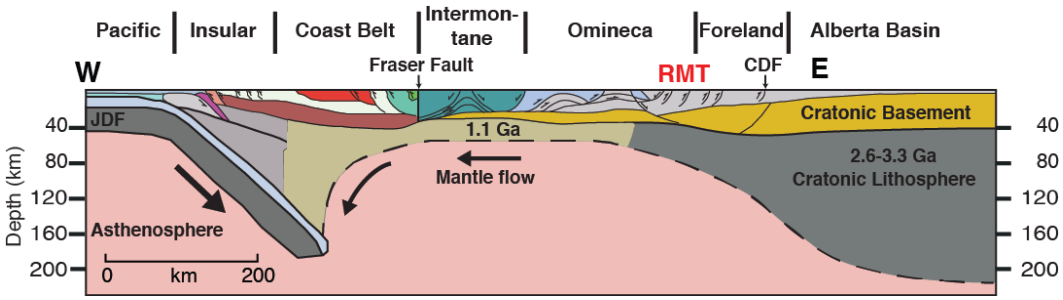


Figure 2.4 A schematic cross-section showing the structural transition from the Cordillera to craton in southwestern Canada. Modified after Monger et al. (2002). The location of the cross-section is marked by the black line in Figure 2.3. The vertical exaggeration is about 1.2:1.

### 2.2.3 Subsurface structures

The subsurface structures of the Cordillera are mainly constrained by a few deep seismic reflection and refraction lines. The synthesis of seismic observations from these profiles, in combination with geological information from stratigraphic, petrologic, geochronological studies, provide the first-order structural constraints on the across-strike variation of the Cordilleran lithosphere

(see Figure 2.4). According to this schematic cross-section, much of the Cordillera is built atop the cratonic lower crust, which extends from the Foreland Belt to the Kootenay Arc in the westernmost Omineca Belt (Price, 1981) or as far west as the Coast Belt (Cook et al., 1992). In other words, the Cordillera is mainly assembled by a collage of thin crustal rocks derived from non-North American sources, which were termed 'suspect terranes' in the earlier study (Coney et al., 1980).

As one of the circum-Pacific back arcs (Currie & Hyndman, 2006), the Canadian Cordillera is characterized by the uniformly high temperatures (1200 ºC) beneath a thin (~60 km) mantle lithosphere over a length-scale of more than 900 km (Hyndman & Currie, 2011). The hot thermal state, which is also evidenced by high heat flow values (75 $mW/m^2$), and the resulting thermal expansion are largely responsible for the high elevation (>1000 m) of the mountain belt in spite of a shallow crustal root of ~35 km (Hyndman & Currie, 2011). These observations contrast with the low-elevated (500 m), thick (40-45 km) craton in the east. Geophysical studies have also reported a pronounced variation in physical properties associated with the Cordillera-Craton transition, which mainly include the crustal/mantle seismic velocities (Clowes et al., 1995; Frederiksen et al., 1998; Nettles & Dziewoński, 2008; Sigloch et al., 2008; Mercier et al., 2009; Schaeffer & Lebedev, 2014; Yuan et al., 2014), surface heat flow (Hyndman & Lewis, 1999) and mantle electrical conductivity (Rippe et al., 2013). In addition, the significant increases in crust (>10 km; Clowes et al., 1995) and lithosphere (>200 km; Cook & Erdmer, 2005; Bao et al., 2014) thicknesses were found near the Rocky Mountain Trench, a prominent topographic low separating the Foreland Belt from the Omineca Belt (see Figure 2.4).

## 2.3 Previous seismic studies

### 2.3.1 Active source surveys

The first active source studies of the WCSB were conducted to examine crustal structures in terms of velocity, thickness, faulting and internal layering (e.g., Richards & Walker, 1959; Kanasewich & Cumming, 1965; Kanasewich, 1968; Clowes et al., 1968; Kanasewich et al., 1969; Chandra & Cumming, 1972; Ganley & Cumming, 1974). Motivated by these pioneering works, the Canadian geoscience initiative of LITHOPROBE project was launched in 1990's and became a major impetus for the advance in tectonic theories of the WCSB (Ross, 2002b; Clowes et al., 2010). Seismic reflectivity on LITHOPROBE transects, in combination with other geophysical observations (e.g., seismic velocity, electrical resistivity and potential fields; Boerner et al., 2000; Hope & Eaton, 2002; Gu & Shen, 2015), played a fundamental role in elucidating the tectonic evolutionary history of the WCSB (Ross, 2002a). These studies have revealed syn- to post-collisional structures across the inferred sutures, which are consistent with a convergent tectonic environment in the Proterozoic era (Hoffman, 1989; see Ross, 2002a for review). The rest of the section will highlight the key findings on the respective survey lines.

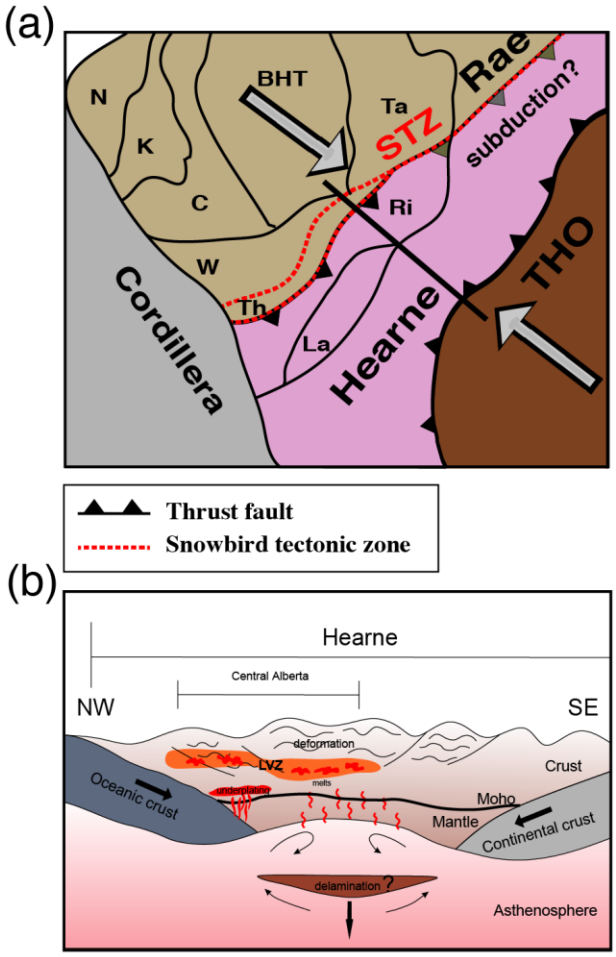


Figure 2.5 (a) A schematic regional tectonic map showing a 'Tectonic Vise' framework for development of Hearne province. (b) A schematic diagram to demonstrate the major tectonic events including the subduction of oceanic crust, collisional crustal thickening, melting and lithosphere delamination during plate convergences. The vertical scale of the crust has been exaggerated for a better visual inspection.

Central Alberta Transect (CAT), a 521 km long profile recorded 1991, sampled a crustal corridor from ~100 km to the west of Edmonton to the Saskatchewan border (Bouzidi et al., 2002; see Figure 1.3a). This transect highlighted the role of the STZ as a collisional boundary (Ross et al., 1995; Eaton

& Cassidy, 1996) and revealed thrust-imbricated crust beneath the Hearne province (Ross et al., 1995, 2000). These seismic observations, together with increased mantle conductivity (Boerner et al., 1999, 2000), led to the 'Tectonic Vise' model in central Alberta (Ross et al., 2000; Ross, 2002a), where the Hearne province was suggested to be trapped between oceanic subduction along the STZ in the northwest (Ross et al., 1991, 1995; Eaton & Cassidy, 1996) and the coeval underthrusting of the THO in the southeast, resulting to a collisional Plateau (Lucas et al., 1993; Lewry et al., 1994; Corrigan et al., 2005) (Figure 2.5a). The mechanically thickened Hearne mantle lithosphere may induce gravitational instability and trigger a delamination event (Figure 2.5b), a mechanism will be examined in detail in chapter 5.

Following the accomplishment of the first phase (i.e., CAT) of LITHOPROBE, the Peace River Arch Industrial Seismic Experiment (PRAISE) that consists of 608 km of profiles were acquired in 1994 in northwestern Alberta. The scientific goal of this experiment was to elucidate the enigmatic nature of the Peace River Arch (Eaton et al., 1999b) and provide new insight into the complex assembly history of northern Alberta (Ross & Eaton, 2002). In addition, the prominent mid-crustal sub-horizontal reflectors (i.e., Winagami reflection sequence) revealed along this profile offered evidence for intrusive mafic sheets emplaced during the brittle indentation of the Slave craton into western Canadian Shield (Ross & Eaton, 1997; Welford & Clowes, 2006).

Seismic observations from active source experiments (Snelson et al., 1998; Clowes et al., 2002; Gorman et al., 2002) in southern Alberta and northern Montana offer only a limited window into the basement structure, due to a thick sedimentary cover. Among these studies, the Vibroseis Augmented Listen Time (VAULT; Eaton et al., 1999a; Lemieux et al., 2000; Bouzidi et al., 2002) and DEEPPROBE transects of the SALT experiment (Clowes et al., 2002; Gorman et al., 2002) laid the groundwork for a regional tectonic evolutionary model of the

southern WCSB. Based on seismic velocity structures along an 800 km-long transect, this model features the early Archean amalgamation of the MHB and its subsequent collisions with the Wyoming (south) and Hearne (north) provinces (Clowes et al., 2002; Gorman et al., 2002). This unique assembly process was further supported by a recent magnetotelluric survey in southern Alberta, which attributed the origin of an upper mantle conductor along the VS to an enrichment event during the plate convergence (Nieuwenhuis et al., 2014). Among the key findings, P wave reflections recorded by the DEEPPROBE (Gorman et al., 2002) suggested the existence of a high-velocity lower crustal layer (LCL) beneath the MHB in southern Alberta, which deepens across the GFTZ along a southeast striking transect roughly parallel to the foothills of the Rocky Mountains (see SAREX profile in Figure 1.3a). A critical observation from this transect is the presence of a thick (60 km) high (>7 km/sec) velocity lower crust underlying much of the MHB and Wyoming craton, which has been interpreted to be a magmatic underplated layer during Paleoproterozoic (Clowes et al., 2002; Gorman et al., 2002). Chapter 4 will provide new insights into this underplating process and the accompanied tectonothermal modifications.

### 2.3.2 Passive source studies

Crustal constraints from LITHOPROBE form the basic tectonic framework of the WCSB. Further knowledge of crust and underlying mantle structures was gained through passive source imaging with broader data coverage and greater penetrating power, which offers improved sensitive to the thermal, chemical and elastic properties of the deep Earth (Liu & Gu, 2012; Tesoniero et al., 2015). Earlier continental-scale seismic tomographic models provide preliminary constraints on mantle structures beneath the WCSB (Frederiksen et al., 1998; Frederiksen et al., 2001; Van Der Lee & Frederiksen, 2005). On a regional scale, studies using receiver functions computed at two permanent stations from

Canadian National Seismograph Network (CNSN) (see Figure 1.3b) revealed 1D crustal structures (Cassidy, 1995; Eaton & Cassidy, 1996). Later Chen et al. (2015) expanded the receiver function analysis and constructed 1D velocity profiles at 12 stations in central-southern Alberta. An earlier effort of regional seismic tomography was made by Shragge et al. (2002) using a temporal array of 11 stations deployed in the same region (see Figure 1.3a), the model of which showed high velocities beneath the Archean Hearne province down to ~300 km. The temporal teleseismic experiments in northwestern Canada, e.g., the Canadian Northwest Experiment (CANOE) and the Portable Observatories of Lithospheric Analysis and Research Investigating Seismicity (POLARIS) arrays, enabled more detailed examinations of the crust and upper mantle beneath the Cordilleran portion of the WCSB. Mercier et al. (2009) utilized the data from these networks to invert for the first regional-scale P- and S-wave velocity models of the upper mantle in western Canada. The high-resolution images showed a sharp transition in seismic velocities at the Cordilleran Deformation Front (CDF) from the slow Phanerozoic Cordillera to the fast Precambrian cratons. This structural transition was further supported by the results of ambient noise tomography at crustal depths (Dalton et al., 2011; Kao et al., 2013).

Despite the seminal contributions from these earlier broadband analyses, relatively restrictive station distributions and short deployment time presented major challenges to the investigation of the detailed mantle structure beneath the WCSB. These data related issues have been largely resolved by the establishment of regional seismic networks in recent years, most notably the Canadian Rockies and Alberta Network (CRANE; Gu et al., 2011), which initiated in mid-2006 and rapidly expanded after 2010, the Regional Alberta Observatory for Earthquake Studies Network (RAVEN; since 2013; Schultz & Stern, 2015) and TransAlta Dam Monitoring Network (TD; since 2013) (see Figure 1.3b for network distributions). These arrays form the backbone for regional structural analysis (Gu et al., 2011, 2015; Chen et al., 2015; Gu & Shen, 2015;) and seismicity

monitoring (Schultz et al., 2014, 2015, 2018; Wang et al. 2016, 2017, 2018). By combining all the available recordings from CRANE and surrounding networks, the data volume and distribution far exceed those from earlier broadband seismic analyses in this region. Benefiting from the array data*, recent broadband studies offered improved seismic constraints on the velocity (Bao et al., 2014; Bao & Eaton, 2015) and anisotropic structures of the mantle lithosphere near the southern WCSB (Bao et al., 2016; Wu et al., 2018).

* Seismic data for USArray, RAVEN, and CANOE networks are provided by IRIS Data Management Center (http://ds.iris.edu/ds/nodes/ dmc/). Seismic data for CNSN network could be requested from Canadian National Data Center (http://www. earthquakescanada.nrcan.gc.ca/ stndon/CNDC/index-en.php). Traveltime data could be accessed through website https://sites.google. com/a/ualberta.ca/seisworld/data. The tomographic models will be made available from the IRIS Earth Model Collaboration website.

# Chapter 3 Passive seismic imaging techniques

## 3.1 Receiver function method

### 3.1.1 Overview

Receiver Function (RF) is one of the most commonly used seismic imaging techniques in passive source studies. It utilizes the scattered body waves (P-to-S or S-to-P) generated at major impedance interfaces to probe the structures beneath a recording station (Langston, 1977, 1979). The strong sensitivity of RF to subsurface discontinuities has made it an effective tool to image the Moho (e.g., Gilbert, 2012; Schmandt et al., 2015), mid-lithospheric discontinuities (e.g., Abt et al., 2010; Hopper & Fischer, 2015; Chen et al., 2018), Lithosphere-Asthenosphere boundary (LAB; e.g., Lekić & Fischer, 2014; Liu & Gao, 2018; see Kind et al., 2012 for a review) and mantle transition zone interfaces (e.g., A. Li et al., 1998; X. Li et al., 2000; Chen & Ai, 2009; Gao & Liu, 2014; Gu et al., 2015).

A schematic diagram of receiver function is shown in Figure 3.1, where a plane wave incident upon a discontinuity (e.g., Moho) beneath a three-component station. The vertical and radial components seismogram, $Z(t)$ and $R(t)$, contain the responses of subsurface to the incoming P wave and are expressed by time series

$$\begin{aligned} Z(t) &= \sum_{k=0}^{n} z_k s(t - t_k) \\ R(t) &= \sum_{k=0}^{n} r_k s(t - t_k) \end{aligned}, \tag{3.1}$$

where $s(t)$ is the source time function, variables $z_k$ and $r_k$ are the amplitude of the $k$-th ray on the vertical and radial components, respectively and $t_k$ is the corresponding arrival time.

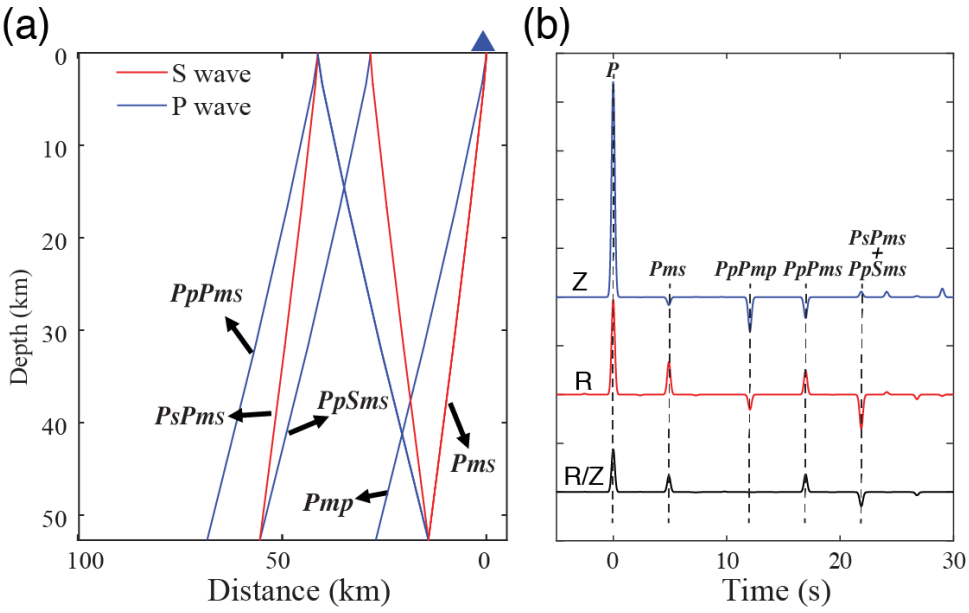


Figure 3.1 (a) Schematic diagram of ray paths of incident waves. (b) Vertical (Z), radial (R) component seismograms and the receiver function (R/Z) generated by the response of a layer over half space model to an incoming plane P wave.

The removal of the source term (source equalization) is a critical step for improving the coherency of the scattered wave energy, which is typically conducted by deconvolving the vertical response (Ammon, 1991), an approximation of the source time function, from the radial-component seismogram. In frequency domain, the source equalization is conducted by

$$RF(\omega) = \frac{R(\omega)Z^*(\omega)}{\max\{Z(\omega)Z^*(\omega), c \cdot \max[Z(\omega)Z^*(\omega)]\}} e^{-(\frac{\omega}{2\alpha})^2}, \tag{3.2}$$

where $R(\omega)$ and $Z(\omega)$ are the frequency spectra of the radial and vertical component seismograms, respectively, symbol '*' represents conjugate, $c$ is the 'water-level' parameter, a threshold determines the minimum amplitude allowed in the denominator, and $\alpha$ is the Gaussian parameter controls the frequency range of the filter. We obtain a source equalized radial-component seismogram upon inverse Fourier transform, which is defined as the receiver function. Except for the 'water-level' approach (Clayton & Wiggins, 1976), typical deconvolution schemes include the time domain deconvolution (Gurrola et al., 1995), the frequency-based multi-taper deconvolution (Park & Levin, 2000) and the time-domain iterative deconvolution (Ligorría & Ammon, 1999). The last approach, due to its objectivity in the choice of parameters, is widely used for automating the RF processing (e.g., EarthScope Automated Receiver Survey; Trabant et al., 2012) and is adopted in this thesis.

This time-domain approach, instead of performing a deconvolution operation, conducts an iterative least-squares optimization to minimize the difference between the observed and synthetic radial-component seismograms (Ligorría & Ammon, 1999). As a first step, the vertical- and radial-component seismograms are cross-correlated to extract the information of the largest spike (amplitude and lag) in the correlation function:

$$A(t) = \begin{cases} \max\{\int Z(\tau)R(\tau + t)d\tau\}, t = t_0 \\ 0, \text{ elsewhere} \end{cases}, \tag{3.3}$$

where $t_0$ is the delay time of the spike. The maximum amplitude $A(t_0)$ is weighted by the squared amplitude of the direct P wave for approximating the response in the RF. This current RF estimate is then convolved with the vertical recording to compute a 'synthetic' seismogram of the radial component:

$$R_s(t) = Z(t) * A(t). \tag{3.4}$$

The synthetic waveform is subsequently subtracted from the actual radial-component seismogram to obtain a new estimate

$$R'(t) = R(t) - R_s(t), \tag{3.5}$$

which is again cross-correlated with the vertical-component seismogram to extract a new spike. This process proceeds in an interactive manner to gradually increase the RF response until a predefined misfit threshold or the maximum iteration number is reached.

The coherency of scattered wave energy is significantly improved through deconvolution. Still, a single RF often suffers from a low signal-to-noise ratio (SNR), causing difficulty in identifying the weak phases. A common remedy is to stack the RFs from a single or multiple stations while assuming an averaged (horizontal layering) structure near the recording station. Alternatively, one can consider the directional variation of the structures and group the RFs based on the spatial proximity of the conversion points on the subsurface discontinuities (Dueker & Sheehan, 1997; Yuan et al., 1997). The common conversion point (CCP) gather provides a 2D or 3D illumination of the subsurface with significantly improved horizontal resolution. More sophisticated stacking is achieved through migration imaging that back-propagates the scattered wavefield to its scattering source in the subsurface (Yilmaz, 2001). This well-established imaging approach in exploration seismology relies on closely spaced seismic stations to provide dense spatial sampling of the wavefield. It has recently become available in passive source studies thanks to the development of seismic arrays. Compared to the CCP stacking that assumes a (locally) 1D earth, teleseismic migration imaging considers scatterings from realistic 2D or 3D structures (Rondenay, 2009), and hence is more effective in resolving complex geological targets (e.g., steep faults, dipping slab and laterally discontinuous interfaces). Theoretical studies have been focused on teleseismic migration

methods with ray-based Kirchhoff (e.g., Ryberg & Weber, 2000; Cheng et al., 2016), Generalized Radon Transform (e.g., Bostock et al., 2001; Rondenay et al., 2005) and wave-equation based schemes (e.g., Chen et al., 2005; Shang et al., 2012). Along with the theoretical improvements, the teleseismic migration techniques have been successfully applied to conducting high-resolution scattering imaging in various tectonic settings including continental cratons (e.g., Levander et al., 2005; Chen, 2009), subduction zones (e.g., Rondenay et al., 2008; Cheng et al., 2017) and orogenic belts (e.g., Chen et al., 2006; Shang et al., 2017; Wang et al., 2018). Except for the aforementioned time-domain stacking methods, transformation based approach such as *H*-$\kappa$ stacking (Zhu & Kanamori, 2000) is routinely applied to measure the Moho depth and Vp/Vs ratio around the globe. In this thesis, we utilize both *H*-$\kappa$ and CCP stacking methods to image the crustal structures in the study region (chapter 4). The following sections provide more details on the RF processing and these two imaging methods.

### 3.1.2 Receiver Function processing

For the investigations in this thesis we calculate RFs at 158 stations using earthquakes occurred between 1991 and 2017 with moment magnitudes greater than 5.5 and epicentral distances ranging between 30° and 90° (Figures 3.2a and 3.2b). These requirements are ideal for a RF analysis (Langston, 1977; Vinnik, 1977; Ammon, 1991; Rondenay, 2009) due to near-vertical incidence angles of the P wave ray paths and free of interfering phases (e.g., mantle triplication and PcP). After the removal of instrument responses, we rotate the original components to vertical, radial, and transverse orientations, and subsequently apply a Butterworth band-pass filter with corner frequencies of 0.02 Hz and 3.5 Hz; this frequency range was empirically chosen based on experimentation to maximize the energy of the converted phases (Chen et al., 2015). Then the standard deviation of the vertical-component seismogram is computed in the time window

of 1-25 s after the predicted P wave arrival time based on the PREM (Dziewonski & Anderson, 1981). The ratio between this value and that of the noise window, which is similarly defined for the time window of 105-5 s prior to P, is used as the SNR criterion to eliminate noisy records; we retain 19,085 (45% of the original data) high-quality source-station pairs with SNR>2 for the analysis of RFs. The back azimuths of the station pairs favor a northwest-southeast orientation that precludes a comprehensive analysis of azimuth-dependent effects beneath most of the stations (Figure 3.2c).

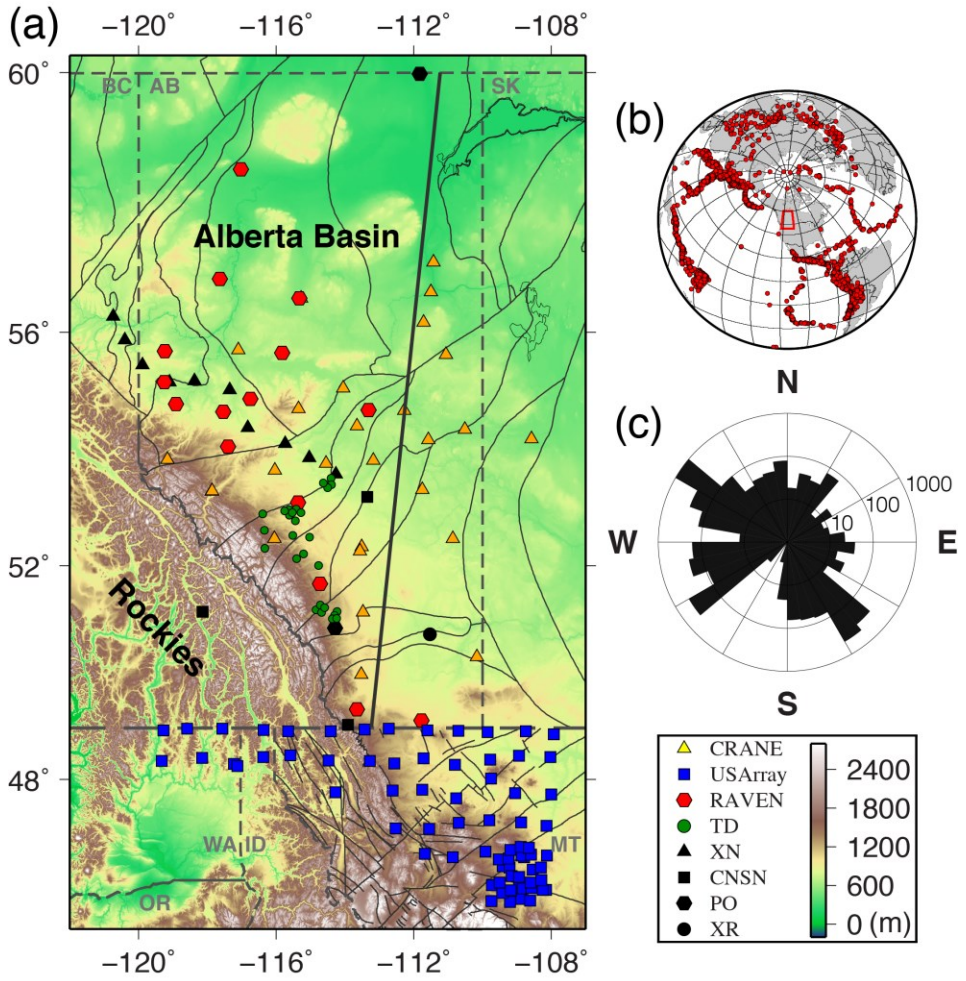


Figure 3.2 (a) Distribution of regional seismic stations examined in this thesis. The thin black lines indicate the tectonic boundaries within the WCSB and fault networks in northern Montana. The thick black line marks the location of a receiver function profile shown in Figure 4.1 in chapter 4. (b) Earthquakes (red circles) analyzed in this study. The study region is indicated by the red-colored polygon at the center of map. (c) A rose diagram (in logarithmic scale) showing the azimuth distribution of the earthquakes.

The RFs are computed using the iterative time domain deconvolution technique of Ligorría & Ammon (1999) and an empirically determined Gaussian

filter width of 2.5 (see section 3.1.1 for details). Up to 400 iterations are performed during the least-squares minimization to ensure the convergence of the solutions, while a minimum 0.001% data fit improvement is imposed on each additional spike (Chen et al., 2015; Gu et al., 2015). The data misfit and percentage match to the original data allow further selection of the data set: RFs with a misfit greater than 20% are automatically rejected. This procedure improves the quality of the converted phases (rather than the dominant P phase), which yields 11,763 high-quality RFs for the subsequent processing. We then inspect each trace to further refine our data set and remove traces with week Moho conversions or anomalously large reverberated energies; 10,043 traces are eventually retained after manual quality control.

### 3.1.3 *H*-$\kappa$ Stacking

To improve the crustal constraints, we simultaneously determine crustal thickness ($H$) and the ratio between P and S velocities ($\kappa$) based on the $H$-$\kappa$ stacking method of Zhu & Kanamori (2000). This approach performs a grid search for the most energetic stack of the direct *Ps* phase and crustal multiples such as *PpPms*, *PsPms* + *PpSms* based on predicted delays relative to the incident P wave (Zhu & Kanamori, 2000; Yeck et al., 2013; see Figure 3.1). We improve the stability and flexibility of Zhu & Kanamori (2000) further through a ray tracing-based approach (Niu et al., 2007) and a multilayer global crustal model (CRUST1.0; Laske et al., 2013). The arrival times of *Ps* and the first order reverberated phases are calculated by

$$t_{Ps} = \int_{z=0}^{z=h} \left(\sqrt{\frac{1}{V_s(z)^2} - p^2} - \sqrt{\frac{1}{V_p(z)^2} - p^2}\right) dz, \tag{3.6}$$

$$t_{PpPs} = \int_{z=0}^{z=h} \left(\sqrt{\frac{1}{V_s(z)^2} - p^2} + \sqrt{\frac{1}{V_p(z)^2} - p^2}\right) dz, \tag{3.7}$$

$$t_{PpPs+PsPs} = \int_{z=0}^{z=h} 2\sqrt{\frac{1}{V_s(z)^2} - p^2}\,dz, \tag{3.8}$$

where $p$ is the ray parameter of the incident P wave, $h$ is a presumed crustal thickness. This implementation allows the inclusion of known regional structures such as sediment depth and crustal velocities beneath a given seismic station. Given a pair of values of crustal thickness ($H$) and Vp/Vs ratio ($\kappa$), the stacked amplitude of three phases is calculated a weighted sum:

$$A(H,\kappa) = w_1 r(t_{Ps}) + w_2 r(t_{PpPs}) + w_3 r(t_{PpSs+PsPs}), \tag{3.9}$$

where $r(t)$ is the amplitude of receiver function at phase arrival times predicted with equations (3.6)-(3.8) and $w_i$ is the weighting factor subject to constraint $\sum w_i = 1$. Equal weights (i.e., 1/3) are applied to the three converted phases during energy stacking in view of the robust waveforms recorded by the majority of the stations (Figures 3.3a and 3.3c). The optimal combination of crustal thickness and Vp/Vs ratio is determined by the peak amplitude in the $H$-$\kappa$ plot (Figures 3.3b and 3.3d). As an example, the measurement at station CLA at the Rocky Mountain foothills renders respective crustal thickness and Vp/Vs ratio of ~53 km and 1.74, and the measurement at station RW2 in the Alberta basin shows the respective values of ~40 km and 1.75. In comparison with a single-layer approximation, maximum energies from ray tracing-based approach generally agree to within 0.2 km in crustal thickness and 0.01 in Vp/Vs ratio. The ray tracing-based approach yields more coherent stacking energy in the $H$-$\kappa$ domain than the earlier approach, hence is adopted in this study.

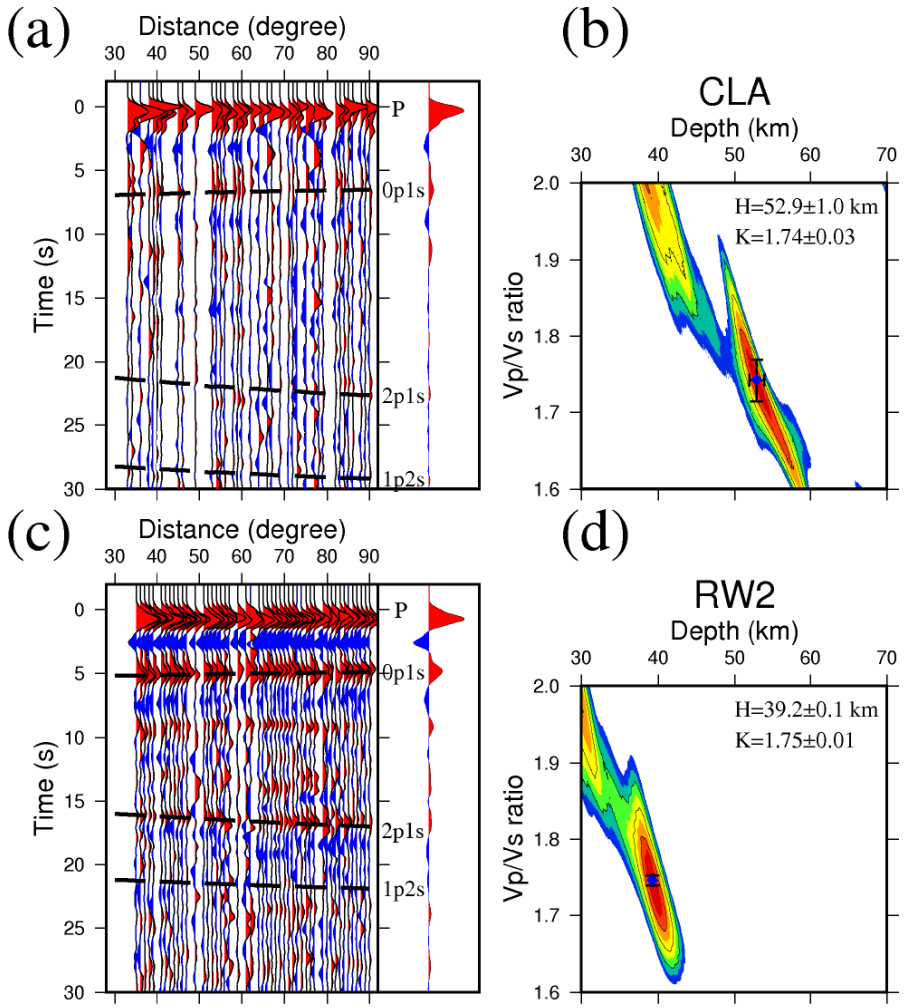


Figure 3.3 (a) RFs from station CLA. The dashed black lines mark the predicted arrival times of converted phases from *H*-κ analysis. *Pms* phase with 1 leg of S converted wave is defined by 0p1s, and 2p1s and 1p2s are defined similarly for the other two scattering phases. The stacked trace is shown on the right panel. The stacking amplitude of reverberated phase is low due to the presence of moveout. (b) The *H*-κ diagram of RFs from station CLA. (c)-(d) Same as (a)-(b) but for station RW2.

### 3.1.4 Common Conversion Point Stacking

Compared to the *H*-κ stacking that provides a point estimate of near-station structure, the CCP imaging considers the actual locations where conversions

occur, hence providing a better lateral sampling to the subsurface. For CCP imaging using P-wave RF, a critical step is to locate the piercing points of the P-to-S converted waves, which are generally distributed in a close (<30 km) proximity of the recording station at crustal depths (Figure 3.4).

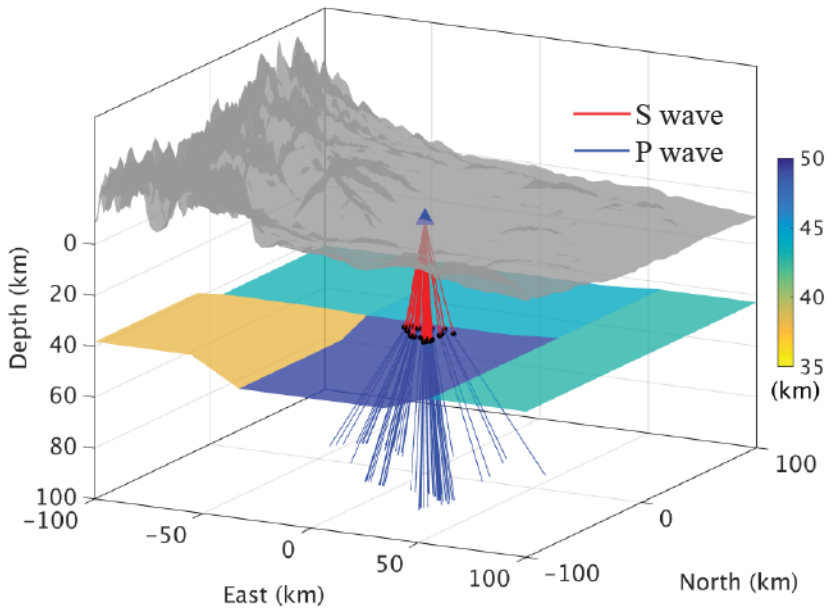


Figure 3.4 A schematic diagram demonstrating the ray paths of P-to-S conversions beneath a station in the foothills. The conversion points are marked by the black circles on the Moho interface. Compressional and shear waves are indicated using blue and red colors, respectively.

The location determination is usually conducted by tracing the ray-path of (converted) shear wave through an assumed 1D velocity model. At depth $z$, the horizontal position of the conversion point is computed by

$$X(p) = \int_{z=0}^{z=h} \frac{p\, dz}{\sqrt{\frac{1}{V_s(z)^2} - p^2}}, \tag{3.10}$$

where $p$ is the ray parameter of the P-wave in view of a minimal difference between $P$ and $Ps$ ray paths at teleseismic (>30º) distance. To map RF travel times to depths, we use equation (3.6) while assuming all phases on the RF are the P-to-S scattering mode. In a recent study by Schmandt et al. (2015), the latter two scattering phases (2p1s and 1p2s; see Figure 3.3) were migrated similarly using equations (3.7)-(3.8), which, in combination with the result from 0p1s phase, provided a better illumination of the subsurface structure. An example CCP gather is shown in Figure 3.5, where the relatively small station spacing (~30 km) leads to overlapped imaging area at the Moho depth (~40 km). More detailed analysis on the choice of bin size and the horizontal resolution of CCP imaging will be provided in chapter 4.

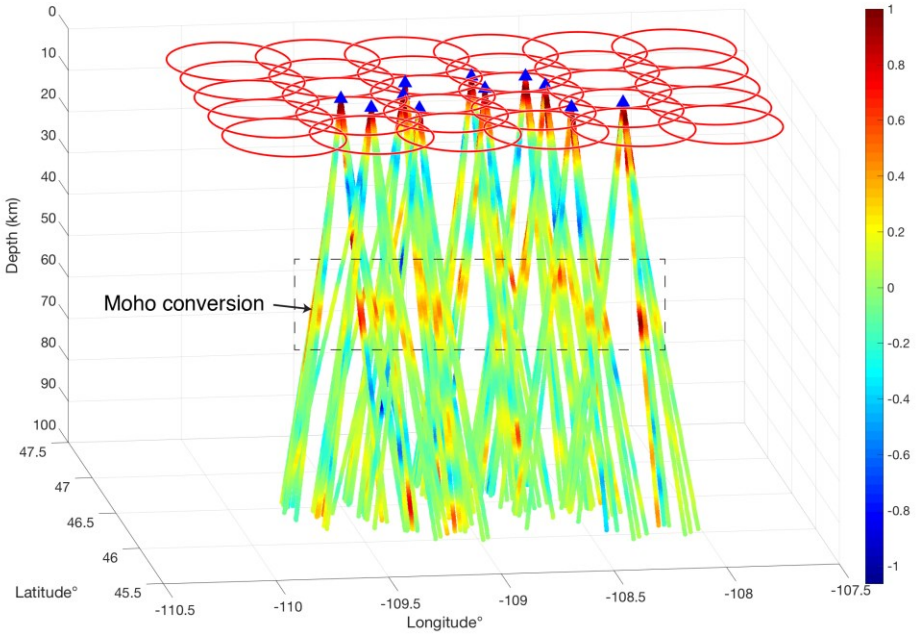


Figure 3.5 A CCP gather constructed with RFs from 11 stations in northern US. The RF amplitude is color-coded and the Moho interface is characterized by the strong positive conversions in the enclosed area. The circles at the surface represent the bins used in the RF stacking.

## 3.2 Teleseismic P-wave travel time tomography

### 3.2.1 Overview

Seismic tomography is one of the most effective imaging tools to map the elastic parameters (e.g., velocity, density, attenuation, anisotropy), thermal state (temperature) and composition (e.g., rock type, metamorphic grade, water content) of the Earth's interior, providing critical constraints on the structures and dynamics from the crust to the core. Tomographic methods are highly diversified and differ in terms of source type (active versus passive), phase selection (body versus surface waves), data type (travel time versus waveform), model scale (regional versus global) and wave propagation theory (ray versus finite-frequency approximations) (Van Der Hilst & Kárason, 1999; Dahlen et al., 2000; Hung et al., 2000, 2004; Montelli et al., 2004a, 2004b; Liu & Tromp, 2006; Tape et al., 2007, 2009; Liu & Gu, 2012). This thesis focuses on a specific tomography category that utilizes travel times of teleseismic body waves recorded at a regional array to probe the underlying velocity structures. The origin of this tomographic approach can be traced back to 1977, when Aki, Christofersson and Husebye published the seminal study using the Norsar array (Aki et al., 1977), and since then this method was named as the ACH tomography after the three authors' initials. The ever-growing seismic data volume from digital stations, especially the dense regional/continental scale arrays (e.g. USArray, Hi-net, ChinArray), has greatly motivated the development of tomographic techniques in terms of travel-time measurements (e.g., ; VanDecar & Crosson, 1990; Rawlinson & Kennett, 2004), model parameterizations (Sambridge, 1990; Sambridge & Guđmundsson, 1998), propagating theory (e.g., Dahlen et al., 2000; Hung et al., 2000) and inversion methods (Humphreys & Clayton, 1988; Tromp et al., 2005; Liu & Tromp, 2006; Tape et al., 2007, 2009).

The idea of teleseismic tomography is similar to that of the computer aided tomography in medical imaging. The imaging target (crust and mantle) is sampled by the rays (seismic waves) emitted by the source (earthquakes) and received by the sensor (seismic stations). The travel times of rays are determined by the geometry and velocity distribution along the ray path. The material properties (elastic parameters) of the crust and mantle rocks can then be resolved by solving an inverse problem using travel times and a projection function governed by physics of wave propagation (Iyer & Hirahara, 1993; Liu & Gu, 2012). The following sections introduce each of the key elements in tomographic imaging, including travel-time measurement, correction and kernel computation.

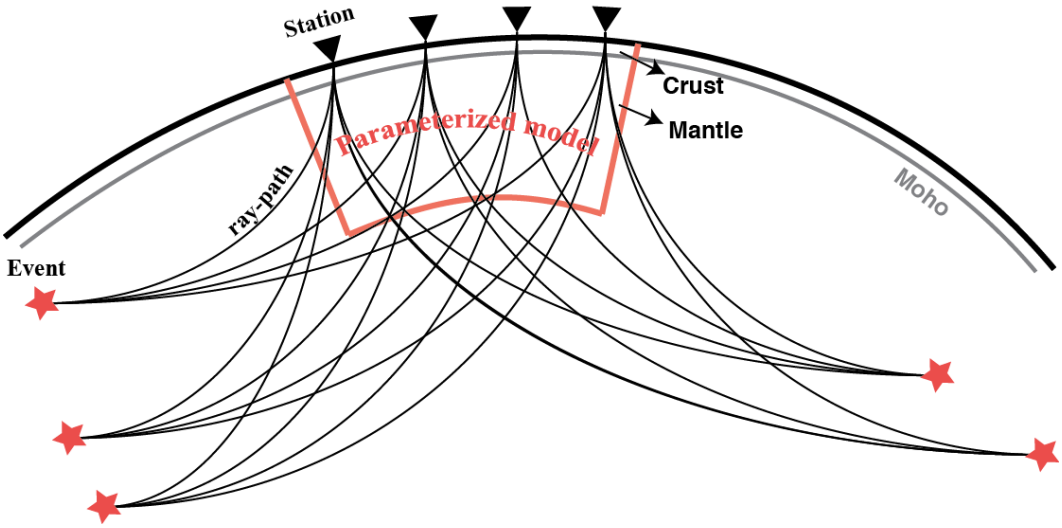


Figure 3.6 A schematic diagram showing the concept of teleseismic body wave tomography. Modified after Chen (2014).

### 3.2.2 Travel-time measurement

Travel times are measured at all stations recording the same teleseismic event. As a first step, preliminary travel times of P and S phases are predicted based on AK135 (Kennett et al., 1995), a 1D reference continental earth model; at

this stage, heterogeneities become apparent from the misalignment of the arrivals (Figure 3.7a). Then time shifts between station pairs are measured using the Multi-Channel Cross-Correlation method (MCCC; VanDecar & Crosson, 1990). For each station pair, the relative time delay between phase arrivals is determined by

$$\phi_{ij}(\tau) = \frac{\delta t}{T} \sum_{k=1}^{T/\delta t} x_i\left(t_i^p + t_0 + k\delta t + \tau\right) x_j\left(t_j^p + t_0 + k\delta t\right), \tag{3.11}$$

where $x_i$ is the waveform of the $i$-th trace, $t_i^p$ is the preliminary phase arrival time calculated based on a reference Earth model (e.g. AK135), $t_0$ is the difference between the preliminary time and the beginning of the correlation window surrounding the phase of interest (e.g., P wave), $\tau$ is the time lag, $T$ is the length of the correlation window and $\delta t$ represents the sampling interval. The time lag between each station pair ($\tau_{ij}^{\max}$) is determined as the time shift that leads to the maximum cross-correlation value. The combination of time lag and differential preliminary time defines the relative travel time between two stations:

$$\delta t_{ij} = t_i^p - t_j^p - \tau_{ij}^{\max}. \tag{3.12}$$

Consequently, a group of $N$ stations results in $N(N-1)/2$ relative travel-time measurements, which forms a system of linear equations with the form

$$t_i - t_j = \Delta t_{ij}, \tag{3.13}$$

where $t_i$ and $t_j$ are travel times at the $i$-th and $j$-th stations, respectively. Further least-squares optimization is applied to this inverse problem while being subjected to a constraint of $\sum t_i = 0$ to minimize the inconsistency of travel times across the array due to data noise or measurement uncertainties.

As a simple example with three stations, teleseismic P waves arrive at respective times of $t_1$, $t_2$ and $t_3$. The relative delay time between stations 1 and 2 is calculated by $t_1 - t_2 = \Delta t_{12}$, and $\Delta t_{23}$ and $\Delta t_{31}$ are calculated similarly for the other two station pairs. In an ideal case, the summation of these differential travel times is zero (i.e., $\Delta t_{12} + \Delta t_{23} + \Delta t_{31} = 0$), whereas the presence of noise often complicates the cross-correlation measurement, causing a non-zero shift. To alleviate this inconsistency, we seek an optimized solution via solving a system of linear equations

$$\begin{bmatrix} 1 & -1 & 0 \\ 1 & 0 & -1 \\ 0 & 1 & -1 \\ 1 & 1 & 1 \end{bmatrix} \begin{bmatrix} t_1 \\ t_2 \\ t_3 \end{bmatrix} = \begin{bmatrix} \Delta t_{12} \\ \Delta t_{13} \\ \Delta t_{23} \\ 0 \end{bmatrix}, \tag{3.14}$$

where the last row ($t_1 + t_2 + t_3 = 0$) is the additional constraint term for average removal, which effectively minimizes the travel-time uncertainties associated with the source effects (location and origin time). However, a key drawback is that the demean process also eliminates the information of the absolute velocity of the model, resulting in perturbations relative to an unknown regional mean. The MCCC optimized travel times show much improved coherency across the seismic array (Figure 3.7b), leading to high-accuracy measurements of the travel-time perturbations among all recording stations (Figure 3.7c).

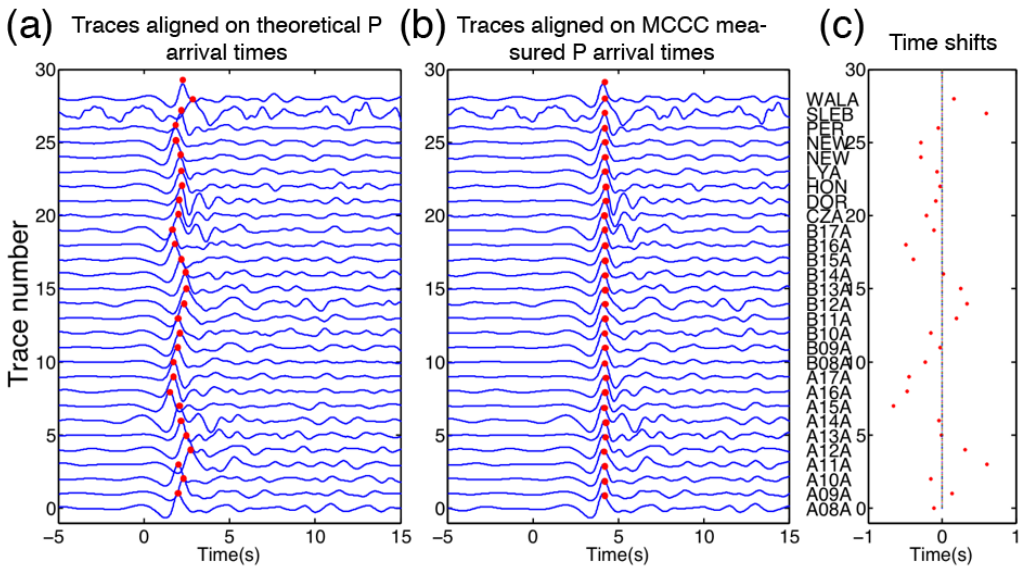


Figure 3.7 Sample travel-time measurements for an event recorded at seismic array. The seismic traces are aligned on the (a) theoretical and (b) MCCC optimized P-wave arrival times. The red circles mark the peaks of P phases. (c) Time shifts relative to the average travel time of all recording stations for this event.

Finally, the relative travel-time residual is computed by

$$\delta t_i = (t_i^{\text{obs}} - \bar{t}^{\text{obs}}) - (t_i^{\text{ak135}} - \bar{t}^{\text{ak135}}), \tag{3.15}$$

where the first bracket encloses the cross-correlation optimized relative travel time using equation (3.14) (i.e., $t_i^{\text{obs}} - \bar{t}^{\text{obs}} = t_i$) and the second bracket represents the corresponding demeaned (i.e., average-removed) theoretical (AK135 predicted) arrival time.

### 3.2.3 Travel-time correction

The raw travel times contain the structural information of both crust and the underlying mantle. However, teleseismic body waves incident nearly vertically

beneath a recording array, which results in poor vertical resolutions at shallow (especially crustal) depths (see Figure 3.6). Consequently, crustal velocities and depth could be incorrectly mapped into the underlying mantle (Hung et al., 2004). To mitigate this problem, time shifts are applied to correct for the crustal contribution. To account for lateral variations in both crustal depth and velocity, we trace rays through CRUST1.0 (Laske et al., 2013), a 1×1 degree global crust model, to the surface while assuming a fixed geometrical path predicted from AK135 continental model. The crustal travel time is calculated by

$$\tau = \int_0^h \frac{1}{c}\sqrt{1 - c^2 p^2}, \tag{3.16}$$

where $c$ is the velocity along the ray path and $h$ is the depth to the Moho. The resulting crustal correction is defined by

$$\delta t_c = \tau_{3D} - \tau_{1D}, \tag{3.17}$$

where $\tau_{3D}$ and $\tau_{1D}$ are crustal travel times in CRUST1.0 and AK135 models, respectively. The travel time perturbation due to topography (i.e., topographic correction) is calculated similarly and both correction terms are subsequently subtracted from the relative travel-time residuals to remove the effects of crust.

### 3.2.4 Kernel construction

The fundamental theoretical basis of travel-time tomography is the formulation

$$t = \int_L u(\mathbf{x}) dl, \tag{3.18}$$

where $u(\mathbf{x})$ is the slowness (i.e., inverse of velocity) at point $\mathbf{x}$ along the ray path (Nolet, 2008). Based on the Fermat's principle, the travel time remains stationary under a small perturbation to the ray path, which suggests that the effect of ray-path perturbation on the travel-time variation is secondary compared to the velocity variations. Consequently, the tomographic problem can be simplified into a linear form as

$$\delta t = \int_L \delta u(\mathbf{x}) dl, \tag{3.19}$$

where the sensitivity kernel for the travel-time inversion is simply the length of a small path segment $dl$ (Nolet, 2008). Equation (3.19) forms the core of the ray-theory based tomography, which shows that the travel-time perturbation is accumulated along the geometrical ray path in the presence of slowness anomalies. However, this assumption is only strictly valid for seismic wave travels at infinite frequency, which is unfortunately far from realistic even for high frequency body waves (e.g., 2 Hz P wave used in this study). One well-known phenomena associated with the finite-frequency waves is the non-negligible propagation effect of wavefront healing. In such case, the travel-time delay caused by a (low) velocity body will gradually diminish if the scale of anomaly (halfwidth) is comparable to the dominant wavelength of the seismic wave (Hung et al., 2001; Nolet, 2008).

On the other hand, finite-frequency theory properly considers the band-limited nature of seismic waves thereby the scattering related effects on the travel times. In the framework of finite-frequency theory, the cross-correlation determined travel times are affected by the region surrounding the geometrical ray path (i.e., the Fresnel zone) (Dahlen et al., 2000; Hung et al., 2000), where heterogeneities with cross-path dimension similar to the wave-lengths of the seismic waves can all contribute to the observed travel time shift. As a result, instead of a line

integration, as used by the ray theory (equation 3.19), the finite frequency formulation of a tomographic problem becomes

$$\delta t = \iiint_{\oplus} K(\mathbf{x})\delta c(\mathbf{x})/c(\mathbf{x})d^3(\mathbf{x}), \tag{3.20}$$

where $K(\mathbf{x})$ is the Fréchet derivative (i.e., sensitivity kernel; Dahlen et al., 2000) that maps the velocity perturbation $\delta c$ at a point **x** within in model volume $\oplus$ to relative travel-time residual $\delta t$. The kernel is derived based on the Born theory, which assumes that the scattered energy arises from the interaction between an incoming unperturbed wavefield with the scattering anomalies (Hudson & Heritage, 1981; Dahlen et al., 2000; Nolet, 2008). As a result, the computation of the kernel requires tracing all possible forward (station to scatter) and backward (receiver to scatter) rays to every scattering point in the model space, which is a computationally intensive procedure due to repeated ray tracing. The kernel calculation is greatly simplified by the paraxial* approximation that only considers similar type of scattering occurring in the vicinity of the central geometrical ray (Dahlen et al., 2000). The paraxial kernel is given by

$$K(\mathbf{x}) = -\frac{1}{2\pi c_x}\left(\frac{\mathscr{R}_{rs}}{c_r \mathscr{R}_{xr}\mathscr{R}_{xs}}\right)\frac{\int_0^\infty \omega^3 |\dot{m}(\omega)|^2 \sin[\omega \Delta T(\mathbf{x})] d\omega}{\int_0^\infty \omega^2 |\dot{m}(\omega)|^2 d\omega}, \tag{3.21}$$

where $c_x$ and $c_r$ are the respective wavespeeds at the scattering point **x** and receiver **r**, and $\mathscr{R}_{rs}$, $\mathscr{R}_{xs}$ and $\mathscr{R}_{xr}$ are geometrical spreading factors for rays associated with source-receiver, scatter-source and scatter-receiver, respectively. The detour travel time is defined by $\Delta T = T_{xs} + T_{xr} - T_{rs}$, where the subscript *rs*, *xs* and *rx* represent the ray paths from source to receiver, source to scatterer, and receiver to scatterer, respectively. The frequency-dependence of travel time delay

* Paraxial ray only considers the source-to-scatterer-to-receiver path within the first Fresnel zone.

of a perturbed ray is represented the power spectrum of source-time function $|\dot{m}(\omega)|^2$ .

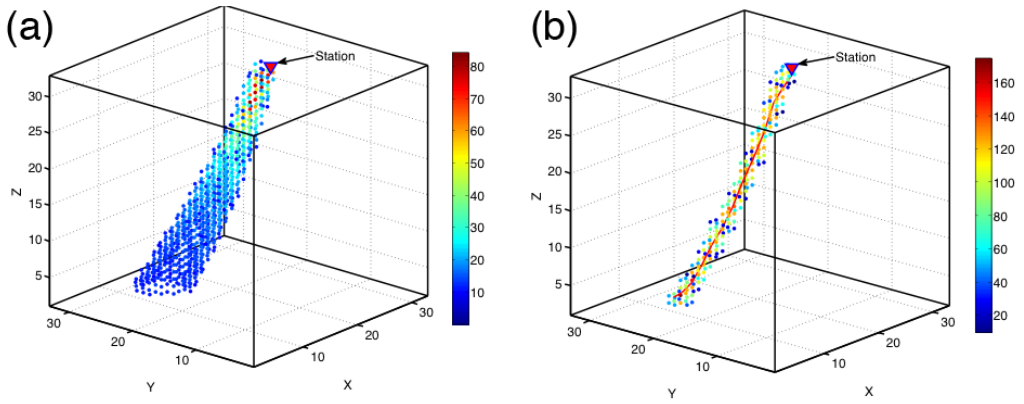


Figure 3.8 Station-side inversion kernels derived from (a) finite-frequency and (b) traditional ray theories, constructed using high-frequency P-wave measurements for a teleseismic earthquake at an epicenter distance of 85º. The finite-frequency kernel provides the varying volumetric wave sensitivity to slowness perturbations surrounding the propagating ray-path. Contrary to a constant sensitivity predicted from ray theory, the sensitivity (amplitude) of the finite-frequency kernel scales inversely with the size of the Fresnel zone.

The finite-frequency kernel provides volumetric, rather than linear, model sensitivity along the geometrical ray path (Figure 3.8). The sensitivity volume gradually broadens from the tips of the ray paths (station and location) to the mid-point (turning point), which resembles the shape of a banana. Contrary to the ray-theory based kernel that is strictly sensitive to the anomalies along the ray path, finite-frequency kernel has zero sensitivity along the central ray, producing a 'hole' inside the 'banana' (Dahlen et al., 2000; Tromp et al., 2005). As a result, the finite frequency kernel is also nicknamed the 'Banana-Doughnut kernel' (Hung et al., 2000).

## 3.3 Ambient noise tomography

### 3.3.1 Overview

Ambient noise imaging is a fast-growing research field in Earth science. Since the pioneering work by Lobkis & Weaver (2001), which showed that the inter-station Green's function can be extracted by cross-correlating the diffuse acoustic wavefields at two receivers, the study of ambient noise has made significant progresses in both theoretical understanding (e.g., Snieder, 2004; Tsai, 2009) and practical applications (e.g., Shapiro & Campillo, 2004; Yang et al., 2007; Lin et al., 2008). Different from the classical earthquake-based methods (e.g., teleseismic travel-time tomography introduced in section 3.2), ambient noise approach utilizes the source of Earth's vibration generated by ocean waves and wind that are typically manifested as background (ambient) noise on seismograms. Despite its chaotic and noise-like appearance, the diffused wave consists of scattered energy propagating through the medium and carries valuable information of the subsurface. Both theoretical and experiential studies have shown that correlation of seismic-noise traces at two stations can yield the elastic response to a point source (Aki, 1957; Claerbout, 1968; Snieder, 2004), which essentially provides a virtual earthquake source that is co-located with the receiver.

The development of ambient noise technique provides an unprecedented opportunity to image regions poorly sampled by earthquake data. One of the most successful applications is the ambient noise tomography (ANT) that utilizes the surface waves emerged from noise recordings to map the crustal and shallow upper mantle structures. These noise-induced surface waves have similar nature (e.g., velocity, dispersion) to those from earthquakes, therefore all imaging techniques that are commonly applied to earthquake data can be readily

implemented in the framework of ambient noise imaging. In addition, the ANT method is applicable to shorter-period surface waves from noise fields than available from teleseismic earthquakes, which offers significantly improved constraints on crustal properties in terms of velocity (e.g., Bensen et al., 2007; Dalton et al., 2011; Kao et al., 2013; Gu & Shen, 2015), anisotropy (e.g., Moschetti et al., 2010; Lin et al., 2011) and attenuation (e.g., Prieto et al., 2009; Lawrence & Prieto, 2011) in many parts of the world. The key processing steps of the ANT method are briefly summarized in the following sections.

### 3.3.2 Ambient noise processing

We closely follow the well-establish processing protocol proposed by Bensen et al. (2007) to process the ambient noise data, which includes data preparation, instrument response removal, temporal normalization, spectrum whitening and correlation measurement. As a first step, the continuous vertical component waveform is cut into small segments of 24-hours recording, the choice of which is mainly prompted by convenience rather than any scientific concern. A recent study showed that the adoption of a shorter noise window could contribute to a faster emergence of signals (Seats et al., 2012), and therefore is ideal for temporal arrays with limited recording times. Our study is mainly based on (semi-)permanent networks with an average recording duration is 520 days, which enables a robust extraction of high-quality noise correlation function (NCF) regardless of the choice of window length. To ensure the stability in processing, traces with recording gap larger than 10% are rejected. The traces passed the initial selection criteria are down-sampled to 1 Hz (Figure 3.9a) prior to the instrument response removal (Figure 3.9b).

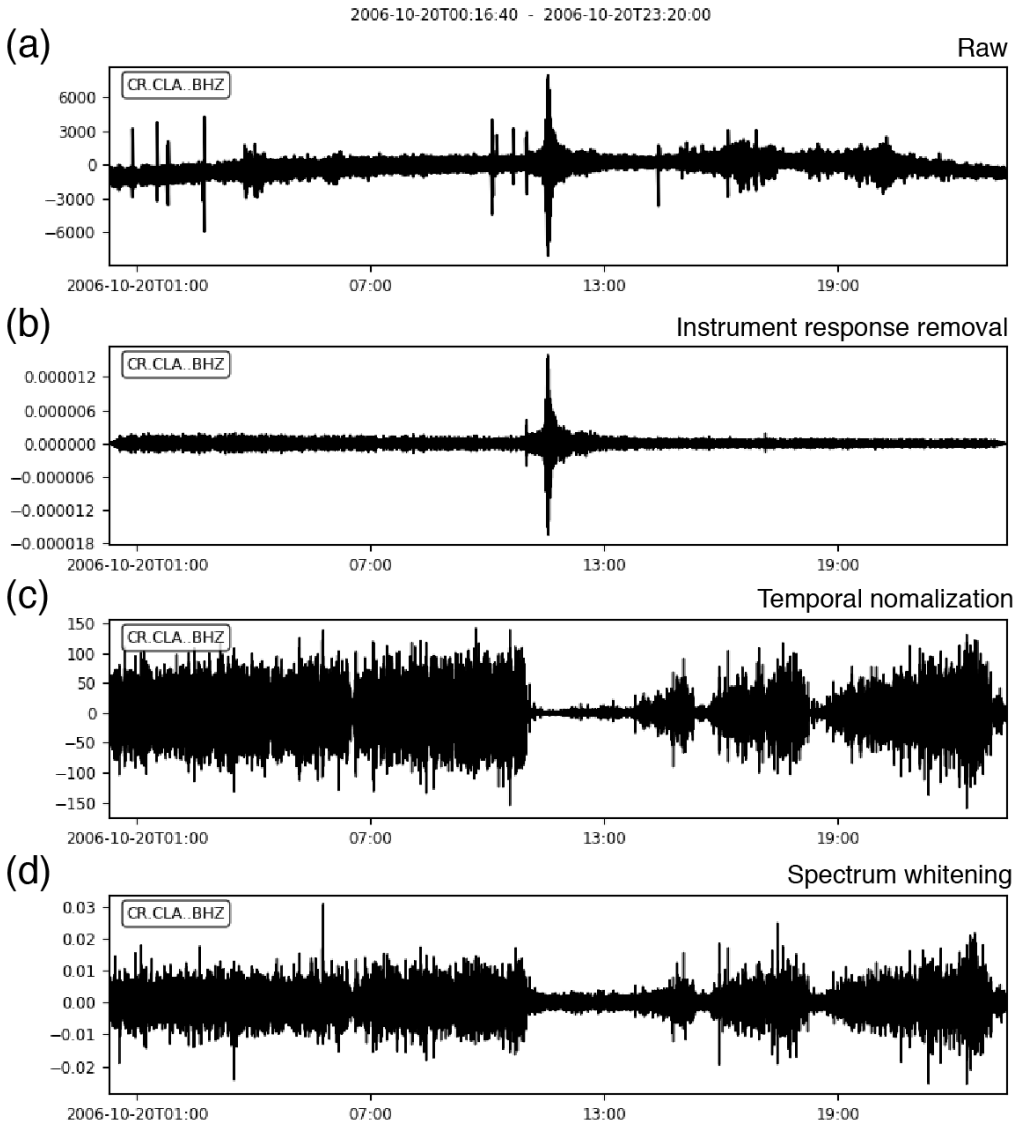


Figure 3.9 Ambient noise processing for a daily recording at station CLA. An earthquake signal is clearly visible at ~12:00 am in the (a) raw and (b) corrected seismogram after instrument response removal. The earthquake energy is effectively suppressed after (c) temporal normalization and (d) spectrum whitening.

The most important preprocessing step is the temporal normalization, which is critical to minimize the effects of earthquake signals, instrument irregularities and non-stationary near-station ambient sources (Bensen et al., 2007). As shown in Figure 3.9b, an earthquake signal is clearly visible around noon time, which, if not suppressed, will introduce spurious precursory arrivals to the NCF. The temporal normalization performs a running average to the waveform with a user defined window length (80-sec in our study). For each time window, a normalization factor is defined as the inverse of mean absolute amplitude of the filtered data within earthquake band (15-50 sec). The earthquake related energy is effectively minimized after temporal normalization (Figure 3.9c), hence would not contribute to the correlation measurement. Finally, spectral whitening is applied to smooth the amplitude spectrum (Figure 3.9d), which simultaneously broadens the bandwidth of the signal and suppresses the noise peaks associated to persistent monochromatic sources (Bensen et al., 2007).

The preprocessed recordings at each station pair are cross-correlated to compute the NCF, which primarily contains the fundamental mode Rayleigh wave propagating between stations. Stacking is subsequently applied to daily NCF to improve the phase clarity. The improvement in SNR follows a power law relationship as SNR $\propto t^{1/n}$, where $t$ is the length of time series and $n$ is a period (frequency) dependent constant (Bensen et al., 2007). An example correlation measurement is shown in Figure 3.10, where clear Rayleigh energy is emerged at both positive and negative time lag, corresponding to waves propagating in opposite directions. We define the convergence rate as the correlation coefficient between the short- and long-term (3 months) NCFs, which improves rapidly from 0.4 to 0.8 within 2 weeks and gradually slows down afterward. The asymmetric waveforms indicate a non-uniform distribution of noise sources, which will be discussed in more detail in chapter 7.

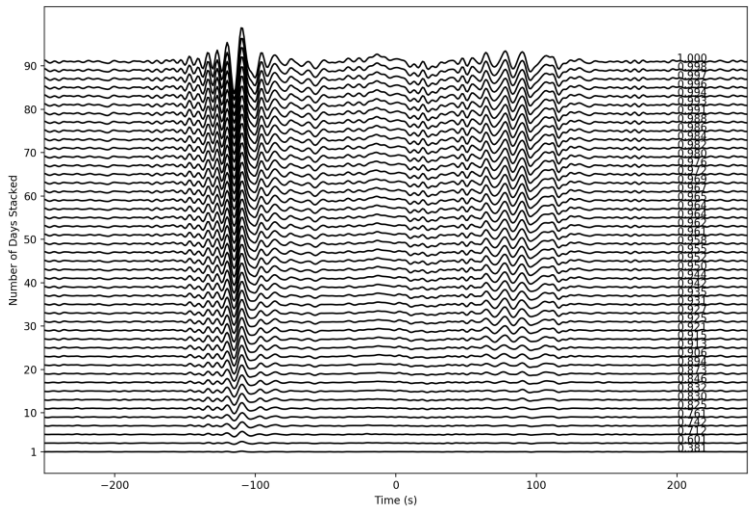


Figure 3.10 NCFs computed between stations BRU and JOF from CRANE. The stable Rayleigh waves emerge as the number of days used in stacking increases. The number labeled beside each trace indicates the correlation coefficient between the short-term (current stacking) and long-term (90-days stacking) NCFs.

### 3.3.3 Dispersion measurement

Dispersion is a well-known phenomenon of Rayleigh propagation, in which case waves with different frequencies travel at different speeds (Figure 3.11a), leading to distinct group and phase arrival times at the recording station. We utilize the Frequency Time Analysis (FTAN) method to determine the frequency-dependant group velocities. For a surface wave embedded in a time series $s(t)$, the analytical signal is constructed by zeroing out the negative frequencies:

$$S_a(\omega) = S(\omega)(1 + \mathrm{sgn}(\omega)), \tag{3.22}$$

where $S(\omega) = \int_{-\infty}^{\infty} s(t)e^{i\omega t}dt$ is the frequency spectrum. To separate the surface wave energy at different frequencies, a series of Gaussian filters with varying center frequency $\omega_0$ are applied to the analytical signal:

$$S_a(\omega, \omega_0) = S(\omega)(1 + \mathrm{sgn}(\omega))G(\omega - \omega_0), \tag{3.23}$$

where $G(\omega - \omega_0) = e^{-\alpha(\frac{\omega - \omega_0}{\omega_0})^2}$ is the Gaussian filter, sgn is the operation taking the sign of the value.

Based on an inverse Fourier transform, we obtain a complex signal in the time-domain as

$$S_a(t, \omega_0) = |A(t, \omega_0)|\, e^{i\phi(t,\omega_0)}, \tag{3.24}$$

where the amplitude and phase terms are represented by $|A(t, \omega_0)|$ and $\phi(t, \omega_0)$, respectively. The former term essentially defines an envelope function of the filtered Rayleigh wave, where its group arrival time $\tau(\omega_0)$ is determined from the peak amplitude. To obtain a less biased estimate of group times, the center frequency is often replaced with the 'instantaneous frequency' (Levshin et al., 1992), which is defined as the rate of phase change at the determined group time $\omega = |\frac{d\phi(t, \omega_0)}{dt}|_{t=\tau(\omega_0)}$. The extraction of a continuous group velocity dispersion curve is facilitated by constructing a FTAN image, a period-velocity plot with each column represents the logarithm of the squared envelope function, $\log|A(t, \omega_0)|^2$ (Figure 3.11b). The optimal group velocities are measured by tracking the dispersion ridge and interpolation is performed in the presence of small glitches to obtain a smoothly varying curve.

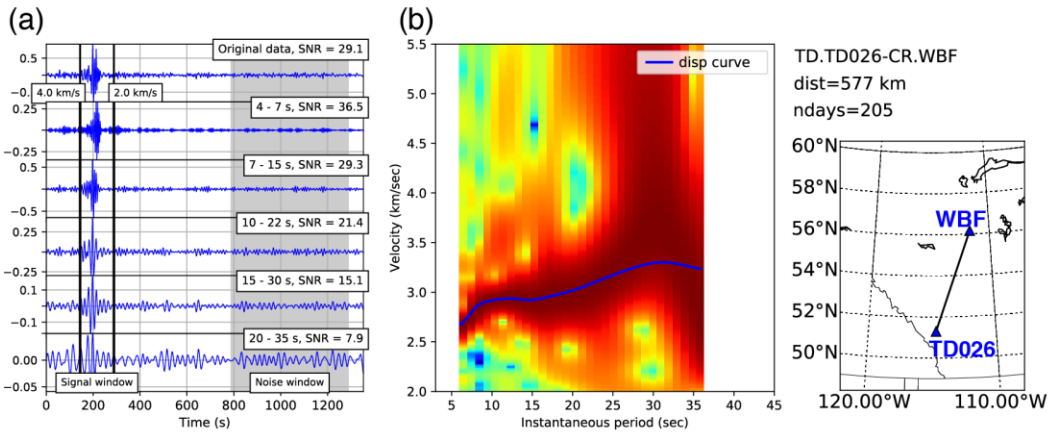


Figure 3.11 A sample FTAN measurement of station pair WBF-TD026. (a) The NCF filtered at various period bands. (b) The FTAN image that shows the amplitude of the filtered analytical signal as a function of instantaneous period. The measured dispersion curve is marked by the blue line. The inset shows the location of the two stations.

### 3.3.4 Group velocity inversion

The dispersion curve from the NCF provides frequency-dependant constraints on the velocity structure between each station pair. These path-averaged velocities can be integrated to construct a 2D group velocity map at each frequency. In a homogenous medium with constant velocity $c_0$, the Rayleigh wave propagates along the great circle path connecting two stations. Based on the ray theory, the forward problem of surface tomography is expressed as

$$\delta t = \int_{\text{path}} \frac{m}{c_0} ds, \tag{3.25}$$

where $m = (c_0 - c)/c$ is the percentage of velocity perturbation. This equation can be rewritten into matrix form as

$$\mathbf{d^{obs}} = \mathbf{Gm} + \mathbf{n}, \tag{3.26}$$

where **m** is parameterized model space in Cartesian or spherical coordinates, **G** is the inversion kernel defined by the length of ray segment in each cell divided by background velocity $c_0$ and $\mathbf{d^{obs}}$ is the data vector contains the measured travel-time perturbations of group arrivals and **n** represents the noise in the measurement. We seek a least-squares solution of the model parameters by minimizing the following cost function:

$$J = (\mathbf{Gm} - \mathbf{d^{obs}})^T \mathbf{C}^{-1} (\mathbf{Gm} - \mathbf{d^{obs}}) + \alpha^2 \|\mathbf{Fm}\|_2^2 + \beta^2 \|\mathbf{Hm}\|_2^2, \tag{3.27}$$

where the three terms represent the model misfit, spatial smoothing condition and weighed model norm, respectively. Specifically, matrix **C** in the misfit term is the covariance matrix of errors in group time measurements. The relative contributions between spatial smoothing and model norm terms is controlled by the damping parameters $\alpha$ and $\beta$. Their optimal values are usually determined by the turning point of the trade-off curve for misfit and model norm terms (e.g., Gu & Shen, 2015). In the second term, the spatial smoothing operator **F** is an M×M matrix with each element given by

$$F_{ij} = \begin{cases} 1 & i = j \\ -S(\mathbf{r}_i, \mathbf{r}_j)/p & i \neq j,\ p = \sum_j S(\mathbf{r}_i, \mathbf{r}_j) \end{cases}, \tag{3.28}$$

where $S(\mathbf{r}_i, \mathbf{r}_j) = e^{-\frac{|\mathbf{r}_i - \mathbf{r}_j|^2}{2\sigma^2}}$ and $\sigma$ is the correlation length. The matrix **H**, with the same dimension as **F**, accounts for the density of the ray paths and is defined as

$$H_{ij} = \begin{cases} e^{-\lambda \rho(\mathbf{r}_j)} & i = j \\ 0 & i \neq j \end{cases}, \tag{3.29}$$

where $\lambda$ is a (user-defined) constant and $\rho$ is the path density near location $\mathbf{r}_j$. The least-squares estimate of the model is obtained by

$$\hat{\mathbf{m}} = (\mathbf{G}^T\mathbf{C}^{-1}\mathbf{G} + \mathbf{Q})^{-1}\mathbf{G}^T\mathbf{C}^{-1}, \tag{3.30}$$

where $\mathbf{Q}$ is the regularization matrix combining $\mathbf{F}$ and $\mathbf{H}$ and is defined as

$$\mathbf{Q} = \alpha\mathbf{F}^T\mathbf{F} + \beta\mathbf{H}^T\mathbf{H}. \tag{3.31}$$

This inversion approach has been widely applied in the surface wave inversions at both regional and global scales. As will be shown in chapter 7, the combination of the reliable inversion method and the substantially increased regional seismic data enables much greater spatial resolution beneath the WCSB compared with the earlier studies.

# Chapter 4 Precambrian tectonic discontinuities in western Laurentia: broadband seismological perspectives on the Snowbird and Great Falls Tectonic Zones

## 4.1 Background

Identification and interpretations of the STZ and GFTZ are fundamental to the understanding of craton formation and evolution in western Laurentia. Unfortunately, largely due to limited surface geological exposure and two-dimensional (2-D) receiver geometries, the task of validating the crustal imprints and origins of these proposed structural boundaries has been challenging. For example, despite prominent potential field observations (e.g., Ross et al., 1991), which are the basis of crustal domain definitions, seismic constraints on the location, depth, and nature of the STZ have mostly relied on linear active-source experiments deployed sporadically across the study region (Figure 4.1a). It remains speculative whether the STZ faithfully follows Rimbey (STZS in Figure 4.1b), a proposed magmatic arc (Gibb & Walcott, 1971; Eaton & Cassidy, 1996; Ross & Eaton, 2002) or bifurcates around the Proterozoic accreted Wabamun domain (Ross et al., 1991; STZN in Figure 1b). Instead of a collisional origin (Gibb & Walcott, 1971; Hoffman, 1988; Berman et al., 2007), alternative interpretations of the STZ as a Precambrian intracontinental shear zone (Hanmer et al., 1994; Boerner et al., 2000), rift (e.g., Flowers et al., 2006), or a reactivated block boundary (Regan et al., 2017) cannot be dismissed based on the existing data alone.

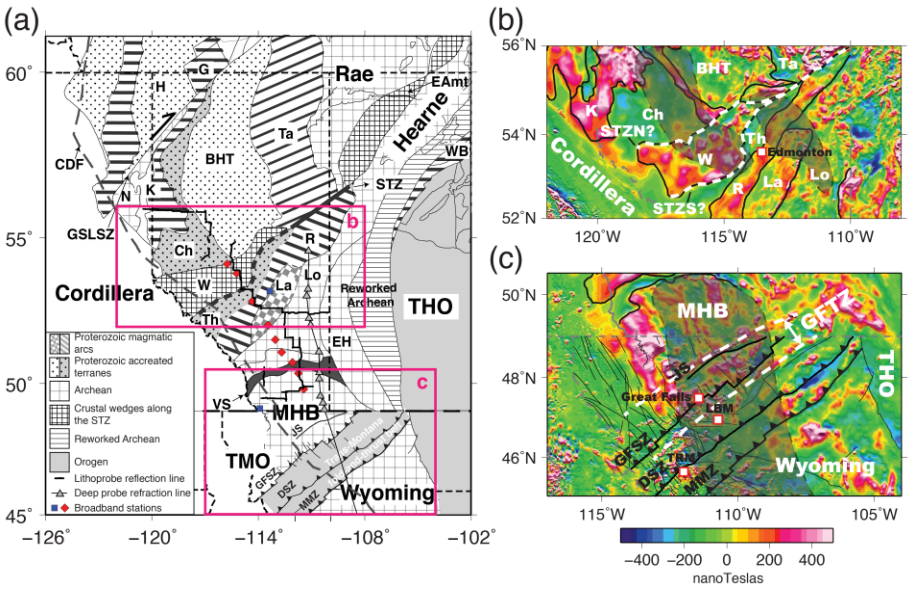


Figure 4.1 (a) Tectonic map of western Laurentia. The two proposed tectonic boundaries (STZ and GFTZ) are highlighted by the red rectangles. (b) Aeromagnetic field strengths within the highlighted region (see Figure 4.1a) around the STZ. The white dashed lines mark the earlier-proposed (e.g., Ross et al., 1991; Ross & Eaton, 2002) northern (STZN) and southern (STZS) branches of the STZ. The shaded areas show the distributions of mafic (west) and felsic (east) magmatic intrusions imaged by earlier geophysical analyses (Ross & Eaton, 1997; Bouzidi et al., 2002; Ross, 2002a; Welford & Clowes, 2006; Chen et al., 2015). (c) Aeromagnetic anomalies within the highlighted region (see Figure 4.1a) containing the GFTZ. The white dashed lines indicate the suggested location of the GFTZ based on NE trending aeromagnetic gradients (e.g., Lemieux et al., 2000; Gorman et al., 2002). The heavy barbed lines mark the fold-and-thrust belts of the Trans-Montana Orogen (TMO). The distribution of a high-velocity lower crustal layer (LCL) from Ross (2002a) is indicated by the shaded region. 'Great Falls' denotes the township location of Great Falls in northwestern Montana. Tobacco Root Mountain (TRM) and Little Belt Mountain (LBM) are two of the few locations showing the outcrop of the Precambrian basement rocks within the TMO. Abbreviations: DSZ, Dillon Shear Zone; EAmt, East Athabasca mylonite triangle; GFSZ, Great Falls Shear Zone; JS, Joplin Structure; MMZ, Madison Mylonite Zone; STZN, northern STZ; STZS, southern STZ; see Figure 2.2 caption for other domain abbreviations.

Similar to the STZ, the exacting location and origin of the GFTZ has been long debated. It has been widely associated with Precambrian plate convergence (O'Neill & Lopez, 1985; Hoffman, 1988; Clowes et al., 2002; Gorman et al., 2002; Mueller et al., 2002; Whitmeyer & Karlstrom, 2007; Porritt et al., 2014). However, some geochemical data in the presumed Canadian segment of the GFTZ share common signatures between the bounding blocks of the MHB and Wyoming craton, which favor the GFTZ as an intra-continental fault system/shear zone (Buhlmann et al., 2000) instead of a Proterozoic suture (Mueller et al., 2002). The GFTZ bears distinctive signatures from the Proterozoic (1.60-1.85 Ga; Hayden & Wehrenberg, 1960; Giletti, 1966), but minettes from the igneous complex in Milk River (Alberta) and Sweet Grass Hills (Montana) north of the GFTZ contain coarse-grained mantle xenoliths rich in phlogopite, mica, feldspar, clinopyroxene, and apatite (Buhlmann et al., 2000), consistent in age with those found in the interior of Wyoming craton (>2.5 Ga; Giletti, 1966). This intraplate hypothesis was supported by the lack of distinctive electromagnetic or magmatic arc signatures across the GFTZ to the south and the THO to the east (Boerner et al., 1998). For this reason, Boerner et al. (1998) questioned the role of the GFTZ as a suture zone during the Proterozoic assembly of western Laurentia. On the other hand, evidence of arc magmatism and thrust belt signatures south of the originally proposed GFTZ (Sims et al., 2004) clearly favors plate convergence and subduction (O'Neill & Lopez, 1985; Mueller et al., 2002; Mueller & Frost, 2006).

Since the original discovery of the GFTZ by O'Neill and Lopez (1985), the understanding of this highly deformed region has been greatly advanced through multidisciplinary investigations, though its interpretations suffered from inconsistent, often confusing, definitions from geophysical, geological, and geochemical perspectives. One of such complications is the location of the GFTZ with respect to major structural lineaments in northwestern Montana, which, from north to south, are Joplin Structure (JS), Great Falls Shear Zone (GFSZ), Dillon

Shear Zone (DSZ), and Madison Mylonite Zone (MMZ; see Figure 4.1c). Among these faults, the JS coincides with a linear trend of potential field (magnetic and gravity) anomalies, which outlines the northern boundary of the GFTZ in earlier geophysical investigations (e.g., Boerner et al., 1998; Lemieux et al., 2000; Clowes et al., 2002; Gorman et al., 2002). The southern boundary of the GFTZ was then defined either as the linear negative gravity gradient near the JS (e.g., Clowes et al., 2002; Gorman et al., 2002) or the southern edge of northeast trending magnetic fabrics slightly north of the GFSZ (e.g., Boerner et al., 1998; Lemieux et al., 2000; see Figure 4.1c). By this definition, the GFTZ is a relatively narrow geological boundary zone confined within these two potential field lineaments. Alternatively, the GFSZ was defined as the northern limit of the GFTZ in recent geological and geochemical analyses (e.g., Buhlmann et al., 2000; Mueller et al., 2002; Foster et al., 2006; Mueller & Frost, 2006). According to this hypothesis, the GFTZ extends southeastward to the DSZ, possibly reaching as far as the MMZ (Sims et al., 2004, 2005; see Figure 4.1c). The apparent discrepancies in the location and dimension of the GFTZ are largely responsible for its questionable role during the assembly of western Laurentia.

Regardless of the nature of the GFTZ, the crusts of both the MHB and Wyoming craton exhibit isotopic signatures consistent with an overprinted lower crust due to a mantle enrichment event during the Paleoproterozoic era (Buhlmann et al., 2000; Levander & Miller, 2012). With a P wave velocity exceeding 7 km/s, this mafic LCL (Ross, 2000; Clowes et al., 2002; Gorman et al., 2002; Levander & Miller, 2012; see Figure 4.1c) has been linked to concurrent Proterozoic collisions along the THO in the east and an orogenic belt near the western margin of MHB-Wyoming system (Davis et al., 1995; Mueller et al., 1995). The top and bottom of the lower crustal layer (LCL) have been mainly delineated through active source seismic data (see Figure 2.3a), which jointly suggest a thickened crust beneath the southeastern MHB and the northern Wyoming craton across and/or along the GFTZ (Clowes et al., 2002; Gorman et

al., 2002; Ross, 2002a). This anomalous layer was interpreted as evidence for underplating (Ross, 2000; Clowes et al., 2002; Gorman et al., 2002), a process commonly associated with the emplacement of mafic and ultramafic magma at the base of continental crust (Furlong & Fountain, 1986; Fyfe, 1992; Cox, 1993; see Thybo & Artemieva, 2013 for a review), during Archean (Clowes et al., 2002; Gorman et al., 2002) or Proterozoic (O'Neill, 1998; Sims et al., 2004, 2005; Mueller & Frost, 2006) collisions between the MHB and the Wyoming craton. While this model was partially supported by the outcomes of an active-source experiment in northwestern United States (i.e., CD-ROM; Karlstrom et al., 2005), the precise location, age, and nature of the underplated layer remain debated. Furthermore, the east-west dimension of the LCL and its connection to the GFTZ is speculative since the existing interpretations (e.g., Clowes et al., 2002; Gorman et al., 2002; Ross, 2002a) were exclusively based upon crustal structural variations along NS oriented 2-D seismic profiles (see Figure 4.1a).

In view of the highly-controversial roles of these important tectonic boundaries, the overarching goal of this chapter is to place the latest broadband seismic observations, as well as existing geological and geophysical constraints, within a self-consistent regional tectonic framework of western Laurentia. We aim to answer the following two fundamental questions:

1. What, and how significant, are the crustal and mantle seismic expressions of the STZ?

2. Where is the GFTZ based on broadband seismological crustal constraints and if/how is it linked to underplating?

By acquiring answers to these questions through updated broadband seismic observations, we are able to provide an unbiased appraisal of the existing

hypotheses pertaining to the proposed boundary zones near the western margin of the North American craton. Our findings clearly favor the STZ and GFTZ as critical suture zones during the Paleoproterozoic amalgamation of microcontinents in western Laurentia.

## 4.2 Data and Method

The main goal of this study is to assess the robustness of key observations of the STZ and GFTZ, two proposed structural discontinuities vital for the understanding of the tectonic evolution of western Laurentia. To accomplish this, we combine new crustal seismic observations based on the most complete broadband station coverage in the WCSB and northern Montana, coupled with existing geological and geophysical constraints from recently published studies of this region. Our latest regional data consist of recordings from three stations from Canadian National Seismograph Network (CNSN; June 1991 to March 2015), 27 stations from CRANE (September 2006 to October 2015), 73 stations from USArray (mainly from 2008 to 2009), 27 stations from TD (July 2014 to July 2016), 15 stations from RAVEN (November 2013 to April 2017) and 13 stations from temporal arrays (see Figure 3.2a). A subset of this data that contains over 17,253 first arrivals was inverted for mantle velocities in a recent analysis of finite-frequency body wave tomography (Chen et al., 2017; see chapter 5 for details). We also incorporate the results of ambient noise tomography (Gu & Shen, 2015) for detailed comparisons. The data constraints on the GFTZ are primarily based on 73 stations from USArray, which were concurrent with several CRANE stations in Canada between 2007-2008.

The main contributions of this chapter are updated maps of Moho depth and crustal Vp/Vs ratios determined from P-to-S converted wave at the Moho interface (*Pms*) and its higher-order reverberations. In comparison with travel times (chapter 5) and dispersion curves (chapter 7), this data set offers greater

constraints on the Moho depth, impedance contrasts, and composition, which are essential elements in the appraisal of potential boundary zones in western Laurentia. The main steps in processing this data set are presented in section 3.1 of this thesis.

## 4.3 Result

### 4.3.1 General Assessment

With few exceptions, conversions from the Moho (i.e., *Pms*) are clearly detected at times ranging from ~5 sec beneath the northern part of the array (e.g., FMC) to over 6 sec beneath station CLA in southern Alberta (Figure 4.2a). Conversions beneath the Alberta basin consistently arrive within 5 sec relative to P (see Figure 4.2a), which are 1-3 sec earlier than those beneath the foothills of the Rockies. The time delays of *Pms* are accompanied by a notable amplitude drop-off near the foothills of the Rockies, where dipping Moho interfaces (Cassidy, 1992), sedimentation (Sheehan et al., 1995; Julià et al., 2004) and/or anisotropy with a non-horizontal axis of symmetry (Levin & Park, 1997) could all contribute to scattering and defocusing. A relatively flat Moho in the Alberta basin results in clear converted phases (Figure 4.2b) and focused energy in the *H*-$\kappa$ domain (Figure 4.2c).

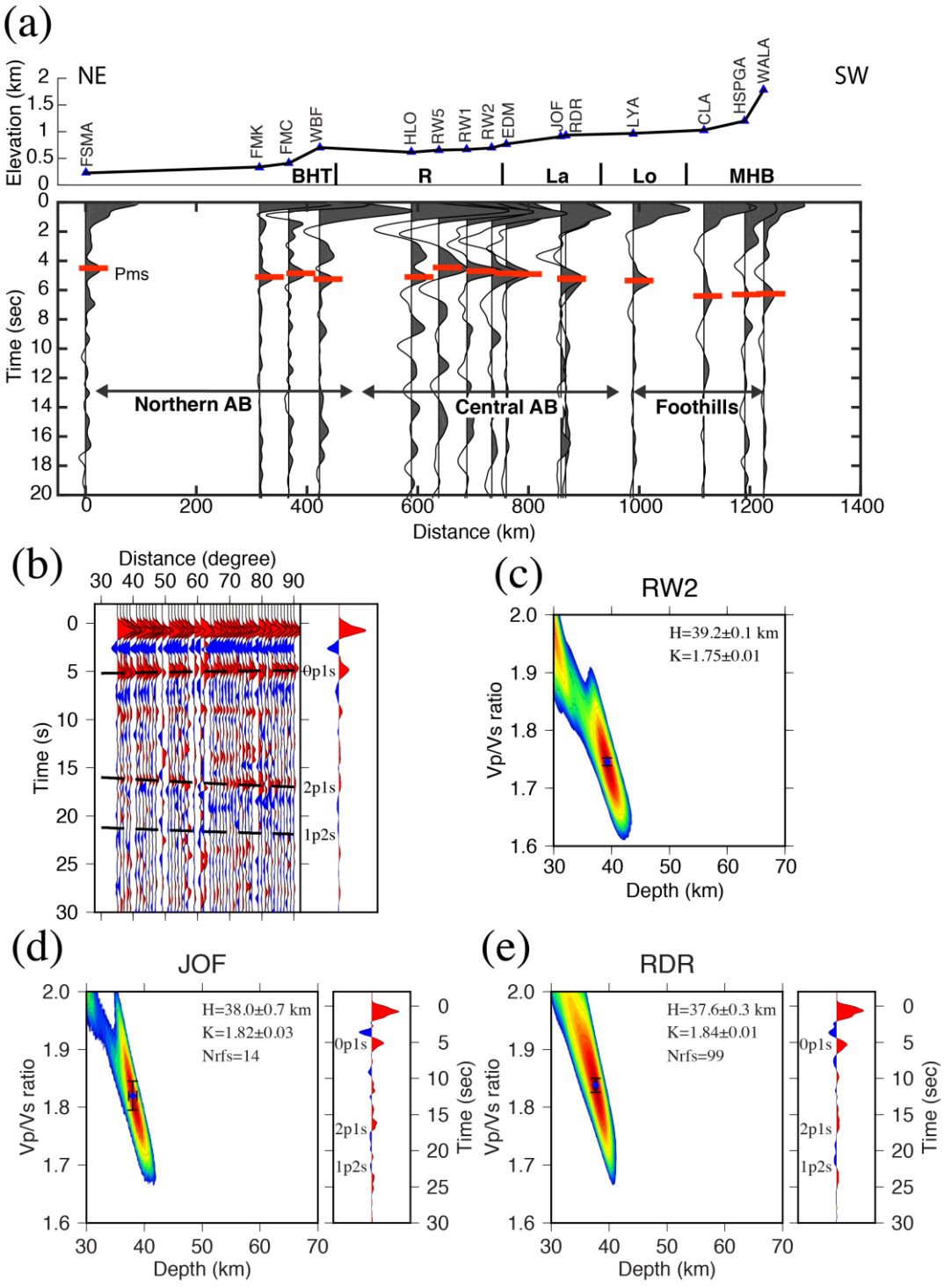
(a)
NE
SW
Elevation (km)
FSMA
FMK
FMC
WBF
HLO
RW5
RW1
RW2
EDM
JOF
RDR
LYA
CLA
HSPGA
WALA
BHT
R
La
Lo
MHB
Pms
Time (sec)
Northern AB
Central AB
Foothills
Distance (km)
(b)
Distance (degree)
Time (s)
0p1s
2p1s
1p2s
(c)
RW2
H=39.2±0.1 km
K=1.75±0.01
Vp/Vs ratio
Depth (km)
(d)
JOF
H=38.0±0.7 km
K=1.82±0.03
Nrfs=14
(e)
RDR
H=37.6±0.3 km
K=1.84±0.01
Nrfs=99

Figure 4.2 (a) A profile of stacked receiver functions (RFs) showing Moho variations from northern Alberta to the foothills of the Rocky Mountains (see Figure 3.2a for profile location). Station located within 50 km distance of the profile, which approximately equals the lateral resolution of the RF, are projected on the profile. The elevation and name of each station are indicated above the RF. The red line marks the *Pms* phase. (b) RFs from station RW2. The dashed black lines mark the predicted arrival times of converted phases from $H$-$\kappa$ analysis. The stacked trace is shown on the right panel. (c) The $H$-$\kappa$ diagram of RFs from station RW2. (d and e) The $H$-$\kappa$ diagrams for two stations (JOF and RDR) that are 8.5 km apart. The stacked RFs are shown on the right-hand side.

We compute the uncertainties of $H$ and $\kappa$ using the bootstrap resampling method (Efron & Tibshirani, 1986) instead of the traditional derivative-based approach (Zhu & Kanamori, 2000). The uncertainties of Moho depth range from 1 to 4 km, showing an average of ~2 km. The average uncertainty of $\kappa$ is ~0.04, though values at certain stations (e.g., EDM, RW4) could be as large as 0.09. A further consideration is the uncertainty of average crustal P velocities in the region, as a perturbation of 0.1 km/s can cause a depth uncertainty up to 0.5 km. A pessimistic estimate of 0.4 km/s deviation from our assumed crustal velocities from CRUST1.0 model yields a depth error of ~2 km, which is considerably smaller than the key Moho gradients (5-10 km generally) detailed in the subsequent sections. The number of data traces and installation type (e.g., temporary versus permanent) do not appear to have major influences on the observed patterns. The stability of the measurements is best reflected by the outcomes of stations JOF and RDR (Figures 4.2d and 4.2e), which were installed on private farms that are 8.5 km and 4 years apart. The maxima of these two nearby stations are within 0.02 in Vp/Vs ratio and 0.4 km in Moho depth, well

below the average uncertainty (~0.04 and ~2 km, respectively) in crustal property estimates.

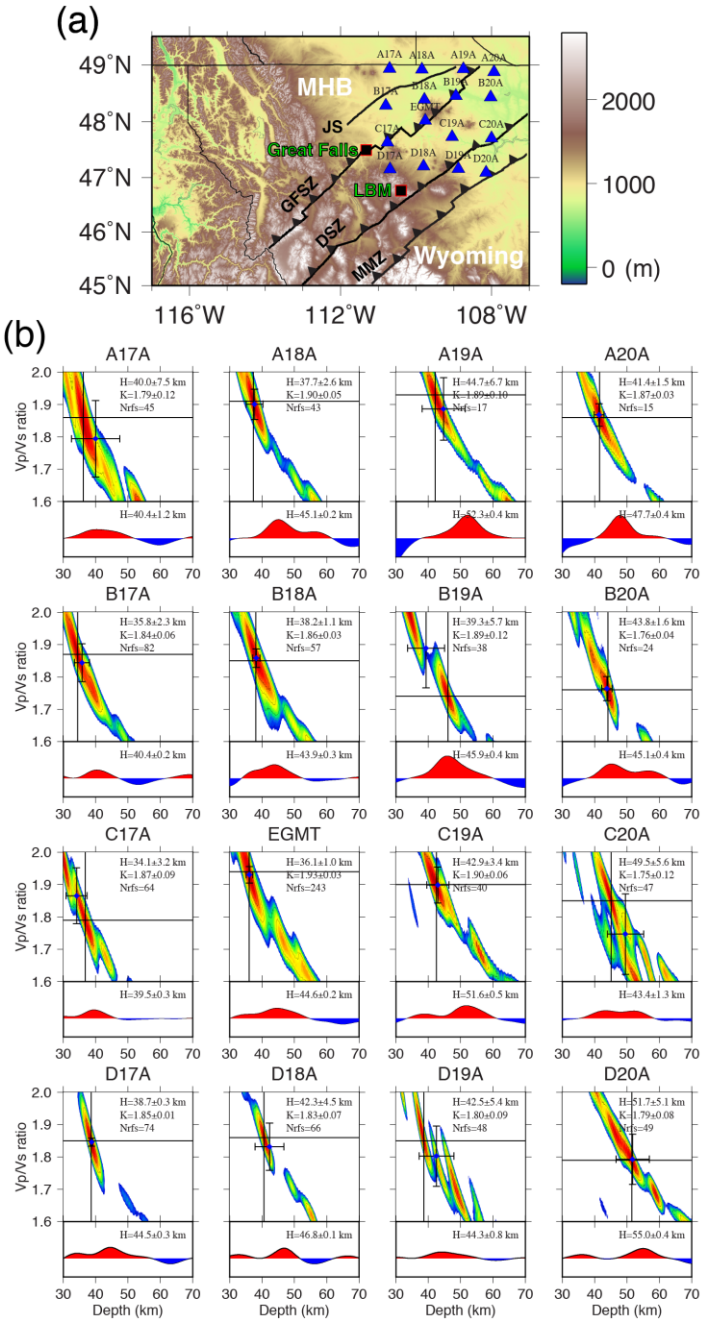

Figure 4.3 (a) Stations showing sample *H*-$\kappa$ measurements near the Great Falls Tectonic Zone. (b) In each plot, the upper panel shows the *H*-$\kappa$ stack and the crosshair indicates the optimal *H*-$\kappa$ values. The blue circle indicates the bootstrap average and the error bars indicate the associated uncertainties (labeled). Several stations (e.g., B19A, C19A, D19A) exhibit multiple local maxima. The lower panel shows depth-converted receiver function stacks near the *Pms* phase. The depth of the peak amplitude is labeled.

While it is tempting to measure Moho properties exclusively using the *H*-$\kappa$ method, the outcomes are prone to severe errors in both crustal Vp/Vs ratio and Moho depth in the case of multiple energy foci in the *H*-$\kappa$ domain (Zhu & Kanamori, 2000; Chen et al., 2010; Lowry & Pérez-Gussinyé, 2011) due to crustal structural complexities. In our study region, a number of USArray stations in northern Montana show double or complex *H*-$\kappa$ maxima (e.g., station B19A, EGMT, C19A, D19A and D20A; Figure 4.3). Most of them reside within the region of early Proterozoic underplating revealed from the active source surveys (Clowes et al., 2002; Gorman et al., 2002) and present a major challenge to the evaluation and interpretation of true Moho depth; a detailed discussion of this important observation can be found in section 4.4. To mitigate crustal complexities and verify the measured Moho depths based on *H*-$\kappa$ analysis, we convert the arrival times of *Pms* on the stacked RFs to Moho depths based on P and S velocities from CRUST1.0 (Laske et al., 2013). This approach assumes a near-constant Poisson's ratio of 1.75 from CRUST1.0, which is only an averaging approximation for the true crustal values, but the measured Moho depth is more resistant to anomalously large Poisson's ratios and multiple local *H*-$\kappa$ maxima.

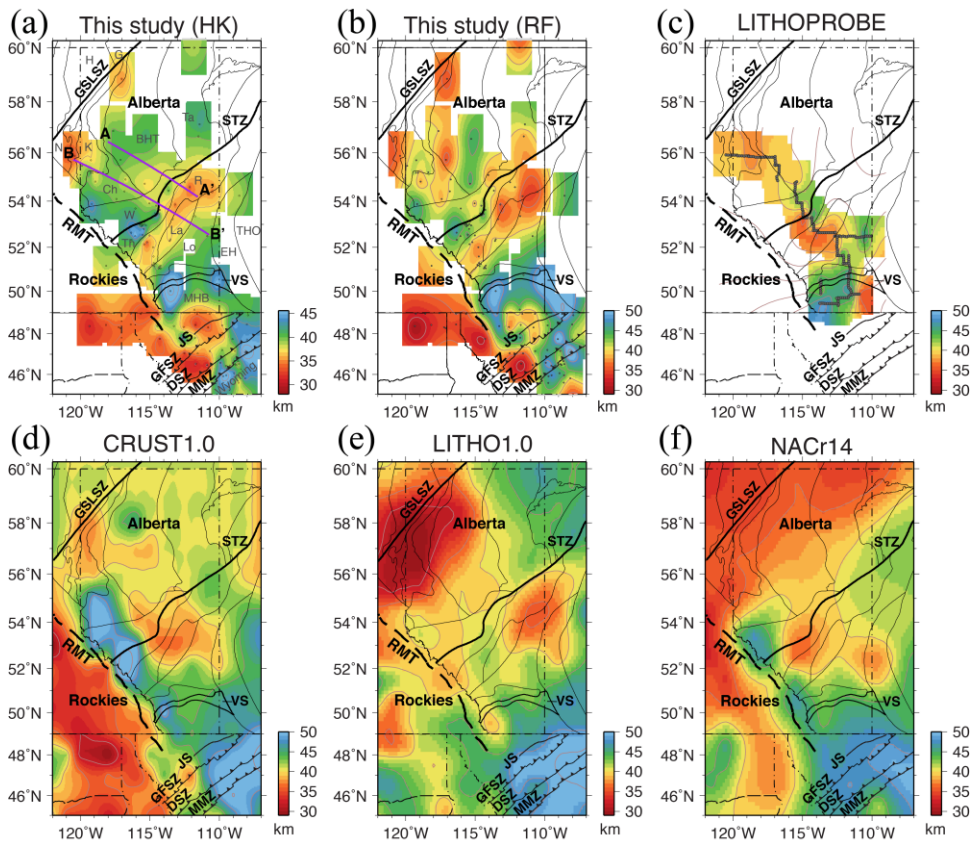


Figure 4.4 Maps of Moho depth from (a) *H*-*κ* stacking (this thesis), (b) time-to-depth conversion (this thesis), (c) an interpolated map of Bouzidi et al. (2002) based on LITHOPROBE reflection/refraction surveys, (d) CRUST1.0 (Laske et al., 2013), (e) LITHO1.0 (Pasyanos et al., 2014), and (f) NACr14 (Tesauro et al., 2014) models. The locations of two linear transects across the STZ are indicated by the purple lines. The small gray circles indicate the locations of stations. Station elevation is subtracted from crustal thickness (*H*) to calculate the Moho depth.

The resulting Moho depths from transform and conversion-based approaches are highly consistent in regions with robust *H*-*κ* signals, showing an average depth of ~40 km in the Alberta basin. Both maps contain a shallow Moho directly south of the STZ in the Alberta basin, which is identifiable in size and amplitudes to those of the processed sections from regional active-source surveys (Bouzidi et al., 2002, Figure 4.2c), global crust (CRUST1.0; Laske et al., 2013; Figure 4.4d),

mantle lithosphere (LITHO1.0; Pasyanos et al., 2014; Figure 4.4e), or continent-wide (NACr14; Tesauro et al., 2014; Figure 4.4f) models. In contrast, a deep Moho is an essential fixture among all five models beneath the foothills of Rocky Mountains, particularly near the southern Canadian Rockies in the latitude range of 49-51°N (see Figure 4.4). Coupled with a flat, shallow (~35 km) Moho to the west of the Rocky Mountain Trench, this transition produces the steepest lateral Moho gradient in the study region. Part of this gradient could be attributed to an anomalously deep (~47 km) Moho beneath western segment of the VS. The anomaly is further evidenced by regional active source data (see Figure 4.4c), though its presence is only marginally supported (see Figure 4.4d) or unsubstantiated (see Figures 4.4e and 4.4f) in the remaining three Moho maps; we attribute these differences to insufficient resolution of global/continent-scale models. The RF stacks further suggest a deep Moho (~44 km) beneath eastern VS, resulting in an average Moho depth of 45.5 km along this east-trending geological structure (see Figure 4.4b). Unfortunately, we are unable to reliably resolve Moho depths in central VS due to the lack of local seismic stations.

Farther south, the Moho deepens toward the southeastern corner of the study region in northern Montana in all models (see Figure 4.4). Unlike northern MHB in southern Alberta, where the Moho exceeds 45 km (in most models), our receiver-function based results show significantly shallower Moho directly north of the GFSZ than the earlier studies (see Figure 4.4a). This observation is supported by the outcomes of both $H$-$\kappa$ stacking and depth converted RFs, regardless of the presumed Vp/Vs ratios of ~1.84 and ~1.74, respectively. There are other notable differences among the various crustal depths shown in Figure 4.4: for example, the scales of the anomalies in our maps are generally smaller than those in the earlier studies, which we attribute to increased lateral resolution due to improved station coverage from regional broadband arrays. The sections below mainly focus on the characteristics of the Moho near the STZ and GFTZ, the two best constrained geological structures by our regional data set.

### 4.3.2 Crust and Mantle Beneath the STZ

The combined station coverage from regional networks allows us to examine crustal imprints and lateral dimensions of the STZ from a broadband seismic perspective. Based on Figure 4.4, the Moho depth in central Alberta is divided into northwestern and southeastern halves, bordered by a crust that is 5-10 km thicker along the presumed southern strand of the STZ (Ross et al., 1991) than the regional average. This anomaly covers the entire Alberta section of the STZ, eventually merging with the deeper Moho along the eastern Taltson Magmatic Zone (Ta in Figure 4.4a) in the northeast and terminating within the Cordilleran foreland belt in the southwest. The Moho depth ranges from 37 to 40 km south of the STZ, which are consistent with those reported by Bouzidi et al. (2002) within a spatially confined corridor of active source experiments (see Figure 4.4c). In comparison with CRUST1.0 (see Figure 4.4d), this zone of depressed Moho is much more significant along the STZ in our model (see Figures 4.4a and 4.4b).

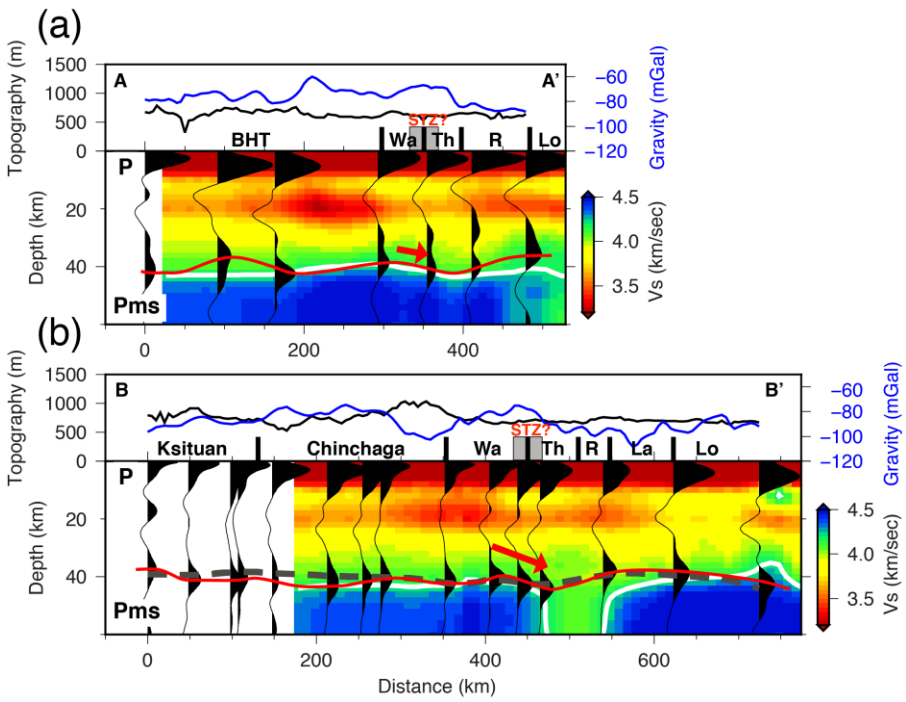


Figure 4.5 Two profiles of receiver functions in central Alberta showing the crustal structure variations across the STZ. (a) Topography (black) and Bouguer gravity (blue) along the profile. (b) Receiver functions (black) superimposed on shear velocities from ambient-noise tomography (Gu & Shen, 2015). The Moho determined from the *Pms* phase and shear velocity (4.2 km/s contour) are highlighted using the red and white lines, respectively. The dashed black line represents the Moho depth from Bouzidi et al. (2002) based on LITHOPROBE reflection/refraction surveys. The red arrows indicate the orientations of Moho dip beneath the STZ. See Figure 2.2 captions for domain name abbreviations.

Figure 4.5 shows the Moho depths and crustal shear velocities along two semi-linear transects roughly perpendicular to the STZ (see Figure 4.4a for profile locations). Along the easternmost transect (profile AA', Figure 4.5 a), the Moho is significantly deeper beneath the BHT (by ~7 km) and the Thorsby (by 5 km) domains than beneath the STZ (~35 km). The latter anomaly is confined within the proposed boundary beneath the Thorsby domain, followed by a substantially

shallower Moho beneath the Hearne province to the southeast. The Moho depth along the profile closely tracks the depth of a shear velocity of 4.2 km/s (white line, see Figure 4.5a), the average shear velocity between crust (~3.9 km/s) and mantle (~4.5 km/s, as defined in CRUST1.0; Laske et al., 2013), which we interpret as a gradational Moho interface due to inherent smoothing in noise correlation tomography (Gu & Shen, 2015). The first-order agreement between these two studies is highly encouraging, especially considering the substantially lower station spacing and data volume included in Gu & Shen (2015).

In transect BB', the Moho deepening beneath the Thorsby domain becomes more apparent, reaching the maximum regional depth of ~44 km (Figure 4.5b). This transect overlaps extensively with active-source lines 1-5 of the Central Alberta Transects of the LITHOPROBE project, where a sharp Moho depression of 5+ km was observed (dashed line, see Figure 4.5b) and interpreted as evidence for mantle faulting beneath the STZ (Bouzidi et al., 2002). The dimension and location of the Moho dip are consistent (see Figure 4.5) between these two studies despite different data frequencies and types. The interpreted average Moho depth based on shear velocities (42.3 km) in the overlapping areas fits within the RF estimate (41.5 km) from this study. In the vicinity of Thorsby/Rimbey domain, the location of the Moho dip, we observe substantially reduced mantle shear velocities down to a minimum depth of 60 km. The significance of which will be discussed in conjunction with similar observations near the GFTZ in section 4.4.

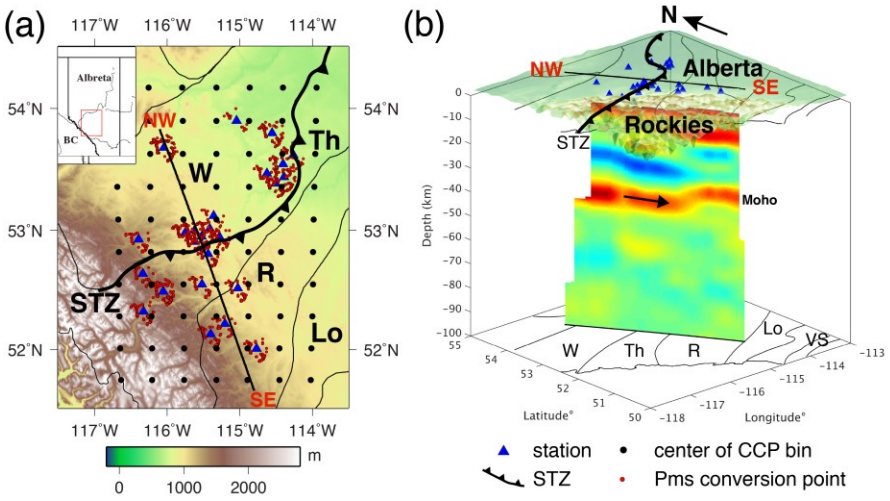


Figure 4.6 (a) A tectonic map of western STZ (Ross et al., 1991). The blue triangles mark the seismic stations used in the construction of common conversion point (CCP) gathers. The black circles indicate the centers of the CCP bins, and the red circles denote the P-to-S conversion locations at 40-km depth. The black line shows the location of the receiver function transect. The map area is shown by the enclosed region in the inset. (b) A 3-D perspective plot of the receiver function transect extracted from the CCP gathers. Red and blue colors represent the positive and negative amplitudes, respectively. The Moho is delineated by a positive (*Pms*) phase at ~40-km depth, and its dipping direction beneath the STZ is indicated by the arrow.

Taking advantage of the recently installed TD array (see Figure 3.2a), which was designed predominantly to increase local receiver densities for microseismicity monitoring, we are able to resolve the Moho topography across the STZ with greater clarity using the common conversion point (CCP) stacking technique (Dueker & Sheehan, 1997; Rondenay, 2009; Levander & Miller, 2012). The CCP volume is constructed using over 2000 RFs from 25 stations near the STZ (Figure 4.6a). Each RF is migrated to depth using AK135 (Kennett et al., 1995) and corrected for local heterogeneities based on CRUST1.0 (Laske et al., 2013) while assuming a fixed ray path. Each CCP gather is a stack of RFs with conversion points that fall within a common bin, and the distance between bins is

controlled by the width of the Fresnel zone (Červený & Soares, 1992). Considering a frequency of 1.2 Hz and average crustal shear velocity of ~3.45 km/s, the width of the Fresnel zone is about 15 km at 40 km depth (Ryberg & Weber, 2000), which defines the maximum horizontal resolution of the CCP profile. It is worth noting that owing to irregular station distribution and incomplete azimuthal ray coverage, the maximum achievable resolution is usually significantly less in practice. We set the bin spacing to 30 km, which approximately equals the station spacing in the center of the imaging volume (Figure 4.6a). We apply spatial smoothing to the CCP image using a 40-km running average window to minimize imaging gaps and improve the coherences of converted energy (Frassetto & Thybo, 2013). The resulting stacked RFs provide further evidence of a ~50-km wide Moho deepening (Figure 4.6b). This anomaly initiates near the northern boundary of the Thorsby domain, as evidenced by the depth gradients in both the Moho conversion and the negative phase preceding it, and eventually terminates in the vicinity of southern Rimbey domain where 1) the Moho surface raises by ~8 km toward the south and 2) the conversion amplitude decreases due to nonplanar structures.

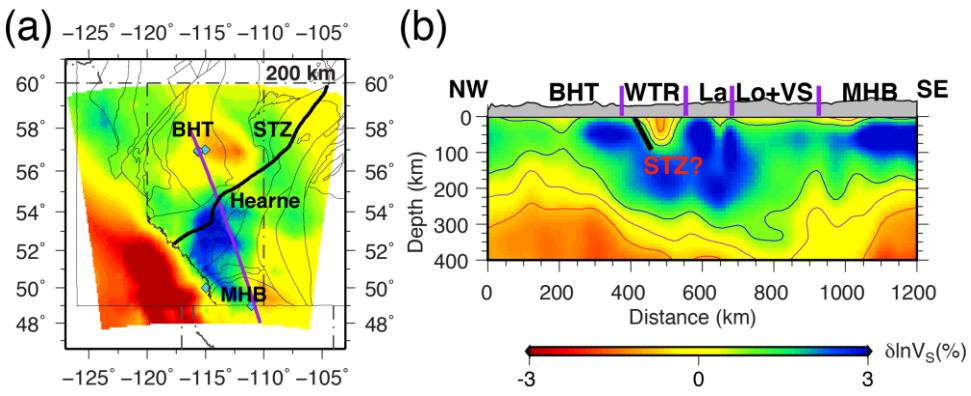


Figure 4.7 (a) Shear velocity perturbations at 200-km depth from finite-frequency travel-time tomography (see chapter 5 for details). The blue diamonds show the location of xenoliths (Buhlmann et al., 2000; Canil et al., 2003; Aulbach et al., 2004). (b) A cross-section of shear velocity profile. Its location is indicated by the purple line in (a), and the potential subsurface extension of the STZ is indicated by the thick black line. The domain boundaries are marked by the purple lines near the surface. WTR represents the region across the STZ that includes the Wabamum, Throsby, and Rimbey domains. See Figure 2.2 caption for other abbreviated domain names.

To explore the depth extent of the STZ, we carefully examine the mantle shear velocities extracted from S wave finite frequency tomography (Figure 4.7). This model takes advantage of the most up-to-date regional array data and the inversion considers the volumetric sensitivity of seismic waves to the mantle structure (Hung et al., 2004). On the basis of standard 'checkerboard' test (see chapter 5 for details), the nominal lateral resolution is sufficient to resolve the structure around the STZ in central Alberta. Our shear velocity model shows distinctive high-velocity clusters beneath the BHT domain and Hearne craton (Figure 4.7b), separated by a low-shear velocity zone that extends down to ~80 km depth.

### 4.3.3 Moho and Shallow Mantle Structure Beneath the GFTZ

In comparison with northern central Alberta, the Moho is generally deeper beneath southern Alberta and northern Montana, showing an overall average of 42 km in this study (see Figure 4.4a) and 46 km in CRUST1.0 (Laske et al., 2013; see Figure 4.4d). The most significant dip is observed in the southeastern corner of the study region, reaching ~50 km beneath the DEEPPROBE active source profile (Clowes et al., 2002; Figures 4.8a and 4.8b). At 48° N in northernmost Montana (Figure 4.8b), the Moho depth increases sharply from 40 km to ~50 km along the eastern provincial boundary of Alberta. The position of this anomalous dip roughly overlaps with the proposed LCL structure (Gorman et al., 2002), which was later supported by broadband seismic analyses using RFs (Gilbert, 2012; Levander & Miller, 2012; Schmandt & Lin, 2014). This east-west Moho gradient is notably absent in global crustal models (e.g., CRUST1.0; Laske et al., 2013; see Figure 4.4d), however.

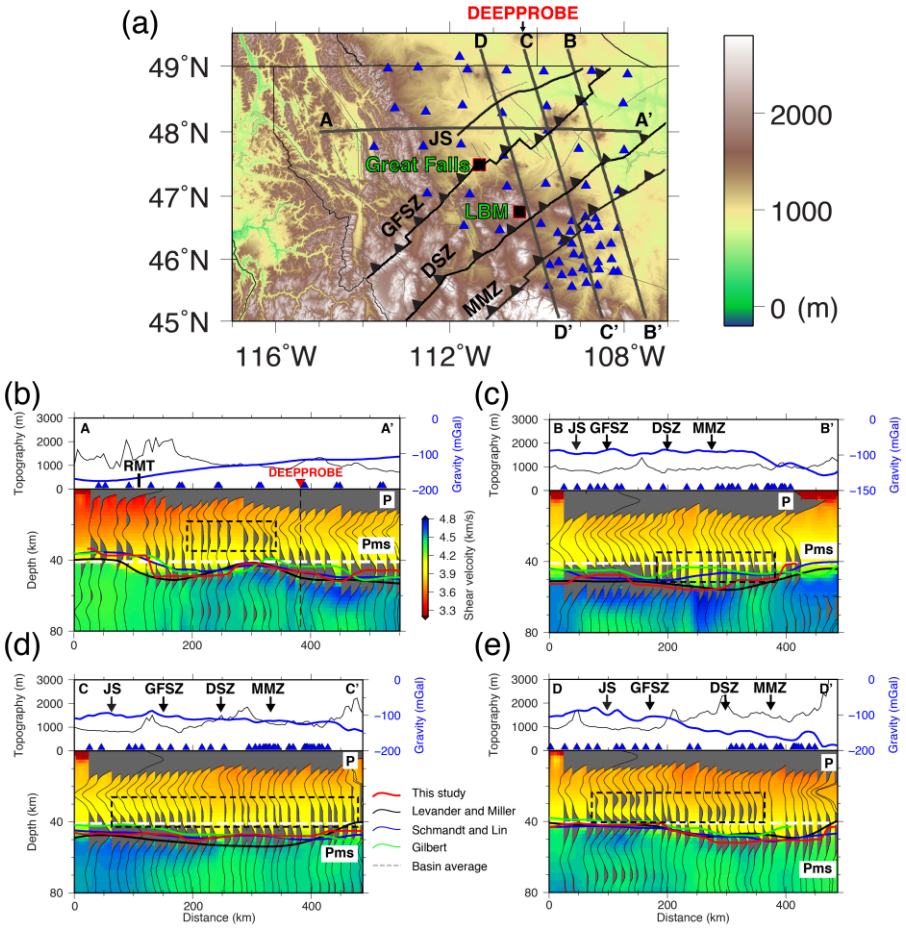


Figure 4.8 (a) Surface topography near the GFTZ in northwestern United States. The blue triangles mark the station locations, and thin black lines indicate four major northeast orientated faults. (b-e; top) Topography (black) and Bouguer gravity (blue) along the profiles shown in (a). The intersections between known faults and seismic profiles are highlighted by the arrows. (bottom) RF transects constructed from the CCP gathers. The background color shows the shear velocities from Shen & Ritzwoller (2016). The solid lines track the Moho depth obtained from this thesis (red) and earlier (Gilbert, 2012; Levander & Miller, 2012; Schmandt & Lin, 2014) studies. The averaged Moho depth in the Alberta basin is shown by the white dashed line. In general, stations with delayed, high-amplitude Moho conversions are underlain by above-average shear velocities. The stacked traces from these stations often show waveform broadening or multiple arrivals (enclosed by the dashed rectangles).

Figures 4.8c-4.8e showcase three cross-sections of depth-converted RFs parallel to the DEEPPROBE line (Clowes et al., 2002; Gorman et al., 2002) in northern Montana. The depths of the Moho along these transects, which are expected to intersect the GFTZ at progressively greater offsets from the northeast, shed further light on the robustness of this proposed suture zone between the MHB and the Wyoming craton. In all three cases, the Moho exhibits shallow depths beneath the MHB northwest of the boundary, but deepens substantially below the DSZ and MMZ. The positions of the Moho dip are generally consistent among published regional studies based on broadband data (see Figure 4.8). All three transects across the GFTZ contain a weak seismic arrival prior to *Pms* and its corresponding station location roughly overlaps with the region of the proposed Proterozoic underplating (Clowes et al., 2002; Gorman et al., 2002).

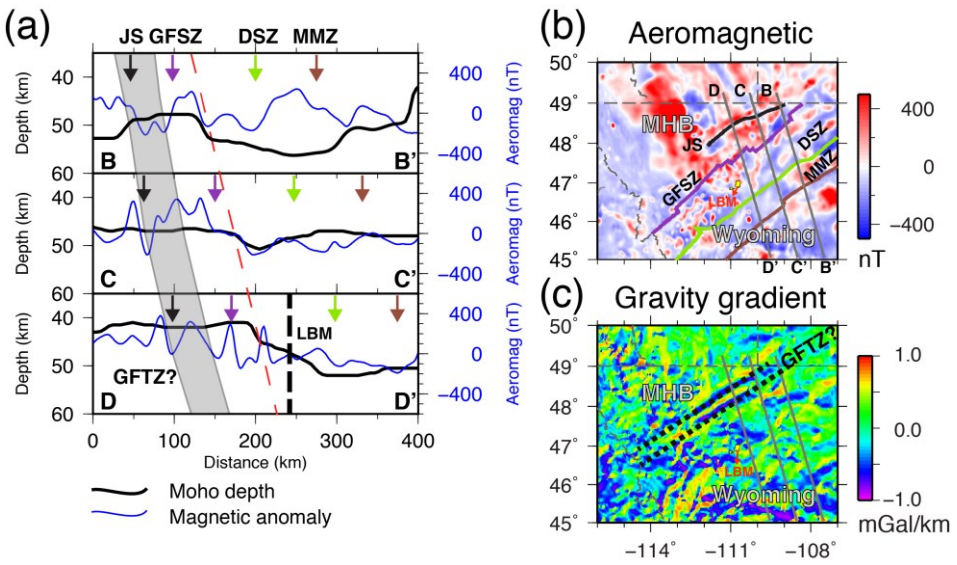


Figure 4.9 (a) Moho depth along three profiles that traverse the GFTZ. The intersections between the profiles and faults are indicated by the arrows. The shaded region indicates the location of the GFTZ defined by the gravity gradients shown in (c). The red dashed line marks the onset of crustal thickening. (b) Aeromagnetic anomalies near the GFTZ. Three sample cross-sections are marked by gray lines, and faults are delineated by thick lines in various colors. (c) Normalized gravity gradients near the GFTZ. The GFTZ is originally defined as a narrow zone between the two parallel, negative gravity gradient lineaments (dashed lines) in northern Montana (e.g., Clowes et al., 2002; Gorman et al., 2002); this definition is challenged by the results of this thesis.

This sharp gradient in Moho depth runs progressively southward (Figure 4.9a) and overlaps with a broad aeromagnetic low south of the GFSZ (Sims et al., 2004; see Figures 4.9a and 4.9b). This Moho anomaly extends to the southeast of the LBM (see Figure 4.9a, cross-section DD'), where significant earlier Proterozoic signatures were identified based on geological and geochemical data (Mueller & Frost, 2006). The overall correlation between potential field and Moho depth is low in the study region; for example, the Moho is flat beneath the two sharp northeast trending potential field gradients along the JS and GFSZ in the northernmost Montana (Figures 4.9b and 4.9c).

## 4.4 Discussion

This chapter presents new broadband seismic observations on the continental crust beneath the western margin of the North American craton. Whereas resolution remains a work-in-progress beneath parts of the WCSB, especially along the northeastern MHB, the seismic observations from regional broadband array presented in this chapter are the most substantial to date and offer new constraints on the tectonic development and crustal processes. The updated data and models enable an unbiased appraisal of the existing theories based largely on potential field and active source data.

### 4.4.1 General Appraisal of Existing Models of Moho Depth and Composition

Despite the wide range of adopted data constraints, the proposed depths of the Moho beneath the WCSB, the bulk of the study region, are generally correlated among various studies (see Figure 4.4). Prime examples are the Alberta basin, northwestern Alberta, and Cordillera, beneath which the Moho is consistently shallower (i.e., thin crust) than the regional averages. This is supported further by earlier findings from RFs at a few select locations (Eaton & Cassidy, 1996; Gu et al., 2011; Shragge et al., 2002). Sprinkled in between are areas of deep Moho (thick crust), for example, beneath the foothills of the Rockies, most notably in western Wabamun domain and VS/MHB. The most notable differences among the various studies are the amplitudes and resolutions of the major anomalies in the WCSB. For example, due to the use of regional stations, our maps show significantly greater details on Moho depth (see Figure 4.4) than previous published models that were derived from limited active-source data (CRUST1.0) or surface waves (LITHO1.0). Furthermore, the transition from the Alberta basin (thin crust) to the foothills (thick crust) is sharper (i.e., better

defined) in our model than in LITHO1.0, which we partly attribute to the effects of damping/smoothing in the earlier global model due to spatial undersampling within the WCSB. Differences aside, the Moho depth measurements of the WCSB do not appear to be strongly affected by the data type (i.e., active-source versus broadband).

A similar conclusion cannot be reached for the crustal structures in northern central Montana, however. The average Moho depth determined from USArray data by our study (~45 km; see Figure 4.4 for map and Figure 4.8b for E-W cross-section) is nearly 5 km shallower than those from maps that relied heavily on the active-source data (see Figure 4.4d). A part of this discrepancy could be attributed to fewer surface seismic surveys (e.g., mainly along a linear DEEPPROBE transect) in comparison with the WCSB, which adversely affected the lateral resolutions of the existing global crustal models such as CRUST1.0 and LITHO1.0. Complexities associated with complex crustal structures (e.g., underplating and mantle intrusion), which are reflected in the differences (~6 km) between $H$-$\kappa$ (see Figure 4.4a) and time-to-depth conversion (see Figure 4.4b) methods, will be explored further in the following sections of this chapter.

### 4.4.2 Implications for the STZ

Of all the broadband seismic observations examined in this study, a deep Moho is the most compelling observational constraint for the presence of the STZ across the WCSB. Supported by migrated RFs (see Figure 4.6), the deep Moho overlaps with the earlier report of a 10 km Moho step associated with a high-angle fault (Bouzidi et al., 2002). Similar crustal thickening has been documented near Rae-Chesterfield in eastern STZ and interpreted as a consequence of subduction circa 1.9 Ga (Berman et al., 2007). While the timing and process of crustal thickening in western STZ remains debated due to the scarcity of geological samples, collisional tectonics certainly offer a simple and compelling explanation

supported by other observational constraints. For instance, a thick crust beneath the Thorsby basin (presumed Proterozoic suture; Ross et al., 1991) is compatible with the lower-than-average value of Bouguer gravity in the vicinity of the STZ. Formerly known as Edmonton-Kasba low (e.g., Bouzidi et al., 2002; Ross et al., 1991), a gravity anomaly (see Figure 4.5) was identified slightly south of the depressed Moho near the Thorsby domain in central Alberta. While its clarity and linearity are highly dependent on 1) the processing method and 2) structural complexities (e.g., nearby fault or intrusive sill; Pană, 2002), a thick and low-density crust (compared to mantle) could certainly contribute to a reduced Bouguer gravity value.

Seismological expressions of the STZ are evident in crust (Gu & Shen, 2015) and mantle (see chapter 5 for details) shear velocities. In both studies, a distinctive low shear velocity zone is present in the lower crust-upper mantle beneath Thorsby/Rimbey domain (see Figure 4.7b). Sandwiched between two distinct high-velocity zones, which were interpreted as the cratonic roots of the Archean Hearne province and BHT (Chen et al., 2017), this low-velocity zone is symptomatic of a possible tectonic suture (Porritt et al., 2014; Youssof et al., 2015). The steep basal relief on the mantle lithosphere, producing a major structural gradient across the cratons (Chen et al., 2017), may be further evidence for a plate boundary if the difference between basement domains extends vertically down to lithospheric depths (see Figure 4.7).

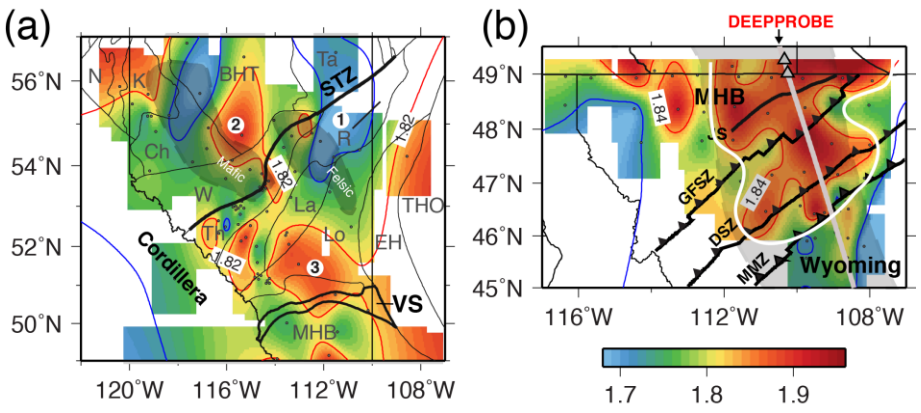


Figure 4.10 Vp/Vs ratios near the (a) STZ and (b) GFTZ. Labels 1-3 highlight the major anomalies. The DEEPPROBE refraction transect and shot points (Clowes et al., 2002; Gorman et al., 2002; Henstock et al., 1998) are indicated by the white line and grey triangles, respectively. The shaded areas show the reported mafic and felsic magmatic intrusions from earlier geophysical studies (Bouzidi et al., 2002; Ross & Eaton, 1997; Ross, 2002; Welford & Clowes, 2006; Chen et al., 2015). The region of underplating (i.e., lower crustal layer) inferred from elevated Vp/Vs ratios is enclosed by the white line.

Further insights on the crustal composition and the existence of potential suture zones could be gained from Vp/Vs ratios (Zandt & Ammon, 1995; Christensen, 1996; Zhu & Kanamori, 2000; Niu et al., 2007). We construct a Vp/Vs ratio map using the *H*-$\kappa$ results in combination with earlier measurements from five stations in southern Alberta (Shragge et al., 2002; Figure 4.10a). The entire STZ is divided into two distinct segments, a western central Alberta segment with four distinct clusters of high (>1.82) Vp/Vs ratios and a northeastern segment embedded within an elongated, north-south oriented belt with below-average (<1.73) values (see zone 1 in Figure 4.10a). The former observation could be linked to a suture, where arc magmatism and intrusion of mafic mantle melt may have transpired during the subduction of the Thorsby domain circa 1.8 Ga. Similar observations have been made in various collisional zones globally (e.g., Yuan et al., 2000; Darbyshire et al., 2017). This cluster of

enhanced Vp/Vs values is interrupted in eastern central Alberta near the Taltson Magmatic Zone, a proposed Proterozoic (2.02-1.91 Ga) orogen between the Slave and Superior cratons (2.3-2.0 Ga, Ross et al., 1991; Boerner et al., 2000). As potentially a southern segment of the Thelon orogen (Hoffman, 1988; De et al., 2000; Ross & Eaton, 2002; Berman et al., 2007), the Taltson Magmatic Zone has been linked to Paleoproterozoic collisions (Berman et al., 2007). Further geochemical analyses of granitoids (De et al., 2000) suggest the Thelon-Taltson belt to be akin to felsic, intra-continental mountain belt similar to Tian Shan in central Asia (Chacko et al., 2000; De et al., 2000). Based on our RF $H$-$\kappa$ analysis, the Vp/Vs values (~1.70) are consistently low beneath the Taltson Magmatic Zone, which corroborates the earlier findings based on isotopic data. It is worth noting that below-average Vp/Vs ratios are also observed directly south of the STZ, overlapping an earlier reported zone of high heat flow and low crustal shear velocities (see Figure 4.10; Chen et al., 2015). Anatectic melting in response to the tectonic vise model may be responsible (Chen et al., 2015).

Enhanced Vp/Vs ratios in the Wabamun/BHT (zone 2 in Figure 4.10a) and southern Alberta (zone 3 in Figure 4.10a) have further implications for Precambrian tectonics. Extensive intrusive sills have been discovered in the former region, which manifest into thin, high-velocity reflective layer known as the 'Winagami reflection sequence' (Ross & Eaton, 1997; Welford & Clowes, 2006; Chen et al., 2015). The origin and precise age of these sills remain unclear, but it is highly probable that their existence required the participation of the ultramafic upper mantle. A similar argument could be made regarding the crustal composition south of the STZ, where a low-resistivity zone known as the 'Red Deer conductor' has been identified and linked to a north dipping subduction zone beneath the VS by a recent magnetotelluric survey (Nieuwenhuis et al., 2014). Further discussion of this southern Alberta anomaly is given in section 4.4.5 in connection with the VS.

### 4.4.3 Location and Crustal Origin of the GFTZ

RFs offer new geophysical constraints on the tectonic history of the MHB and northern Wyoming province. Similar to the STZ, a characteristic depression on the Moho interface is identified in the vicinity of the LBM (see Figures 4.8 and 4.9a), one of the few exposed locations with solid geochemical evidence for Proterozoic overprinting (1.9-1.8 Ga; Mueller et al., 2002). We interpret this observation as new seismological support for the existence of the Wyoming-MHB collisional suture. While crustal thickening can result from a wide range of processes (Haschke & Günther, 2003; Thybo & Artemieva, 2013; see section 4.4.4), Paleoproterozoic plate convergence between the MHB and northern Wyoming province offers a simple mechanism consistent with the earlier-proposed tectonic framework of western Laurentia (O'Neill & Lopez, 1985; Ross, 2002a; Mueller et al., 2006). The zone of deep Moho coincides with the Trans-Montana Orogen (TMO; Sims et al., 2004; see Figures 4.4a and 4.8), which is terminated by the THO (~1.8 Ga) in the east and the transitional crust of Mesozoic-Paleozoic in the west (O'Neill, 2007). The onset of this crustal anomaly resides ~50–100 km northwest of the DSZ (see Figures 4.8c-4.8e and 4.9a), a proposed suture zone during the Paleoproterozoic collision, and the southern edge of this anomaly (near MMZ) appears to be an integral part of the fold-and-thrust belt of the TMO (Sims et al., 2004, 2005; O'Neill, 2007).

Since the first report of the GFTZ based largely upon observations of a northeast trending major fault system (O'Neill & Lopez, 1985), the detailed characteristics and origin of the Wyoming-MHB collisional suture have caused considerable confusion in the literature. Questions have surfaced regarding both the location (Hoffman, 1989; Clowes et al., 2002; Mueller et al., 2002; Sims et al., 2004) and the age (Proterozoic versus Archean) of the suture (Clowes et al., 2002; Gorman et al., 2002; Whitmeyer & Karlstrom, 2007). With limited geological

sampling this suture is often quantified as 1) a narrow structure confined between the JS and GFSZ, two potential field gradients (Clowes et al., 2002; Gorman et al., 2002; see Figure 4.9 c), or 2) a broad, hundreds-of-kilometer-wide (Sims et al., 2004, 2005) geological structure demarcated by the GFSZ as its northwestern boundary.

The crustal observations from this chapter are able to refine the boundary zone definition and make important inferences. First, there is a clear spatial separation (by ~200 km) between the northeast trending crustal thickening under DSZ (see Figures 4.8c-4.8e) and the potential-field gradient zone near the JS (see Figure 4.9). The Moho anomaly coincides with Paleoproterozoic magmatic belt and the foreland region of the TMO based on geological evidence of thrust sheets (Sims et al., 2004), despite the absence of present-day surface elevations. Its tectonothermal origin is reinforced by a sharp increase of Vp/Vs ratios that potentially resulted from mafic mantle intrusions (Figure 4.10b). On the other hand, the Joplin potential field anomaly (which coincides with the JS) and extensive fault systems of the GFSZ ~50 km to the southeast were likely the ductile shear zones in the hinterland of the TMO formed during the Paleoproterozoic collisional events. This interpretation is corroborated by 1) a flat Moho across the JS (see Figures 4.8c-4.8e), which suggests predominantly strike-slip motion and/or limited depth extension, and 2) the apparent lack of magmatic signatures in the magnetotelluric data in the presumed Canadian segment of the GFSZ (Boerner et al., 1998).

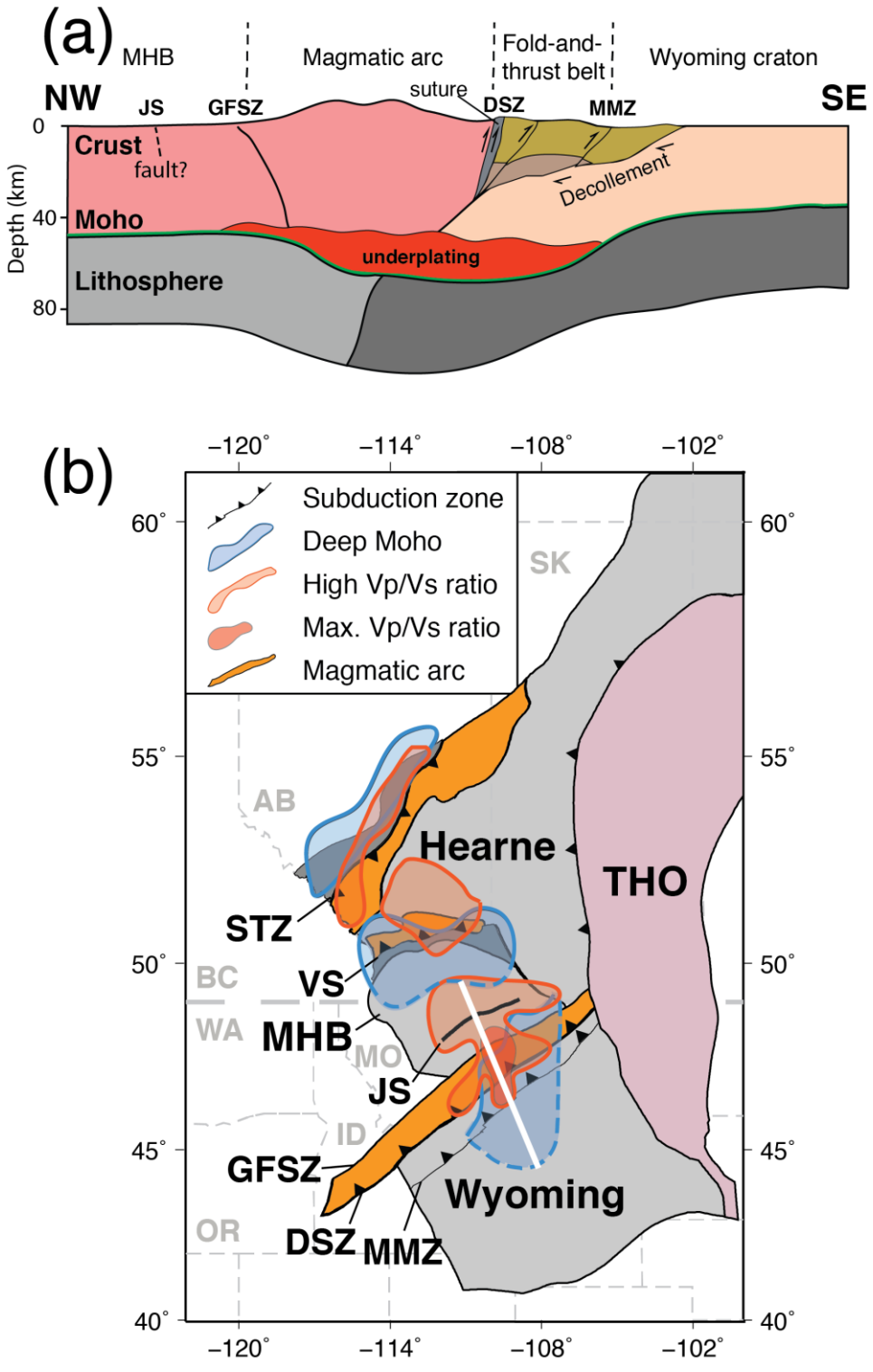
(a)
MHB
Magmatic arc
Fold-and-thrust belt
Wyoming craton
NW
JS
GFSZ
suture
DSZ
MMZ
SE
0
Crust
fault?
Moho
40
Depth (km)
underplating
Lithosphere
80
Decollement
(b)
−120°
−114°
−108°
−102°
60°
55°
50°
45°
40°
Subduction zone
Deep Moho
High Vp/Vs ratio
Max. Vp/Vs ratio
Magmatic arc
SK
AB
Hearne
THO
STZ
BC
VS
WA
MHB
MO
JS
ID
GFSZ
Wyoming
OR
DSZ
MMZ

Figure 4.11 (a) A schematic cross-section showing the mechanisms of crustal thickening near the GFTZ. The location of the profile is shown by the white line in (b). The crust could be thickened by arc magmatism, arc-continent collision, load of the fold-and-thrust belts and magmatic underplating. Note that the JS, originally defined as the northern boundary of the GFTZ, does not show a significant increase in Moho depth and likely represents an intracontinental structure. (b) A map showing the Hearne-MHB-Wyoming (HMW) tectonic system, which is featured by contemporaneous (2.0-1.8 Ga) subductions, continent-continent collisions, and the associated magmatic events on the western margin of Laurentia. Superimposed regions with a deep Moho (blue contours) and high Vp/Vs ratios (red contours) are selected based on threshold values of 38 km and 1.82, respectively, near the STZ. The corresponding contour values near the VS and GFTZ are 40 km and 1.84, respectively. The dashed contour indicates questionable boundaries of deep Moho due to insufficient data.

Details of cross-sections of RFs along the GFTZ enables a reexamination of other proposed tectonic processes in the study region (Figure 4.11a). First, aside from anomalously high values (~1.90) near the LBM (see Figure 4.10b), which may be associated with the aforementioned Paleoproterozoic magmatic processes, Vp/Vs ratios throughout northern Montana (~1.84) are generally higher than the southern Alberta (1.75-1.80, see Figure 4.10a). The elevated Vp/Vs ratios could reflect widespread mantle intrusions, hence increased average crustal mafic content, due to either Paleoproterozoic intrusions or the reactivation of the extensive network of basement-controlled faults near the GFSZ since then (Sims et al., 2004). Furthermore, we detect a potential weak reflector that coincides with the Moho dip (see Figure 4.8), which spatially overlaps with the earlier-proposed high-velocity, underplated Proterozoic layer (Clowes et al., 2002; Gorman et al., 2002; Levander & Miller, 2012; see Figure 4.11a). The presence of this layer is further suggested by recent models of shear velocities (Shen et al., 2013; Shen & Ritzwoller, 2016; see Figure 4.8), despite moderate differences between Moho depth deduced from our RF analysis (45-50 km), and values along the DEEPPROBE profile suggested by Gorman et al. (2002; 50-60 km). This

anomalous lower crustal layer has been recently examined through RF simulations (Schulte-Pelkum et al., 2017), and factors such as 1) lower depth resolution in broadband RFs and 2) inaccuracies during the depth migration of active-source data could have contributed to the systematic difference (~10 km) among these studies. It is nonetheless encouraging that a lower crustal reflector, a deep Moho interface, and enhanced lower crustal/shallow mantle seismic velocities at the base of the crust are consistent with an underplated high velocity LCL. The inferred dimensions of this potential LCL also highlight considerable departures between our observations (see Figure 4.11a) and findings based on active-source data. For example, Clowes et al. (2002) reported a flat, thick (>10 km) LCL and very weak seismic signatures directly associated with the Wyoming-MHB suture (Gorman et al., 2002). Their anomaly initiates from the southern MHB and continues southward across the GFTZ to the southern Wyoming craton (see Figure 4.11b), extending over a distance of more than 600 km. The widespread lower crustal conversions support a relatively broad LCL surrounding the DEEPPROBE transect (e.g., Ross, 2002a). However, judging from the localized deep Moho and sharp termination of the Vp/Vs ratio along the MMZ, the LCL is clearly confined to a northeast striking zone no wider than 300 km in the TMO (see Figures 4.10b and 4.11a); that is, the north-south extent of the LCL is considerably smaller than earlier suggested (see Figures 4.1c and 4.10b). The affinity of the crustal anomaly to the TMO based on RFs is compelling support for the more recently proposed spatial location of Trans-Montana orogeny (Sims et al., 2004, 2005; Mueller & Frost, 2006), as well as its defining role, during Paleoproterozoic plate convergence.

### 4.4.4 Potential Mechanisms for Crustal Thickening

Arc magmatism at convergent margins is an effective process for crust thickening and differentiation (Haschke & Günther, 2003). There are certainly

parallels between the STZ and GFTZ, where subduction of ocean plates (Thorsby and Wallace oceans, respectively) preceded continent-continent collisions (Ross et al., 1991; Sims et al., 2005). During the first stage of the collisional process, the crust beneath the continental domains thickens through a wide range of mechanisms. Based on data compiled from global subduction zones, Karlstrom et al. (2014) highlights the critical roles of arc magmatism in both arc front migration and crustal thickening of the overlying continental plate. Intrusion of mantle melts from the dehydration of hydrous minerals can thicken subarc crust through 1) magmatic underplating at the base of the crust (e.g., Haschke & Günther, 2003; Thybo & Artemieva, 2013), 2) intercrustal thickening and chemical differentiation, and 3) surface generation of new continental crust via arc volcanism (Stern, 2002; Karlstrom et al., 2014). All three mechanisms may have commenced during the early Proterozoic, contributing to a thick crust in a similar fashion as the present-day crustal growth landward of the Juan de Fuca subduction zone (Calvert et al., 2006; Bostock, 2013). It has been suggested that following the completion of oceanic subduction during the early Proterozoic (Ross et al., 1993, 2000; Sims et al., 2004, 2005), continent-continent subduction became the dominant tectonic process along both the STZ and the GFTZ. During this later stage of plate convergence, tectonic thickening likely occurred, resulting in further crustal growth beneath the orogenic belts near the collisional boundaries. The overthrusting occurs in zones with high strain concentration and forms foreland-verging structures (Godin et al., 2006), which could have created the downward flexure of lithosphere due to the mass load (Beaumont, 1981; see Figure 4.11a). The style of convergence and crustal thickening could be comparable to those beneath the Zagros mountain belt formed during the collision between Arabian and Eurasian plates (Paul et al., 2006; Pirouz et al., 2017) and the Paleoproterozoic THO (directly east; Weller & St-Onge, 2017). While the fractional crustal growth from various mechanisms during these Proterozoic collisional episodes remains unclear without further constraints, the total crustal thickness has been suggested to reach 55 km in both the STZ and GFTZ at their

time(s) of formation (Bouzidi et al., 2002; Barnhart et al., 2012). Between these two sutures, the extent of the crustal thickening beneath the DSZ (averaging ~20 km, collision of two Archean microcontinents) is considerably larger than that beneath the STZ (by 5-10 km, collision of a Proterozoic Wabamun domain with an Archean Hearne craton), which may reflect differences both in the collisional/thickening processes over the last 1.8 Ga and in the rate of erosion. Judging from the history of the nearby THO, which has been recently likened to the evolution of the Tibetan plateau (Weller & St-Onge, 2017), both the surface elevation and the depth of the crustal root along the GFTZ during the Paleoproterozoic era most likely have been substantially greater than the present-day values (~50 km).

We find clear evidence of crustal thickening beneath the GFTZ via underplating, which is widely believed to be an efficient mechanism for crustal growth or differentiation under subduction or in rifting environments (Furlong & Fountain, 1986; Rudnick & Gao, 2003; Thybo & Artemieva, 2013). A dense, high-velocity LCL could result from mantle magmatic intrusions and contain a mixture of mafic granulites, pyroxenites, and eclogite (Clowes et al., 2002; Thybo & Artemieva, 2013; Thurner et al, 2015). Eclogitization of the lower crust (Gilligan et al., 2016) under high-pressure, low-temperature metamorphism (e.g., in ocean-continent subduction zones; Darbyshire et al., 2017) may also play an important role. Both northern Montana (Clowes et al., 2002; Gorman et al., 2002) and Colorado Plateau (Karlstrom et al., 2005), which are adjacent to the western Canadian platform, have been linked to rift-related underplating in the early Proterozoic (Barnhart et al., 2012; Mahan et al., 2012). A recent study by Schulte-Pelkum et al. (2017) systematically analyzes RFs from USArray data and provides compelling evidence of multiple RF conversions in the lower crust. Through waveform modeling they substantiate the existence of a high-velocity layer, which is corroborated by a recent crustal shear velocity model (Shen & Ritzwoller, 2016). This finding is supported by multiple lower crustal

conversions in our stacked RFs and elevated Vp/Vs ratios for stations near the GFTZ, since the intrusion of mafic/ultramafic mantle melts would modify the lower crust and greatly increase the average Poisson's ratio within the crustal column (Christensen, 1996; Figure 4.11b). Similar observations of multiple crustal conversions and a deep Moho were documented along the THO directly east of our study region (Thurner et al., 2015; Weller & St-Onge, 2017). In other words, crustal underplating may be more pervasive during the Proterozoic eon than previously thought in western Laurentia.

### 4.4.5 Other Implications for the Tectonic Model and Constraints

While the data coverage does not allow us to unequivocally resolve the crustal signatures surrounding VS, three nearby broadband seismic stations (see Figure 3.2) do provide a first-order assessment of this potential suture zone. Two of these stations suggest an anomalously deep Moho (see Figures 4.4a and 4.4b) and increased Vp/Vs ratios (see Figure 4.10a). These observations are, to first order, consistent with those of STZ and GFTZ. The relative positions of the Moho dip (south of the VS, which may be associated with the suture) and increased Vp/Vs ratio (north of the VS, the potential magmatic arc) appears to favor a north-dipping subduction morphology (Ross et al., 1991).

The common crustal seismic signatures from all three proposed boundary zones (STZ, VS, and GFTZ) in our study may have far-reaching implications for the overall tectonic history of western Laurentia. It was suggested earlier that, based on the proposed reset time of the GFTZ, the circum-Wyoming Proterozoic tectonic events, for example, along THO and Great Falls, could all be at least partly coeval during the Proterozoic eon (Mueller et al., 2002). North of this region, overlapping ages of the basement rock samples from the WCSB have been strongly linked to a dual collisional (i.e., 'Tectonic Vise') model (Ellis et al., 1998; Ross et al., 2000; Clowes et al., 2002) centering around Hearne during the

Paleoproterozoic era. Judging from similar rock ages ranging from 1.85 to 1.70 Ga from the basement of the WCSB and crustal characteristics (depressed Moho and high Vp/Vs ratios) near all three boundary zones, it is plausible that convergent tectonics dominated not only the Wyoming craton (Lemieux et al., 2000), but a broader Proterozoic lithosphere collisional system comprised of the Hearne, MHB, and Wyoming. The 'Hearne-MHB-Wyoming' system (see Figure 4.11b) experiences major compression and deformation due to plate convergences across the Tobacco Root Mountain in the west/southwest, THO in the east, and GFTZ/VS/STZ northeastward, resulting in thickening of continental crust (Chen et al., 2015) and the lithospheric mantle (e.g., Hearne Province; Bao & Eaton, 2015; Chen et al., 2017).

## 4.5 Conclusions

This chapter analyzes the broadband seismic data recorded by USArray and the most complete set of regional seismic networks to date. The measurements show major improvements in the resolution of Moho depths and Vp/Vs ratios over existing regional and global models. Stacked RFs suggest lateral variations in Moho depth from the WCSB to the adjacent Cordillera, and strong gradients in Moho depth and Vp/Vs ratios across proposed Paleoproterozoic suture zones. Combining with existing potential field and geological observations, the following key conclusions can be reached.

1. We observe significant crustal thickening and Vp/Vs ratio increases near the STZ and GFTZ, which favor a collisional origin for both proposed tectonic boundaries.

2. We dispute the earlier geophysical definition of the GFTZ based on linear northeast striking potential field gradients near the U.S.-Canada border.

The outcomes of our RF analysis suggest that the true suture is located ~150 km to the southeast within the TMO, consistent with earlier surface geological observations.

3. Based on confined zones of high Vp/Vs ratio and depressed Moho, we stipulate that the spatial extent of crustal underplating near the GFTZ is significantly smaller than earlier reported and is mainly confined to the TMO.

Finally, in view of similar rock ages from all parts of northern Montana and the WCSB basement, we conjecture that the Rae, Hearn, MHB, and Wyoming cratons were all active during the Paleoproterozoic era and their interactions, particularly coeval subductions and collisions, are largely responsible for the basement geology beneath western Laurentia.

# Chapter 5 Finite-frequency travel-time tomography of the mantle lithosphere of western Laurentian craton

## 5.1 Background

The lithosphere beneath the WCSB has recorded almost three quarters of Earth history (3.3 Ga), and thus provides an excellent natural laboratory to investigate the evolution of continental lithosphere as far back as to Archean time. Chapter 4 conducts a detailed investigation of the crustal imprints of this protracted geological period, which contributes to the improved understanding of the tectonic architecture and assembly processes of western Laurentia at the crustal level. However, questions remain on 1) how these crustal subdivisions are manifested in the mantle lithosphere, 2) how these tectonic events initiated and/or modified the intrinsic stability of the craton, and 3) what surface expressions (e.g., gravity, heat flow, discoveries of kimberlites) are attributable to mantle dynamics. Answers to these questions are predicated on improved imaging, and proper integration, of mantle P- and S- wave speeds beneath the WCSB, which are the overarching objectives of this chapter.

This chapter summarizes the results of travel-time tomographic imaging from two consecutive studies. The first one presents the first finite-frequency P-wave velocity model of the central-southern Alberta, which focus on 1) investigating the integrity and characteristics of the lithospheric mantle and 2) providing a general appraisal of the existing regional tectonic framework and model for the Precambrian evolution. The second part expands upon the first

study by 1) presenting an updated P velocity and a new S velocity models covering all of Alberta, and 2) performing an integrated analysis that combines seismic velocities with constraints from heat flow, gravity and kimberlite data. The new high-resolution P and S velocity models permit a systematic examination of the structures and properties (density, velocity and inferred composition) of mantle lithosphere. This offers new insight on the potential link between mantle velocity gradients and diamond-bearing kimberlites in the northern WCSB, an under-sampled region by pre-existing seismic data.

## 5.2 Data and method

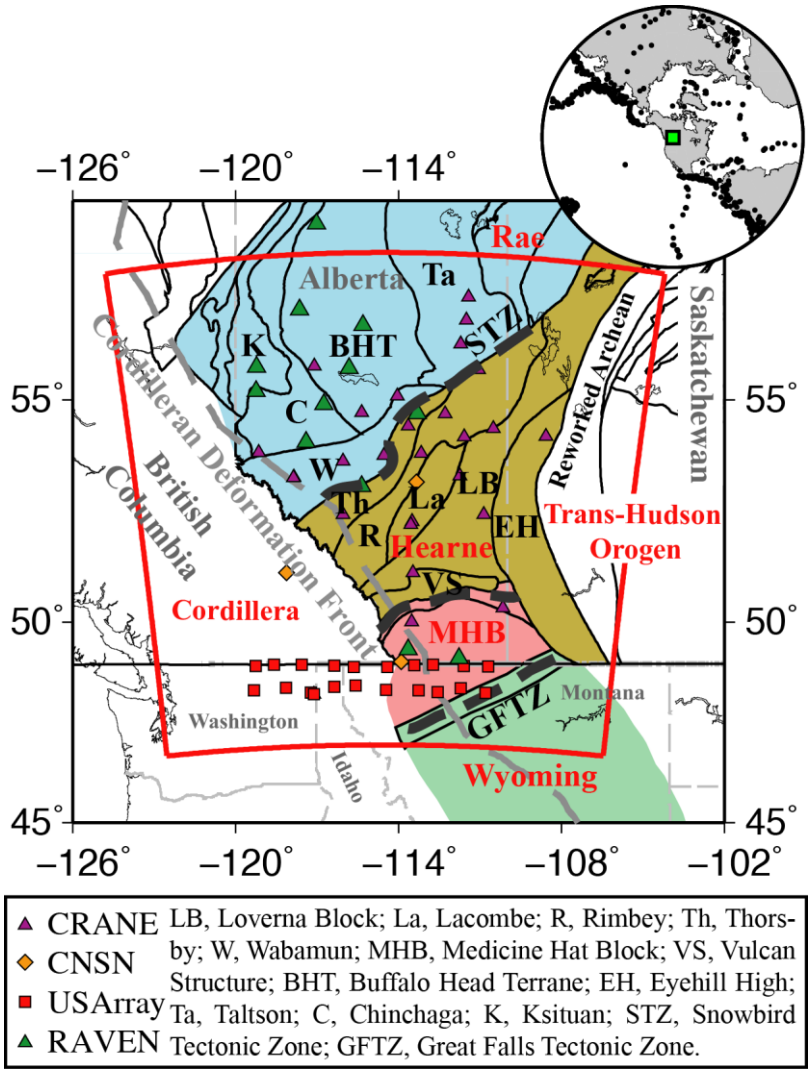


Figure 5.1 The tectonic domains in western Laurentia. The red lines mark the boundaries of P-wave velocity model. The black and grey dashed lines indicate the respective locations of major structural discontinuities (i.e., the STZ, VS and GFTZ) and the Cordilleran Deformation Front. The various symbols denote the stations used in this study. The earthquake epicenters are shown in the map inset and the green square marks the region of study.

The dataset used to construct the first P-wave model consists of recordings from 63 stations from 4 regional seismic networks (Figure 5.1). Teleseismic (30-90°) P-wave data from 1566 Mw N 5.5 earthquakes, recorded between 2006 and 2015, are included (see Figure 3.1), which accounts for a subset of the data analyzed in chapter 4. The second investigation updates the P-wave dataset by extending the recording period (up to early 2017) and including additional 26 broadband stations from the CANOE (2003-2005) array for resolution improvement near the northern WCSB. The resulting dataset comprises 1,729 and 1,263 earthquakes for P and S-wave analyses, respectively. The details of station and data statistics are summarized in Table 5.1.

| | P | P (UPDATE) | S |
|---|---|---|---|
| Number of Station | 63 | 89 | 89 |
| Number of Event | 1,565 | 1,761 | 1,263 |
| Number of travel-time measurements | 21,041 | 23,123 | 17,253 |
| Model coverage (deg) | 11×11 | 12×12 | 12×12 |
| Model depth (km) | 800 | 800 | 800 |

Table 5.1 Station, data and model parameter summaries for models from the first (2nd column) and second investigations (3rd and 4th columns).

The data processing procedures are largely identical between P and S data and are briefly summarized. We refer readers to chapter 3 for processing details. After removing the instrument responses, we filter the seismic signals into multiple bandwidths by applying a third order bandpass Butterworth filter with frequency ranges of 0.03-0.125 Hz (low) and 0.3-2.0 Hz (high) for P waves on the

vertical component and 0.03-0.1 Hz (low) and 0.1-0.2 Hz (high) for S waves on the tangential component. The P-wave frequency range is carefully determined to minimize the effect of a noise peak at ~0.2 Hz potentially caused by ambient noise in the secondary microseism band (10 s) originating from the nearby coastlines (Yang & Ritzwoller, 2008). We then measure the relative P(S)-wave arrival times for each station pair using the multi-channel cross-correlation method (VanDecar & Crosson, 1990). For all recording stations, the travel-time differences for a specific event are first determined as time delays that lead to the maximum cross-correlation coefficients. Subsequently, these delays are subjected to least-squares optimization, and the final travel-time residuals are calculated by subtracting the demeaned theoretical relative arrival times (AK135; Kennett et al., 1995) from the optimized values. The corrected differential travel times show consistent variation between P and S waves but differ in strength: P results accounts for about 40% of the S counterparts (Figure 5.2). The travel-time pattern can visually be subdivided into two distinctive halves, a positive (time delay) Cordillera and a negative (time advance) craton separated roughly by the CDF, and suggesting large structural variations across the study region.

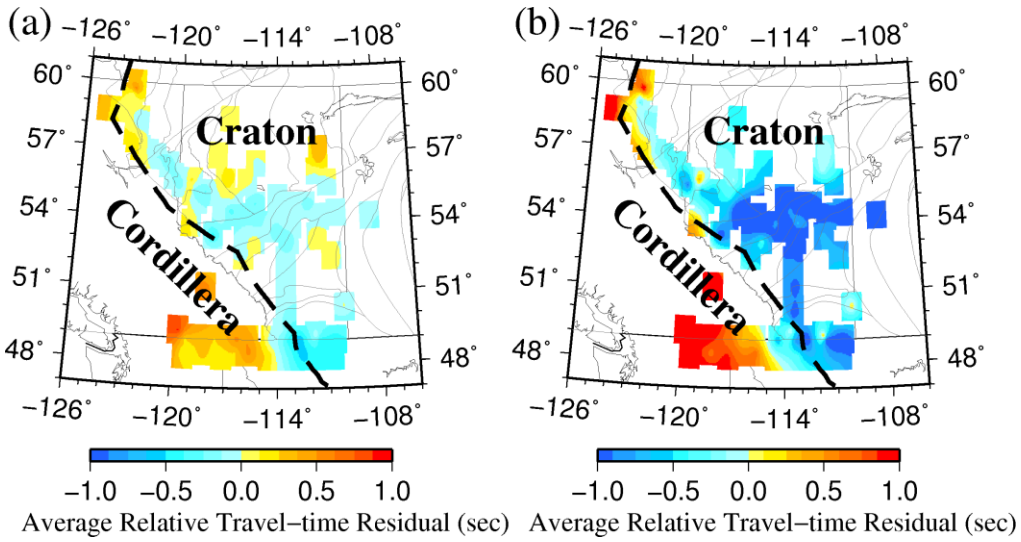


Figure 5.2 Color-coded (a) P-wave and (b) S-wave average relative travel-time residual at each station after minor spatial interpolation. Positive and negative values represent time delay and advance relative to regional mean, respectively. The dashed line marks the CDF.

The relative travel-time residuals are inverted for velocity perturbations. We parameterize our region, which covers most of the WCSB, into a spherical grid covering an area with lateral dimension of 11-12 degrees, depending on the model, and extending to 800 km in depth (see Table 5.1). We assign 33 nodes along each direction, which translate into a semi-uniform (spherical) grid size of about 40 km, 40 km, and 25 km in latitude, longitude and depth, respectively. The model parameters can be solved by formulating equation (2) into a concise matrix form

$$\mathbf{d} = \mathbf{G}\mathbf{m}, \tag{3}$$

where $\mathbf{d}$ is the data vector contains M relative travel-time residuals and $\mathbf{m}$ is the model vector contains N (33×33×33=35,937) slowness cells. The corresponding inversion kernel $\mathbf{G}$ is then a M×N matrix that defines the sensitivity of the datum

(**d**) to a slowness perturbation (**m**). Instead of solving equation (3) directly in a grid-based parameterization, we recover P and S velocities independently and transform the model vector and inversion kernel to the wavelet domain. We then seek a damped least-squares (DLS) solution for wavelet coefficients corresponding to each wavelet basis (i.e., hierarchical scale). This approach takes advantage of a data-adaptive scheme of non-stationary regularization and enables spatially varying resolution in the resulting model. The optimal model solution is determined by choosing the damping parameter associated with the turning point on the trade-off curve between model norm and variance reduction. More details on finite-frequency theory and multiscale parameterization can be found in Hung et al. (2011).

## 5.3 Resolution test

To avoid over-interpreting the outcomes of the inversions we first examine the spatial resolution of our model using a 'checkerboard' test. To do so, an input model is constructed with alternating velocity perturbations with amplitudes of 3% and 5% for P- and S-wave models, respectively. The checker size varies between 5-7 nodes, corresponding to a lateral dimension of 150-250 km, to investigate the resolving power of our data (Figure 5.3). Synthetic data (relative travel-time residuals) are computed using the actual station-event geometries with added Gaussian noise that is comparable to the observed travel-time standard deviations (0.05 sec for P model and 0.16 sec for S model). An inversion is then performed by adopting the same parameterization (wavelet transform) and damping schemes as those of the actual inversion.

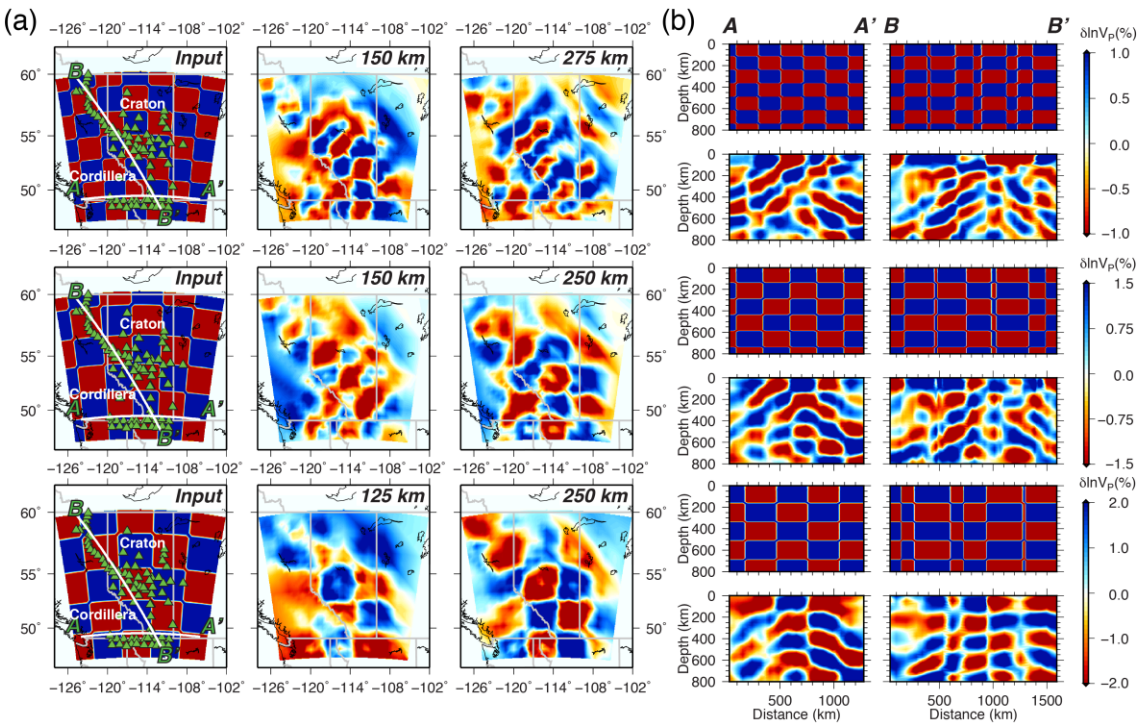


Figure 5.3 'Checkerboard' resolution test using various anomaly sizes. (a) Input P-wave velocities (left panel) and the recovered pattern near 150 km (middle panel) and 250 km (right panel) depths. The green triangles indicate the seismic stations. (b) The corresponding checkerboard test results along two cross-sections marked by the white lines in the input model.

The mantle 'checkerboard' anomalies are successfully recovered in the southern half (below 55º N) of the models in all test cases (Figure 5.3). The highest nominal spatial resolution is observed in southern-central Alberta and southwestern British Columbia (BC) at depths greater than 150 km, where velocity anomalies with lateral and vertical dimensions of ~100 km are robustly resolved. The well-constrained model space directly contributes to a robust determination and analysis of the cratonic structures in the southern WCSB. The smearing becomes more severe towards the northern corners of the model due to reduced ray coverage (see Figure 5.3a), where anomalies smaller than ~200 km

cannot be robustly resolved (see recovered models near 250 km depth in Figure 5.3a). The location of vertical boundaries between 'checkers' with alternating signs are accurately recovered in the southernmost Alberta (see cross-section AA' in Figure 5.3b) as a consequence of higher lateral sensitivity of teleseismic body-waves, which provides ideal resolution to constrain the Cordillera-Craton boundary, a key imaging target in this study. The corresponding S resolution test results suggest a minimum resolvable scale of ~200 km laterally, which is sufficient for imaging major seismic anomalies (e.g., deep craton root and large-scale Cordillera-Craton transition structures (see chapter 6)) in this region (Figure 5.4).

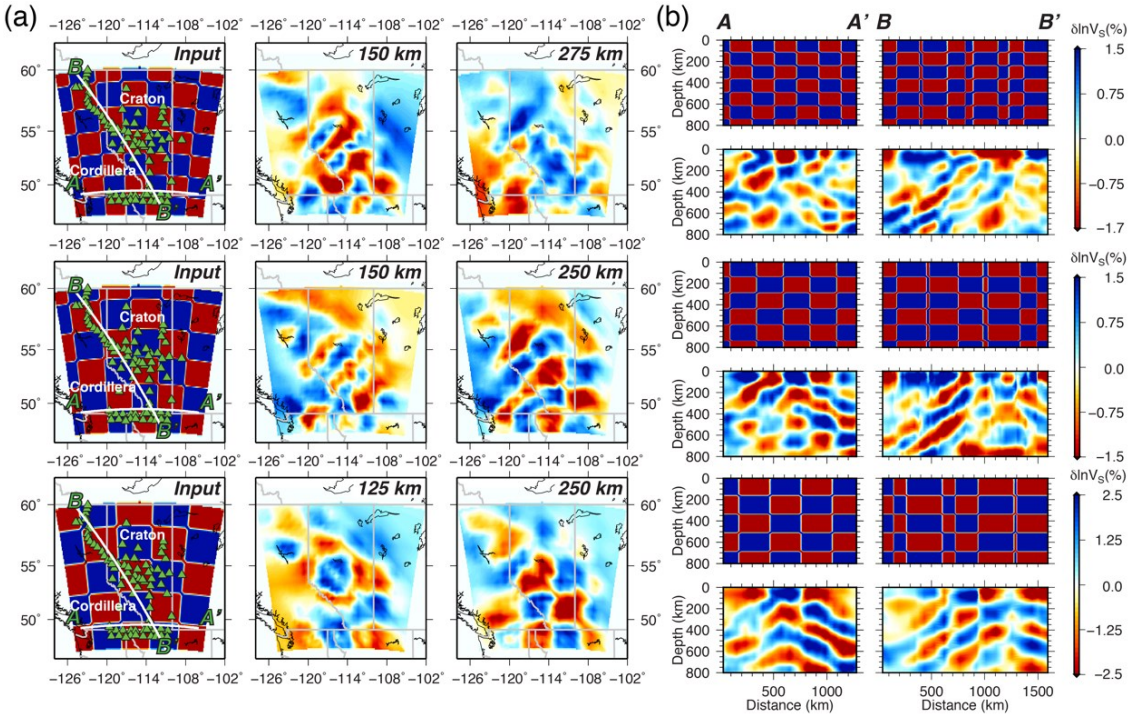


Figure 5.4 S-wave checkerboard test results. See Figure 5.3 caption for interpretation of the symbols.

## 5.4 Integrity and growth of the Laurentian craton

### 5.4.1 Upper mantle structures

The P-wave model from our finite-frequency travel-time tomography shows two groups of prominent seismic anomalies at the depths above 300 km in the upper mantle: 1) a low-velocity zone beneath the Rockies, and 2) a broad high-velocity region under the Precambrian basement of Alberta (Figure 5.5a). The P velocity increases by ~2% from the southern Canadian Cordillera (<-1%) to the Alberta basin (>1%) within a lateral distance of 50 km (Figure 5.5b). This sharp (>2%) eastward increase in seismic velocity approximately coincides with the steep (1000 m) topographic relief and a reduction in heat flow by 20 $mW/m^2$ (see Figure 5.5b), which imply different thermal regimes in the upper mantle between the Cordillera and the adjacent craton(s) (Frederiksen et al., 2001; Lewis et al., 2003; Mercier et al., 2009; Hyndman, 2010; Hyndman & Currie, 2011; Kao et al., 2013). A detailed examination of the Cordillera-Craton transition structure by combining both P- and S-wave models will be provided in chapter 6.

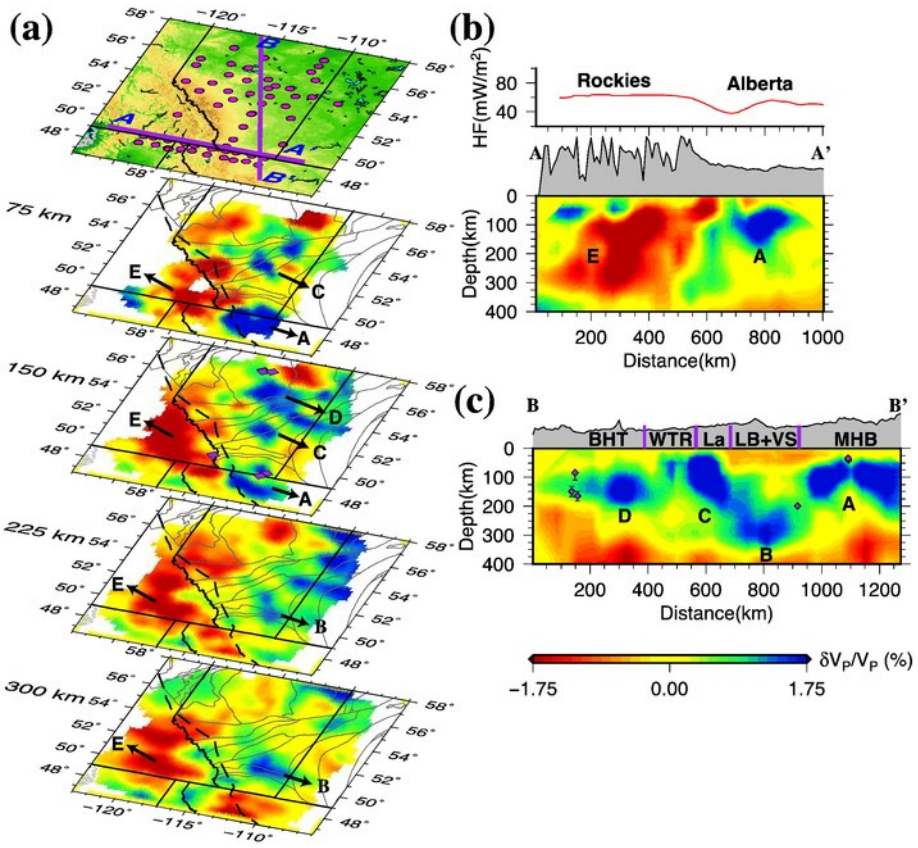


Figure 5.5 (a) P-wave velocities at four mantle depths. Poorly sampled grids have been removed prior to plotting. The purple lines and circles superimposed on surface topography indicate the locations of the profiles and stations, respectively. Five major anomalies have been labeled. The tectonic domain boundaries and the Cordilleran Deformation Front are indicated by the thin solid and thick dashed lines, respectively. The locations of mantle xenoliths (Buhlmann et al., 2000; Canil et al., 2003; Aulbach et al., 2004) are plotted at 150 km depth. (b) P velocity perturbations along the AA' profile. The topography is shaded in grey and heat flow (J. A. Majorowicz, 2018) is plotted above the surface topography. (c) Similar to (b), but for profile BB'. The purple lines mark the locations of the domain boundaries and the diamond symbols indicate the reported locations of xenoliths projected onto the cross-section. The error bars indicate the depth range of xenoliths. WTR: Wabamun, Thorsby and Rimbey. See Figure 5.1 legend for the other abbreviated domain names.

The distribution of high velocities east of the Cordillera shows significant spatial variations among the known basement domains of the WCSB (Ross et al., 1991; Villeneuve et al., 1993). In the depth range of 75-150 km, we identify distinct zones of high (>2%) velocities (see Figure 5.5a) beneath the Precambrian provinces Hearne (C), BHT (D) and MHB (A). The latter two anomalies (A and D) become less significant (~0.5%) at ~200 km (see map at 225 km depth in Figure 5.5a), below which the P velocities quickly become indistinguishable from the surrounding mantle (e.g., at 300 km depth). On the other hand, the high velocity zone beneath the Hearne province (anomaly C) exhibits downward continuity, extending obliquely to 350 km depth or greater (see B in Figure 5.5a). This deep, circular-shaped anomaly (with a rough radius of 200 km) is characterized by ~1.5% positive velocity perturbations, spanning the entire area within the crustal domain boundaries of the LB. In the same region, the P velocity decreases to -0.5% at depths above ~70 km, which is representative of a low velocity structure at crustal to shallow mantle depths.

## 5.4.2 Hypothesis test

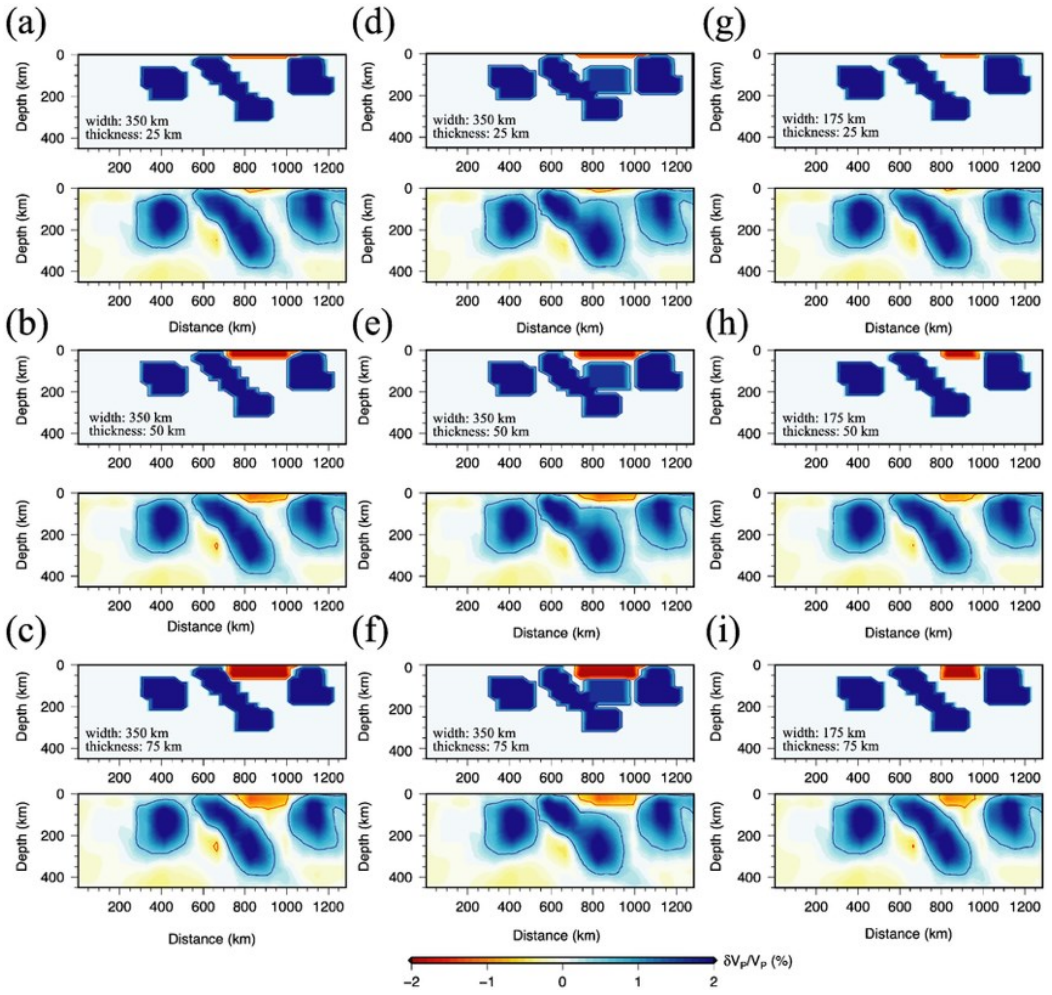


Figure 5.6 Hypothesis tests with variable input upper mantle structures (top panels). The output models (bottom panels) are recovered using the same data coverage and smoothing parameters as those from the actual inversion. The widths and thicknesses of the input low velocity anomalies are labeled.

The presence of relatively small-scale anomalies (e.g., the low velocities down to 75 km at location B, see Figure 5.5c) inevitably raises questions about the sensitivity of our dataset to secondary heterogeneities. To further assess the resolving power of the data, we perform three groups of hypothesis tests with

input models (top panels in Figure 5.6) that capture the geometries of the main findings detailed in section 5.4.1 (see Figure 5.5c). The amplitudes of the input low and high velocity anomalies are -2% and 1.5-3%, respectively, to account for the effects of damping and smoothing in the inversion. All synthetic tests adopt the same data coverage and choice of damping as those used in the actual inversion. The first group of models contain a 1.5% low velocity layer with variable thicknesses ranging from 25 to 75 km, which correspond to layers 1-3 of the parameterized model (Figures 5.6a-5.6c). Our inversion can recover 60% of the maximum amplitude of the input low velocity structures with thicknesses >50 km, but a 25 km thick layer is beyond the resolution of the data. Both the lateral and vertical dimensions of the input structures are reasonably constrained with minimal smearing effects. In the second test group, we introduce a 1.5% positive anomaly in the shallow mantle (Figures 5.6d-5.6f). The model recovery is comparable to those of the first group, except that the boundary between the crust and upper mantle is less apparent after the inversion. This suggests limited vertical resolution to sharp changes within the crust and the top 20-30 km of the upper mantle. In the final series of tests (Figures 5.6g-5.6i), we reduce the lateral dimension of the low velocity layer to half its original size, which approximately equals to the width of the VS inferred from the domain boundaries. With a recovery of 50% of the input amplitude, the outcome is satisfactory for an input 50-75 km thick low velocity layer despite a slightly reduced lateral dimension.

### 5.4.3 Depth extent of cratons

The dense regional teleseismic data enable us to examine the vertical extent of cratonic structures in western Laurentia at a higher resolution than before. We associate the high velocity anomalies to the east of the CDF with the mantle lithosphere beneath Precambrian cratons, which assumes vertically continuous structures from crust to mantle (i.e., crustal and mantle age are correlated; Lee et

al., 2011) due to the lack of reported mantle age from geochronological dating in the study region. To determine the depths of the cratons we compute the average 1D velocities corresponding to the high velocity zones labeled in Figure 5.5 (Figure 5.7a). The P velocities are vertically continuous below the MHB (A), Lacombe domain (C) and BHT (D) down to ~200 km depth, with positive perturbations in excess of 1% (Figure 5.7b); these are nearly opposite to the velocities (<-1%) beneath the Rockies (E). The mantle beneath the southern Hearne province (B) is visibly more complex, showing a velocity reversal from low (-0.5%) to high (0.5%) values at ~180 km depth (see the shaded area in Figure 5.7b). To determine the base of the lithosphere at a given region, we compute the velocity derivatives with respect to depth. Assuming the base of the craton is defined by the depth of the maximum negative velocity gradient (Priestley & Debayle, 2003; Hopper & Fischer, 2015), the depths of the lithosphere beneath the MHB (A), southern Hearne province (B), Lacombe domain (C) and BHT (D) are 230 km, 350 km, 220 km and 185 km, respectively. These values are determined based on the assumptions that 1) the background velocity model (e.g., AK135 model) contains a relatively constant velocity gradient at lithospheric depths and 2) the P-wave velocity transition is generally sharp across the lithosphere-asthenosphere boundary (LAB). The former criterion results in uncertainties that are <10 km, which are considerably smaller than the vertical resolution of body waves. The latter assumption is favoured by strong S-to-P converted phases resulting from the depth of a potential LAB (Fischer et al, 2010).

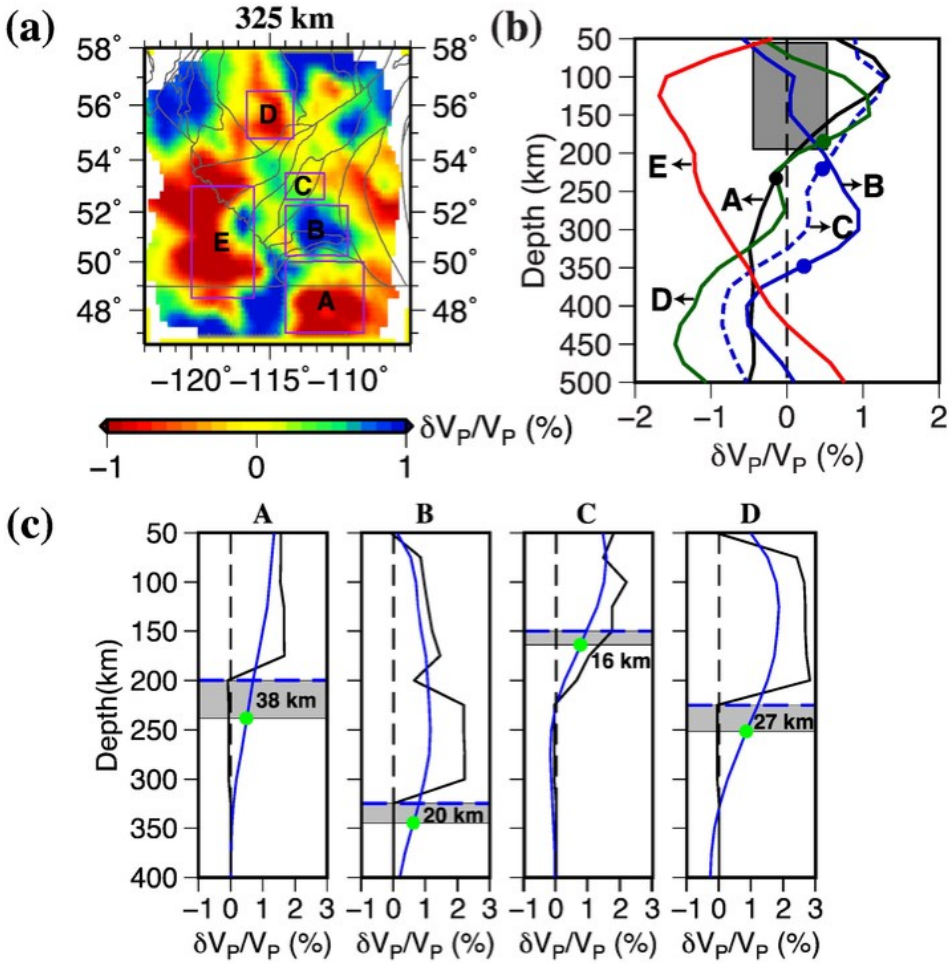


Figure 5.7 (a) P-wave velocity perturbations at 325 km depth. The enclosed regions highlight the lateral extents of major upper mantle anomalies. (b) Average 1D velocities computed from the regions defined in (a). The circles mark the base of the cratons. The shaded area highlights a low velocity mantle in region B. (c) Average 1D velocities of four cratonic regions calculated from the hypothetical input (black) and output (blue) models shown in Figure 5.6e. The craton depths of the input and output models are marked by the blue dashed lines and green circles, respectively. The shaded areas indicate variable amounts of vertical smearing. The base of the Lacombe domain (region C) is not well defined due to the dipping input structure (see Figure 5.6).

Because the depth extents of the seismic anomalies are often overestimated by body-wave tomography due to the effect of vertical smearing, it is critical to assess the degree of overestimation in our model space and make the appropriate corrections. To do so, we calculate the difference of the craton depths between the input (150-325 km) and output average 1D velocity models based on the hypothesis test (see models in Figure 5.6e). In this synthetic example, the base of the lithosphere is determined using the same criterion (i.e., the maximum negative velocity gradient) as that of the actual observation. The resultant raw craton depths from the recovered models overestimate those of the ground truth (i.e., input values) by 16 to 38 km, depending on the region (Figure 5.7c).

### 5.4.4 Comparison of craton depths

After correcting for the vertical smearing (~20 km, see Fig. 5.7c), we obtain a cratonic root of ~330 km beneath the southern Hearne province (region B). This observation is consistent with an earlier finding (~300 km) from body wave tomography (Shragge et al., 2002), though it is considerably deeper than a recent estimate (~260 km) from surface waves (Bao & Eaton, 2015). Garnet xenocrysts from the southwestern margin of the Hearne province (see Figure 5.5a for the kimberlite location) suggest a mantle root that was at least 200 km deep in the Triassic (Canil et al., 2003). This value is considerably shallower than our estimate (330 km), though the preferential distribution of kimberlites around the craton margins, instead of at the centers (Griffin et al., 2009), may be partially responsible. A recent magnetotelluric survey reported a 250 km deep craton beneath the MHB and southern Hearne (Nieuwenhuis et al., 2014), which falls well within our respective estimates of 200 km and 330 km.

Further north, our estimated craton thickness decreases to ~200 km beneath the Lacombe domain, a subdivision of the Hearne province consisting of low-grade metavolcanic and metasedimentary rocks with age ~2.3 Ga (Ross et al.,

1991). Beneath the BHT, a Proterozoic (1.99-2.34 Ga) component of the predominantly Archean Rae province (Ross, 2002a), the thickness of the lithosphere becomes ~185 km (160 km after correction), which is over 100 km thinner than that beneath the Hearne province. This value is generally consistent with the LAB depth estimates from xenoliths (180 km; Aulbach et al., 2004; see Figure 5.5a for sample locations), electrical resistivity (180-220 km; Türkoglu et al., 2009) and heat flow (200 km; Majorowicz et al., 2014) data, but it is significantly shallower than the reported value (260 km; Bao & Eaton, 2015) from surface wave tomography.

### 5.4.5 Global comparison of craton depths

Lithospheric thicknesses in western Laurentia enable a systematic comparison with those of other cratons. On a global scale, the reported depths of the cratonic roots from tomographic models can vary by 100 km or more (Figure 5.8a). Assuming coeval continental crust and mantle formation (Lee et al., 2011), the relatively intact cratons examined in recent literature exhibit no significant correlation between crustal age and lithospheric thickness (Simons & Van Der Hilst, 2002; Darbyshire et al., 2013; see Figure 5.8a). Aside from potentially distinct formation ages between the crust and its underlying mantle (Canil, 2008), the lack of correlation largely reflects the impact of secular evolution, such as growth and destruction, of the lithosphere (Griffin et al., 2009; Lee et al., 2011). Measurement techniques may also play a role: for example, the depth values obtained from body wave tomography are 60 km larger than those inferred from surface waves on average. This systematic shift, which is primarily due to the limited vertical resolution of body waves (McKenzie & Priestley, 2008), may be partially responsible for a deeper Hearne craton from this thesis (body wave; 330 km) relative to that from Bao & Eaton (2015; surface wave; 260 km). Regardless of the data types (body or surface waves), the southern Hearne province

consistently ranks among the deepest cratons in the world (see Figure 5.8a; Ritsema et al., 1998; Feng et al., 2004; Fishwick et al., 2005; Li & Burke, 2006; Priestley et al., 2006; Frederiksen et al., 2013; de Azevedo et al., 2015; Youssof et al., 2015). The thickness of its mantle lithosphere is, at a minimum, 100 km greater than those beneath the neighboring BHT and MHB. This substantial thickness variation within a relatively short (<150 km) lateral distance causes a major lithospheric depth gradient on either side of the Archean Hearne province along the NW-SE orientation (see Figures 5.5c and 5.8a).

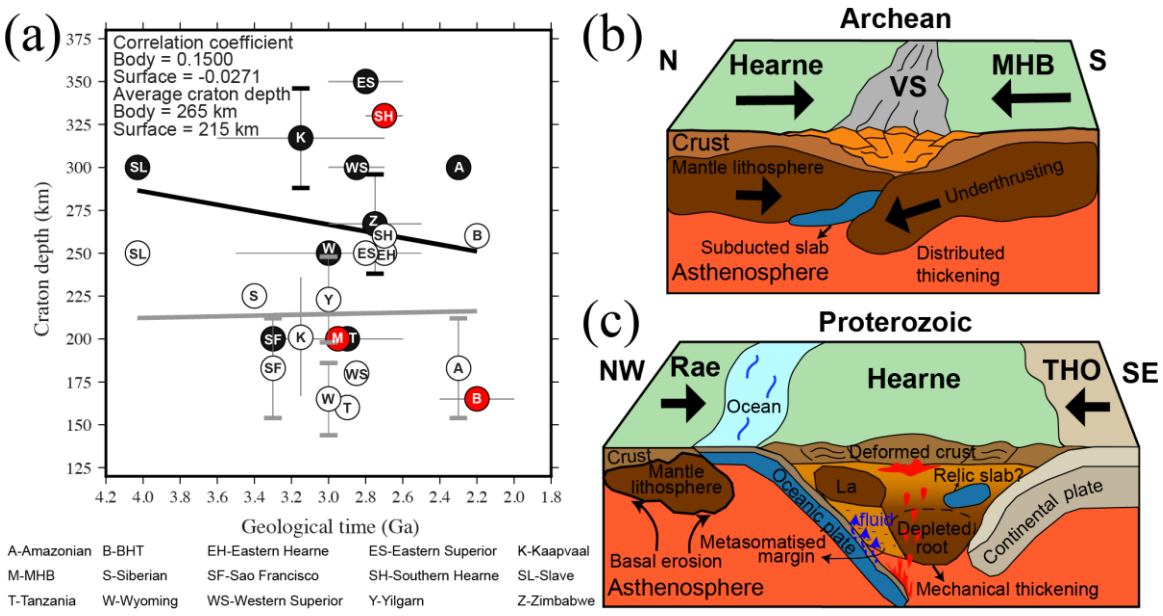


Figure 5.8 (a) A summary of the depths and crustal ages of cratons. The craton depths are obtained from recent literature based on surface (white circle) and body (black circle) wave tomographic inversions. The depth estimates from our study are marked by the red circles. The black and grey lines show the linear regressions for the body and surface waves, respectively. The age of Slave craton is based on the oldest rock of the 4.03 Ga Acasta genisses and is potentially biased. The younger granitoids with age less than 2.6 Ga have also been discovered from the Slave craton. (b) A schematic diagram showing Archean lithospheric growth (subduction, collision and distributed thickening) of the Hearne province. (c) A model showing the Proterozoic lithospheric growth beneath the Hearne province, which involves mechanical thickening and modification of the upper mantle during the Proterozoic dual-subduction process. Lithosphere beneath the Rae craton (BHT) was eroded by the convective mantle flow.

## 5.4.6 Assessments of earlier models of tectonic assembly

A deep Hearne craton, in conjunction with the low average velocities (-0.5-0.5%) in the crust and shallow mantle (see shaded area in Figure 5.7b), is consistent with the regional tectonic framework involving reported tectonic

assembly events during: 1) the Archean plate convergence between the MHB (3.8-2.6 Ga) and the Hearne province (2.71-1.78 Ga; Lemieux et al., 2000; Clowes et al., 2002; Gorman et al., 2002), and 2) the post-Archean (Proterozoic) dual-subduction and reworking of the Hearne craton (Boerner et al., 2000; Ross et al., 2000; Ross, 2002a). The former process (Archean collision; Ross et al., 1991; Eaton et al., 1999a) is consistent with our observation of reduced seismic velocities overlying the deepest root beneath the southern Hearne province and the Archean suture zone of the VS (see Figures 5.5c and 5.7b). In the same region, Gorman et al. (2002) reported a north-dipping seismic reflector in the upper mantle and interpreted it as a relic subducted oceanic lithosphere. It is plausible that the fertile peridotite within the subducted slab or metasomatic fluids from slab dehydration could have enriched the overlying mantle (Figure 5.8b), thereby lowering seismic velocity of an otherwise chemically-depleted (i.e., fast) craton (Jordan, 1978; Griffin et al., 2008). The resultant fertilized upper mantle is compatible with the increased mantle conductivity in this region (Nieuwenhuis et al., 2014). Following this subduction, the lithosphere near the collisional boundary (i.e., the VS) may have undergone distributed thickening (Pysklywec et al., 2002) in response to the continent-continent collision (see Figure 5.8b).

Proterozoic (2.0-1.8 Ga) tectonic events (Figure 5.8c) may have also impacted the growth of the lithospheric keel of the Hearne craton. It has been suggested that contemporaneous subduction took place along the STZ and THO during the terminal collisions that amalgamated the Hearne province with the Rae province to its NW (Ross et al., 1991; Eaton & Cassidy, 1996) and with the Superior province to its southeast (Lucas et al., 1993; Corrigan et al., 2005; see Figure 5.8c). The entrapment of Hearne between Rae and THO may have induced mechanical thickening (i.e., thickening in response to the horizontal shortening; Conrad, 2000) due to the compressive stresses exerted by the strong plate coupling (Ross, 2002a; Bao & Eaton, 2015). During this process, the coeval tectonothermal events (Clowes et al., 2002; Ross, 2002a) may have significantly

modified the mantle lithosphere, as suggested by the absence of Archean signature from mantle garnet xenocrysts (Canil et al., 2003) and increased mantle conductivity (Boerner et al., 2000), and further enhance the compositional differentiation of the Hearne craton (see Figure 5.8c). For example, the margin of the Hearne craton (Lacombe domain) may have undergone metasomatic enrichment due to the transfer of fluids and melts from the underthrusting oceanic plate (i.e., the Thorsby domain; Ross, 2002a; see Figure 5.8c). A similar subduction-driven modification has been documented along the eastern margin of North American craton (Boyce et al., 2016).

The Precambrian tectonic history provides an ideal geological frame-work to interpret the observed velocity anomalies beneath the Hearne craton. More recent (Mesozoic) terrane accretion and subduction beneath the western margin of Laurentia could have significantly impacted the shallow mantle structure within the cratonic lithosphere. One such modification is documented in the Wyoming craton, which collided with the MHB during Archean assembly events along the GFTZ (see Figure 5.1). It was suggested that the Wyoming lithosphere underwent delamination and the subsequent emplacement of an oceanic plateau in association with the subduction of Farallon slab (Humphreys et al., 2015). Considering the geographical affinity between the Wyoming craton and our study area, this process provides a simple and attractive explanation to most of the observed velocity anomalies. Under this assumption, the high velocity root of the Hearne province could represent an accreted, basalt-depleted oceanic plate, while the overlying low velocities can be attributed to metasomatic enrichment induced by the fluid dehydration of the slab. However, this hypothesis remains speculative, as 1) there is limited geophysical evidence for the basement reactivation of the Hearne craton since the Paleoproterozoic (1.8 Ga; Ross & Eaton, 1999) and 2) the expected effect of the Farallon subduction would be the most significant along the southwest-northeast orientation rather than trench parallel (see cross-section BB' in Figure 5.5). A further study involving more

detailed geophysical imaging, geochronological dating and geodynamical modeling will be required to ascertain the effects of the Mesozoic subduction on the structure beneath the Precambrian cratons.

In addition to the lithospheric growth events illustrated in Figures 5.8b and 5.8c, the first-order difference in lithospheric thickness between the Hearne craton (~330 km) and its adjacent Precambrian domains (~200 km) may have been further enhanced by the subsequent destruction processes, most notably connective erosion (Artemieva & Mooney, 2002; Lee et al., 2011). Our observations fall within the bimodal distribution of craton thickness globally, which is interpreted as the by-product of the preferential erosion of cratons with different sizes following the break-up of a supercontinent (Artemieva & Mooney, 2002). This hypothesis provides a partial explanation for a shallow lithosphere beneath the BHT, as a smaller BHT is subjected to greater erosion by the convective mantle flow than a larger Hearne province in response to possible asthenospheric upwelling and incipient rifting along the STZ (Flowers et al., 2006). This convective removal process may have been further enhanced by the metasomatic refertilization via the movements of melts or fluids (Foley, 2008; Lee et al., 2011), which would effectively reduce the bulk velocities of the lithospheric mantle in the vicinity of the BHT (e.g., beneath the WTR; see Figure 5.5c for location). Melt generation was evidenced by the asthenospheric-derived silicate magma (Aulbach et al., 2004) and the subsequent Paleoproterozoic melt intrusion into the shallow lithosphere beneath the BHT (Welford & Clowes, 2006). This mechanism was invoked to explain the partial removal of the lithosphere beneath the central Rae craton (Liu et al., 2016).

## 5.5 A new appraisal of lithospheric structures

This section continues on the results and discussion of the earlier P-wave model. The new P and S models enable us to examine the robustness and

consistency of the mantle images. More importantly, the new models offer critical seismic constraints to previously undersampled region of the northern Alberta and shed new light on the composition of the cratonic mantle lithosphere.

### 5.5.1 Craton structures revealed from P- and S-wave models

The new P- and S-wave tomographic models reveal consistent mantle velocity variations across the region of study. Similar to the observations from the earlier P-wave model, the dichotomy of velocities is apparent as negative velocities dominate the upper mantle beneath the Canadian Cordillera and positive velocities underlie much of the Precambrian basement of the WCSB (Figure 5.9). The new P velocity model validates the presence of a pronounced high-velocity zone in the depth range of 200-300 km (region 1 in Figure 5.9) and a low-velocity zone between 100-200 km depth beneath the Hearne province (see Figure 5.10a and section 5.4.3). To first order, the S model shows consistent velocity variations with the P-wave counterparts (Figure 5.10b). The deepest lithospheric root, as indicated by vertically coherent high velocities, is found beneath the Hearne province, and the lithosphere becomes substantially thinner (~200 km) towards the BHT and MHB. A common observation in both models is the well-defined transition from thick to thin lithospheres in central Alberta. The base of the craton is determined using the same derivative based approach (see section 5.4.3) and the resulting lithosphere depths in northern and southern Alberta are ~160 km and ~300 km after correcting for vertical smearing in respective regions, consistent with the measurement based on earlier P-wave model. Between the P and S models, the latter shows similar decreased velocities beneath the southernmost Hearne province but less definitive horizontal mantle stratifications (e.g., associated with the LAB). This discrepancy could be partly explained by reduced model resolution due to fewer crossing ray paths (see Figure

5.4), though spatial averaging due to lower frequency S waves (hence broader sensitivity kernels) could be partially responsible.

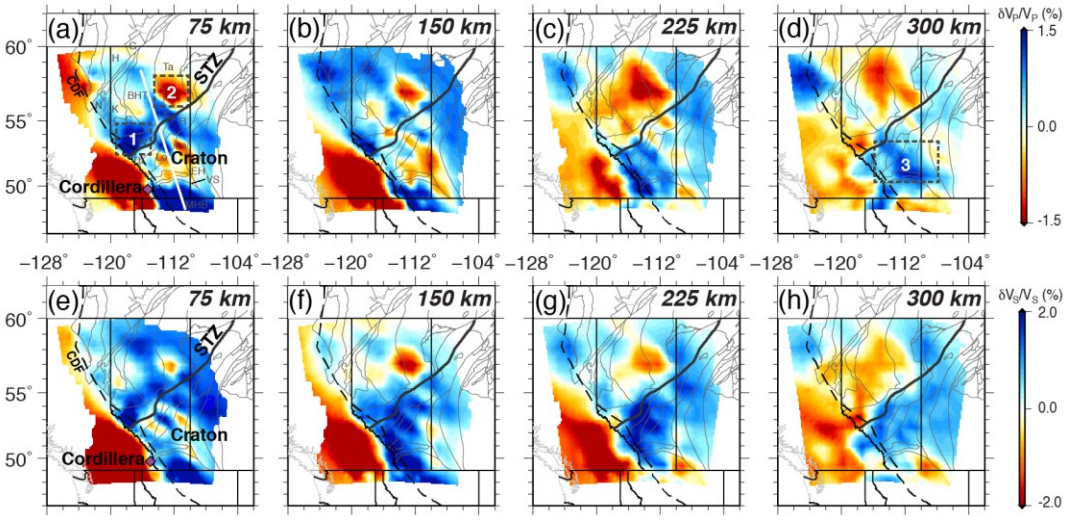


Figure 5.9 (a)-(d) New P- and (e)-(h) S-wave tomographic models between 75-300 km depths. The numbers label the key structures discussed in this study. Regions with less data sampling are masked. The dashed line marks the CDF, which approximately divides the low velocities in the west from the high velocities in the east. The white line indicates the location of the profile shown in Figure 5.10. Kimberlite intrusion site sampling the southwestern Hearne province is marked by the purple diamond at 75 km (Canil et al., 2003).

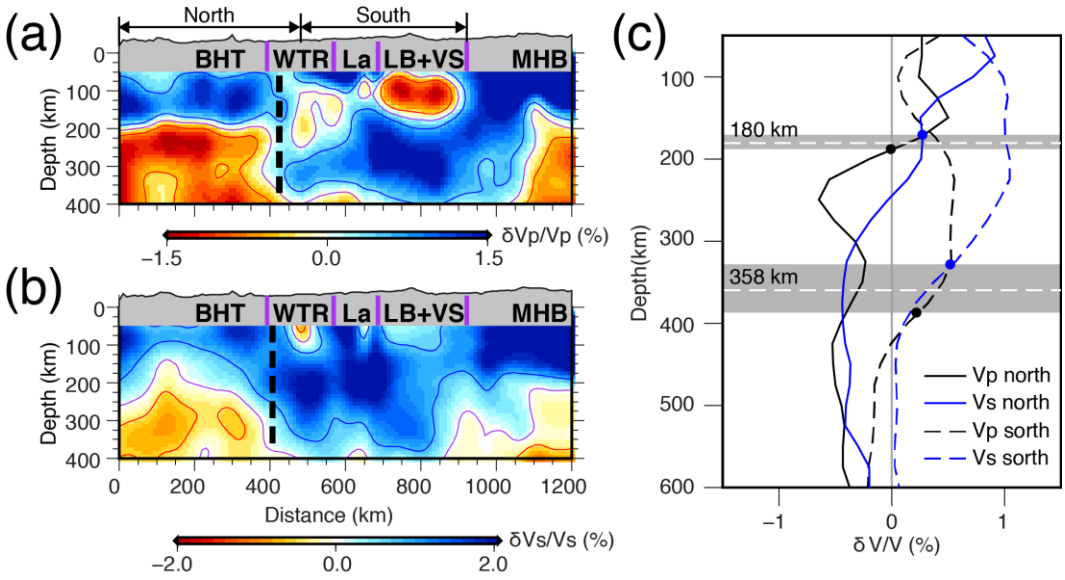


Figure 5.10 (a) P- and (b) S-wave velocities along a cross-section in the Alberta basin. The dashed line marks the transition from thin (north) to thick (south) lithospheres across the STZ in central Alberta. The location of the cross-section is indicated by the white line in Figure 5.9. The red, purple and blue lines indicate -0.5 (-0.75), 0 and 0.5 (0.75) percent P (S) velocity contours, respectively. (c) Average 1D velocities for crustal domains to the north and south of the STZ. The circles mark the base of the lithosphere determined from the maximum velocity gradients. The shaded regions show the range of lithosphere depths from P and S models and white dashed lines indicate the mean values.

Benefiting from an improved data coverage in northern Alberta, the new models show a pronounced low-velocity zone on both P- and S-wave models (see region 2 in Figure 5.9a). Although this anomaly has also been imaged in the earlier P-wave model, its marginal position and a reduced model resolution precludes a comprehensive analysis of its significance. This low velocity body emerges at 75 km depth and extends sub-vertically downward to ~300 km, where its amplitude reduces and equilibrates with the surrounding mantle (see Figure 5.9). Due to the presence of this first-order structure, the velocity beneath the Taltson magmatic zone (Ta) is significantly slower than the BHT (see Figure 5.9).

These two domains were suggested to represent a single Paleoproterozoic crustal entity evolved from variable contributions of depleted mantle (McNicoll et al., 2000). In this case, the higher velocity beneath the BHT may result from a greater extent of mantle depletion. This low velocity zone coincides with regions of increased heat flow, which may suggest potential high mantle temperatures and partially contribute to the reduced seismic velocities (Griffin et al., 2003; Artemieva et al. 2006). However, in view of a proposed conductive cooling age since 1.9 Ga of the BHT (Ross & Eaton, 2002), a more plausible explanation is the compositional modification to the depleted Archean mantle lithosphere (Aulbach et al. 2004). Both the BHT and Taltson have been suggested as the upper plates during subduction and their crusts have been overprinted by post-collisional magmatism (Ross & Eaton, 2002). The subducted oceanic plate could have induced dehydration melting of the slab, which would effectively enrich the overlying continental lithosphere through melt percolation. Similar mechanism of subduction-driven metasomatism was invoked to explain the velocity decrease at the eastern margin of the North American craton (Boyce et al., 2016). This interpretation was supported by the mantle xenolith and xenocryst data from the Buffalo Head Hills kimberlites, which suggest that mantle has undergone at least two episodes of metasomatism by respective silicate and volatile-rich melts in the deep and shallow lithospheres (Aulbach et al., 2004). During protracted period of melt-interaction, the velocity of an originally depleted lithosphere could be reduced through 1) refertilization of the mantle lithosphere (Griffin et al., 1998; Lee et al., 2011) and 2) modification (increase) of temperature due to concentrations of radioactive elements (Artemieva, 2009; Hieronymus & Goes, 2010). This joint thermochemical effects could explain seismic anomalies up to 3-4.5% in Vs and 2.5-4% in Vp (Hieronymus & Goes, 2010), which are sufficient to explain the observed low velocities in this region.

## 5.5.2 Comparisons of seismic velocities to heat flow

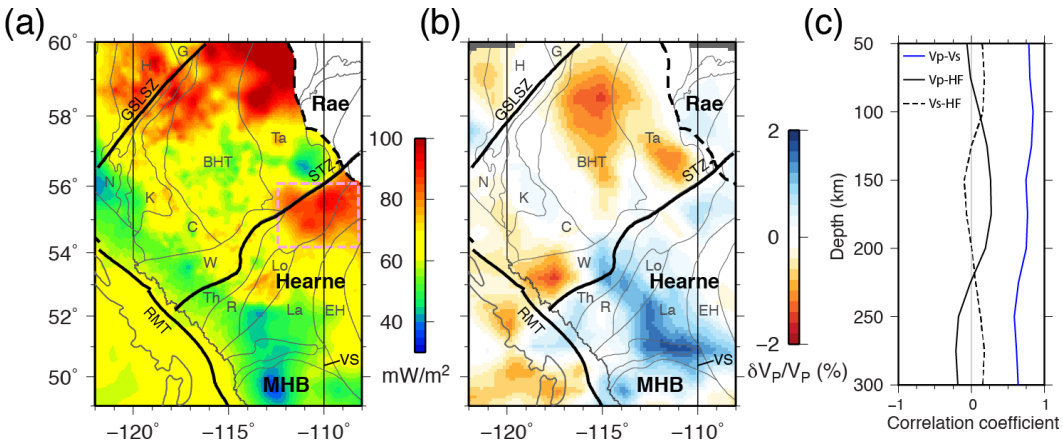


Figure 5.11 (a) Heat flow of the WCSB (J. A. Majorowicz, 2018). The enclosed area shows high heat flow, which overlaps with an earlier reported crustal low velocity zone (Chen et al., 2015). (b) Averaged P-wave velocities between 50-300 km depths. (c) Correlation between heat flow and seismic velocity at each depth. The blue line indicates the correlation between P and S velocities.

Global seismic tomography reveals positive velocity anomalies beneath all cratons and defines the seismic lithosphere characterized by a high-velocity lid (Polet & Anderson, 1995; Artemieva, 2009). Arguments have concentrated on the compositional vs. non-compositional (thermal) contributions to the variation of continental seismic velocities (Forte & Perry, 2000; Deschamps et al., 2002; Artemieva, 2009). The diverse mantle regimes sampled by our model, which range from the Precambrian basement of the WCSB to a Phanerozoic Cordilleran orogen, offer a rare opportunity to examine age-dependent variations in these physical properties and their effects on the seismic velocities of the continental lithosphere.

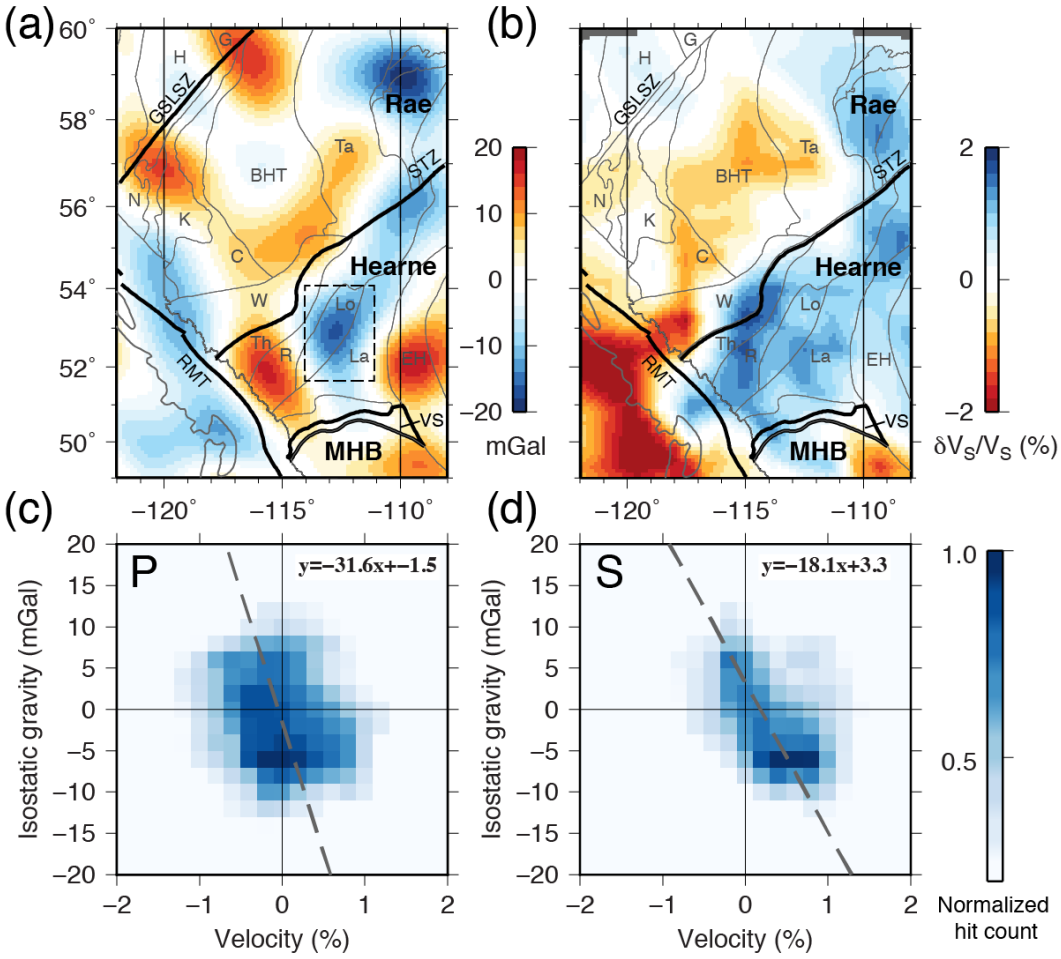


Figure 5.12 (a) Long wave-length isostatic gravity field (Jobin et al., 2017). The enclosed region highlights a significant gravity low in the southern Hearne province. The thick lines indicate the major tectonic boundaries. (b) Averaged shear velocities between 100-300 km depths. The gravity lows are generally underlain by high shear velocities to the south of the Snowbird Tectonic Zone. Correlation between isostatic gravity and (c) P and (d) S velocities. The color shows the normalized hit counts of grid points with certain gravity and velocity values. The dashed line indicates a weighted linear regression computed using grids with number of hits larger than 0.6 to capture the regional trend. For example, the Cordilleran region is excluded due to low hit count.

Seismic velocity and heat flow have been widely used to infer the temperature and thermal thickness of mantle lithosphere, which is typically defined by the depth of 1300 ºC isotherm (Goes et al., 2000; Röhm et al., 2000; Artemieva, 2006). The correlations between thermal thickness, seismic velocity and tectonic age have been examined on both global (Röhm et al. 2000; Artemieva & Mooney 2001; Artemieva 2006, 2009) and continental (Furlong et al., 1995; Goes et al., 2000; Godey et al., 2004) scales. In this thesis, we investigate this correlation beneath the western margin of Laurentia based on the combination of our models and a compilation of thermal data from Majorowicz (2018). The heat flow varies substantially from high values (80±10 mW/m$^2$) in the northern part of our study region to low values (50±7 mW/m$^2$) in southern Alberta (Figure 5.11a). The latter region covers the Archean-aged Hearne and MHB cratons that are underlain by the highest (>2%) velocity perturbations (Figure 5.11b) and generally agrees with the average Archean heat flow (42±10 mW/m$^2$) in the Canadian Shield (Jaupart et al., 1998). However, the overall regional correlation between the seismic velocities and the surface heat flow is low, showing coefficients (typically less than 0.2, Figure 5.11c) that are statistically insignificant. Our measurement is similar to the low correlations found in the upper mantle of Europe (Goes et al., 2000) but deviates from a moderate anti-correlation (coefficient of 0.6) trend reported in the earlier continental-scale studies of North America (Röhm et al., 2000; Godey et al., 2004). This strong regional variability could reflect a change in the dominant heat flow sources of the crustal heat production and mantle heat flow. Earlier studies have suggested that the thickness of high heat production layer is required to vary by as much as a factor of 2 to account for the large heat flow perturbation across the WCSB (see Figure 5.11a; Majorowic, 2018). This argument is supported by a pronounced heat flow high that flanks the STZ to the south in central Alberta (see Figure 5.11a), a region intruded by granitic rocks at upper-middle crustal depths (Bouzidi et al., 2002; Chen et al., 2015). The thick (>10 km) granitic layer that enriched in heat generation elements could serve as an effective heat reservoir and

cause an elevated heat flow in this region. The dominant crustal contribution of the surface heat flow infers a relatively constant and low mantle heat flux (15±5 $mW/m^2$; Majorowicz, 2018) beneath the WCSB, which is supported by the lack of correlation between mantle velocity and heat flow in our study.

### 5.5.3 Comparisons of seismic velocities to gravity

Globally, a pronounced correlation between the crustal age and mantle chemical composition has been suggested to reflect the secular depletion of the mantle lithosphere (Jordan, 1988; Griffin et al., 2008). The degree of depletion generally increases with tectonic age (Artemieva, 2009; Lee et al., 2011). For instance, the Archean mantle is characterized by a strongly depleted composition due to loss of Fe and Al during secular melt extraction, whereas Proterozoic and Phanerozoic lithospheres show intermediate and fertile compositions, respectively (Griffin et al., 2003; Artemieva, 2009). A key factor determines the degree of depletion is the iron content in the mantle olivine (Deschamps et al., 2002), which is quantitatively defined as Mg number (Mg#=Mg/[Mg+Fe]). There is a general decreasing trend of density with increasing Mg# (Lee, 2003; Schutt & Lesher, 2006). Although a direct measurement of Mg# (i.e., the degree of depletion) is hampered by a lack of xenolith samples in the WCSB, density variations reflected from the gravity field provide the first-order constraints on lithospheric compositions.

Earlier studies have focused either on a direct examination (e.g., Ross et al., 1991; Pilkington et al., 2000; Bouzidi et al., 2002) or modeling (e.g., Lemieux et al., 2000; Hope & Eaton, 2002, 2003; Lynn et al., 2005) of gravity data to resolve subsurface structures of the WCSB. Our study benefits from the new mantle velocity constraints and allows a detailed examination of sub-crustal structures and the associated density variations. We use isostatically-corrected Bouguer anomaly (i.e., isostatic anomaly) to minimize the effects of deep crustal roots (e.g.,

~50 km near the foreland thrust-and-fold belts; see chapter 4) on the measured gravity fields. The resulting (isostatic) anomaly represents an integrated effect of the mass distribution in the lithosphere, contributed by diverse sources with different characteristic wavelengths. To isolate various source contributions, we filter the gravity data into intermediate wavelength (280-1400 km) to suppress the shallow structures assuming the maximum source depth is a quarter of the wavelength (Lynn et al., 2005). As a result, the selected corner frequency (280 km) effectively removes gravity anomalies from sources shallower than 70 km, a depth range poorly constrained by our tomographic model.

A significant isostatic low is observed in the southern Hearne province (Figure 5.12a), which suggests the topography is isostatically overcompensated (i.e., the estimated root is smaller than actual; Lowrie, 2007). However, this argument is inconsistent with a relatively shallow Moho in this region (Bouzidi et al., 2002; Gu et al., 2018; see chapter 4) and implies a possible deeper (sub-crustal) gravity source. Considering a dominant upper mantle contribution to the gravity anomaly beneath the North America craton (Thompson et al., 2011), we suggest this isostatic low is likely caused by the deep cratonic root of the southern Hearne province (Figure 5.12b). On the other hand, northern Alberta shows a broad region of isostatic high in association with a shallow lithosphere (see Figure 5.12c). A quantitative comparison shows a clear negative correlation between the filtered isostatic gravity and velocities (Figures 5.12c and 5.12d), suggesting a possible common controlling factor for both physical properties. In other words, it is conceivable that the highly-depleted cratons (e.g., Hearne province) in our region, which are characterized by high seismic velocities and low densities, are the products of extensive melt extraction of the Archean mantle lithospheres (Lee et al., 2003; Schutt & Lesher, 2006). This interpretation is consistent with global trends of major iron-depleted deep lithospheric keels in the Slave/Hearne cratons of the Canadian Shield, the western part of the East European Craton, the Siberian craton, and south and west African cratons (Artemieva, 2009).

## 5.5.4 Correlation with kimberlite locations

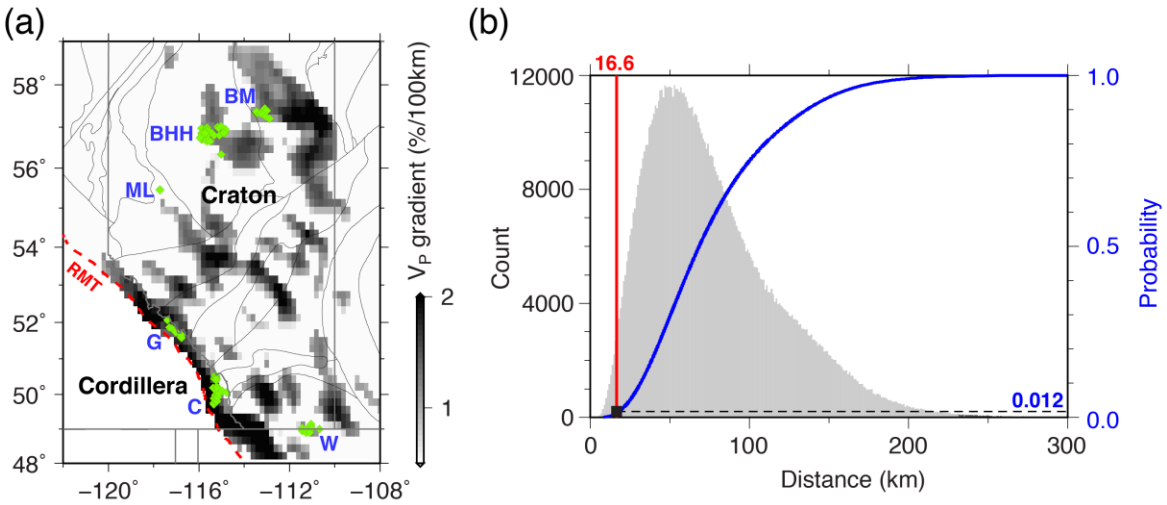


Figure 5.13 (a) Average P velocity gradient of craton within the diamond stability field (150-250 km depths). The green diamonds mark the location of kimberlite and lamproite intrusions from World Kimberlite database (Faure, 2010). Abbreviation: BH, Birch Mountains; BHH, Buffalo Head Hills; C, Cross; G, Golden; ML, Mountain Lake; W, Williams. (b) Monte Carlo simulation of kimberlite locations. The observed average distance between kimberlite clusters and the high velocity gradient zones (HVGZ) is indicated by the red line. The blue line shows the cumulative probability of the average kimberlite-HVGZ distance distribution (histogram). The black square indicates the intersection of these two lines. The horizontal dashed line marks the probability that kimberlite clusters distribute at distances less than the observed value (16.6 km).

The cratonic basement of the WCSB has been intruded by several kimberlite groups during the Mesozoic. Our new seismic model permits a detailed examination the potential relationship between the deep lithosphere structure and shallow kimberlite deposits. To this end, we calculate the average horizontal P velocity gradient between 150-250 km depths, a range with ideal pressure-temperature conditions for diamond preservation, and the resulting model shows

an excellent spatial correlation between the high velocity gradient zones (HVGZ) and kimberlite sites (Figure 5.13a). The mean distance between kimberlite clusters and the nearest HVGZ is calculated by a weighted average based on the number of reported samples (Faure, 2010). Our result shows that the kimberlites are generally distributed within 20 km lateral distance from the HVGZ. To examine the statistical significance of our observations, we perform a Monte Carlo simulation while assuming the kimberlite locations follow a uniform distribution, i.e., the kimberlite has equal probability to fall into any grid in the map area. A total of $10^6$ simulations are conducted and an average kimberlite-HVGZ distance of all 6 clusters is calculated in each realization. The summarized distribution resembles a skewed Gaussian function with a gradually tapering tail at greater distances (Figure 5.13b). Our observed value intersects with the cumulative density function at 1.2%, a low probability to recover the observed kimberlite distribution pattern, which suggests that the observed spatial association is unlikely to be coincidental.

These results establish a statistically robust relationship between the kimberlites and mantle lithosphere structures in the WCSB. Similar kimberlite distribution patterns were reported in Australia, where surface wave tomography shows the diamondiferous intrusion appear preferentially at the craton margins (Jaques & Milligan, 2004), and the nearby THO, in which the Cretaceous diamondiferous kimberlites occur above or near the rims of a pronounced low velocity anomaly. These observations might reflect the regional/local structural controls on the diamond concentration, which is also evidenced by the alignment of kimberlites with the potential field discontinuities (Jaques & Milligan, 2004). Furthermore, the convincing link between the kimberlite and HVGZ could suggest either preferential formation or intrusion of the kimberlites. On a global scale, the analyses of kimberlite distributions have revealed a strong spatial association with the mantle hotspots (Crough et al. 1980) and plume-generation zones (Torsvik et al., 2010). On a regional scale, the seismic surveys of the

eastern North American craton and the THO respectively attributed the kimberlite and the associated low velocity anomalies to hotspot track (Boyce et al., 2016) and plume erosion of the mantle lithosphere (Bank et al., 1998). The close spatial affinity between the THO and our study region (a few hundreds of kilometers apart) may suggest the same mechanism involving mantle plume activities (Davies et al., 2004), though further studies are required to establish a more convincing relationship between these two regions. Alternatively, the HVGZ could have delineated a pre-existing weak or boundary zone in the lithosphere, which provides a practical pathway for the eruption of the kimberlites. The metasomatic enrichment during the eruption process could have reworked the lithosphere, which results in significantly reduced lithosphere velocities in an otherwise intact cratonic mantle and produces a large velocity gradient near the eruption site.

## 5.6 Conclusions

A multi-scale finite-frequency tomography method, in combination with data from regional seismic arrays, enables us to conduct a high-resolution survey of the upper mantle beneath the southern WCSB. This chapter provides a detailed appraisal of the lithospheric structures beneath the WCSB and the key conclusions are as follows:

1 The cratonic lithospheres, characterized by high velocities beneath the BHT, Wabamun domain, Hearne province and MHB, are well correlated with their overlying crustal domains. Lithosphere thickness varies significantly from ~300 km beneath the Archean Hearne craton to an average of ~160 km underlying the Proterozoic terranes in northern Alberta., which reflect a multi-stage lithosphere growth and potential destruction of western Laurentia.

2. Mantle seismic velocity shows no apparent correlation with surface heat flow, which suggests a dominant crustal contribution to regional heat flow variation. On the other hand, a clear relationship (i.e., anti-correlation) exists between velocity and long-wavelength isostatic gravity, suggesting melt depletion and enrichment beneath the cratonic mantle lithosphere of western Laurentia.

3. The kimberlite xenoliths occur near the zones of high velocity gradient. Monte Carlo simulation shows that this spatial correlation is statistically robust with a probability of less than 2% to occur by chance. The concentration pattern could reflect either preferential formation or eruption of kimberlites at the lithospheric weak zones marked by the high velocity gradients.

# Chapter 6 Seismic evidence for a mantle suture and collisional origin for the southern Canadian Cordillera

## 6.1 Background

The origin of the North American Cordilleran orogen and its affinity with the bounding North American craton are subjects of contentious debate. Different hypothetical models [e.g., retro-arc thrusting (DeCelles, 2004), flat slab subduction (Liu et al., 2010), archipelago convergence (Sigloch & Mihalynuk, 2013) and ribbon continent collision (Johnston, 2008)] have been proposed to explain this protracted (150-50 Ma) orogenic period, with arguments centering on the provenance, extent and geometry of the accreted terranes that make up the Cordillera (Monger & Ross, 1971; Johnston, 2001; Johnston & Borel, 2007; Percival et al., 2012; Sigloch & Mihalynuk, 2013). The prevailing idea supports the successive emplacements of thin crustal flakes (exotic terranes; Coney et al., 1980) over the autochthonous craton margin since at least early Jurassic (Monger & Price, 2002; Cook & Erdmer, 2005; Percival et al., 2012). In this scenario, the ancient Laurentia craton constitutes the upper plate above an east-directed subducting Farallon slab. Alternative hypotheses favor episodes of westward subduction that produce the Cordilleran composite (upper plate) in form of intra-oceanic arcs (i.e., Insular terrane; Sigloch & Mihalynuk, 2017) or a preassembled micro-continent (Johnston, 2001, 2008; Hildebrand, 2009) prior to their collision with the craton. In short, the presumed roles of the Cordilleran terranes and their affiliation to the bounding craton largely decide the styles of the orogenesis

(accretionary vs. collisional) during the Mesozoic growth of the North American continent.

Keys to distinguishing among these models are the predictions regarding the nature, location and geometry of the boundary between the Cordillera and craton (Dewey, 1977; Hildebrand, 2009). The accretionary model, with its subsurface structures mainly constrained from deep crustal seismic reflection/refraction surveys (Cook & Erdmer, 2005), suggests that much of the Cordillera is built upon a continuous cratonic basement bounded beneath by a landward (eastward) dipping mantle lithosphere (Cook & Erdmer, 2005) and extends as far west as the Coast Belt (Percival et al., 2012; Figure 6.1). This distinctive boundary geometry could reflect the initial rifted (i.e., inherited; Percival et al., 2012) structure or a destructive (i.e., reshaped) margin that has been modified by (episodic) lithospheric removal events (DeCelles et al., 2009; Bao et al., 2014). This model and its inferred boundary processes have ostensibly become a 'textbook example' of an accretionary orogenic belt. In contrast, the collisional model differs from the accretionary concept by predicting 1) a late (Cretaceous) terminal collision along a (cryptic) suture in the orogenic foreland (Johnston, 2008) and 2) a lithospheric-scale boundary between the ribbon continent and North America (Johnston, 2001, 2008). The boundary potentially preserves an oceanward (i.e., westward) dipping geometry of a relic craton margin following the subduction of an intervening oceanic plate (Johnston, 2008; Hildebrand, 2009; Figure 6.1b). Based on a range of geological and geophysical (primarily paleomagnetic) observations (Johnston, 2008), the suture (boundary) is assumed to run along, or adjacent to, a carbonate-shale (C-S) facies boundary directly east of the Rocky Mountain Trench (RMT; Figure 6.1). The C-S boundary separates the Paleozoic platformal carbonate sequences of the eastern Foreland Belt from the basinal chert and shale of the western Foreland Belt (Cecile et al., 1997; Figure 6.1b). Although both models provide a self-consistent tectonic framework for the Canadian Cordillera, they differ in terms of the predicted sub-crustal structures

and modification processes. Consequently, the knowledge of the mantle lithosphere, especially the location and geometry of the Cordillera-Craton boundary (CCB) and its associated thermal state, offer critical kinematic and dynamic constraints on the onset and development of the Cordillera. Unfortunately, the precise location and morphology of the CCB, especially at sub-crustal depths, are not well-known and remain speculative due to insufficient spatial sampling in previous geophysical surveys. In this chapter, we integrate high-resolution seismic imaging (see chapter 5 for details) with thermal calculations and surface geology, the results of which provide much improved constraints on the mantle structures and dynamics near the CCB, and thus sheds new light on the nature of the southern Canadian Cordillera.

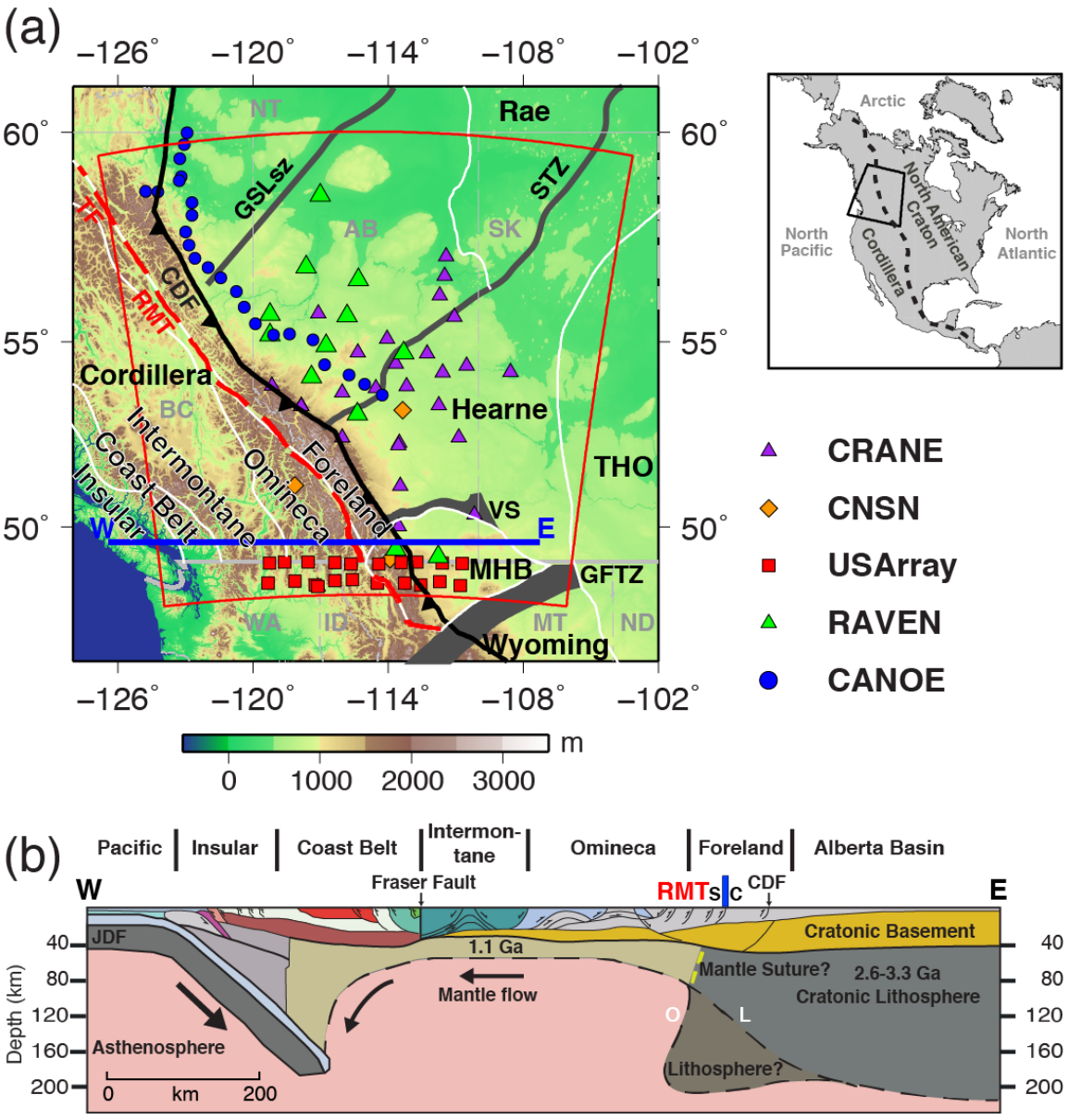
(a)
−126°
−120°
−114°
−108°
−102°
60°
55°
50°
NT
Rae
AB
SK
GSLsz
STZ
TF
CDF
RMT
Cordillera
BC
Hearne
Intermontane
Coast Belt
Insular
Omineca
Foreland
THO
VS
W
E
MHB
GFTZ
WA
ID
MT
ND
Wyoming
m
0
1000
2000
3000
Arctic
North American Craton
Cordillera
North Pacific
North Atlantic
CRANE
CNSN
USArray
RAVEN
CANOE
(b)
Pacific
Insular
Coast Belt
Intermon-tane
Omineca
Foreland
Alberta Basin
W
E
Fraser Fault
RMTs
c
CDF
JDF
1.1 Ga
Cratonic Basement
Mantle Suture?
2.6-3.3 Ga
Cratonic Lithosphere
Mantle flow
O
L
Lithosphere?
Asthenosphere
Depth (km)
40
80
120
160
200
0
km
200

Figure 6.1 (a) Tectonic map of western Canada. The boundaries of the tomographic model are denoted by the red polygon. Seismic stations are shown by the symbols superimposed on topography. The thick grey lines represent the important structural discontinuities within the craton and the white lines are the major domain boundaries in southwestern Canada (Ross et al., 1991). The black barbed and red dashed lines mark the location of the Cordilleran Deformation Front (CDF) and Rocky Mountain Trench (RMT)-Tintina Fault (TF) system, respectively. The map area relative to North America is shown by the enclosed region in the inset. The black dashed line indicates the CDF separating the Cordillera from the craton. (b) A schematic cross-section showing the structural transition from the Cordillera to craton in southwestern Canada (location indicated by the blue line in (a)). The blue bar marks the proposed surface suture of carbonate (C) to shale (S) facies boundary. The thin dashed lines mark the presumed lithosphere-asthenosphere boundary (LAB), with either a landward (L) or oceanward (O) dip inferred for accretionary and collisional models, respectively. Modified after Monger et al. (2002). See Figure 2.2 caption for domain abbreviations.

## 6.2 Data and method

We refer readers to chapter 5 for details on tomographic data and methodology. In this section, we explain the method applied to determine the location of the CCB, which is critical for an objective assessment of boundary characteristics among different tomographic models. The interpretations of tectonic structures in tomographic images are often based on visual perceptions of colors. Consequently, the targeting geological structures (e.g., slab, continental lithosphere and hot plume) are typically associated to anomalies confined within a certain velocity contour. This may lead to potential interpretation biases (e.g., underestimate or overestimate of anomalies) result from a subjective choice of contour value. In addition, even tomographic models of the same region can exhibit considerable variations due to different data type/coverage, model parameterization as well as inversion and damping schemes (Figure 6.2). As a

result, the comparisons of key structures (e.g., the CCB in this study) from different models often lack systematic criterion and remain largely qualitative.

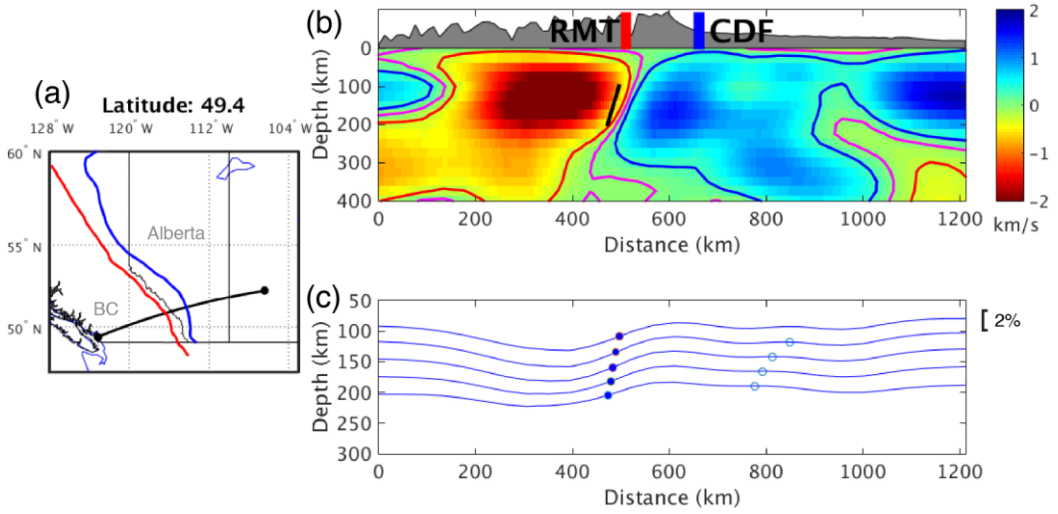


Figure 6.2 (a) The location of a cross-section used for the determination of boundary location. The blue and red lines indicate the location of the CDF and RMT, respectively. (b) P-wave velocity perturbations along the cross-section shown in (a). The red, purple and blue lines show -0.5, 0 and 0.5% velocity contours, respectively. The thick black line indicates the determined boundary location. The locations of the CDF and RMT are marked at the surface. (c) The 1D horizontal velocities computed in depth range of 100-200 km using a 50 km depth running average. Circles on polynomials indicate the location of local maxima in velocity gradient. The solid circles indicate the selected boundary points. The scale length of 2% velocity perturbation is labeled. The y axis only shows approximate depths of these profiles.

To quantitatively determine the location of the transition from tomographic models, we use a maximum velocity gradient approach that is insensitive to the background velocity (i.e., determined by relative velocity perturbation). We compute the horizontal velocities in a depth range of 100-200 km along a series of parallel cross-sections perpendicular to the strike of the Rockies (Figure 6.2a). Assuming that the CCB marks a sharp change in physical parameters (e.g.,

velocities, densities and temperatures), we choose the point of maximum velocity gradient as the optimal boundary location at each depth (Figure 6.2b). This criterion has been applied to the determination of depth of the LAB (Priestley & Debayle, 2003; Hopper & Fischer, 2015). To avoid the spurious maxima caused by noisy data (i.e., high model roughness), we fit the velocity with lower-degree polynomials, which are degree 3 for S and degree 5 for P while considering higher frequency (i.e., shorter wavelength) nature of the latter phase. To capture the trend of local velocity variation along the profile, we use a 500-km wide sliding window during the fitting process, which approximates the wave-length of the slow to fast velocity transition (e.g., from 250 to 750 km in Figure 6.2b). The final boundary location is calculated by averaging all boundary points (Figure 6.2c). The same method is applied to five tomographic models for boundary determination (Figure 6.3). The location of the boundaries and their tectonic implications will be discussed in section 6.3.

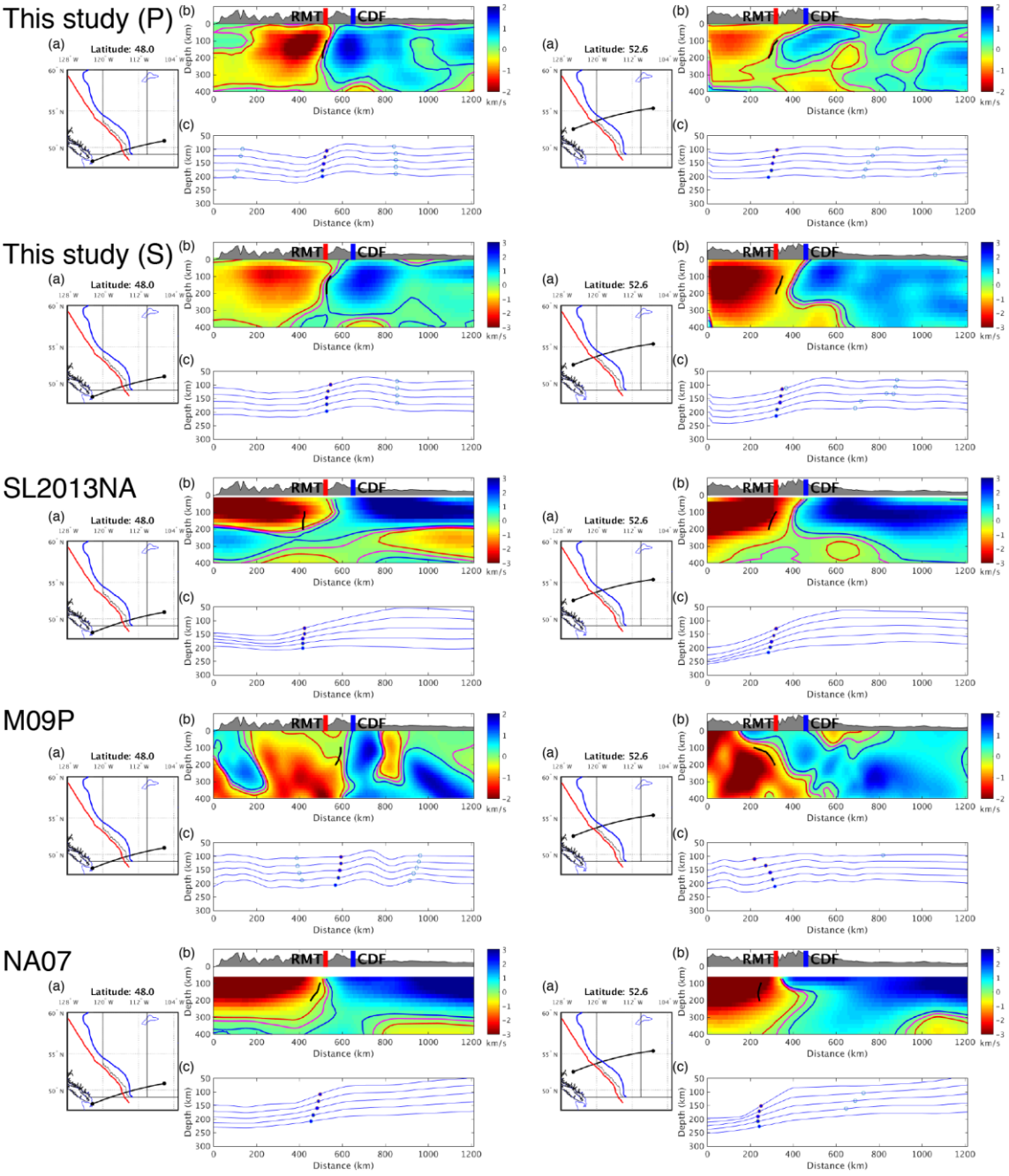


Figure 6.3 Measurements of boundary locations from five different models, which (from top to bottom) are P and S velocity models from this thesis, shear velocity model (SL2013NA) from Schaeffer & Lebedev (2014), P velocity model (M09P) from Mercier et al. (2009), and shear velocity model (NA07) from Bedle & van der Lee (2009).

## 6.3 Results

### 6.3.1 Cordillera-Craton boundary

Our finite-frequency body-wave tomographic models show mantle velocity structures across the region and delineate contrasting low and high wave-speeds to the west and east of the RMT, respectively (Figure 6.4a). We refer readers to chapter 5 for a detailed summary of the craton structures. This chapter focuses on the western margin of the cratonic lithosphere, which is a steeply dipping high-velocity structure juxtaposed to the west with the pronounced low velocities beneath the Canadian Cordillera. This boundary (i.e., CCB) is defined by a high amplitude velocity gradient and shows significant spatial and geometrical complexities along the strike of the mountain belt (Figure 6.4b).

The CCB provides a key structural constraint on the Cordilleran assembly. We determine its location in our P- and S-wave results and three published tomographic models (Bedle & van der Lee, 2009; Mercier et al., 2009; Schaeffer & Lebedev, 2014) using the maximum horizontal velocity gradient (see section 6.2). The resulting location varies among different tomographic models and forms a narrow (<200 km) zone surrounding the RMT (Figure 6.5a). Our P- and S-wave models both place the CCB at a maximum distance of 40-50 km west of the RMT at 150 km depth (Figure 6.5a), with a pronounced westward dip (~10º from the vertical) between 49-52° N (see AA' in Figure 6.5b). The boundary lies directly beneath the RMT north of ~52°N (Figure 3a), where its dip changes to sub-vertical and then east-dipping within a short (<50 km) distance (see BB' in Figure 6.5b). Further north, the boundary merges into the northern Rocky Mountain Trench-Tintina Fault (RMT-TF) system at ~54° N (Figure 6.5a). In this area, the geometry of the craton margin cannot be robustly determined due to reduced station density.

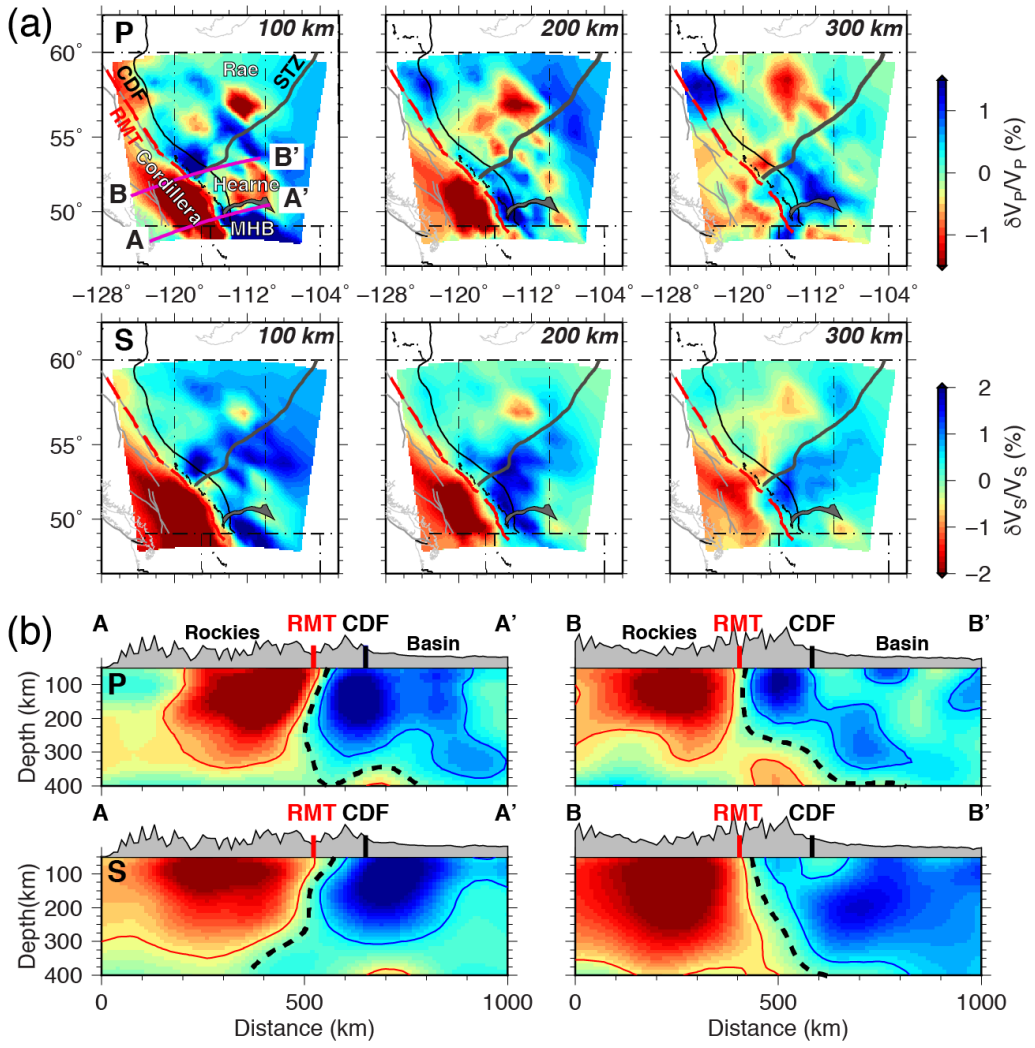


Figure 6.4 (a) P- (top panel) and S-wave (bottom panel) velocity anomalies at 100, 200, and 300 km depths. The locations of two velocity profiles are shown by the purple lines at 100 km depth. The red dashed line marks the RMT. (b) P- (top) and S-wave (bottom) velocity anomalies along two profiles in the southern Canadian Cordillera. The southern (AA') and northern (BB') profiles intersect with the RMT at about 50° and 52° N, respectively. The locations of RMT and CDF are respectively marked by the red and black lines at the surface. The black dashed line indicates the zero percent velocity contour, which approximates the location of the Cordillera-Craton boundary.

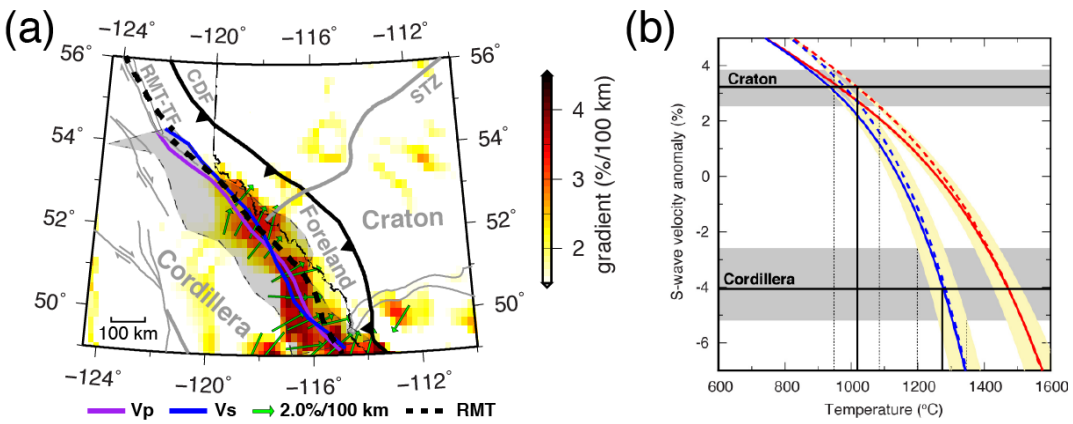


Figure 6.5 (a) Seismic velocity gradient at 150 km depth from an averaged Vp and Vs velocity model scaled using Vp/Vs ratios in the reference model (Kennett et al., 1995). The CCB in the upper mantle determined from P- and S-wave models are shown by purple and blue lines, respectively. The shaded region highlights the spatial variation in the CCB location measured from this study and three recent tomographic models (see Figure 6.4). The green arrows indicate the direction of maximum velocity gradient near the transition boundary. Major faults are marked by the grey lines. (b) S-wave velocity-temperature (Vs-T) relationship at 150 km depth. The horizontal black lines show the respective average S velocities for the Cordillera and craton regions, with the corresponding standard deviations shaded in grey. The solid and dashed curves represent pyrolite (fertile) and dunite (depleted) compositions, respectively, in a dry (50 ppm H/Si; red) and wet (5000 ppm H/Si; blue) mantle. The yellow shaded regions show the variations of Vs-T curves for various frequencies (0.03 to 0.3 Hz) and grain sizes (0.03 to 3 cm).

## 6.3.2 Resolution test

The geometry and sharpness of the boundary provide important structural constraints to the Cordilleran tectonics. We examine and discuss the resolvability of our data to these parameters. The first test includes a gentle westward-dipping boundary separating low (-3.5%) and high (2.5%) P-velocity anomalies (Figures 6.6a-6.6d). For a westward-dipping boundary (Figure 6.6a), the geometry is well-

constrained in the south, but the degree of recovery degrades towards the north, where the boundary is steeper and more diffusive compared with the input. The recovery of amplitude of the anomaly ranges from ~80% in the south and ~50% in the north. The second group of tests adopts the same model input as the first test case except for a vertical boundary (see Figures 6.6e-6.6h). In this test case, the geometry and sharpness of the boundary are both well recovered in the south between 48 and 52° N, whereas an artificial westward dip occurs in the north. By comparing the results of these two tests, we conclude that 1) the observed boundary characteristics (sharpness and dip) are robustly determined in the south and 2) the resolution degrades towards north (above ~52° N) and the dip may be a result of artifact hence cautious needs to be applied when interpreting the boundary geometry in this region. The corresponding test for S model utilizes input low and high velocities of -4.5% and 3.5%, respectively (not shown). The tests show a more severe underestimate of the dip compared to the P model and the geometry cannot be reliably determined in the north. These test results suggest that P waves are more sensitive to boundary geometry compared to S waves. In our model, the boundary geometry transitions from westward to eastward dip at ~52°, which we determine to be a reliable observation since the model recoveries are satisfactory on both P and S models; more importantly, we find no artificial eastward dip occurs at this latitude in all test cases.

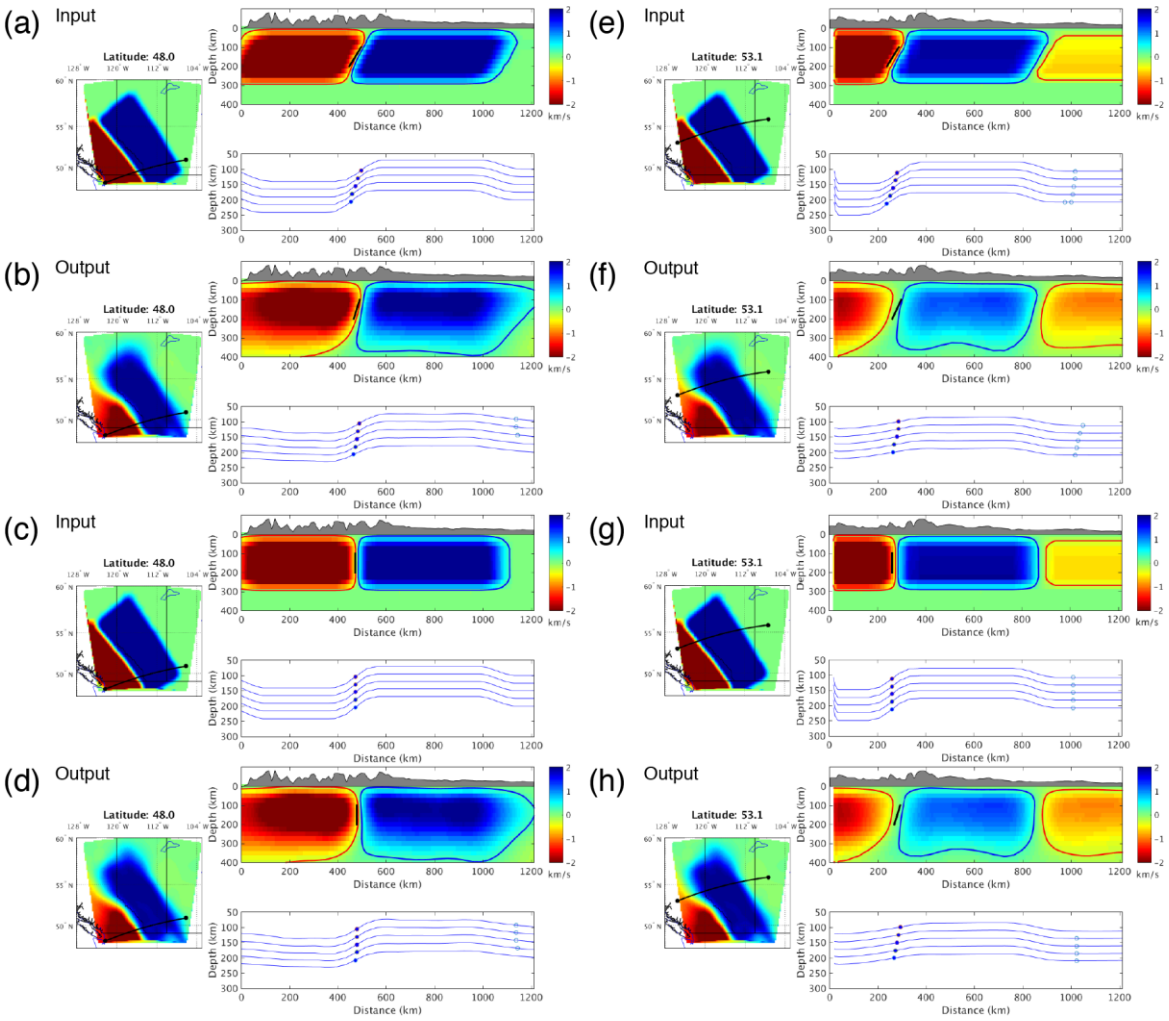


Figure 6.6 Tests of the robustness of the boundary determination algorithm with a hypothetical input P-wave model that contains a dipping or vertical boundary. (a) Input and (b) output models with a dipping boundary. (c) Input and (d) output models with a vertical boundary. (e)-(g) The same as (a)-(d), but for a cross-section in the north. See Figure 6.2 caption for explanation of each subplot.

The results of the same hypothetical tests are used to evaluate the uncertainty in the determined boundary location. In the second group with west-dipping input boundary (see Figures 6.6a and 6.6e). The boundary location is accurately constrained in the south with average discrepancy of 6 km below 51.5º N (Figure

6.7a). The uncertainty increases slightly to 20-30 km in the north (see Figure 6.7a). For the S model, the boundary is well defined in the output model with a difference of 6-30 km compared to the input (Figure 6.7b). For the vertical input boundary, the output models show virtually the same degree of recovery in boundary location, which suggest a relatively minor effect of boundary geometry on the determined location (Figures 6.7c and 6.7d).

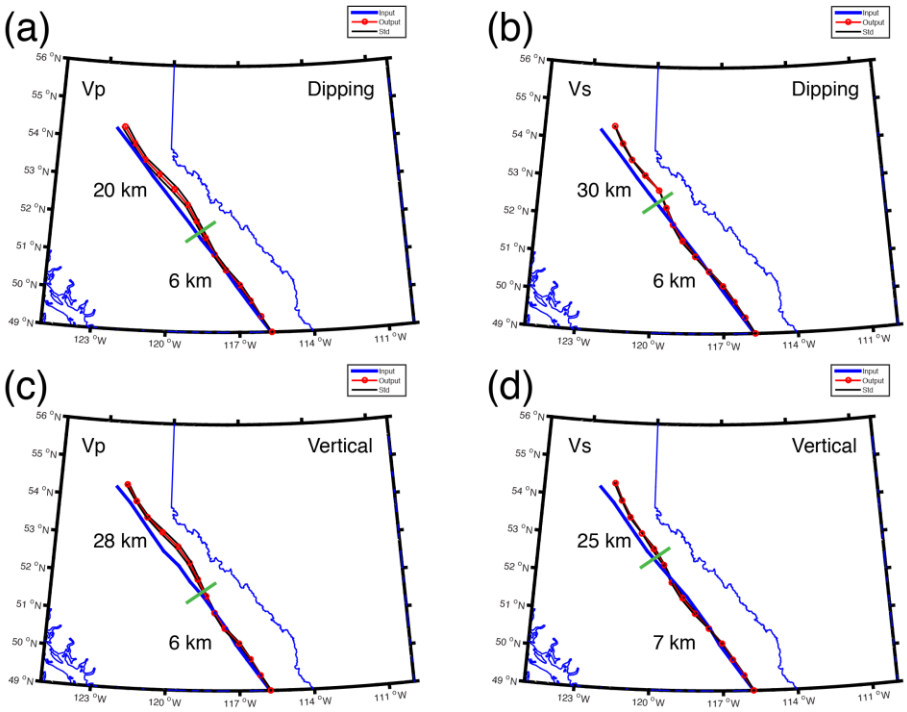


Figure 6.7 The uncertainty in the boundary determination for (a) P and (b) S models. The input and output boundary locations are shown by the blue and red lines, respectively. The uncertainty in the output boundary location is indicated by the black line, which is defined as the standard deviation of the results from inversions with different damping parameters. The number labeled show the average discrepancy for northern and southern segments divided by the green bars. (c) and (d) The same as (a) and (b) but for a vertical input boundary.

### 6.3.3 Thermal constraints on the CCB

The greatest velocity increase occurs within 100 km laterally of the CCB (Figure 6.5a), showing maximum horizontal gradients of 4% and 3.5% per 100 km for P and S velocities at 150 km depth, respectively (see Figure 6.5a). The latter is consistent with the >3% shear-velocity gradient observed in this region in a recent continental-scale study (Schaeffer & Lebedev, 2014). As temperature dominantly affects the upper mantle seismic velocities (Goes & van der Lee, 2002), the observed velocity contrast across the CCB provides constraints on the corresponding temperature variation. At 150 km depth, the P (4.3%) and S (7.0%) velocity contrasts indicate a decrease of 200-300 °C from the Cordillera to craton (Figure 6.5b). The low Cordilleran velocities are consistent with a relatively wet, near-adiabatic mantle (1200-1350 °C). The high-velocity cratonic lithosphere corresponds to temperatures of 950-1100 °C, with slightly higher temperatures for a depleted composition; it is worth noting that craton velocities are insensitive to water content (Goes et al., 2012). These temperatures are in agreement with earlier estimates based on surface heat flow, xenoliths, and seismic velocity (Hyndman & Lewis, 1999; Goes & van der Lee, 2002; Hyndman et al., 2005, 2009), as well as the hypothesis that the Cordillera's thin lithosphere is maintained through small-scale convection of hydrated mantle (Hyndman et al., 2005). Geodynamic simulations show that low craton temperatures and a dry and moderately depleted composition are required to maintain a prominent (sharp and steep) lithospheric step at the craton edge for a minimum timescale of 100 Ma (Hieronymus et al., 2007; Currie & van Wijk, 2016). Specifically, the cratonic mantle lithosphere must be rheologically strong (5-50 times stronger than damp olivine, i.e., consistent with a dry composition) and chemically depleted (20-40 $km/m^3$ less dense than primitive mantle; Currie & van Wijk, 2016). This intrinsically stable and potentially well-preserved mantle boundary thus provides

important temporal constraints on the initiation and evolution of the Cordilleran orogen.

## 6.4 Discussion and conclusion

### 6.4.1 Geological implication

The accretionary model of the Cordillera (Percival et al., 2012) predicts that 1) the craton margin was established by at least the Late Devonian; 2) only the supracrustal rocks of the exotic terranes were added to the North American margin; 3) the Intermontane Belt comprises the easternmost extent of accreted supracrustal sequences and all crust further east is North America (Cook & Erdmer, 2005; Percival et al., 2012); 4) the lower crust and lithosphere beneath the Cordillera is a westward extension of the North American craton; and 5) the lithospheric mantle thins gradually to the west from the craton to Cordillera (Monger & Price, 2002; Percival et al., 2012). This model is difficult to reconcile with the observed location (subjacent to the cryptic suture in the foreland crust), westward-dipping geometry, and the large (>200 km) and abrupt lithosphere thickness contrast at the CCB in our seismic models (see Figure 6.4b). We propose that the observed CCB marks a suture between allochthonous and autochthonous mantle. Paleobotanical, paleomagnetic, geological and geochemical data are consistent with interpretation of the Cordillera as a product of the Late Cretaceous collision between a ribbon continent that was pre-assembled in the Triassic-Jurassic and the North American continent (Johnston, 2001, 2008; Hildebrand, 2009). This implies that the craton margin and its collisional front was established relatively recently (younger than 100 Ma) compared with the Late Devonian age suggested by the accretionary model (Monger & Price, 2002). The shorter timeframe (<100 Ma), and thus reduced

tectonic modification (i.e., reshaping), could be important factors for the preservation the steeply dipping CCB.

The westward-dipping geometry of the mantle CCB and its location relative to the surface suture provide critical spatial constraints on the Cordilleran collision. At 150 km depth, a robustly constrained depth range in our seismic images, the mantle CCB is 50-100 km west of the surface suture (C-S facies boundary east of the RMT) in the southern Cordilleran foreland. In this region, the RMT is interpreted as an Eocene extensional fault (Parrish et al., 1988; vanderVelden & Cook, 1996) that was subject to early Tertiary (~59-40 Ma) extension of up to 100 km (McMechan & Price, 1980; Parrish et al., 1988). Prior to the extension, the amount of the Late Cretaceous and Paleocene shortening as accommodated by the Rocky Mountain thrust-and-fold belt is ~200 km (Price, 1981). According to the collisional model, this compression is attributed to the continuous convergence between the North American craton and Cordillera (Johnston, 2008). During this protracted period of tectonic interaction, the mantle suture, marking the collisional front, moved continuously westwards as a consequence of the underthrusting of the leading-edge of the craton (Hildebrand, 2009) while the overlying crust carried the surface suture eastward along the basal decollement of the thrust-and-fold belt (Johnston, 2008). This provides a simple yet self-consistent interpretation of the observed westward-dipping geometry (a relic collision front; Figure 6.8), as well as the 50-100 km offset between the surface suture and mantle boundary. Similar phenomena have been documented in orogenic belts of Qinling-Dabie in central China (Wang et al., 2005) and Trans-European Suture Zone (Hieronymus et al., 2007). North of 52° latitude, the RMT joins the TF in the northern British Columbia and Yukon and is characterized by >400 km of Eocene dextral strike-slip displacement (Roddick, 1967; Gabrielse, 1985), implying a dominant margin-parallel motion of the Cordillera relative to the craton. This is supported by an overlapped surface suture and mantle

boundary (Figure 6.5a) and potentially favors the TF as a lithosphere penetrating structure (Abraham et al., 2001).

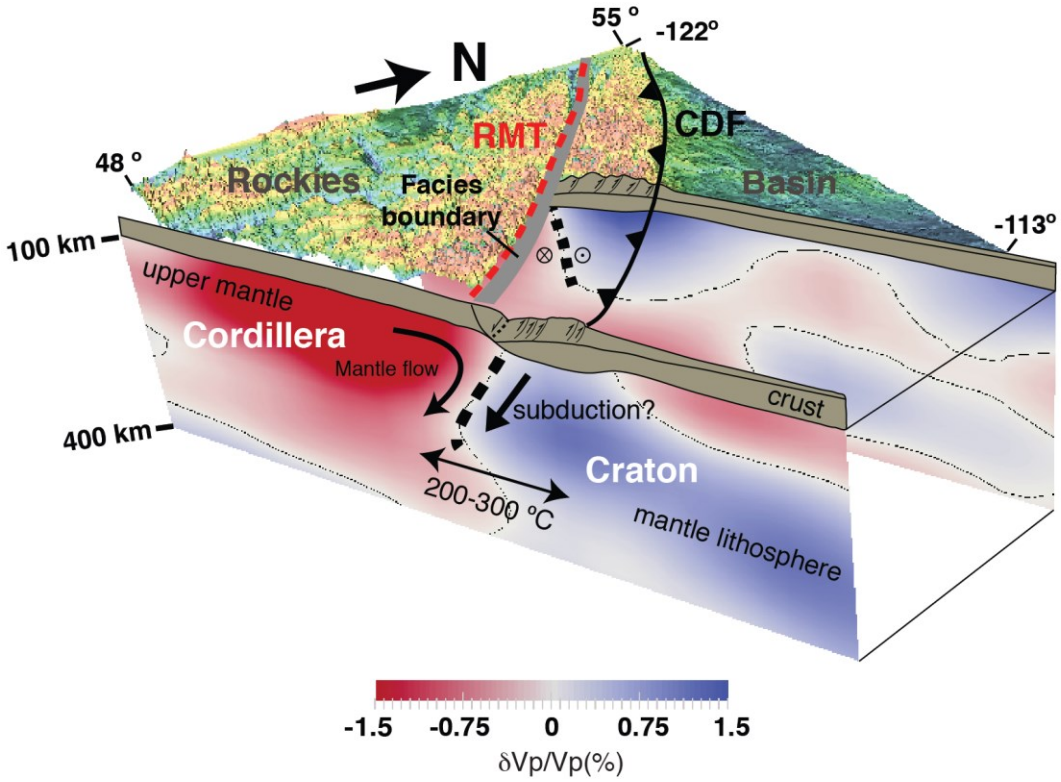


Figure 6.8 A 3D perspective of the CCB. The profile in the south is dominated by a margin-perpendicular displacement whereas the northern profile is characterized by a strike-slip motion. The RMT and CDF are shown by red dashed and black barbed lines, respectively. The surface facies boundary is shaded in grey. The mantle boundary is indicated by the black dashed line on the cross-section.

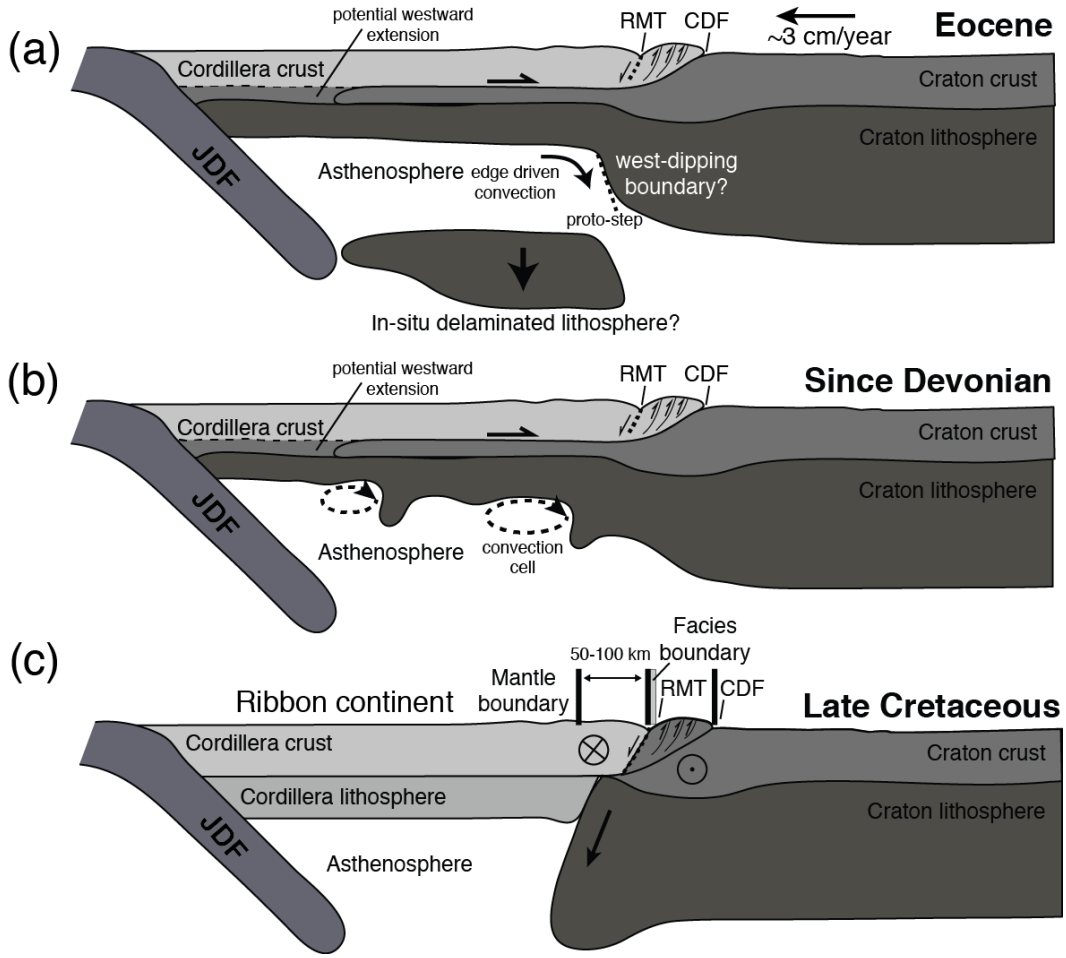


Figure 6.9 Three models that explain the possible mechanisms for the formation of the CCB. The establishment of a destructive boundary through (a) lithosphere delamination (Bao et al., 2014) and (b) viscous thermal erosion favored by the accretionary model. In the delamination model (a), the absolute rate of North America movement is obtained from Van Der Meer et al. (2010). (c) Continental collision that involves a terminal suturing between a ribbon continent and North America.

## 6.4.2 Alternative hypotheses

The interpretation of the CCB as a collisional boundary differs significantly from the earlier views of a destructive CCB from the accretionary model. These

attribute the formation of the sharp CCB to at least two distinctive stages: the initial construction of the Cordillera through the accretionary of exotic terranes followed the lithosphere removal to create (or enforce) the boundary. The latter destructive process could be achieved through lithosphere-scale delamination (Bao et al., 2014) (Figure 6.9a) and/or viscous thinning and thermal erosion of the Cordilleran lithosphere in a retro-arc setting (Currie et al., 2008; DeCelles et al., 2009; Hardebol et al., 2012; Figure 6.9b). In either case, it is unclear why a steeply-dipping destructive boundary formed underneath the Cordilleran foreland far from the coastal subduction zone instead of below the more seaward terranes. According to the delamination model (see Figure 6.9a), the boundary location is controlled by a proto-step beneath the foreland, which, in combination with the edge-driven convection, jointly triggered the delamination (Bao et al., 2014). Although this provides a plausible explanation for the spatial correlation between the CCB and the RMT, such a large-scale delamination event, which removed the entire lithosphere beneath the Canadian Cordillera (Bao et al., 2014), is difficult to reconcile with the observed diverse geometry of the CCB, especially the well-constrained west dip, along the strike of the orogen (see Figure 6.5b). In addition, the interpreted present-day position of the delaminated lithosphere below its point of origin (i.e., west of the CCB and immediately beneath the Cordillera; see Figure 6.9a) conflicts with the continual westward motion of North America. The average absolute North America rate of 3 cm/year since the proposed delamination event at 55 Ma (van der Meer et al., 2010) would place the detached block at least 1650 km to the east relative to the overlying continent.

Alternately, viscous/thermal erosion model requires that the destructive front propagated landward (see Figure 6.9b) and ceased immediately beneath the RMT and subsequently remained stationary. This mechanism is difficult to reconcile with 1) the seismic observation of a sharp CCB, which implies a dry and buoyant craton margin (and its sub-Cordillera extension based on the accretionary model) that is intrinsically resistant to erosion; and 2) the geological evidence of limited

occurrence of metamorphosed rocks near RMT, indicating minimal lithospheric thinning in this region (Price, 1981; Cook et al., 1992).

### 6.4.3 Implication on global orogenesis

For southwestern Canada, our new seismic observations are most compatible with the collisional model that provides a self-supported system (i.e., not dependent on other mechanisms) to explain 1) the steep and well-preserved west-dipping geometry – a young (<100 Ma) collisional front; 2) the sharp velocity, temperature and lithospheric thickness contrasts – a boundary separating two distinctive continents; and 3) an excellent spatial correlation (and offset) with the cryptic surface suture (Figure 6.9c). Collectively, these spatial-temporal constraints of the CCB favor the collisional model that involves distinct periods of ribbon continent formation and its later collision to the autochthonous domains (i.e., North American craton; Johnston, 2008). A similar mechanism has recently been invoked as an alternative interpretation of the archetypal orogenic models for the South American Andes and west European Variscides (Johnston & Gutierrez-Alonso, 2010; Hildebrand & Whalen, 2014;). The former (Andes) has been regarded as a classic ocean-continent Cordilleran orogen, whereas a recent study has associated it with the collision between a ribbon mircocontinent and South America above a westward-dipping subduction zone (Hildebrand & Whalen, 2014). In the latter case, the similar architectures of the North American Cordillera and European Variscan orogens (Johnston & Gutierrez-Alonso, 2010) favor a common origin that involves the buckling of a ribbon continent (J. Shaw & Johnston, 2016). While each of these orogenic systems possesses a unique assembly history, their similarities are reminders of the potentially critical role of microcontinent-continent collision in the growth of continent.

Suture zones place crucial constraints on continental assembly, although recognition of distinctive plate boundaries at shallow (e.g., surface ophiolite belts)

and deep (e.g., lithospheric fault zones) structural levels is challenging (Dewey, 1977). Our analysis of the southern Canadian Cordillera combines deep structural constraints from seismic tomography with surface geology to shed new light on the close relationship between a cryptic crustal suture and its upper mantle expression (see Figures 6.8 and 6.9c). We attribute the sharp structural and temperature gradients associated with the CCB to a stable, underthrust craton margin during collision of a ribbon continent (Cordillera) with the North American craton in the Late Cretaceous. An integrated approach as applied in our study is critical to decipher the style (Sigloch & Mihalynuk, 2013) and initiation (Van Hinsbergen et al., 2012) of orogenesis. As more examples become available in other orogens, new insights into the dynamics of the crust and mantle during orogenesis and continental growth can be gained.

# Chapter 7 Crustal structure from ambient noise tomography

## 7.1 Introduction

The seismic tomographic images presented in chapter 6 reveal complex mantle structures and dynamics associated with the Cordillera-Craton interaction. As an integral part of the Cordilleran orogenic system, the overlying crust offers critical structural constraints on the regional tectonics including assembly age, deformation history and orogenic style. This chapter provides a high-resolution crustal model of the central-southern WCSB using ambient noise imaging. We mainly focus on ambient noise processing, dispersion curve measurements, and group velocity inversion. We show the validity and resolution improvement of our model through checkerboard resolution test and comparisons with earlier tomographic studies in the overlapped region. Also provided are the preliminary interpretations of key observations from group velocity maps in the framework of regional tectonics. This chapter ends with a summary of the current state and future directions towards obtaining a full 3D anisotropic crustal velocity model.

## 7.2 Data and method

In this study, we process over a decade (2006-2017) of continuous seismic recordings from an integrated network of 118 stations from 5 regional networks near the WCSB (Figure 7.1; see chapter 4 for a detailed summary of stations and networks). We use the vertical component of continuous seismic recordings to conduct ambient noise imaging. Data processing follows the steps proposed by Bensen et al. (2007) as detailed in section 3.3 of chapter 3. Overall, an average of

520-days long recording contributes to the robust extraction of high-quality Rayleigh waves from the stacked noise correlation functions (NCFs) between ~4000 station pairs.

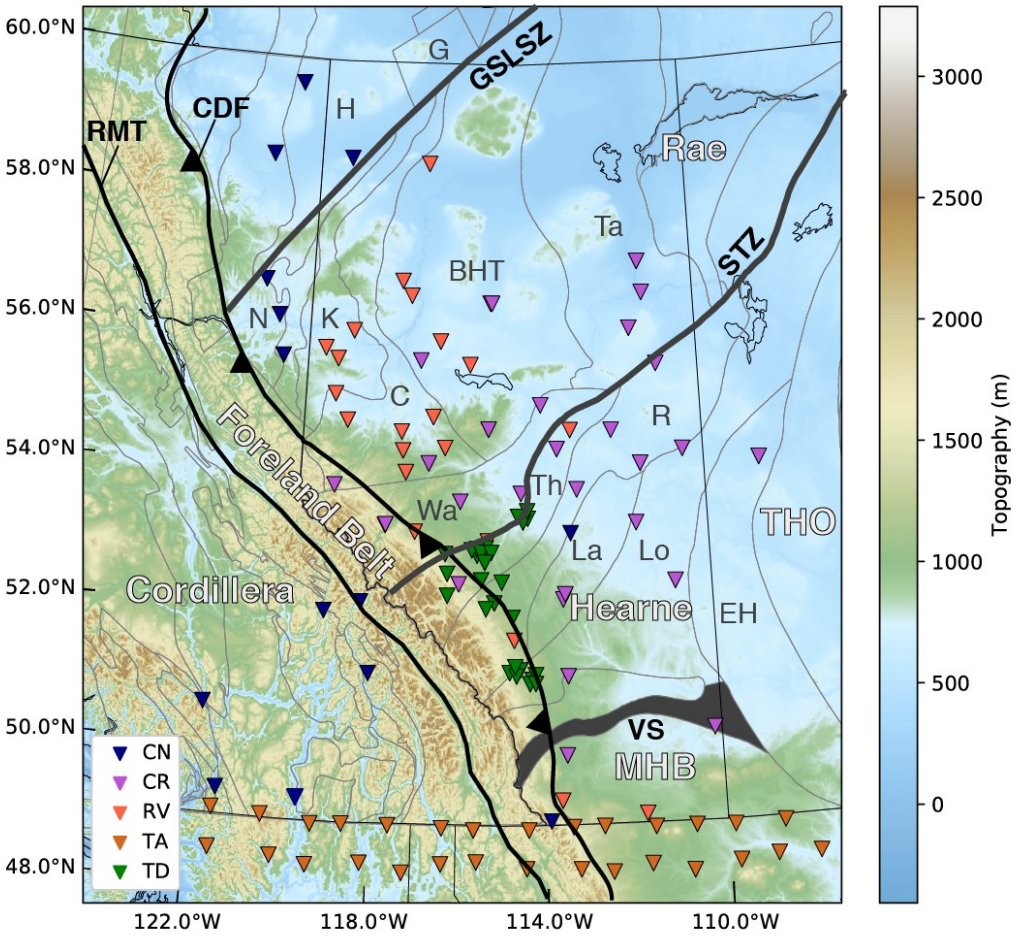


Figure 7.1 Distribution of seismic stations. The major domain boundaries are highlighted by thick lines. See Figure 2.2 for details of the domain abbreviations.

We stack all NCFs based on the interstation distance to examine the data quality. Strong energy emerges at the predicted group arrival window of Rayleigh wave assuming a wavespeed range of 2.5-3.5 km/sec. The signal to noise ratio (SNR) is computed by dividing the maximum amplitude of Rayleigh

wave with the variance of noise in a 500-sec long window trailing the signal, and the results are consistently greater than 20 at all distances. The coherent Rayleigh wave signals observed across the array imply that the ambient noise source distribution is sufficiently homogeneous for unbiased dispersion measurements. The majority of interstation distances fall within a range between 150-550 km, which satisfies the minimum required station spacing of three times the surface wave wavelength for reliable dispersion measurement (Bensen et al., 2007). Consequently, the current network geometry is suitable for extracting dispersion data at periods between 12-45 sec, which is ideal for imaging the crustal structures.

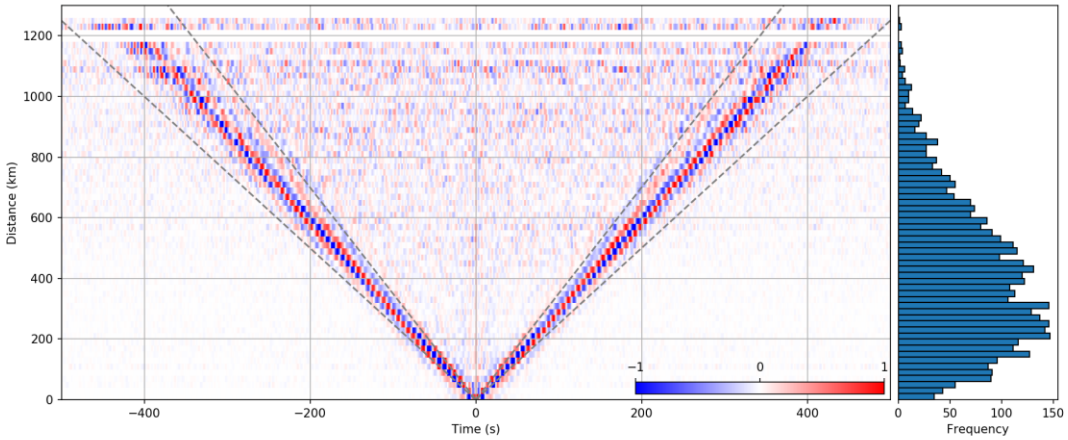


Figure 7.2 The stacked NCFs according to interstation distance. Each trace is computed by summing all NCFs within a 20-km wide bin and the amplitude is normalized to account for the difference in the number of stacking traces used in each bin (right panel). The dashed lines show the surface wave group arrival times predicted using the velocities of 2.5 km/sec and 3.5 km/sec.

## 7.3 Results

### 7.3.1 Ambient source characteristics

The long operation period of CRANE network enables an examination of the long-term spatial-temporal distribution of the ambient noise sources. We choose a pair of stations located in the Alberta basin with 6 years of continuous recording and stack the NCFs on a monthly basis. The results exhibit strong seasonal variations in the waveform characteristics (Figure 7.3). Specifically, fall-winter seasons show relatively weak signals of Rayleigh wave on the negative time lag, whereas the amplitude in the surface wave window is much improved during spring and summer times. The signal variation on the positive axis follows a same 6-months periodicity, though the amplitude pattern is opposite to those observed at negative time lags (i.e., the signal is strong during fall-winter times). The variability potentially reflects a systematic change in the location of dominating noise source throughout the year (Gu & Shen, 2012).

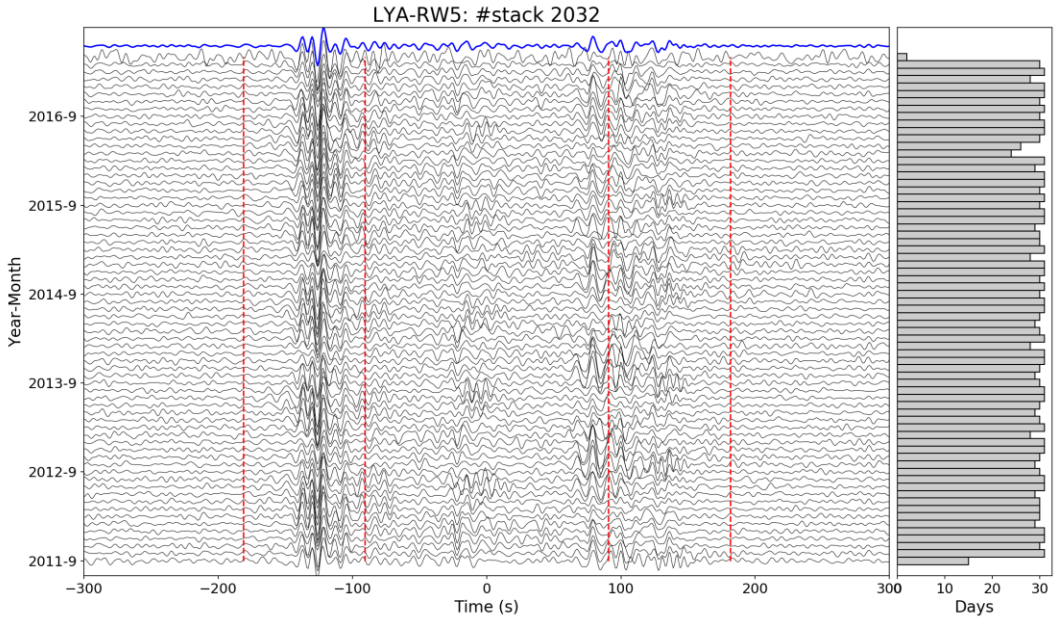


Figure 7.3 Monthly stacks of the NCF from LYA-RW5 station pair. Strong group arrivals are observed in the predicted time window assuming Rayleigh wave velocities between 2.0-4.0 km/sec. The right panel shows the number of days contributing to the stacked trace.

We further analyze the frequency-dependent spatial distribution of ambient noise signals by examining the azimuthal variation of the SNR. At all periods, the highest SNRs are consistently observed in the west direction, approximately pointing to the eastern Pacific coastlines (Figure 7.4). This observation suggests a dominating noise source potentially results from the interaction between ocean waves and continental shelf (Webb, 1998; Stehly et al., 2006; Yang & Ritzwoller, 2008; Brzak et al., 2009; Landés et al., 2010; Ardhuin et al., 2011; Gu & Shen, 2012). Similar patterns have been reported in earlier studies in the northern WCSB, directly to the north of our study region (Dalton et al., 2011), and northwestern US (Bensen et al., 2008). In the longer period band, the secondary peaks emerge in the northeastern quadrant (see 15-30 and 20-35 sec period bands

in Figure 7.4). Considering the comparable amplitude to those of the primary SNR peaks from the west, we suggest the long-period (>20 sec) microseisms from coastlines of the North Atlantic Ocean or Labrador Sea (Capon, 1973; Pawlak et al., 2011) could be largely responsible for the generation of the secondary peaks.

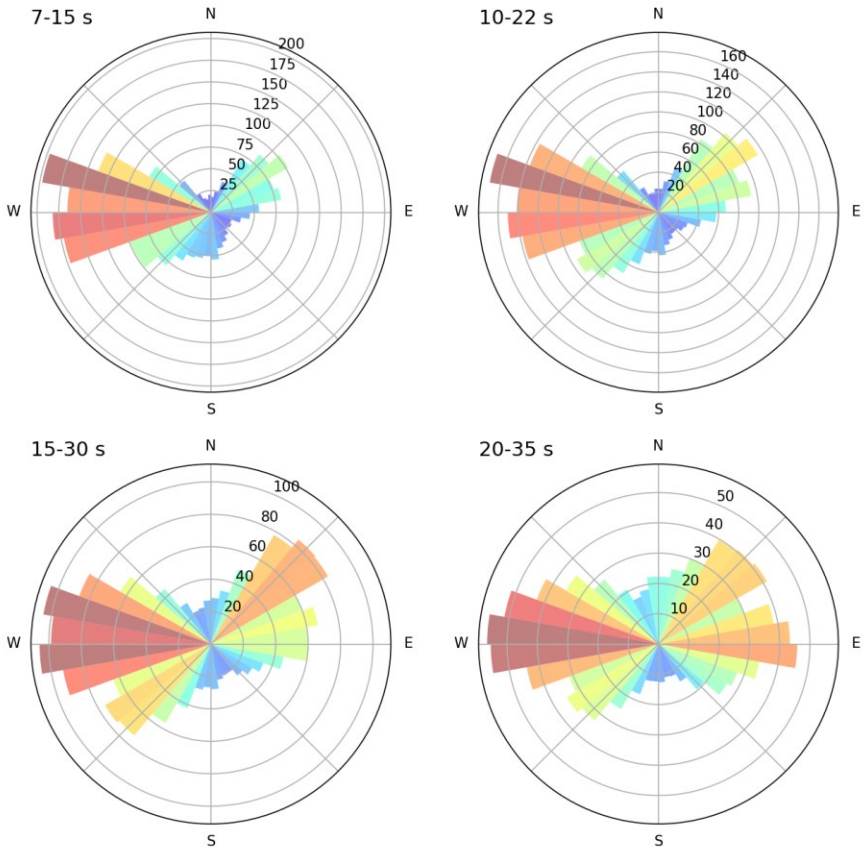


Figure 7.4 Azimuthal distribution of the average SNR for all station pairs in four period bands. Positive and negative components are computed separately to account for seismic waves propagating in opposite directions. For each station pair, the polar histogram is color-coded based on the SNR and points to the back-azimuth, indicating the direction of the source.

### 7.3.2 Dispersion data

The high-quality NCFs permit robust measurements of the frequency dependent Rayleigh wave group arrival times. We utilize the Frequency Time Analysis (FTAN) method (e.g., Dziewonski et al., 1969; Levshin et al., 1972) to extract the dominating surface wave energy within a series of isolated frequency bands (see section 3.3.3 for details). The resulting dispersion measurement provides a path-averaged estimate of the Rayleigh wave group velocity, which could serve as a diagnostic metric to examine the first-order subsurface structure (Figure 7.5). The 8-sec dispersion map is dominated by a patch of below-average values along the Rocky Mountain foothills, where almost all traversing rays show consistent low values regardless of path length differences (Figure 7.5a). Away from this region, the rays sampling the Canadian Cordillera in the southwest and craton in the northeast are characterized by positive wavespeed perturbations relative to the regional average. At longer periods, the velocity pattern becomes more homogeneous, although notable low velocities extend from the foothills westward to the Cordillera, whereas the northeastern corner shows predominately high velocities at both periods (see Figure 7.5b). To qualitatively define the velocities, we subdivide the ray paths into three categories based on their geographical location and compute an average dispersion curve for each subset (Figure 7.5c). The basin center exhibits the lowest velocities at nearly all periods except for at the long-period periods. The averaged dispersion curve from the craton group shows the highest velocities at all periods and runs subparallel with that of the basin center with a static shift of ~0.1 km/sec. The Cordillera group is visually more complex, showing intermediate velocities between 8-20 sec, and the dispersion curve gradually merges with that of the basin center at longer (>20 sec) periods (see 7.5c). These distinctive dispersion relationships suggest a large structural variation associated with a diverse tectonic setting in the study region.

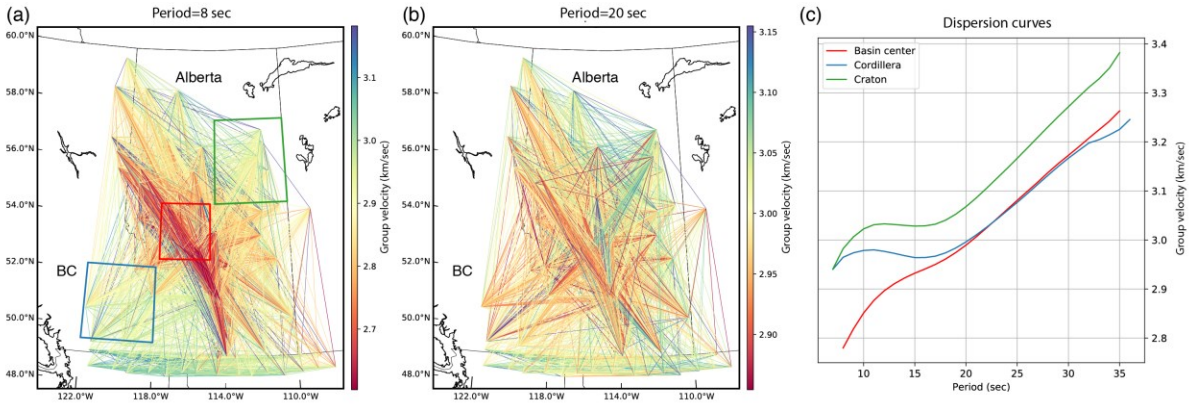


Figure 7.5 Measurements of Rayleigh wave group velocity at (a) 8 sec and (b) 20 sec. The line segment connecting each station pair is color-coded by path-averaged group velocity. (c) Three representative group velocity curves selected from regions highlighted by the rectangles with corresponding colors in (a).

### 7.3.3 Model resolution

Model resolution is a critical aspect for any tomographic problem. We perform a conventional checkerboard test to evaluate the resolvability of our data to small-scale structures. The input velocities consist of alternating positive and negative Gaussian shaped anomalies with a radius of 150 km and maximum amplitude of 10% (Figure 7.6a). Simulated travel times are calculated using the same ray path geometry and random perturbations of 10% standard deviation of the predicted travel times are subsequently added. We then invert synthetic travel times using the same damping and regularizing parameters for an objective comparison. The output model recovers the input pattern well in central-southern Alberta, where the ray path density is the highest (see Figures 7.5a and 7.5b). The velocity structures in the Cordillera are smeared along the NW-SE propagating direction of the rays but the centers of the anomalies are generally well resolved. The resolution remains satisfactory at short to intermediate periods but drops significantly at periods above 25 sec, in which case only central Alberta basin is

reliability constrained. The amplitude recovery also decreases with the increasing periods, varying from 70% at 8 sec period to about 30% at 30 sec. Considering both pattern and amplitude recovery, we conclude that only velocity structures below 56º N at upper-middle crustal depths are robustly constrained by the NCF data.

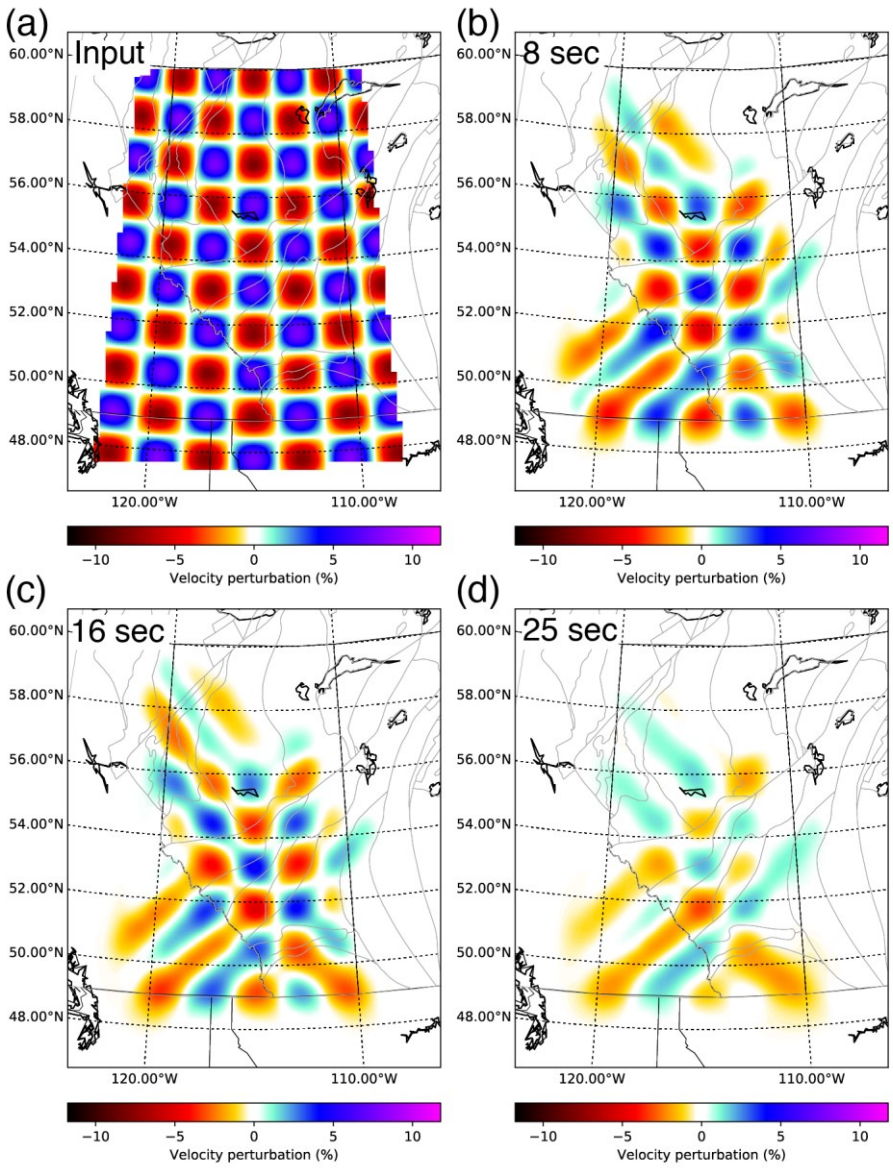


Figure 7.6 Checkerboard resolution test. (a) Input velocity anomalies and output velocities at (b) 8sec, (c) 16 sec and (d) 25 sec.

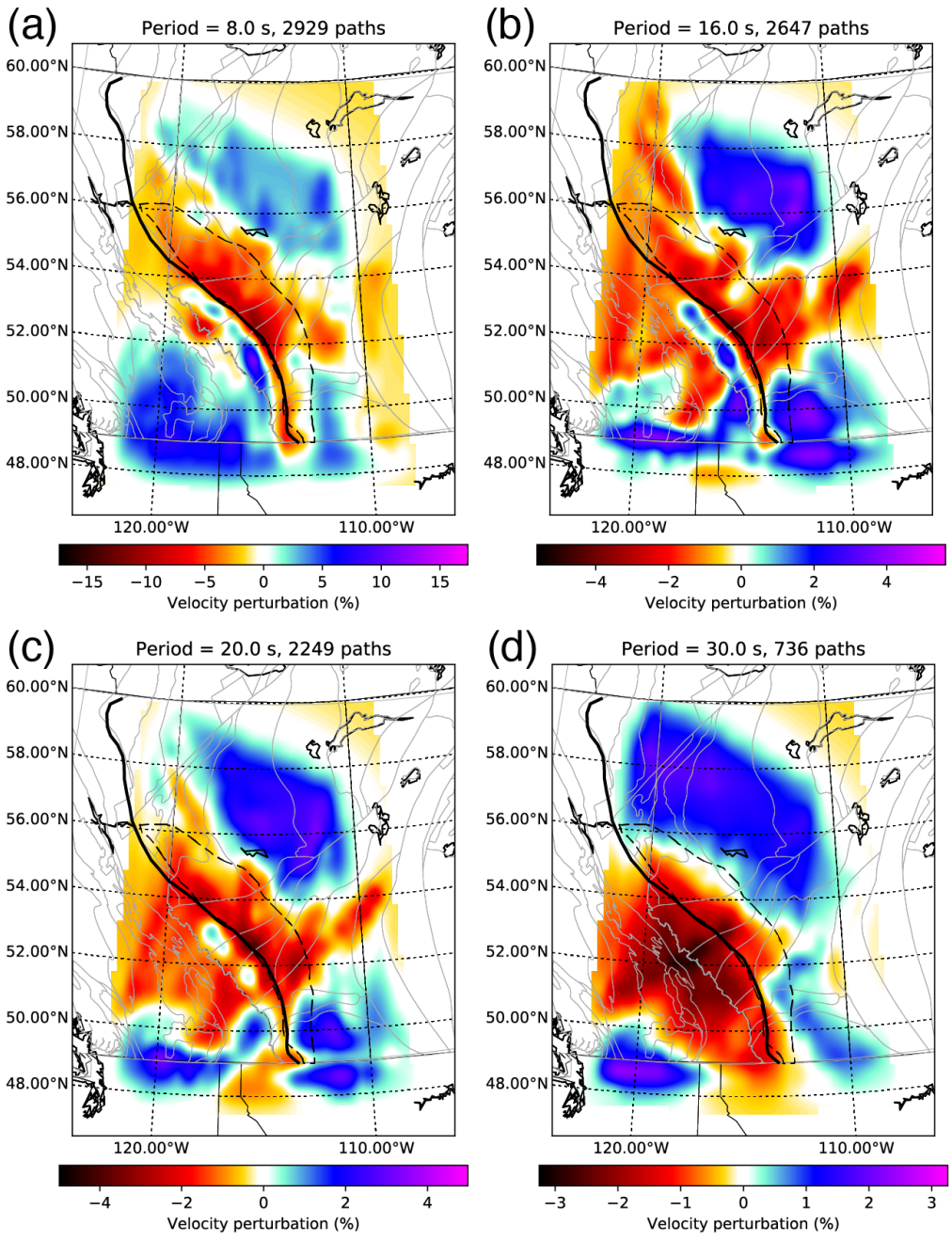


Figure 7.7 Group velocity maps at four periods. The thick black line indicates the Cordillera deformation front marking the eastern boundary of the Foreland Belt. The dashed polygon encloses the deposition center of the Alberta basin.

### 7.3.4 Group velocity model

We construct the velocity model using a linear inversion approach proposed by Barmin et al. (2001) (see section 3.3.4 for details). We limit the inversion of dispersion data to periods above 30 seconds, in view that the sharp drop-off of model resolution at longer periods (Figure 7.6) may lead to poorly constrained velocity structures. The velocity model largely confirms the observed group velocity pattern (Figure 7.5), highlighting a low-velocity zone in central Alberta (i.e., central Alberta low) sandwiched between two high-velocity regions (Figure 7.7a). The 8-sec group velocity map shows predominant low (<5%) velocities in front of the Cordillera Deformation Front (CDF), and its distribution coincides with the deepest Phanerozoic sediments in the deposition center of the Alberta basin with thicknesses in excess of 5 km. This low-velocity zone terminates sharply by a narrow corridor of high (>2%) velocities in the Foreland Belt (hereinafter Foreland Belt high) extending from the US-Canada border to 54º N in central Alberta. At longer periods, the low velocities persist and extend into the surrounding regions (Figures 7.7b-7.7d), whereas the strength of the high-velocity corridor gradually diminishes and completely disappears at periods above 25 seconds; the former observation (i.e., central Alberta low) is consistent with an earlier study that shows a low-velocity crust at depths above 20 km in the WCSB (Kao et al., 2013). Within the cratons, vertically continuous, high-velocity crust spans much of the region in northern and southernmost Alberta (see Figures 7.7b and 7.7c). Structures beneath these two regions differ from the central Alberta low by at least 4% in group velocities across potential boundary zones.

## 7.4 Discussion

### 7.4.1 Comparison with earlier studies

The availability of earlier tomographic models covering the study region permits a systematic comparison and evolution of model resolution. The most direct comparison is made by comparing with regional crustal model from Gu & Shen (2015) (hereafter GS15), which utilized a subset of the data analyzed in this chapter with an average of 1.5 years of recording from 23 stations. At short periods, the velocity variations are largely consistent between GS15 and our model (Figure 7.8a). For example, both models reveal a clear transition from the central Alberta low to the Foreland Belt high (see Figure 7.8a). The velocity anomalies and the associated transition in our model are much sharper than those defined in GS15, which we attribute to a significantly improved data resolution due to ~8-fold data density differences. In northern Alberta, high velocities characterize both models beneath the Buffalo Head Terrane (BHT) and Talton magmatic zone (Ta), two proposed Proterozoic accreted terranes.

At longer periods, the overall correlation between these two models is lower than its shorter period counterpart. Similar observations include the increased velocity beneath the Archean domain of the Medicine Hat Block (MHB) and pronounced low-velocity anomaly extending from the foothills northeastward to the eastern Loverna block (Lo), the Archean core of the southern Hearne craton. In both models, the transition region between these two velocity regimes approximately coincides with the Vulcan Structure, which potentially marks a collisional boundary between these cratons. A major difference is manifested in the Foreland Belt high, which is well-defined in our model but is only inferred from slightly above-average velocities in GS15. In addition, our model shows dominating high velocities in northern Alberta in contrast to low velocities in

GS15, although the reduced resolution in both models may contribute to the apparent inconsistencies in this region.

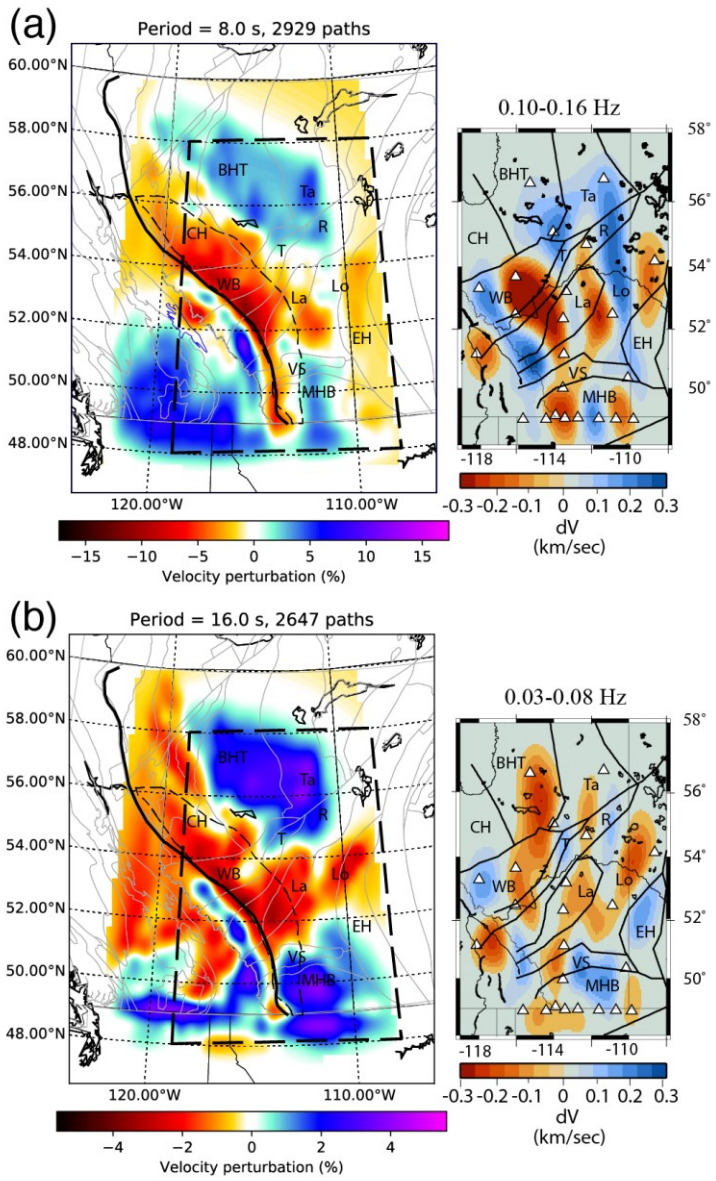


Figure 7.8 A comparison of group velocities between this study (left panel) and Gu & Shen (2015) (right panel) at two period bands.

Further comparisons are made with two regional (Dalton et al., 2011; hereafter Dalton11) and continental scale models (Kao et al., 2013; hereafter Kao13) at longer periods. The regional model overlaps with the northwestern portion of our study area (Figure 7.9a), where both models show prevailing low velocities in the Alberta basin. The first-order structure in Dalton11 is the velocity transition across the southwestern segment of the Great Slave Lake Shear Zone (GSLSZ), which separates the Proterozoic terranes in northern Alberta from the Wopmay orogen further north. This velocity transition is not well resolved in our model due to the lack of ray coverage across the boundary, but a high-velocity region immediately bounding the GSLSZ to the southeast is consistent with the observation from Dalton11. On the other hand, the continental-scale model is characterized by a modest velocity perturbation in Alberta partly due to the large aperture of the seismic array and coarse model parameterization (1-degree spherical grid) used in Kao13. Despite a potential difference in resolving power, the correlation between these two models shows consistent trends from high velocities in the southwestern corner, to a low-velocity Cordillera foothills zone, and ending with high velocities in northern Alberta. Overall, through systematic comparisons with both regional (GS15 and Dalton11) and continental scale models (Kao13), our model largely confirms the major velocity observations in the earlier studies at much-improved resolution, which contributes to a more detailed examination of the crustal structures in this region.

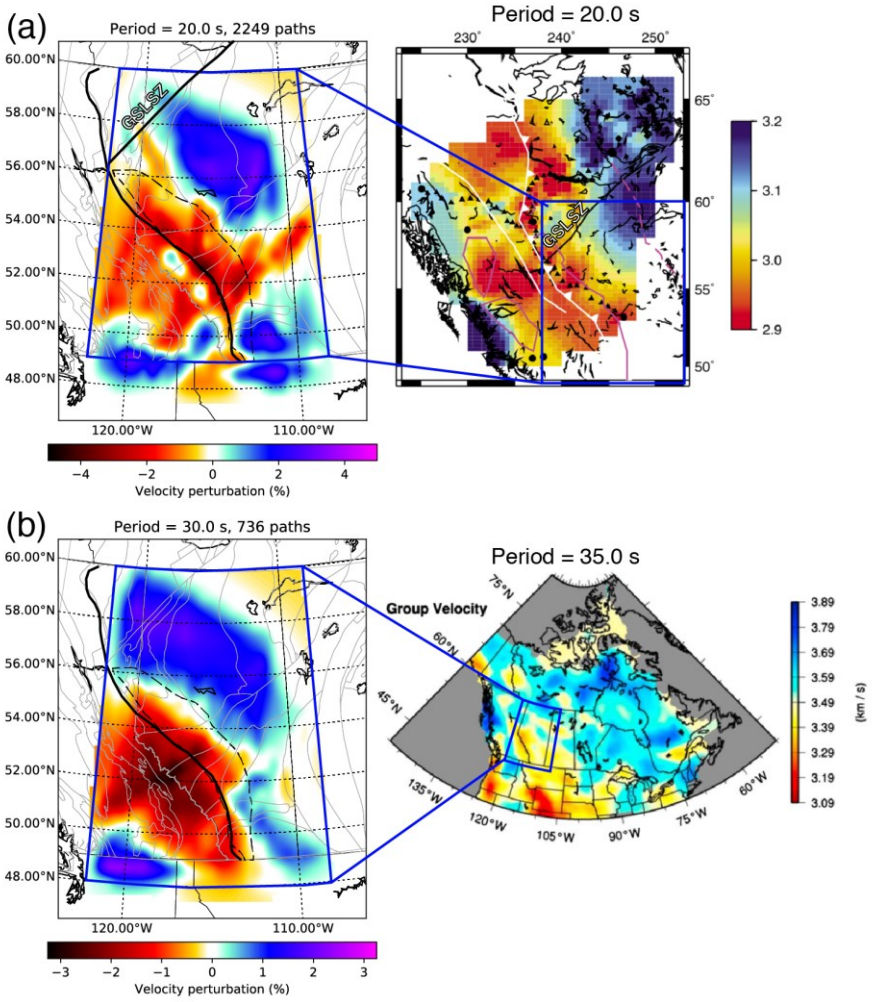


Figure 7.9 Comparison of group velocities from this study (left panel) with those from (a) Dalton et al. (2013) and (b) Kao et al. (2013) (right panel) at two period bands. The blue rectangles highlight the common imaging area in both models.

## 7.4.2 Foreland Belt structure

The Cordillera Foreland Belt is one of the best-constrained areas in our model due to significantly improved station density near the Rocky Mountain foothills (see Figure 7.1). An intriguing observation is the high-velocity zone within the Foreland Belt (i.e., Foreland Belt high) that is clearly detectable in all

group velocity maps at periods less than 20 seconds (see Figure 7.7). This narrow (<100 km) zone extends continuously for ~500 km along the strike of the Rocky Mountains (Figure 7.10a). Its spatial distribution is in excellent agreement with the high elevation terrains of the fold-and-thrust belts (Figure 7.10b). An accurate understanding of the lateral and vertical scales of this anomaly requires a full 3D velocity model (e.g., Bensen et al., 2008; Gu & Shen, 2015; Bao et al., 2016) that is conducted by inverting the group dispersion using a linear inversion scheme (Herrmann, 2013) and will be deferred to a future study. Instead, we seek preliminary constraints on the depth extent of the Foreland Belt high by examining the Rayleigh wave sensitivity kernels, which are computed by Gu & Shen (2015) using a 1-D regional model obtained from the receiver function analysis (Chen et al., 2015). The amplitude of the curve presents the sensitivity of group velocity variations to shear velocity perturbations at different depths. For instance, the 8-sec kernel provides primary sensitivity to the shallowest 10 km of the crust. Based on the kernel constraint, the 20-sec group velocity is most sensitive to the depth range between 15-25 km, which suggests that the Foreland Belt high could potentially be a deep-rooted structure extending down to the middle crust.

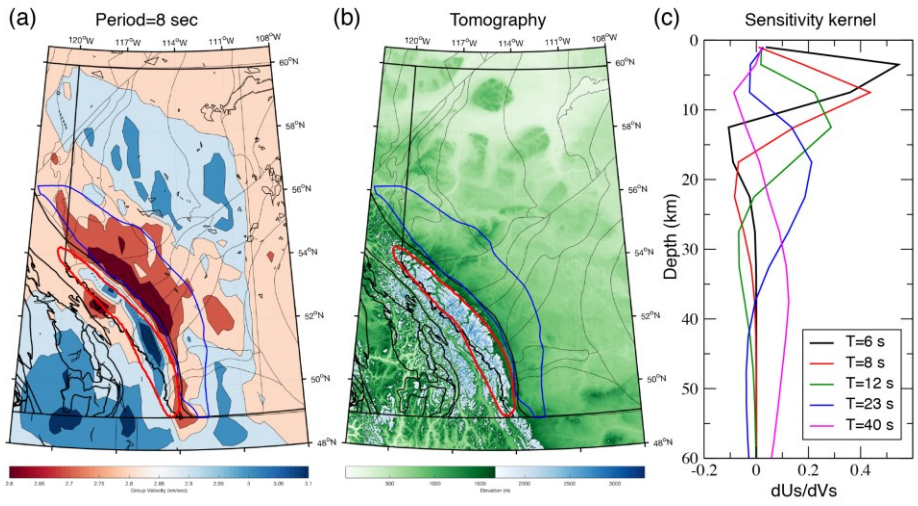


Figure 7.10 (a) Group velocity map at 8-sec. (b) Surface wave topography. The blue polygon outlines the depocenter of the Alberta basin. The red polygon highlights the high velocity and high elevation region in the Foreland Belt. (c) Rayleigh wave sensitivity kernel at different periods according to Gu & Shen (2015).

Preliminary outcomes of our group velocity structures are supported by earlier exploration seismic constraints. For example, seismic reflection and refraction surveys conducted by the Lithoprobe project sampled a narrow corridor across the southernmost Canadian Cordillera (Cook et al., 1992; Clowes et al., 1995). In these studies, the seismic reflectivity and velocity along these profiles delineate the geometry of east-verging thrust sheets that extend from beneath the Foreland Belt along a basal detachment to the Fraser river fault at the boundary between the Coast Belt and the Intermontane Belt. This wedge-shaped layer tapers gradually eastward and reaches a thickness of 10-15 km beneath the Foreland Belt based on the interpreted cross-section (Clowes et al., 1995), which roughly agrees with the depth estimate from our model. The underlying crust contains the Proterozoic metasedimentary rocks of North American affinity with thicknesses up to 25-30 km (Snyder et al., 2002). An important conclusion drawn from these transects is that much of the Cordillera crust are only thin slices of

rocks that overthrust the North America margin that comprises the middle-lower crust (Clowes et al., 1995). This argument is further supported by the observations of subparallel reflectivity from the SNORCLE transect in the northern Cordillera (Cook et al., 2004; Cook & Erdmer, 2005). Taken together, these studies derived a tectonic model that attributed the Cordillera to an accretionary orogen formed due to the convergence between the accreted terranes and North America continent (Monger et al., 1982; Cook & Erdmer, 2005; Percival et al., 2012).

The accretionary hypothesis has been carefully investigated in chapter 6 and has been shown to be difficult to reconcile with the mantle seismic image. The crustal observations in the Foreland Belt also raise some questions on such interpretation. The underlying assumption of the accretionary model is that the Cordillera strata, especially the Proterozoic sequence forming the Ancient North American crust, are laterally continuous throughout the Mountain Belt (Cook et al., 2004; Percival et al., 2012). However, our model shows that the Foreland Belt high does not extend beyond (i.e., locates to the east of) the Rocky Mountain Trench, the boundary between the Foreland Belt and the Omineca Belt. A similarly localized high-velocity zone is reported in South American Cordillera, where the thrust belts in the Eastern Cordillera are underlain by higher shear velocities (>3.25 km) contrast sharply with the surrounding low velocities (<3.0 km) down to 15-20 km, suggesting a thick-skinned, basement-involved deformation (Ward et al., 2013). If the observed Foreland Belt high also resulted from a deep deformation process, the dominant view of a thin-skinned thrusting style in the southern Canadian Cordillera may also be questionable. We could not rule out alternative possible explanations for the Foreland Belt high, which include 1) a compositional effect of the deep-rooted thrust sheets of platformal carbonate rocks and/or 2) strong radial anisotropy of highly deformed Proterozoic strata. The validation of these hypothesis requires the development of a full 3D anisotropic model, which will be deferred to a future study.

### 7.4.3 Craton structures

The craton region shows two distinctive high-velocity zones (HVZs) separated by the central Alberta low. The southern HVZ is spatially confined within the domain boundary of the MHB (see Figure 7.7) and is robustly constrained at all periods considered in our inversion. At the longest period (30 sec) MHB is divided into the eastern and western halves. The velocity boundary is subparallel with the northwest-southeast trending aeromagnetic anomaly. In the same region, seismic reflection surveys have revealed crustal scale east-verging ramp coinciding with the potential field lineament, which is interpreted as crustal scale thrust faults formed during the Archean collision of two continental blocks (Lemieux et al., 2000). Based on this tectonic model, the dichotomy of the MHB at longer period could reflect the distinctive characters of two Archean aged continental block. The difference might be enhanced during an episode of underthrusting of the eastern MHB beneath the western counterpart (Lemieux et al., 2000). Alternatively, earlier studies have reported a widespread Proterozoic underplating event based on the findings on a cross-section across the eastern MHB (Clowes et al., 2002; Gorman et al., 2002). This extensive underplated layer formed a thick (>10 km) and high-velocity (>7 km/sec for P-wave) lower crust underlying the MHB and Wyoming craton and may also provide a possible explanation for the observed high-velocity crustal root of the MHB.

The region that is most robustly constrained by our model is the central Alberta, which shows dominating low shear velocities at all periods (see Figure 7.7). The major tectonic units consist of the eastern Alberta orogen and the Loverna block. The entire region was suggested to undergo strong deformation during the dual subductions along the STZ and the THO (Ross et al., 2000; Ross, 2002a). Therefore, the crust might have been significantly modified by the tectonic entrapment and the syn-/post-collisional tectonothermal overprinting

(Chen et al., 2015) that effectively lower the crustal velocities. On the other hand, the signature of the STZ is relatively weak, and is only inferable from small (<2%) velocity variation between the bounding domains (see 16 sec group velocity map on Figure 7.7). This small-scale velocity variation is robustly constrained by the high ray-path density, which provides excellent horizontal resolution approximately equals to the nominal resolution (i.e., the grid size, 0.5 deg) of the model. The high-resolution image confirms the observation of a relatively continuous velocity reported in the earlier study (Gu & Shen, 2015). We concur with the conclusion in chapter 4 that the STZ is mainly evidenced by the sharp Moho depth and mantle seismic velocity contrasts, whereas its presence is not clearly supported by the velocities at crustal depths.

## 7.5 Conclusions

This chapter presents a new Rayleigh wave group velocity model of the central-southern WCSB. Compared with the earlier studies, our model shows significantly improved resolution compared to earlier regional and continental scale investigations, enabling a more detailed examination of the continental crust in this region. The group velocity maps between 8-30 sec reveal complex structures, most notably the Foreland Belt high, associated with Phanerozoic cordillera orogenesis. The craton is subdivided into three broad regimes based on distinctive velocity characters, which include a central Alberta low and two high-velocity zones underlying the MHB and northern Alberta Proterozoic domains. Overall, this chapter highlights the complex foreland crustal structures and marks the first step towards the development of a full 3D anisotropic regional model that will ultimately contribute to a more comprehensive understanding of the evolution of the WCSB.

# Chapter 8 Conclusions

The lithosphere beneath western Canada records more than three billion-years of tectonic development of the North American continent, evolving from the Precambrian assembly of the Laurentian craton (Hoffman, 1988; Ross et al., 1991) to the Phanerozoic Cordilleran orogenesis (Dickinson, 2004; Johnston, 2008). The rapid expansion of regional seismic networks has offered an unprecedented opportunity to investigate the lithospheric structures and mantle dynamics. In this thesis, we exploit the data recorded from more than 100 broadband sensors during the past 10 years and employ three passive source imaging techniques, each of which has a unique resolving power and depth sensitivity, to map the seismic structures of lithosphere at different depth levels. The list below succinctly summarizes the key observations and interpretations of each chapter.

Chapter 4 shows substantial spatial variations in crustal structure and thickness across both the STZ and GFTZ based on an integrated analysis of P-to-S receiver functions, shear velocities, and potential field measurements. Seismic observations of increased Moho depth and Vp/Vs ratio characterize the crust near both discontinuities. These are consistent with the interpretation of the Paleoproterozoic continental suture zones. The location of the seismically defined GFTZ is consistent with the geologically mapped Dillion suture within the Trans-Montana Orogen. We find evidence for crustal underplating beneath the GFTZ, although this anomalous layer is smaller than previous estimates and appears to be confined to the Trans-Montana Orogen in view of a limited spatial distribution of high Vp/Vs ratios.

Chapter 5 conducts a high-resolution survey of the mantle P- and S-wave velocities using finite-frequency tomography. Our models show pronounced

eastward increases of 4% P- and 6% S-wave velocities beneath the foreland region. In the cratonic region, distinctive high (>2%) velocity anomalies representing depleted mantle lithospheres are well correlated with major Precambrian crustal domains. The largest lithosphere thickness contrast coincides with the STZ, where the Hearne province extends down to ~300 km, nearly 100 km deeper than the Proterozoic terranes in northern Alberta. In the latter region, a pronounced cylindrical negative velocity anomaly extends sub-vertically from 75 km to ~300 km depth, which could suggest significant tectonothermal modifications during subduction and/or plume activities. At basin scale in the mantle, seismic velocities show no apparent correlation with surface heat flux, suggesting a minimum mantle contribution to the regional thermal variability. Furthermore, the long wavelength isostatic gravity correlates negatively with the velocities, which confirms that the melt extraction from Precambrian cratons is responsible for the formation of highly depleted mantle lithospheres. Moreover, our model reveals the increased concentrations of kimberlites and lamproites near the zones of high horizontal velocity gradients. The distinct spatial pattern may reflect either preferential formation or eruption of potentially diamondiferous rocks at lithospheric weak zones near the western margin of Laurentia.

Chapter 6 provides new seismic constraints beneath the Canadian Cordilleran foreland and show, for the first time, a mantle suture associated with a sharp and structurally complex Cordillera-Craton mantle boundary. The corresponding craton collisional front dips steeply to the west beneath the southern Rocky Mountain Trench, contrary to the commonly assumed eastward-thickening geometry of the accretionary model that attributes the Cordilleran orogenesis to episodic terrane accretions. These observations establish an intrinsic yet previously missing link between shallow structures and deep mantle processes during an episode of westward subduction of the North American craton in the Late Cretaceous, favouring a collisional origin for the southern Canadian Cordillera.

Chapter 7 presents a new crustal velocity model using ambient noise tomography. The Rayleigh waves extracted from noise correlation provide a dense data sampling to the study region, leading to significantly improved model resolution than available in previous studies. The group velocity maps between 8 and 30 seconds reveal complex velocity variations near the Cordillera foreland region. The Foreland Belt is underlain by a prominent high-velocity zone extending to middle crustal depths, which is interpreted as a deep-rooted structure potentially connected to the fold-and-thrust belts. The Alberta basin is characterized by low velocities at all periods, interpreted to represent the low wavespeed basin sediments and a potentially strongly reworked crust. On the other hand, high-velocity crust spans much of southern and northern Alberta, suggesting relatively minor tectonic modifications to these cratonic areas.

The seismic investigations conducted in this thesis provide new insight into the major scientific questions defined in chapter 1. At crustal depths, the STZ and GFTZ are characterized by the common seismic structures of a thickened crust and increased Vp/Vs ratio. The STZ coincides with the magnetic low of the Thorsby domain and separates the Archean Hearne craton from the Proterozoic accreted terranes in northern Alberta. The GFTZ is located near the Dillion suture that is interpreted as the collisional boundary between the MHB (north) and Wyoming craton (south). These observations provide improved constraints on the subsurface location and the nature of these two tectonic boundary zones. However, challenges still remain in 1) reconciling diverse tectonic processes proposed along the STZ [e.g., collisional suture (Hoffman et al., 1988; Hanmer et al., 1995; Ross, 2002a; Berman et al., 2007; Gu et al., 2018), intra-continental shear (Hanmer et al., 1995) or rift zones (Flowers et al., 2006)], and 2) understanding the kinematic roles of STZ and GFTZ in the Precambrian growth and reworking of Laurentia. An integrated approach involving geophysical imaging, geological mapping, geochronological dating, geodynamic modeling, paleomagnetic reconstruction is needed to address these questions.

Our seismic models reveal complex mantle lithosphere structures that are well-correlated with the crustal domains. The Archean MHB and Hearne province are underlain by high velocities that are interpreted as the cratonic mantle lithosphere. The deep (~300 km) Hearne lithospheric keel is consistent with a collisional tectonic framework derived from the crustal observations (chapter 4). The Proterozoic accreted terranes are instead characterized by reduced seismic velocities, suggesting significant reworking of mantle lithosphere during episodes of subduction events. Mantle seismic velocity is uncorrelated with surface heat flow but negatively correlated with gravity anomaly, supporting the melt depletion as a major factor in the formation of high-velocity, low-density lithosphere. These analyses are based on independent data (i.e., velocity, heat flow and gravity) and provide a preliminary assessment of the nature of mantle lithosphere. Future investigations should focus on differentiating the thermal and non-thermal (compositional) contributions to seismic velocity through 1) joint inversion of seismic and gravity data (e.g., Deschamps et al., 2002) and 2) quantitative interpretation of seismic velocity with petrological and thermal constraints (e.g., Artemieva, 2009). In addition, our model reveals a close spatial association of kimberlite field with lateral velocity gradient zone. However, the nature of kimberlite (e.g., plume, subduction, mantle transition zone origins) remains enigmatic and more detailed understanding requires integrating seismological, geochemical, geochronological and petrological constraints in future studies.

Our mantle image shows a sharp seismic Cordillera-Craton boundary that is consistent with a collisional model of the Cordilleran orogen. Future efforts should be made to validate/test the collisional hypothesis by 1) locating the collisional suture in the crust and 2) reproducing the seismic observations with numerical simulations. The first objective requires high-resolution seismic images of the crustal structures of the Cordilleran foreland region, while the latter could benefit from 3D geodynamic modelling based on simulation of lithosphere

deformation during continent collision (e.g., Pysklywec et al., 2010) or inverse mantle convection model that assimilates seismic structures (e.g., Liu et al., 2008).

These proposed future research directions demand substantial efforts in a number of aspects. First, the station distribution in the WCSB is uneven. The increasing research interest in the induced seismicity have greatly improved the station coverage near hydraulic fracturing sites on the shale formations in central-western Alberta. In comparison, the station density in southern and northern Alberta remains sparse and inevitably leads to a poorly spatial sampling and limits the overall understanding of the tectonic evolution of the WCSB. For example, the Peace River Arch and Buffalo Hills, two regions containing important geological targets and potential economically-beneficial resources (e.g., diamonds), are not yet directly sampled by broadband stations.

Second, improvement in seismic imaging method is required to enhance the quality and resolution of the subsurface image. For example, the velocity and anisotropy structures of the basin sediments can be obtained by inverting the Rayleigh wave ellipticity (H/V ratio) from ambient noise (Lin et al., 2014) or earthquake data (Lin et al., 2012). The lithospheric interfaces (e.g. LAB and mid-lithospheric discontinuities) can be more accurately constrained by S-to-P receiver functions (e.g., Kind et al., 2012; Hopper & Fischer, 2015). In addition, more advanced techniques such as migration imaging and full waveform inversion could contribute to a better understanding of the basin structures with improved constraints on velocity, attenuation and anisotropy properties. For instance, the current model can be refined to resolve the density and anisotropy structures, which requires full waveform modeling of both ambient noise and earthquake data through spectral element simulation and adjoint tomography (e.g., Tape et al., 2009).

Finally, improvements in data and technology should work hand-in-hand to achieve the ultimate goal of developing a community model (Shaw et al., 2015). This model will integrate all seismic imaging results (i.e., velocity, Vp/Vs ratio and Moho depth) from this thesis with constraints from exploration seismics, well-log, borehole/lab measurements and geologic horizons (Branscombe et al., 2018). It could provide useful community resources and tools for purposes of geological/tectonic investigations, seismic hazard mitigation, mineral exploration and geoscience education.

# Bibliography


Abraham, A.-C., Francis, D., & Polve, M. (2001). Recent alkaline basalts as probes of the lithospheric mantle roots of the northern Canadian Cordillera. *Chemical Geology*, *175*(3), 361–386.

Abt, D. L., Fischer, K. M., French, S. W., Ford, H. A., Yuan, H., & Romanowicz, B. (2010). North American lithospheric discontinuity structure imaged by Ps and Sp receiver functions. *Journal of Geophysical Research: Solid Earth*, *115*(B9).

Aki, K. (1957). Space and time spectra of stationary stochastic waves, with special reference to microtremors. *Bulletin of the Earthquake Research Institute*, *35*(1), 415–457. https://doi.org/http://hdl.handle.net/2261/11892

Aki, K., Christoffersson, A., & Husebye, E. S. (1977). Determination of the three-dimensional seismic structure of the lithosphere. *Journal of Geophysical Research*, *82*(2), 277–296.

Ammon, C. (1991). The isolation of receiver effects from teleseismic P waveforms. *Bulletin of the Seismological Society of America*. https://doi.org/10.1029/2005JB004161

Ardhuin, F., Stutzmann, E., Schimmel, M., & Mangeney, A. (2011). Ocean wave sources of seismic noise. *Journal of Geophysical Research: Oceans*. https://doi.org/10.1029/2011JC006952

Arndt, N. T., Coltice, N., Helmstaedt, H., & Gregoire, M. (2009). Origin of Archean subcontinental lithospheric mantle: Some petrological constraints. *Lithos*, *109*(1–2), 61–71.

Artemieva, I. M. (2006). Global 1× 1 thermal model TC1 for the continental lithosphere: implications for lithosphere secular evolution. *Tectonophysics*, *416*(1), 245–277.

Artemieva, I. M. (2009). The continental lithosphere: reconciling thermal, seismic, and petrologic data. *Lithos*, *109*(1), 23–46.

Artemieva, I. M., & Mooney, W. D. (2001). Thermal thickness and evolution of Precambrian lithosphere: a global study. *Journal of Geophysical Research: Solid Earth*, *106*(B8), 16387–16414.

Aulbach, S., Griffin, W. L., O'Reilly, S. Y., & McCandless, T. E. (2004). Genesis and evolution of the lithospheric mantle beneath the Buffalo Head Terrane, Alberta (Canada). *Lithos*, *77*(1–4 SPEC. ISS.), 413–451. https://doi.org/10.1016/j.lithos.2004.04.020

Bank, C., Bostock, M., Ellis, R., Hajnal, Z., & VanDecar, J. (1998). Lithospheric mantle structure beneath the Trans-Hudson Orogen and the origin of diamondiferous kimberlites. *Journal of Geophysical Research*, *103*(B5), 10103–10114. https://doi.org/10.1029/97JB03746

Bao, X., & Eaton, D. W. (2015). Large variations in lithospheric thickness of western

Laurentia: Tectonic inheritance or collisional reworking? *Precambrian Research*, *266*, 579–586. https://doi.org/10.1016/j.precamres.2015.05.010

Bao, X., Eaton, D. W., & Gu, Y. J. (2016). Rayleigh wave azimuthally anisotropic phase velocity maps beneath western Canada. *Journal of Geophysical Research: Solid Earth*, *121*(3), 1821–1834.

Bao, X., Eaton, D. W., & Guest, B. (2014). Plateau uplift in western Canada caused by lithospheric delamination along a craton edge. *Nature Geoscience*, *7*(11), 830–833. https://doi.org/10.1038/ngeo2270

Barmin, M. P., Ritzwoller, M. H., & Levshin, A. L. (2001). A fast and reliable method for surface wave tomography. In *Monitoring the Comprehensive Nuclear-Test-Ban Treaty: Surface Waves* (pp. 1351–1375). Springer.

Barnhart, K. R., Mahan, K. H., Blackburn, T. J., Bowring, S. A., & Dudas, F. O. (2012). Deep crustal xenoliths from central Montana, USA: Implications for the timing and mechanisms of high-velocity lower crust formation. *Geosphere*, *8*(6), 1408–1428.

Beaumont, C. (1981). Foreland Basins. *Group*, (il), 1–11. https://doi.org/10.1002/9781444303810

Bedle, H., & van der Lee, S. (2009). S velocity variations beneath North America. *Journal of Geophysical Research: Solid Earth*, *114*(B7).

Bensen, G. D., Ritzwoller, M. H., Barmin, M. P., Levshin, A. L., Lin, F., Moschetti, M. P., … Yang, Y. (2007). Processing seismic ambient noise data to obtain reliable broad-band surface wave dispersion measurements. *Geophysical Journal International*, *169*(3), 1239–1260.

Bensen, G. D., Ritzwoller, M. H., & Shapiro, N. M. (2008). Broadband ambient noise surface wave tomography across the United States. *Journal of Geophysical Research: Solid Earth*, *113*(B5).

Berman, R. G., Davis, W. J., & Pehrsson, S. (2007). Collisional Snowbird tectonic zone resurrected: Growth of Laurentia during the 1.9 accretionary phase of the Hudsonian orogeny. *Geology*, *35*(10), 911–914. https://doi.org/10.1130/G23771A.1

Berman, R. G., Pehrsson, S., Davis, W. J., Ryan, J. J., Qui, H., & Ashton, K. E. (2013). The Arrowsmith orogeny: Geochronological and thermobarometric constraints on its extent and tectonic setting in the Rae craton, with implications for pre-Nuna supercontinent reconstruction. *Precambrian Research*, *232*, 44–69.

Boerner, D. E., Craven, R. D., Kurtz, R. D., Ross, G. M., & Jones, F. W. (1998). The Great Falls Tectonic Zone: suture or intracontinental shear zone? *Canadain Journal of Earth Sciences*, *35*(2), 175–183. https://doi.org/10.1139/cjes-35-2-175

Boerner, D. E., Kurtz, R. D., Craven, J. A., Rondenay, S., & Qian, W. (1995). Buried Proterozoic foredeep under the Western Canada Sedimentary Basin? *Geology*, *23*(4), 297–300. https://doi.org/10.1130/0091-7613(1995)023<0297:BPFUTW>2.3.CO;2

Boerner, D. E., Kurtz, R. D., Craven, J. a, Ross, G. M., & Jones, F. W. (2000). A synthesis of electromagnetic studies in the Lithoprobe Alberta Basement Transect: constraints on Paleoproterozoic indentation tectonics. *Canadian Journal of Earth Sciences*, *37*(11), 1509–1534. https://doi.org/10.1139/e00-063

Bond, G. C., & Kominz, M. A. (1984). Construction of tectonic subsidence curves for the early Paleozoic miogeocline, southern Canadian Rocky Mountains: Implications for subsidence mechanisms, age of breakup, and crustal thinning. *Geological Society of America Bulletin*, *95*(2), 155–173.

Bostock, M. G. (1998). Mantle stratigraphy and evolution of the Slave province. *Journal of Geophysical Research: Solid Earth*, *103*(B9), 21183–21200.

Bostock, M. G. (2013). The Moho in subduction zones. *Tectonophysics*, *609*, 547–557.

Bostock, M. G., Rondenay, S., & Shragge, J. (2001). Multiparameter two-dimensional inversion of scattered teleseismic body waves 1. Theory for oblique incidence. *Journal of Geophysical Research: Solid Earth*, *106*(B12), 30771–30782.

Bouzidi, Y., Schmitt, D. R., Burwash, R. A., & Kanasewich, E. R. (2002). Depth migration of deep seismic reflection profiles: crustal thickness variations in Alberta. *Canadian Journal of Earth Sciences*, *39*(3), 331–350. https://doi.org/10.1139/e01-080

Boyce, A., Bastow, I. D., Darbyshire, F. A., Ellwood, A. G., Gilligan, A., Levin, V., & Menke, W. (2016). Subduction beneath Laurentia modified the eastern North American cratonic edge: Evidence from P wave and S wave tomography. *Journal of Geophysical Research: Solid Earth*, *121*(7), 5013–5030.

Boyd, F. R. (1989). Compositional distinction between oceanic and cratonic lithosphere. *Earth and Planetary Science Letters*, *96*(1–2), 15–26.

Branscombe, P., MacCormack, K., Corlett, H., Hathway, B., Hauck, T., Peterson, J., … Regulator, A. E. (n.d.). Building a 3D Provincial Geological Framework Model of Alberta–Version 1: Integrating decades of geological interpretation and 620,812 data points.

Brzak, K., Gu, Y. J., Ökeler, A., Steckler, M., & Lerner-Lam, A. (2009). Migration imaging and forward modeling of microseismic noise sources near southern Italy. *Geochemistry, Geophysics, Geosystems*. https://doi.org/10.1029/2008GC002234

Buhlmann, A., Cavell, P., Burwash, R., Creaser, R., & Luth, R. (2000). Minette bodies and cognate mica-clinopyroxenite xenoliths from the Milk River area, southern Alberta: Records of a complex history of the northernmost part of the Archean Wyoming craton. *Canadian Journal of Earth Sciences*, *37*, 1629–1650. https://doi.org/10.1139/e00-058

Calvert, A. J., Ramachandran, K., Kao, H., & Fisher, M. A. (2006). Local thickening of the Cascadia forearc crust and the origin of seismic reflectors in the uppermost mantle. *Tectonophysics*, *420*(1), 175–188.

Canil, D. (2004). Mildly incompatible elements in peridotites and the origins of mantle lithosphere. *Lithos*, *77*(1–4), 375–393.

Canil, D. (2008). Canada's craton: a bottoms-up view. *GSA TODAY*, *18*(6), 4.

Canil, D., Schulze, D. J., Hall, D., Hearn Jr., B. C., & Milliken, S. M. (2003). Lithospheric roots beneath western Laurentia: the geochemical signal in mantle garnets. *Canadian Journal of Earth Sciences*, *40*(8), 1027–1051. https://doi.org/10.1139/e03-003

Cant, D. J., & Stockmal, G. S. (1989). The Alberta foreland basin: relationship between stratigraphy and Cordilleran terrane-accretion events. *Canadian Journal of Earth Sciences*, *26*(10), 1964–1975. https://doi.org/10.1139/e89-166

Capon, J. (1973). Analysis of Microseismic Noise at LASA, NORSAR and ALPA. *Geophysical Journal of the Royal Astronomical Society*. https://doi.org/10.1111/j.1365-246X.1973.tb02413.x

Carlson, R. W., Irving, A. J., Schulze, D. J., & Hearn Jr, B. C. (2004). Timing of Precambrian melt depletion and Phanerozoic refertilization events in the lithospheric mantle of the Wyoming Craton and adjacent Central Plains Orogen. *Lithos*, *77*(1–4), 453–472.

Carlson, R. W., Pearson, D. G., & James, D. E. (2005). Physical, chemical, and chronological characteristics of continental mantle. *Reviews of Geophysics*, *43*(1).

Carlson, S. M., Hillier, W. D., & Hood, C. T. (1999). The Buffalo Hills kimberlites: a newly-discovered diamondiferous kimberlite province in north-central Alberta, Canada. In *8th International Kimberlite Conference* (Vol. 1, pp. 109–116).

Cassidy, J. F. (1992). Numerical experiments in broadband receiver function analysis. *Bulletin of the Seismological Society of America*, *82*(3), 1453–1474.

Cassidy, J. F. (1995). A comparison of the receiver structure beneath stations of the Canadian National Seismograph Network. *Canadian Journal of Earth Sciences*, *32*(7), 938–951.

Cavell, P. A., Burwash, R. A., & Nelson, D. B. (1993). Enriched mantle beneath southern Alberta: isotopic evidence for a northern extension of the Wyoming block into southern Alberta. In *Geological Association of Canada–Mineralogical Association of Canada Program with Abstracts* (Vol. 18, p. A-17).

Cecile, M. P., Morrow, D. W., & Williams, G. K. (1997). Early Paleozoic (Cambrian to Early Devonian) tectonic framework, Canadian Cordillera. *Bulletin of Canadian Petroleum Geology*, *45*(1), 54–74.

Červený, V., & Soares, J. E. P. (1992). Fresnel volume ray tracing. *Geophysics*, *57*(7), 902–915.

Chacko, T., De, S. K., Creaser, R. A., & Muehlenbachs, K. (2000). Tectonic setting of the Taltson magmatic zone at 1.9-2.0 Ga: a granitoid-based perspective. *Canadian Journal of Earth Sciences*, *37*(11), 1597–1609. https://doi.org/10.1139/e00-029

Chandra, N. N., & Cumming, G. L. (1972). Seismic refraction studies in western Canada. *Canadian Journal of Earth Sciences*, *9*(9), 1099–1109.

Chen, C., Gilbert, H., Fischer, K. M., Andronicos, C. L., Pavlis, G. L., Hamburger, M. W., … Yang, X. (2018). Lithospheric discontinuities beneath the US Midcontinent–signatures of Proterozoic terrane accretion and failed rifting. *Earth and Planetary Science Letters*, *481*, 223–235.

Chen, L., & Ai, Y. (2009). Discontinuity structure of the mantle transition zone beneath the North China Craton from receiver function migration. *Journal of Geophysical Research: Solid Earth*, *114*(B6).

Chen, L., Wen, L., & Zheng, T. (2005). A wave equation migration method for receiver

function imaging: 1. Theory. *Journal of Geophysical Research: Solid Earth*. https://doi.org/10.1029/2005JB003665

Chen, Y. (2014). Lithospheric structure imaging of alberta from regional broadband seismic network. *MSc Thesis, University of Alberta*.

Chen, Y., Gu, Y. J., Dokht, R. M. H., & Sacchi, M. D. (2015). Crustal imprints of Precambrian orogenesis in western Laurentia. *Journal of Geophysical Research: Solid Earth*, *120*(10), 6993–7012. https://doi.org/10.1002/2014JB011353

Chen, Y., Gu, Y. J., & Hung, S.-H. (2017). Finite-frequency P-wave tomography of the Western Canada Sedimentary Basin: Implications for the lithospheric evolution in Western Laurentia. *Tectonophysics*, *698*, 79–90.

Chen, Y., Gu, Y. J., & Hung, S. H. (2018). A new appraisal of lithospheric structures of the Cordillera-Craton boundary region in western Canada. Tectonics.

Chen, Y., Niu, F., Liu, R., Huang, Z., Tkalčić, H., Sun, L., & Chan, W. (2010). Crustal structure beneath China from receiver function analysis. *Journal of Geophysical Research: Solid Earth*, *115*(B3).

Cheng, C., Bodin, T., & Allen, R. M. (2016). Three-dimensional pre-stack depth migration of receiver functions with the fast marching method: A Kirchhoff approach. *Geophysical Journal International*. https://doi.org/10.1093/gji/ggw062

Cheng, C., Bodin, T., Tauzin, B., & Allen, R. M. (2017). Cascadia subduction slab heterogeneity revealed by three-dimensional receiver function Kirchhoff migration. *Geophysical Research Letters*, *44*(2), 694–701.

Christensen, N. I. (1996). Poisson's ratio and crustal seismology. *Journal of Geophysical Research*, *101*(B2), 3139. https://doi.org/10.1029/95JB03446

Claerbout, J. F. (1968). SYNTHESIS OF A LAYERED MEDIUM FROM ITS ACOUSTIC TRANSMISSION RESPONSE. *GEOPHYSICS*. https://doi.org/10.1190/1.1439927

Clayton, R. W., & Wiggins, R. A. (1976). Source shape estimation and deconvolution of teleseismic bodywaves. *Geophysical Journal International*, *47*(1), 151–177.

Clowes, R., & Hyndman, R. D. (2010). The consequences of Canadian Cordillera thermal regime in recent tectonics and elevation: a reviewThis article is one of a series of papers published in this Special Issue on the theme <i>Lithoprobe — parameters, processes, and the evolution of a continen. *Canadian Journal of Earth Sciences*, *47*(5), 621–632. https://doi.org/10.1139/E10-016

Clowes, R. M., Burianyk, M. J., Gorman, A. R., & Kanasewich, E. R. (2002). Crustal velocity structure from SAREX, the Southern Alberta Refraction Experiment. *Canadian Journal of Earth Sciences*, *39*(3), 351–373. https://doi.org/10.1139/e01-070

Clowes, R. M., Kanasewich, E. R., & Cumming, G. L. (1968). Deep crustal seismic reflections at near-vertical incidence. *Geophysics*, *33*(3), 441–451.

Clowes, R. M., Zelt, C. A., Amor, J. R., & Ellis, R. M. (1995). Lithospheric structure in the southern Canadian Cordillera from a network of seismic refraction lines.

*Canadian Journal of Earth Sciences*, *32*(10), 1485–1513.

Clowes, R. M., Zelt, C. A., Amor, J. R., & M., E. R. (1995). Lithospheric structure in the southern Canadian Cordillera from a network of seismic refraction lines. *Canadian Journal of Earth Sciences*, *32*(10), 1485–1513.

Colpron, M., & Nelson, J. L. (2011). A digital atlas of terranes for the northern Cordillera. *BC GeoFile*, *11*.

Coney, P. J. (1989). Structural aspects of suspect terranes and accretionary tectonics in western North America. *Journal of Structural Geology*, *11*(1–2), 107–125.

Coney, P. J., Jones, D. L., & Monger, J. W. H. (1980). Cordilleran suspect terranes. *Nature*, *288*(5789), 329–333.

Conrad, C. P. (2000). Convective instability of thickening mantle lithosphere. *Geophysical Journal International*, *143*(1), 52–70.

Cook, F. A., Clowes, R. M., Snyder, D. B., van der Velden, A. J., Hall, K. W., Erdmer, P., & Evenchick, C. A. (2004). Precambrian crust beneath the Mesozoic northern Canadian Cordillera discovered by Lithoprobe seismic reflection profiling. *Tectonics*, *23*(2).

Cook, F. A., Varsek, J. L., Clowes, R. M., Kanasewich, E. R., Spencer, C. S., Parrish, R. R., … Price, R. A. (1992). Lithoprobe crustal reflection cross section of the southern Canadian Cordillera, 1, Foreland thrust and fold belt to Fraser River fault. *Tectonics*, *11*(1), 12–35.

Cook, F. a, & Erdmer, P. (2005). An 1800 km cross section of the lithosphere through the northwestern North American plate: lessons from 4.0 billion years of Earth's history. *Canadian Journal of Earth Sciences*, *42*(6), 1295–1311. https://doi.org/10.1139/e04-106

Cooper, C. M., Lenardic, A., Levander, A., & Moresi, L. (2006). Creation and preservation of cratonic lithosphere: seismic constraints and geodynamic models. *GEOPHYSICAL MONOGRAPH-AMERICAN GEOPHYSICAL UNION*, *164*, 75.

Corrigan, D., Hajnal, Z., Németh, B., & Lucas, S. B. (2005). Tectonic framework of a Paleoproterozoic arc-continent to continent-continent collisional zone, Trans-Hudson Orogen, from geological and seismic reflection studies. *Canadian Journal of Earth Sciences*, *42*(4), 421–434. https://doi.org/10.1139/e05-025

Corrigan, D., Pehrsson, S., Wodicka, N., & de Kemp, E. (2009). The Palaeoproterozoic Trans-Hudson Orogen: a prototype of modern accretionary processes. *Geological Society, London, Special Publications*, *327*(1), 457–479. https://doi.org/10.1144/SP327.19

Courtier, A. M., Gaherty, J. B., Revenaugh, J., Bostock, M. G., & Garnero, E. J. (2010). Seismic anisotropy associated with continental lithosphere accretion beneath the CANOE array, northwestern Canada. *Geology*, *38*(10), 887–890.

Cousens, B. L., Aspler, L. B., Chiarenzelli, J. R., Donaldson, J. A., Sandeman, H., Peterson, T. D., & LeCheminant, A. N. (2001). Enriched Archean lithospheric mantle beneath western Churchill Province tapped during Paleoproterozoic orogenesis. *Geology*, *29*(9), 827–830.

Cox, K. G. (1993). Continental Magmatic Underplating. *Philosophical Transactions of the Royal Society A: Mathematical, Physical and Engineering Sciences*, *342*(1663), 155–166. https://doi.org/10.1098/rsta.1993.0011

Crough, S. T., Morgan, W. J., & Hargraves, R. B. (1980). Kimberlites: their relation to mantle hotspots. *Earth and Planetary Science Letters*, *50*(1), 260–274.

Currie, C. A., Huismans, R. S., & Beaumont, C. (2008). Thinning of continental backarc lithosphere by flow-induced gravitational instability. *Earth and Planetary Science Letters*, *269*(3–4), 436–447.

Currie, C. A., & Hyndman, R. D. (2006). The thermal structure of subduction zone back arcs. *Journal of Geophysical Research: Solid Earth*, *111*(8), 1–22. https://doi.org/10.1029/2005JB004024

Currie, C. A., & van Wijk, J. (2016). How craton margins are preserved: Insights from geodynamic models. *Journal of Geodynamics*, *100*, 144–158.

Dahlen, F. A., Hung, S.-H., & Nolet, G. (2000). Fréchet kernels for finite-frequency traveltimes-I. Theory. *Geophysical Journal International*, *141*(1), 157–174. https://doi.org/10.1046/j.1365-246X.2000.00070.x

Dalton, C. A., Gaherty, J. B., & Courtier, A. M. (2011). Crustal V<inf>S</inf> structure in northwestern Canada: Imaging the Cordillera-craton transition with ambient noise tomography. *Journal of Geophysical Research: Solid Earth*, *116*(12), 1–30. https://doi.org/10.1029/2011JB008499

Darbyshire, F. A., Bastow, I. D., Petrescu, L., Gilligan, A., & Thompson, D. A. (2017). A tale of two orogens: Crustal processes in the Proterozoic Trans-Hudson and Grenville Orogens, eastern Canada. *Tectonics*, *36*(8), 1633–1659.

Darbyshire, F. A., Eaton, D. W., & Bastow, I. D. (2013). Seismic imaging of the lithosphere beneath Hudson Bay: Episodic growth of the Laurentian mantle keel. *Earth and Planetary Science Letters*, *373*, 179–193.

Dave, R., & Li, A. (2016). Destruction of the Wyoming craton: Seismic evidence and geodynamic processes. *Geology*, *44*(11), 883–886.

Davies, R. M., Griffin, W. L., O'Reilly, S. Y., & McCandless, T. E. (2004). Inclusions in diamonds from the K14 and K10 kimberlites, Buffalo Hills, Alberta, Canada: Diamond growth in a plume? *Lithos*, *77*(1–4 SPEC. ISS.), 99–111. https://doi.org/10.1016/j.lithos.2004.04.008

Davis, W. J., Berman, R., Kjarsgaard, B., & Ross, G. M. (1995). U–Pb geochronology and isotopic studies of crustal xenoliths from the Archean Medicine Hat block, northern Montana and southern Alberta: Paleoproterozoic reworking of Archean crust. In *Alberta Basement Transects Workshop: Lithoprobe Report* (Vol. 47, pp. 330–335).

Davis, W. J., Jones, A. G., Bleeker, W., & Grütter, H. (2003). Lithosphere development in the Slave craton: a linked crustal and mantle perspective. *Lithos*, *71*(2–4), 575–589.

de Azevedo, P. A., Rocha, M. P., Soares, J. E. P., & Fuck, R. A. (2015). Thin lithosphere between the Amazonian and São Francisco cratons, in central Brazil, revealed by

seismic P-wave tomography. *Geophysical Journal International*, *201*(1), 61–69.

De, S. K., Chacko, T., Creaser, R. A., & Muehlenbachs, K. (2000). Geochemical and Nd-Pb-O isotope systematics of granites from the Taltson Magmatic Zone, NE Alberta: Implications for early Proterozoic tectonics in western Laurentia. *Precambrian Research*, *102*(3–4), 221–249. https://doi.org/10.1016/S0301-9268(00)00068-1

DeCelles, P. G. (2004). Late Jurassic to Eocene evolution of the Cordilleran thrust belt and foreland basin system, western USA. *American Journal of Science*, *304*(2), 105–168.

DeCelles, P. G., Ducea, M. N., Kapp, P., & Zandt, G. (2009). Cyclicity in Cordilleran orogenic systems. *Nature Geoscience*, *2*(4), 251.

Deschamps, F., Trampert, J., & Snieder, R. (2002). Anomalies of temperature and iron in the uppermost mantle inferred from gravity data and tomographic models. *Physics of the Earth and Planetary Interiors*, *129*(3), 245–264.

Dewey, J. F. (1977). Suture zone complexities: a review. *Tectonophysics*, *40*(1–2), 53–67.

Dickinson, W. R. (2004). Evolution of the North American Cordillera. *Annual Review of Earth and Planetary Sciences*, *32*(1), 13–45. https://doi.org/10.1146/annurev.earth.32.101802.120257

Dickinson, W. R. (2009). Anatomy and global context of the North American Cordillera Anatomy and global context of the North American Cordillera, *1204*(01), 1–29. https://doi.org/10.1130/2009.1204(01).For

Dueker, K. G., & Sheehan, A. F. (1997). Mantle discontinuity structure from midpoint stacks of converted P to S waves across the Yellowstone hotspot track. *Journal of Geophysical Research: Solid Earth*. https://doi.org/10.1029/96JB03857

Dziewonski, A., Bloch, S., & Landisman, M. (1969). A technique for the analysis of transient seismic signals. *Bulletin of the Seismological Society of America*, *59*(1), 427–444.

Dziewonski, A. M., & Anderson, D. L. (1981). Preliminary reference Earth model. *Physics of the Earth and Planetary Interiors*, *25*(4), 297–356.

Eaton, D. W., & Hope, J. (2003). Structure of the crust and upper mantle of the Great Slave Lake shear zone, northwestern Canada, from teleseismic analysis and gravity modelling. *Canadian Journal of Earth Sciences*, *40*(9), 1203–1218. https://doi.org/10.1139/e03-038

Eaton, D. W., Ross, G. M., & Clowes, R. M. (1999). Seismic-reflection and potential-field studies of the Vulcan structure, western Canada: A Paleoproterozoic Pyrenees? *Journal of Geophysical Research*, *104*(B10), 23255. https://doi.org/10.1029/1999JB900204

Eaton, D. W., Ross, G. M., Cook, F. a, & VanderVelden, a. (2000). Seismic imaging of the upper mantle beneath the Rocky Mountain foreland, southwestern Alberta. *Canadian Journal of Earth Sciences*, *37*, 1493–1507. https://doi.org/10.1139/e00-068

Eaton, D. W., Ross, G. M., & Hope, J. (1999). The rise and fall of a cratonic arch: A regional seismic perspective on the Peace River Arch, Alberta. *Bulletin of Canadian*

*Petroleum Geology*, *47*(4), 346–361.

Eaton, W., & Cassidy, J. F. (1996). A relic Proterozoic subduction zone in western Canada: New evidence from seismic reflection and receiver function data. *Geophysical Research Letters*, *23*(25), 3791–3794.

Efron, B., & Tibshirani, R. (1986). Bootstrap methods for standard errors, confidence intervals, and other measures of statistical accuracy. *Statistical Science*, 54–75.

Evenchick, C. (2007). A synthesis of the Jurassic–Cretaceous tectonic evolution of the central and southeastern Canadian Cordillera: Exploring links across the orogen. *... Society of America ...*, *i*(06), 117–145. https://doi.org/10.1130/2007.2433(06).For

Faure, S. (2010). World Kimberlites CONSOREM Database (Version 3). *Consortium de Recherche En Exploration Minerale CONSOREM, Universite Du Quebece Montreal.—2010.—Www. Consorem. Ca*.

Feng, M., Assumpçao, M., & Van der Lee, S. (2004). Group-velocity tomography and lithospheric S-velocity structure of the South American continent. *Physics of the Earth and Planetary Interiors*, *147*(4), 315–331.

Fischer, K. M., Ford, H. A., Abt, D. L., & Rychert, C. A. (2010). The lithosphere-asthenosphere boundary. *Annual Review of Earth and Planetary Sciences*, *38*, 551–575.

Fishwick, S., Kennett, B. L. N., & Reading, A. M. (2005). Contrasts in lithospheric structure within the Australian craton—insights from surface wave tomography. *Earth and Planetary Science Letters*, *231*(3–4), 163–176.

Flowers, R. M., Bowring, S. A., Mahan, K. H., Williams, M. L., & Williams, I. S. (2008). Stabilization and reactivation of cratonic lithosphere from the lower crustal record in the western Canadian shield. *Contributions to Mineralogy and Petrology*, *156*(4), 529.

Flowers, R. M., Bowring, S. A., & Williams, M. L. (2006). Timescales and significance of high-pressure, high-temperature metamorphism and mafic dike anatexis, Snowbird tectonic zone, Canada. *Contributions to Mineralogy and Petrology*, *151*(5), 558–581. https://doi.org/10.1007/s00410-006-0066-7

Foley, S. F. (2008). Rejuvenation and erosion of the cratonic lithosphere. *Nature Geoscience*, *1*(8), 503.

Forte, A. M., & Perry, H. K. C. (2000). Geodynamic evidence for a chemically depleted continental tectosphere. *Science*, *290*(5498), 1940–1944.

Foster, D. A., Mueller, P. A., Mogk, D. W., Wooden, J. L., & Vogl, J. J. (2006). Proterozoic evolution of the western margin of the Wyoming craton: implications for the tectonic and magmatic evolution of the northern Rocky Mountains. *Canadian Journal of Earth Sciences*, *43*(10), 1601–1619. https://doi.org/10.1139/e06-052

Frassetto, A., & Thybo, H. (2013). Receiver function analysis of the crust and upper mantle in Fennoscandia – isostatic implications. *Earth and Planetary Science Letters*, *381*, 234–246. https://doi.org/10.1016/j.epsl.2013.07.001

Frederiksen, A. W., Bollmann, T., Darbyshire, F., & Van der Lee, S. (2013).

Modification of continental lithosphere by tectonic processes: A tomographic image of central North America. *Journal of Geophysical Research: Solid Earth*, *118*(3), 1051–1066.

Frederiksen, A. W., Bostock, M. G., & Cassidy, J. F. (2001). S-wave velocity structure of the Canadian upper mantle. *Physics of the Earth and Planetary Interiors*, *124*(3–4), 175–191. https://doi.org/10.1016/S0031-9201(01)00194-7

Frederiksen, A. W., Bostock, M. G., VanDecar, J. C., & Cassidy, J. F. (1998). Seismic structure of the upper mantle beneath the northern Canadian Cordillera from teleseismic travel-time inversion. *Tectonophysics*, *294*(1–2), 43–55. https://doi.org/10.1016/S0040-1951(98)00095-X

Frohlich, C. (1998). *Fundamentals of geophysics*. *Eos, Transactions American Geophysical Union* (Vol. 79). Cambridge university press. https://doi.org/10.1029/98EO00138

Furlong, K. P., & Fountain, D. M. (1986). Continental Crustal Underplating' Thermal Considerations And Seismic-Petrologic Consequences. *Journal O¾ Geophysical Research*, *91*(10), 8285–8294. https://doi.org/10.1029/JB091iB08p08285

Furlong, K. P., Spakman, W., & Wortel, R. (1995). Thermal structure of the continental lithosphere: constraints from seismic tomography. *Tectonophysics*, *244*(1–3), 107–117.

Fyfe, W. S. (1992). Magma Underplating of Continental-Crust. *Journal of Volcanology and Geothermal Research*, *50*(1–2), 33–40.

Gabrielse, H. (1985). Major dextral transcurrent displacements along the Northern Rocky Mountain Trench and related lineaments in north-central British Columbia. *Geological Society of America Bulletin*, *96*(1), 1–14.

Ganley, D. C., & Cumming, G. L. (1974). A seismic reflection model of the crust near Edmonton, Alberta. *Canadian Journal of Earth Sciences*, *11*(1), 101–109.

Gao, S., Rudnick, R. L., Carlson, R. W., McDonough, W. F., & Liu, Y.-S. (2002). Re–Os evidence for replacement of ancient mantle lithosphere beneath the North China craton. *Earth and Planetary Science Letters*, *198*(3), 307–322.

Gao, S. S., & Liu, K. H. (2014). Mantle transition zone discontinuities beneath the contiguous United States. *Journal of Geophysical Research: Solid Earth*, *119*(8), 6452–6468.

Gerya, T. (2014). Precambrian geodynamics: concepts and models. *Gondwana Research*, *25*(2), 442–463.

Gibb, R. A., & Walcott, R. I. (1971). A Precambrian suture in the Canadian Shield. *Earth and Planetary Science Letters*, *10*(4), 417–422.

Gilbert, H. (2012). Crustal structure and signatures of recent tectonism as influenced by ancient terranes in the western United States. *Geosphere*, *8*(1), 141–157.

Giletti, B. J. (1966). Isotopic ages from southwestern Montana. *Journal of Geophysical Research*, *71*(16), 4029–4036.

Gilligan, A., Bastow, I. D., & Darbyshire, F. A. (2016). Seismological structure of the 1.8

Ga Trans-Hudson Orogen of North America. *Geochemistry, Geophysics, Geosystems*, *17*(6), 2421–2433.

Godey, S., Deschamps, F., Trampert, J., & Snieder, R. (2004). Thermal and compositional anomalies beneath the North American continent. *Journal of Geophysical Research: Solid Earth*, *109*(B1).

Godin, L., Grujic, D., Law, R. D., & Searle, M. P. (2006). Channel flow, ductile extrusion and exhumation in continental collision zones: an introduction. Geological Society of London.

Goes, S., Armitage, J., Harmon, N., Smith, H., & Huismans, R. (2012). Low seismic velocities below mid-ocean ridges: Attenuation versus melt retention. *Journal of Geophysical Research: Solid Earth*, *117*(B12).

Goes, S., Govers, R., & Vacher, P. (2000). Shallow mantle temperatures under Europe from P and S wave tomography. *Journal of Geophysical Research: Solid Earth*, *105*(B5), 11153–11169.

Goes, S., & van der Lee, S. (2002). Thermal structure of the North American uppermost mantle inferred from seismic tomography. *Journal of Geophysical Research: Solid Earth*, *107*(B3).

Gorman, A. R., Clowes, R. M., Ellis, R. M., Henstock, T. J., Spence, G. D., Keller, G. R., … Miller, K. C. (2002). Deep Probe: imaging the roots of western North America. *Canadian Journal of Earth Sciences*, *39*(3), 375–398. https://doi.org/10.1139/e01-064

Gray, R., & Pysklywec, R. N. (2010). Geodynamic models of Archean continental collision and the formation of mantle lithosphere keels. *Geophysical Research Letters*, *37*(19).

Griffin, W. L., O'Reilly, S. Y., Abe, N., Aulbach, S., Davies, R. M., Pearson, N. J., … Kivi, K. (2003). The origin and evolution of Archean lithospheric mantle. *Precambrian Research*, *127*(1), 19–41.

Griffin, W. L., O'reilly, S. Y., Afonso, J. C., & Begg, G. C. (2008). The composition and evolution of lithospheric mantle: a re-evaluation and its tectonic implications. *Journal of Petrology*, *50*(7), 1185–1204.

Gu, Y. J., Chen, Y., Dokht, R. M. H., & Wang, R. (2018). Precambrian tectonic discontinuities in western Laurentia: Broadband seismological perspectives on the Snowbird and Great Falls tectonic zones. *Tectonics*.

Gu, Y. J., Okeler, A., Shen, L., & Contenti, S. (2011). The Canadian Rockies and Alberta Network (CRANE): New constraints on the Rockies and Western Canada Sedimentary Basin. *Seismological Research Letters*, *82*(4), 575–588. https://doi.org/10.1785/gssrl.82.4.575

Gu, Y. J., & Shen, L. (2012). Microseismic noise from large ice-covered lakes? *Bulletin of the Seismological Society of America*. https://doi.org/10.1785/0120100010

Gu, Y. J., & Shen, L. (2015). Noise correlation tomography of Southwest Western Canada Sedimentary Basin. *Geophysical Journal International*, *202*(1), 142–162. https://doi.org/10.1093/gji/ggv100

Gu, Y. J., Zhang, Y., Sacchi, M. D., Chen, Y., & Contenti, S. (2015). Sharp mantle transition from cratons to Cordillera in southwestern Canada. *Journal of Geophysical Research: Solid Earth*, *120*(7), 5051–5069. https://doi.org/10.1002/2014JB011802

Gurrola, H., Baker, G. E., & Minster, J. B. (1995). Simultaneous time-domain deconvolution with application to the computation of receiver functions. *Geophysical Journal International*. https://doi.org/10.1111/j.1365-246X.1995.tb01837.x

Hammer, P. T. C., Clowes, R. M., Cook, F. A., Vasudevan, K., & van der Velden, A. J. (2011). The big picture: A lithospheric cross section of the North American continent. *GSA Today*, *21*(6), 4–10.

Hanmer, S., Parrish, R., Williams, M., & Kopf, C. (1994). Striding-Athabasca mylonite zone: complex Archean deep-crustal deformation in the East Athabasca mylonite triangle, northern Saskatchewan. *Canadian Journal of Earth Sciences*, *31*(8), 1287–1300.

Hanmer, S., & Relf, C. (2000). Western Churchill NATMAP Project: new results and potential significance. *Proceedings of GeoCanada*, *4*.

Hanmer, S., Williams, M., & Kopf, C. (1995). Striding-Athabasca mylonite zone: implications for the Archean and Early Proterozoic tectonics of the western Canadian Shield. *Canadian Journal of Earth Sciences*, *32*(2), 178–196. https://doi.org/10.1139/e95-015

Hardebol, N. J., Pysklywec, R. N., & Stephenson, R. (2012). Small-scale convection at a continental back-arc to craton transition: Application to the southern Canadian Cordillera. *Journal of Geophysical Research: Solid Earth*, *117*(1), 1–18. https://doi.org/10.1029/2011JB008431

Haschke, M., & Günther, A. (2003). Balancing crustal thickening in arcs by tectonic vs. magmatic means. *Geology*, *31*(11), 933–936.

Hayden, R. J., & Wehrenberg, J. P. (1960). Dating of igneous and metamorphic rocks in Western Montana. *The Journal of Geology*, *68*(1), 94–97.

Heaman, L. M. (1994). 2.45 Ga global mafic magmatism: Earth's oldest superplume. In *8th International Conference on Geochronology, Cosmochronology and Isotope Geology. Edited by MA Lanphere, GB Dalrymple, and BD Turrins. United States Geological Survey, Circular* (Vol. 1107, p. 132).

Heaman, L. M., Kjarsgaard, B. A., & Creaser, R. A. (2004). The temporal evolution of North American kimberlites. *Lithos*, *76*(1–4), 377–397.

Heaman, L. M., & LeCheminant, A. N. (1993). Paragenesis and U-Pb systematics of baddeleyite (ZrO2). *Chemical Geology*, *110*(1–3), 95–126.

Helmstaedt, H., & Schulze, D. J. (1989). Southern African kimberlites and their mantle sample: implications for Archean tectonics and lithosphere evolution. *Kimberlites and Related Rocks*, *1*, 358–368.

Henstock, T. J., Levander, A., Snelson, C. M., Keller, G. R., Miller, K. C., Harder, S. H., … Humphreys, E. D. (1998). Probing the Archean and Proterozoic lithosphere

of western North America. *GSA Today*, *8*(7), 1–5. https://doi.org/10.1130/1052-5173-19.1.40

Herrmann, R. B. (2013). Computer Programs in Seismology: An Evolving Tool for Instruction and Research. *Seismological Research Letters*. https://doi.org/10.1785/0220110096

Hieronymus, C. F., & Goes, S. (2010). Complex cratonic seismic structure from thermal models of the lithosphere: effects of variations in deep radiogenic heating. *Geophysical Journal International*, *180*(3), 999–1012.

Hieronymus, C. F., Shomali, Z. H., & Pedersen, L. B. (2007). A dynamical model for generating sharp seismic velocity contrasts underneath continents: Application to the Sorgenfrei-Tornquist Zone. *Earth and Planetary Science Letters*, *262*(1–2), 77–91. https://doi.org/10.1016/j.epsl.2007.07.043

Hildebrand, R. S. (2009). Did westward subduction cause Cretaceous–Tertiary orogeny in the North American Cordillera? *Geological Society of America Special Papers*, *457*, 1–71.

Hildebrand, R. S., & Whalen, J. B. (2014). Arc and slab-failure magmatism in Cordilleran Batholiths I–The Cretaceous Coastal Batholith of Peru and its role in South American orogenesis and hemispheric subduction flip. *Geoscience Canada*, *41*(3), 255–282.

Hoffman, P. (1990). Geological constraints on the origin of the mantle root beneath the Canadian shield. *Phil. Trans. R. Soc. Lond. A*, *331*(1620), 523–532.

Hoffman, P. F. (1988). United Plates of America, The Birth of a Craton: Early Proterozoic Assembly and Growth of Laurentia. *Annual Review of Earth and Planetary Sciences*, *16*(1), 543–603. https://doi.org/10.1146/annurev.ea.16.050188.002551

Hoffman, P. F. (1989). Precambrian geology and tectonic history of North America. *The Geology of North America*, *A*, 447–512.

Hoffman, P. F. (1991). Did the breakout of Laurentia turn Gondwanaland inside-out? *Science*, *252*(5011), 1409–1412.

Holm, D., & Schneider, D. (2002). 40Ar/39Ar evidence for ca. 1800 Ma tectonothermal activity along the Great Falls tectonic zone, central Montana. *Canadian Journal of Earth Sciences*, *39*(12), 1719–1728.

Hope, J., & Eaton, D. (2002). Crustal structure beneath the Western Canada Sedimentary Basin: constraints from gravity and magnetic modelling. *Canadian Journal of Earth Sciences*, *39*(3), 291–312. https://doi.org/10.1139/e01-060

Hopper, E., & Fischer, K. M. (2015). The meaning of midlithospheric discontinuities: A case study in the northern US craton. *Geochemistry, Geophysics, Geosystems*, *16*(12), 4057–4083.

Hudson, J. A., & Heritage, J. R. (1981). The use of the Born approximation in seismic scattering problems. *Geophysical Journal International*, *66*(1), 221–240.

Humphreys, E., & Clayton, R. W. (1988). Adaptation of back projection tomography to seismic travel time problems. *Journal of Geophysical Research: Solid Earth*,

*93*(B2), 1073–1085.

Humphreys, E. D., Schmandt, B., Bezada, M. J., & Perry-Houts, J. (2015). Recent craton growth by slab stacking beneath Wyoming. *Earth and Planetary Science Letters*, *429*, 170–180.

Hung, S.-H., Dahlen, F. A., & Nolet, G. (2000). Fréchet kernels for finite-frequency traveltimeséII. Examples. *Geophysical Journal International*, *141*(1), 175–203.

Hung, S.-H., Dahlen, F. A., & Nolet, G. (2001). Wavefront healing: a banana–doughnut perspective. *Geophysical Journal International*, *146*(2), 289–312.

Hung, S. H., Chen, W. P., & Chiao, L. Y. (2011). A data-adaptive, multiscale approach of finite-frequency, traveltime tomography with special reference to P and S wave data from central Tibet. *Journal of Geophysical Research: Solid Earth*, *116*(6), 1–26. https://doi.org/10.1029/2010JB008190

Hung, S. H., Shen, Y., & Chiao, L. Y. (2004). Imaging seismic velocity structure beneath the Iceland hot spot: A finite frequency approach. *Journal of Geophysical Research B: Solid Earth*, *109*(8), 1–16. https://doi.org/10.1029/2003JB002889

Hyndman, R. D. (2010). The consequences of Canadian Cordillera thermal regime in recent tectonics and elevation: a review This article is one of a series of papers published in this Special Issue on the theme Lithoprobe-parameters, processes, and the evolution of a continent. G. *Canadian Journal of Earth Sciences*, *47*(5), 621–632.

Hyndman, R. D., & Currie, C. A. (2011). Why is the North America Cordillera high? Hot backarcs, thermal isostasy, and mountain belts. *Geology*, *39*(8), 783–786. https://doi.org/10.1130/G31998.1

Hyndman, R. D., Currie, C. A., Mazzotti, S., & Frederiksen, A. (2009). Temperature control of continental lithosphere elastic thickness, Te vs Vs. *Earth and Planetary Science Letters*, *277*(3–4), 539–548. https://doi.org/10.1016/j.epsl.2008.11.023

Hyndman, R. D., Currie, C. A., & Mazzotti, S. P. (2005). Subduction zone backarcs, mobile belts, and orogenic heat. *GSA Today*, *15*(2), 4–10.

Hyndman, R. D., & Lewis, T. J. (1999). Geophysical consequences of the Cordillera-Craton thermal transition in southwestern Canada. *Tectonophysics*, *306*(3–4), 397–422. https://doi.org/10.1016/S0040-1951(99)00068-2

Iyer, H. M., & Hirahara, K. (1993). *Seismic tomography: Theory and practice*. Springer Science & Business Media.

Jaques, A. L., & Milligan, P. R. (2004). Patterns and controls on the distribution of diamondiferous intrusions in Australia. *Lithos*, *77*(1), 783–802.

Jaupart, C., Mareschal, J.-C., Guillou-Frottier, L., & Davaille, A. (1998). Heat flow and thickness of the lithosphere in the Canadian Shield. *Journal of Geophysical Research: Solid Earth*, *103*(B7), 15269–15286.

Jobin, D. M., Véronneau, M., & Miles, W. (2017). *Isostatic residual gravity anomaly map, Canada/Carte des anomalies isostatiques résiduelles du champ de gravité, Canada*. *Geological Survey of Canada, Open File 8076*.

Johnston, S. T. (2001). The Great Alaskan Terrane Wreck: reconciliation of paleomagnetic and geological data in the northern Cordillera. *Earth and Planetary Science Letters*, *193*(3), 259–272.

Johnston, S. T. (2008). The Cordilleran Ribbon Continent of North America. *Annu. Rev. Earth Planet. Sci*, *36*(January), 495–530. https://doi.org/10.1146/annurev.earth.36.031207.124331

Johnston, S. T., & Borel, G. D. (2007). The odyssey of the Cache Creek terrane, Canadian Cordillera: Implications for accretionary orogens, tectonic setting of Panthalassa, the Pacific superwell, and break-up of Pangea. *Earth and Planetary Science Letters*, *253*(3), 415–428.

Johnston, S. T., & Gutierrez-Alonso, G. (2010). The North American Cordillera and West European Variscides: contrasting interpretations of similar mountain systems. *Gondwana Research*, *17*(2), 516–525.

Jordan, T. H. (1975). The continental tectosphere. *Reviews of Geophysics*, *13*(3), 1–12.

Jordan, T. H. (1978). Composition and development of the continental tectosphere. *Nature*, *274*(5671), 544–548.

Jordan, T. H. (1979). Mineralogies, densities and seismic velocities of garnet lherzolites and their geophysical implications. *The Mantle Sample: Inclusion in Kimberlites and Other Volcanics*, *16*, 1–14.

Jordan, T. H. (1988). Structure and formation of the continental tectosphere. *Journal of Petrology*, (1), 11–37.

Julià, J., Herrmann, R. B., Ammon, C. J., & Akinci, A. (2004). Evaluation of deep sediment velocity structure in the New Madrid Seismic Zone. *Bulletin of the Seismological Society of America*, *94*(1), 334–340.

Kanasewich, E. R. (1968). Precambrian rift: genesis of strata-bound ore deposits. *Science*, *161*(3845), 1002–1005.

Kanasewich, E. R., Clowes, R. M., & McCloughan, C. H. (1969). A buried Precambrian rift in western Canada. *Tectonophysics*, *8*(4–6), 513–527.

Kanasewich, E. R., & Cumming, G. L. (1965). Near-vertical-incidence seismic reflections from the "Conrad" discontinuity. *Journal of Geophysical Research*, *70*(14), 3441–3446.

Kao, H., Behr, Y., Currie, C. A., Hyndman, R., Townend, J., Lin, F., … He, J. (2013). Ambient seismic noise tomography of Canada and adjacent regions: Part I. Crustal structures. *Journal of Geophysical Research: Solid Earth*, *118*(11), 5865–5887.

Karlstrom, K. E., Whitmeyer, S. J., Dueker, K., Williams, M. L., Bowring, S. A., Levander, A., … Keller, G. R. (2005). Synthesis of results from the CD-ROM experiment: 4-D image of the lithosphere beneath the Rocky mountains and implications for understanding the evolution of continental lithosphere. *Geophysical Monograph Series*, *154*, 421–441. https://doi.org/10.1029/154GM31

Karlstrom, L., Lee, C., & Manga, M. (2014). The role of magmatically driven lithospheric thickening on arc front migration. *Geochemistry, Geophysics,*

*Geosystems*, *15*(6), 2655–2675.

Kennett, B. L. N., Engdahl, E. R., & Buland, R. (1995). Constraints on seismic velocities in the Earth from traveltimes. *Geophysical Journal International*, *122*(1), 108–124.

Kind, R., Yuan, X., & Kumar, P. (2012). Seismic receiver functions and the lithosphere–asthenosphere boundary. *Tectonophysics*, *536*, 25–43.

King, S. D. (2005). Archean cratons and mantle dynamics. *Earth and Planetary Science Letters*, *234*(1), 1–14.

Landés, M., Hubans, F., Shapiro, N. M., Paul, A., & Campillo, M. (2010). Origin of deep ocean microseisms by using teleseismic body waves. *Journal of Geophysical Research: Solid Earth*. https://doi.org/10.1029/2009JB006918

Langston, C. A. (1977). The effect of planar dipping structure on source and receiver responses for constant ray parameter. *Bulletin of the Seismological Society of America*.

Langston, C. A. (1979). Structure under Mount Rainier, Washington, inferred from teleseismic body waves. *Journal of Geophysical Research: Solid Earth*, *84*(B9), 4749–4762.

Laske, G., Masters, G., Ma, Z., & Pasyanos, M. (2013). Update on CRUST1. 0—A 1-degree global model of Earth's crust. In *Geophys. Res. Abstr* (Vol. 15, p. 2658).

Lawrence, J. F., & Prieto, G. A. (2011). Attenuation tomography of the western United States from ambient seismic noise. *Journal of Geophysical Research: Solid Earth*, *116*(B6).

Leckie, D. A., Kjarsgaard, B. A., Bloch, J., McIntyre, D., McNeil, D., Stasiuk, L., & Heaman, L. (1997). Emplacement and reworking of Cretaceous, diamond-bearing, crater facies kimberlite of central Saskatchewan, Canada. *Geological Society of America Bulletin*, *109*(8), 1000–1020.

Lee, C.-T. A., Luffi, P., & Chin, E. J. (2011). Building and destroying continental mantle. *Annual Review of Earth and Planetary Sciences*, *39*, 59–90.

Lee, C. A. (2003). Compositional variation of density and seismic velocities in natural peridotites at STP conditions: Implications for seismic imaging of compositional heterogeneities in the upper mantle. *Journal of Geophysical Research: Solid Earth*, *108*(B9).

Lekić, V., & Fischer, K. M. (2014). Contrasting lithospheric signatures across the western United States revealed by Sp receiver functions. *Earth and Planetary Science Letters*, *402*, 90–98.

Lemieux, S., Ross, G. M., & Cook, F. a. (2000). Crustal geometry and tectonic evolution of the Archean crystalline basement beneath the southern Alberta Plains, from new seismic reflection and potential-field studies. *Canadian Journal of Earth Sciences*, *37*(11), 1473–1491. https://doi.org/10.1139/e00-065

Levander, A., & Miller, M. S. (2012). Evolutionary aspects of lithosphere discontinuity structure in the Western U.S. *Geochemistry, Geophysics, Geosystems*, *13*(1), 1–22. https://doi.org/10.1029/2012GC004056

Levander, A., Niu, F., Symes, W. W., & Nolet, G. (2005). Imaging teleseismic P to S scattered waves using the Kirchhoff integral. *GEOPHYSICAL MONOGRAPH-AMERICAN GEOPHYSICAL UNION*, *157*, 149.

Levin, V., & Park, J. (1997). Crustal anisotropy in the Ural Mountains foredeep from teleseismic receiver functions. *Geophysical Research Letters*, *24*(11), 1283–1286.

Levshin, A. L., Pisarenko, V. F., & Pogrebinsky, G. A. (1972). Frequency-time analysis of oscillations. In *Annales de Geophysique* (Vol. 28, p. 211–+). EDITIONS CNRS 20/22 RUE ST. AMAND, 75015 PARIS, FRANCE.

Levshin, A., Ratnikova, L., & Berger, J. (1992). Peculiarities of surface-wave propagation across central Eurasia. *Bulletin of the Seismological Society of America*. https://doi.org/10.1016/0031-9201(83)90119-X

Lewis, T. J., Hyndman, R. D., & Fluck, P. (2003). Heat flow, heat generation, and crustal temperatures in the northern Canadian Cordillera: Thermal control of tectonics. *Journal of Geophysical Research-Solid Earth*, *108*(B6), 18. https://doi.org/2316 Artn 2316

Lewry, J. F., Hajnal, Z., Green, A., Lucas, S. B., White, D., Stauffer, M. R., … Clowes, R. (1994). Structure of a Paleoproterozoic Continent Continent Collision Zone - a Lithoprobe Seismic-Reflection Profile Across the Trans-Hudson Orogen, Canada. *Tectonophysics*, *232*(1–4), 143–160.

Li, A., & Burke, K. (2006). Upper mantle structure of southern Africa from Rayleigh wave tomography. *Journal of Geophysical Research: Solid Earth*, *111*(B10).

Li, A., Fischer, K. M., Wysession, M. E., & Clarke, T. J. (1998). Mantle discontinuities and temperature under the North American continental keel. *Nature*, *395*(6698), 160.

Li, X., Kind, R., Priestley, K., Sobolev, S. V, Tilmann, F., Yuan, X., & Weber, M. (2000). Mapping the Hawaiian plume conduit with converted seismic waves. *Nature*, *405*(6789), 938.

Ligorría, J. P., & Ammon, C. J. (1999). Iterative deconvolution and receiver-function estimation. *Bulletin of the Seismological Society of America*.

Lin, F.-C., Moschetti, M. P., & Ritzwoller, M. H. (2008). Surface wave tomography of the western United States from ambient seismic noise: Rayleigh and Love wave phase velocity maps. *Geophysical Journal International*, *173*(1), 281–298.

Lin, F.-C., Ritzwoller, M. H., Yang, Y., Moschetti, M. P., & Fouch, M. J. (2011). Complex and variable crustal and uppermost mantle seismic anisotropy in the western United States. *Nature Geoscience*, *4*(1), 55.

Lin, F.-C., Tsai, V. C., & Schmandt, B. (2014). 3-D crustal structure of the western United States: application of Rayleigh-wave ellipticity extracted from noise cross-correlations. *Geophysical Journal International*, *198*(2), 656–670.

Lin, F., Schmandt, B., & Tsai, V. C. (2012). Joint inversion of Rayleigh wave phase velocity and ellipticity using USArray: Constraining velocity and density structure in the upper crust. *Geophysical Research Letters*, *39*(12).

Liu, J., Riches, A. J. V, Pearson, D. G., Luo, Y., Kienlen, B., Kjarsgaard, B. A., … Armstrong, J. P. (2016). Age and evolution of the deep continental root beneath the

central Rae craton, northern Canada. *Precambrian Research*, *272*, 168–184.

Liu, L., & Gao, S. S. (2018). Lithospheric layering beneath the contiguous United States constrained by S-to-P receiver functions. *Earth and Planetary Science Letters*, *495*, 79–86.

Liu, L., Gurnis, M., Seton, M., Saleeby, J., Müller, R. D., & Jackson, J. M. (2010). The role of oceanic plateau subduction in the Laramide orogeny. *Nature Geoscience*, *3*(5), 353.

Liu, L., Spasojević, S., & Gurnis, M. (2008). Reconstructing Farallon plate subduction beneath North America back to the Late Cretaceous. *Science*, *322*(5903), 934–938.

Liu, Q., & Gu, Y. J. (2012). Seismic imaging: From classical to adjoint tomography. *Tectonophysics*, *566*, 31–66.

Liu, Q., & Tromp, J. (2006). Finite-frequency kernels based on adjoint methods. *Bulletin of the Seismological Society of America*, *96*(6), 2383–2397.

Lobkis, O. I., & Weaver, R. L. (2001). On the emergence of the Green's function in the correlations of a diffuse field. *The Journal of the Acoustical Society of America*, *110*(6), 3011–3017.

Lowry, A. R., & Pérez-Gussinyé, M. (2011). The role of crustal quartz in controlling Cordilleran deformation. *Nature*, *471*(7338), 353.

Lucas, S. B., Greenf, A., Hajnalit, Z., & White, D. (1993). Deep seismic profile across. *Nature*, *363*, 339.

Lynn, C. E., Cook, F. A., & Hall, K. W. (2005). Tectonic significance of potential-field anomalies in western Canada: results from the Lithoprobe SNORCLE transect. *Canadian Journal of Earth Sciences*, *42*(6), 1239–1255. https://doi.org/10.1139/e05-037

MacRae, N. D., Armitage, A. E., Miller, A. R., Roddick, J. C., Jones, A. L., Mudry, M. P., … Richardson, K. A. (1996). The diamondiferous Akluilak lamprophyre dyke, Gibson Lake area, NWT. *Searching for Diamonds in Canada. Edited by AN LeCheminant, DG Richardson, RNW DiLabio, and KA Richardson. Geological Survey of Canada, Open File*, *3228*, 101–107.

Mahan, K. H., Schulte-Pelkum, V., Blackburn, T. J., Bowring, S. A., & Dudas, F. O. (2012). Seismic structure and lithospheric rheology from deep crustal xenoliths, central Montana, USA. *Geochemistry, Geophysics, Geosystems*, *13*(10).

Mahan, K. H., & Williams, M. L. (2005). Reconstruction of a large deep-crustal terrane: Implications for the Snowbird tectonic zone and early growth of Laurentia. *Geology*, *33*(5), 385–388. https://doi.org/10.1130/G21273.1

Majorowicz, J. A. (2018). Heat flow–heat production relationship not found: what drives heat flow variability of the Western Canadian foreland basin? *International Journal of Earth Sciences*, *107*(1), 5–18. https://doi.org/10.1007/s00531-016-1352-x

Majorowicz, J., Chan, J., Crowell, J., Gosnold, W., Heaman, L. M., Kück, J., … Walsh, N. (2014). The first deep heat flow determination in crystalline basement rocks beneath the Western Canadian Sedimentary Basin. *Geophysical Journal*

*International*, *197*(2), 731–747.

McDonough, M. R., McNicoll, V. J., Schetselaar, E. M., & Grover, T. W. (2000). Geochronological and kinematic constraints on crustal shortening and escape in a two-sided oblique-slip collisional and magmatic orogen, Paleoproterozoic Taltson magmatic zone, northeastern Alberta. *Canadian Journal of Earth Sciences*, *37*(11), 1549–1573. https://doi.org/10.1139/e00-089

McKenzie, D., & Priestley, K. (2008). The influence of lithospheric thickness variations on continental evolution. *Lithos*, *102*(1–2), 1–11.

McLellan, M., Schaeffer, A. J., & Audet, P. (2018). Structure and fabric of the crust and uppermost mantle in the northern Canadian Cordillera from Rayleigh-wave tomography. *Tectonophysics*.

McMechan, R. D., & Price, R. A. (1980). Reappraisal of a reported unconformity in the Paleogene (Oligocene) Kishenehn Formation: Implications for Cenozoic tectonics in the Flathead Valley graben, southeastern British Columbia. *Bulletin of Canadian Petroleum Geology*, *28*(1), 37–45.

McNicoll, V. J., Thériault, R. J., & McDonough, M. R. (2000). Taltson basement gneissic rocks: U-Pb and Nd isotopic constraints on the basement to the Paleoproterozoic Taltson magmatic zone, northeastern Alberta. *Canadian Journal of Earth Sciences*, *37*(11), 1575–1596. https://doi.org/10.1139/e00-034

Mercier, J., Bostock, M. G., Audet, P., Gaherty, J. B., Garnero, E. J., & Revenaugh, J. (2008). The teleseismic signature of fossil subduction: Northwestern Canada. *Journal of Geophysical Research: Solid Earth*, *113*(B4).

Mercier, J. P., Bostock, M. G., Cassidy, J. F., Dueker, K., Gaherty, J. B., Garnero, E. J., … Zandt, G. (2009). Body-wave tomography of western Canada. *Tectonophysics*, *475*(3–4), 480–492. https://doi.org/10.1016/j.tecto.2009.05.030

Miall, A. D., & Blakey, R. C. (2008). The Phanerozoic tectonic and sedimentary evolution of North America. *Sedimentary Basins of the World*, *5*, 1–29.

Monger, J., & Price, R. (2002). The Canadian Cordillera: Geology and Tectonic Evolution. *CGES Recorder*, *27*(2), 17–36. https://doi.org/10.13140/2.1.4483.1520

Monger, J., Price, R., Survey, G., & Price, R. (2002). ARTICLE THE CANADIAN CORDILLERA : Geology and Tectonic Evolution. *CGES Recorder*, *27*(2), 17–36. https://doi.org/10.13140/2.1.4483.1520

Monger, J. W. H., Price, R. A., & Tempelman-Kluit, D. J. (1982). Tectonic accretion and the origin of the two major metamorphic and plutonic welts in the Canadian Cordillera. *Geology*, *10*(2), 70–75.

Monger, J. W. H., & Ross, C. A. (1971). Distribution of fusulinaceans in the western Canadian Cordillera. *Canadian Journal of Earth Sciences*, *8*(2), 259–278.

Montelli, R., Nolet, G., Dahlen, F. A., Masters, G., Engdahl, E. R., & Hung, S.-H. (2004). Finite-Frequency Tomography Reveals a Variety of Plumes in the Mantle. *Science*, *303*(5656), 338–343. https://doi.org/10.1126/science.1092485

Montelli, R., Nolet, G., Masters, G., Dahlen, F. A., & Hung, S. H. (2004). Global P and PP traveltime tomography: Rays versus waves. *Geophysical Journal International*.

https://doi.org/10.1111/j.1365-246X.2004.02346.x

Moschetti, M. P., Ritzwoller, M. H., Lin, F., & Yang, Y. (2010). Seismic evidence for widespread western-US deep-crustal deformation caused by extension. *Nature*, *464*(7290), 885.

Mueller, P. A., & Frost, C. D. (2006). The Wyoming Province: a distinctive Archean craton in Laurentian North America. *Canadian Journal of Earth Sciences*, *43*(10), 1391–1397. https://doi.org/10.1139/e06-075

Mueller, P. A., Heatherington, A. L., Kelly, D. M., Wooden, J. L., & Mogk, D. W. (2002). Paleoproterozoic crust within the Great Falls tectonic zone: Implications for the assembly of southern Laurentia. *Geology*, *30*(2), 127–130.

Mueller, P. A., Shuster, R. D., D'Arcy, K. A., Heatherington, A. L., Nutman, A. P., & Williams, I. S. (1995). Source of the northeastern Idaho batholith: isotopic evidence for a Paleoproterozoic terrane in the northwestern US. *Journal of Geology*, *103*(1), 63–72. https://doi.org/10.1086/629722

Nettles, M., & Dziewoński, A. M. (2008). Radially anisotropic shear velocity structure of the upper mantle globally and beneath North America. *Journal of Geophysical Research: Solid Earth*, *113*(B2).

Nieuwenhuis, G., Unsworth, M. J., Pana, D., Craven, J., & Bertrand, E. (2014). Three-dimensional resistivity structure of Southern Alberta, Canada: Implications for precambrian tectonics. *Geophysical Journal International*, *197*(2), 838–859. https://doi.org/10.1093/gji/ggu068

Niu, F., Bravo, T., Pavlis, G., Vernon, F., Rendon, H., Bezada, M., & Levander, A. (2007). Receiver function study of the crustal structure of the southeastern Caribbean plate boundary and Venezuela. *Journal of Geophysical Research: Solid Earth*, *112*(B11).

Nolet, G. (2008). A breviary of seismic tomography. *Cambridge University Press*, 345. https://doi.org/10.1017/CBO9780511984709

O'Neill, J. M. (2007). Great Divide megashear, Montana and Idaho: An intraplate lithospheric shear zone and its impact on Mesoproterozoic depositional basins. In *Geol. Soc. Am. Abstr. Programs* (Vol. 39, p. 36).

O'Neill, J. M., & Berg, R. B. (1998). The Great Falls tectonic zone, Montana–Idaho: an early Proterozoic collisional orogen beneath and south of the Belt Basin. In *Belt Symposium III—1993: Montana Bureau of Mines and Geology Special Publication* (Vol. 112, pp. 222–228).

O'Neill, J. M., & Lopez, D. A. (1985). Character and Regional Significance of Great Falls Tectonic Zone, East-Central Idaho and West-Central Montana. *American Association of Petroleum Geologists Bulletin*, *69*(3), 437–447. https://doi.org/10.1306/AD462506-16F7-11D7-8645000102C1865D

Pană, D. I. (2002). *Precambrian Basement of the Western Canada Sedimentary Basin in Northern Alberta*. *Earth Sciences Report*. Retrieved from http://www.ags.gov.ab.ca/publications/abstracts/ESR_2002_02.html%5Cnhttp://scholar.google.com/scholar?hl=en&btnG=Search&q=intitle:Precambrian+Basement+o

f+the+Western+Canada+Sedimentary+Basin+in+Northern+Alberta#6%5Cnhttp://www.ags.gov.ab.ca/publications/a

Park, J., & Levin, V. (2000). Receiver functions from multiple-taper spectral correlation Estimates. *Bulletin of the Seismological Society of America*. https://doi.org/10.1785/0119990122

Parrish, R. R., Carr, S. D., & Parkinson, D. L. (1988). Eocene extensional tectonics and geochronology of the southern Omineca Belt, British Columbia and Washington. *Tectonics*, *7*(2), 181–212.

Pasyanos, M. E., Masters, T. G., Laske, G., & Ma, Z. (2014). LITHO1. 0: An updated crust and lithospheric model of the Earth. *Journal of Geophysical Research: Solid Earth*, *119*(3), 2153–2173.

Paul, A., Kaviani, A., Hatzfeld, D., Vergne, J., & Mokhtari, M. (2006). Seismological evidence for crustal-scale thrusting in the Zagros mountain belt (Iran). *Geophysical Journal International*, *166*(1), 227–237. https://doi.org/10.1111/j.1365-246X.2006.02920.x

Pawlak, A., Eaton, D. W., Bastow, I. D., Kendall, J. M., Helffrich, G., Wookey, J., & Snyder, D. (2011). Crustal structure beneath Hudson Bay from ambient-noise tomography: Implications for basin formation. *Geophysical Journal International*. https://doi.org/10.1111/j.1365-246X.2010.04828.x

Pearson, D. G., & Wittig, N. (2008). Formation of Archaean continental lithosphere and its diamonds: the root of the problem. *Journal of the Geological Society*, *165*(5), 895–914.

Percival, J. A., Cook, F. A., & Clowes, R. M. (2012). Tectonic styles in Canada: the LITHOPROBE perspective. Geological Association of Canada.

Pilkington, M., Miles, W. F., Ross, G. M., & Roest, W. R. (2000). Potential-field signatures of buried Precambrian basement in the Western Canada Sedimentary Basin 1. *Canadian Journal of Earth Science*, *1471*(11), 1453–1471. https://doi.org/10.1139/e00-020

Pirouz, M., Avouac, J.-P., Hassanzadeh, J., Kirschvink, J. L., & Bahroudi, A. (2017). Early Neogene foreland of the Zagros, implications for the initial closure of the Neo-Tethys and kinematics of crustal shortening. *Earth and Planetary Science Letters*, *477*, 168–182.

Polet, J., & Anderson, D. L. (1995). Depth extent of cratons as inferred from tomographic studies. *Geology*, *23*(3), 205–208.

Pollack, H. N. (1986). Cratonization and thermal evolution of the mantle. *Earth and Planetary Science Letters*. https://doi.org/10.1016/0012-821X(86)90031-2

Porritt, R. W., Allen, R. M., & Pollitz, F. F. (2014). Seismic imaging east of the Rocky Mountains with USArray. *Earth and Planetary Science Letters*, *402*(C), 16–25. https://doi.org/10.1016/j.epsl.2013.10.034

Porter, J. W., Price, R. A., & McCrossan, R. G. (1982). The Western Canada Sedimentary Basin. *Philosophical Transactions of the Royal Society of London*, *305*(1489), 169–192. Retrieved from

http://rsta.royalsocietypublishing.org/content/305/1489/169.full.pdf+html

Price, R. A. (1981). The Cordilleran foreland thrust and fold belt in the southern Canadian Rocky Mountains. *Geological Society, London, Special Publications*, *9*(1), 427–448.

Price, R. A. (1986). The southeastern Canadian Cordillera: thrust faulting, tectonic wedging, and delamination of the lithosphere. *Journal of Structural Geology*, *8*(3–4), 239–254.

Price, R. A. (1994). Cordilleran tectonics. *Mossop, GD, and Shetsen, I., Compilers, Geological Atlas of the Western Canadian Sedimentary Basin: Canadian Society of Petroleum Geologists and Alberta Research Council*, 13–24.

Priestley, K., & Debayle, E. (2003). Seismic evidence for a moderately thick lithosphere beneath the Siberian Platform. *Geophysical Research Letters*, *30*(3).

Priestley, K., McKenzie, D., & Debayle, E. (2006). The state of the upper mantle beneath southern Africa. *Tectonophysics*, *416*(1–4), 101–112.

Prieto, G. A., Lawrence, J. F., & Beroza, G. C. (2009). Anelastic Earth structure from the coherency of the ambient seismic field. *Journal of Geophysical Research: Solid Earth*, *114*(B7).

Pysklywec, R. N., Beaumont, C., & Fullsack, P. (2002). Lithospheric deformation during the early stages of continental collision: Numerical experiments and comparison with South Island, New Zealand. *Journal of Geophysical Research: Solid Earth*, *107*(B7), ETG-3.

Pysklywec, R. N., Ellis, S. M., & Gorman, A. R. (2010). Three-dimensional mantle lithosphere deformation at collisional plate boundaries: A subduction scissor across the South Island of New Zealand. *Earth and Planetary Science Letters*, *289*(3), 334–346.

Rawlinson, N., & Kennett, B. L. N. (2004). Rapid estimation of relative and absolute delay times across a network by adaptive stacking. *Geophysical Journal International*, *157*(1), 332–340.

Regan, S. P., Williams, M. L., Chiarenzelli, J. R., Grohn, L., Mahan, K. H., & Gallagher, M. (2017). Isotopic evidence for Neoarchean continuity across the Snowbird Tectonic Zone, western Churchill Province, Canada. *Precambrian Research*, *300*, 201–222. https://doi.org/10.1016/j.precamres.2017.07.022

Richards, T. C., & Walker, D. J. (1959). Measurement of the thickness of the Earth's crust in the Albertan plains of western Canada. *Geophysics*, *24*(2), 262–284.

Rippe, D., Unsworth, M. J., & Currie, C. A. (2013). Magnetotelluric constraints on the fluid content in the upper mantle beneath the southern Canadian Cordillera: Implications for rheology. *Journal of Geophysical Research: Solid Earth*, *118*(10), 5601–5624. https://doi.org/10.1002/jgrb.50255

Ritsema, J., Nyblade, A. A., Owens, T. J., Langston, C. A., & VanDecar, J. C. (1998). Upper mantle seismic velocity structure beneath Tanzania, east Africa: Implications for the stability of cratonic lithosphere. *Journal of Geophysical Research: Solid Earth*, *103*(B9), 21201–21213.

Roddick, J. A. (1967). Tintina trench. *The Journal of Geology*, *75*(1), 23–33.

Röhm, A. H. E., Snieder, R., Goes, S., & Trampert, J. (2000). Thermal structure of continental upper mantle inferred from S-wave velocity and surface heat flow. *Earth and Planetary Science Letters*, *181*(3), 395–407.

Rondenay, S. (2009). Upper mantle imaging with array recordings of converted and scattered teleseismic waves. *Surveys in Geophysics*, *30*(4–5), 377–405.

Rondenay, S., Abers, G. A., & Van Keken, P. E. (2008). Seismic imaging of subduction zone metamorphism. *Geology*, *36*(4), 275–278.

Rondenay, S., Bostock, M. G., & Fischer, K. M. (2005). Multichannel inversion of scattered teleseismic body waves: practical considerations and applicability. *GEOPHYSICAL MONOGRAPH-AMERICAN GEOPHYSICAL UNION*, *157*, 187.

Ross, G. M. (2000). Introduction to special issue of Canadian Journal of Earth Sciences: The Alberta basement transect of Lithoprobe. *Canadian Journal of Earth Sciences*, *37*(11), 1447–1452.

Ross, G. M. (2002a). Evolution of Precambrian continental lithosphere in Western Canada: results from Lithoprobe studies in Alberta and beyond. *Canadian Journal of Earth Sciences*, *39*(3), 413–437. https://doi.org/10.1139/e02-012

Ross, G. M. (2002b). Introduction to special issue of Canadian Journal of Earth Sciences: the Alberta Basement Transect of Lithoprobe. *Canadian Journal of Earth Sciences*, *39*(3), 287–288. https://doi.org/10.1139/e02-011

Ross, G. M., & Eaton, D. W. (1997). Winagami reflection sequence: Seismic evidence for postcollisiona magmatism in the Proterozoic of western Canada. *Geology*, *25*(3), 199–202. https://doi.org/10.1130/0091-7613(1997)025<0199:WRSSEF>2.3.CO;2

Ross, G. M., & Eaton, D. W. (2002). Proterozoic tectonic accretion and growth of western Laurentia: results from Lithoprobe studies in northern Alberta. *Canadian Journal of Earth Sciences*, *39*(3), 313–329. https://doi.org/10.1139/e01-081

Ross, G. M., Eaton, D. W., Boerner, D. E., & Miles, W. (2000). Tectonic entrapment and its role in the evolution of continental lithosphere: An example from the Precambrian of western Canada. *Tectonics*, *19*(1), 116–134. https://doi.org/10.1029/1999TC900047

Ross, G. M., Milkereit, B., Eaton, D., White, D., Kanasewich, E. R., & Burianyk, M. J. A. (1995). Paleoproterozoic collisional orogen beneath the Western Canada Sedimentary Basin imaged by Lithoprobe crustal seismic-reflection data. *Geology*, *23*(3), 195–199. https://doi.org/10.1130/0091-7613(1995)023<0195:PCOBTW>2.3.CO;2

Ross, G. M., Parrish, R. R., Villeneuve, M. E., & Bowring, S. A. (1991). Geophysics and geochronology of the crystalline basement of the Alberta Basin, western Canada. *Canadian Journal of Earth Sciences*, *28*(4), 512–522. https://doi.org/10.1139/e91-045

Rudnick, R. L., & Gao, S. (2003). Composition of the continental crust. *Treatise on Geochemistry*, *3*, 659.

Ryberg, T., & Weber, M. (2000). Receiver function arrays: a reflection seismic approach.

*Geophysical Journal International*, *141*(1), 1–11.

Sambridge, M., & Guđmundsson, Ó. (1998). Tomographic systems of equations with irregular cells. *Journal of Geophysical Research: Solid Earth*, *103*(B1), 773–781.

Sambridge, M. S. (1990). Non-linear arrival time inversion: constraining velocity anomalies by seeking smooth models in 3-D. *Geophysical Journal International*, *102*(3), 653–677.

Schaeffer, A. J., & Lebedev, S. (2014). Imaging the North American continent using waveform inversion of global and USArray data. *Earth and Planetary Science Letters*, *402*, 26–41.

Schmandt, B., & Lin, F. (2014). P and S wave tomography of the mantle beneath the United States. *Geophys. Res. Lett.*, 6342–6349. https://doi.org/10.1002/2014GL061231.Received

Schmandt, B., Lin, F. C., & Karlstrom, K. E. (2015). Distinct crustal isostasy trends east and west of the Rocky Mountain Front. *Geophysical Research Letters*, *42*(23), 10290–10298. https://doi.org/10.1002/2015GL066593

Schulte-Pelkum, V., Mahan, K. H., Shen, W., & Stachnik, J. C. (2017). The distribution and composition of high-velocity lower crust across the continental US: Comparison of seismic and xenolith data and implications for lithospheric dynamics and history. *Tectonics*, *36*(8), 1455–1496.

Schultz, R., Atkinson, G., Eaton, D. W., Gu, Y. J., & Kao, H. (2018). Hydraulic fracturing volume is associated with induced earthquake productivity in the Duvernay play. *Science*, *359*(6373), 304–308.

Schultz, R., & Stern, V. (2015). The Regional Alberta Observatory for Earthquake Studies Network (RAVEN). *CSEG Recorder*, *40*(8), 34–37.

Schultz, R., Stern, V., & Gu, Y. J. (2014). An investigation of seismicity clustered near the Cordel Field, west central Alberta, and its relation to a nearby disposal well. *Journal of Geophysical Research: Solid Earth*, *119*(4), 3410–3423.

Schultz, R., Stern, V., Gu, Y. J., & Eaton, D. (2015). Detection threshold and location resolution of the Alberta Geological Survey earthquake catalogue. *Seismological Research Letters*, *86*(2A), 385–397.

Schutt, D. L., Dueker, K., & Yuan, H. (2008). Crust and upper mantle velocity structure of the Yellowstone hot spot and surroundings. *Journal of Geophysical Research: Solid Earth*, *113*(B3).

Schutt, D. L., & Lesher, C. E. (2006). Effects of melt depletion on the density and seismic velocity of garnet and spinel lherzolite. *Journal of Geophysical Research: Solid Earth*, *111*(B5).

Seats, K. J., Lawrence, J. F., & Prieto, G. A. (2012). Improved ambient noise correlation functions using Welch′ s method. *Geophysical Journal International*, *188*(2), 513–523.

Shang, X., De Hoop, M. V., & Van Der Hilst, R. D. (2012). Beyond receiver functions: Passive source reverse time migration and inverse scattering of converted waves.

*Geophysical Research Letters*. https://doi.org/10.1029/2012GL052289

Shang, X., de Hoop, M. V, & van der Hilst, R. D. (2017). Common conversion point stacking of receiver functions versus passive-source reverse time migration and wavefield regularization. *Geophysical Journal International*, *209*(2), 923–934.

Shapiro, N. M., & Campillo, M. (2004). Emergence of broadband Rayleigh waves from correlations of the ambient seismic noise. *Geophysical Research Letters*, *31*(7).

Shaw, J. H., Plesch, A., Tape, C., Suess, M. P., Jordan, T. H., Ely, G., … Graves, R. (2015). Unified structural representation of the southern California crust and upper mantle. *Earth and Planetary Science Letters*, *415*, 1–15.

Shaw, J., & Johnston, S. T. (2016). Oroclinal buckling of the Armorican ribbon continent: An alternative tectonic model for Pangean amalgamation and Variscan orogenesis. *Lithosphere*, *8*(6), 769–777.

Sheehan, A. F., Abers, G. A., Jones, C. H., & Lerner-Lam, A. L. (1995). Crustal thickness variations across the Colorado Rocky Mountains from teleseismic receiver functions. *Journal of Geophysical Research: Solid Earth*, *100*(B10), 20391–20404.

Shen, W., & Ritzwoller, M. H. (2016). Crustal and uppermost mantle structure beneath the United States. *Journal of Geophysical Research: Solid Earth*, *121*(6), 4306–4342.

Shen, W., Ritzwoller, M. H., & Schulte-Pelkum, V. (2013). A 3-D model of the crust and uppermost mantle beneath the Central and Western US by joint inversion of receiver functions and surface wave dispersion. *Journal of Geophysical Research: Solid Earth*, *118*(1), 262–276.

Shragge, J., Bostock, M. G., Bank, C. G., & Ellis, R. M. (2002). Integrated teleseismic studies of the southern Alberta upper mantle. *Canadian Journal of Earth Sciences*, *39*(3), 399–411. https://doi.org/10.1139/e01-084

Sigloch, K., McQuarrie, N., & Nolet, G. (2008). Two-stage subduction history under North America inferred from multiple-frequency tomography. *Nature Geoscience*, *1*(7), 458–462. https://doi.org/10.1038/ngeo231

Sigloch, K., & Mihalynuk, M. G. (2013). Intra-oceanic subduction shaped the assembly of Cordilleran North America. *Nature*, *496*(7443), 50–56. https://doi.org/10.1038/nature12019

Sigloch, K., & Mihalynuk, M. G. (2017). Mantle and geological evidence for a Late Jurassic–Cretaceous suture spanning North America. *GSA Bulletin*, *129*(11–12), 1489–1520.

Simons, F. J., & Van Der Hilst, R. D. (2002). Age-dependent seismic thickness and mechanical strength of the Australian lithosphere. *Geophysical Research Letters*, *29*(11), 21–24.

Sims, P. K., Lund, K., & Anderson, E. (2005). *Precambrian crystalline basement map of Idaho — An interpretation of aeromagnetic anomalies*. *U.S. Geological Survey Scientific Investigations Map 2884*.

Sims, P. K., O'Neill, J. M., Bankey, V., & Anderson, E. (2004). *Precambrian basement geologic map of Montana; an interpretation of aeromagnetic anomalies*.

Sleep, N. H. (2005). Evolution of the continental lithosphere. *Annu. Rev. Earth Planet. Sci.*, *33*, 369–393.

Snelson, C. M., Henstock, T. J., Keller, G. R., Miller, K. C., & Levander, A. (1998). Crustal and uppermost mantle structure along the Deep Probe seismic profile. *Rocky Mountain Geology*, *33*(2), 181–198.

Snieder, R. (2004). Extracting the Green's function from the correlation of coda waves: A derivation based on stationary phase. *Physical Review E*, *69*(4), 46610.

Snyder, D. B., Clowes, R. M., Cook, F. A., Erdmer, P., Evenchick, C. A., Van der Velden, A. J., & Hall, K. W. (2002). Proterozoic prism arrests suspect terranes: insights into the ancient Cordilleran margin from seismic reflection data. *GSA TODAY*, *12*(10), 4–9.

Snyder, D. B., Craven, J. A., Pilkington, M., & Hillier, M. J. (2015). The 3-dimensional construction of the Rae craton, central Canada. *Geochemistry, Geophysics, Geosystems*, *16*(10), 3555–3574.

Stehly, L., Campillo, M., & Shapiro, N. M. (2006). A study of the seismic noise from its long-range correlation properties. *Journal of Geophysical Research: Solid Earth*, *111*(B10).

Stern, R. J. (2002). Subduction zones. *Reviews of Geophysics*, *40*(4), 1–3.

Stewart, J. H. (1972). Initial deposits in the Cordilleran geosyncline: Evidence of a late Precambrian (< 850 my) continental separation. *Geological Society of America Bulletin*, *83*(5), 1345–1360.

Tape, C., Liu, Q., Maggi, A., & Tromp, J. (2009). Adjoint tomography of the southern California crust. *Science*, *325*(5943), 988–992.

Tape, C., Liu, Q., & Tromp, J. (2007). Finite-frequency tomography using adjoint methods—Methodology and examples using membrane surface waves. *Geophysical Journal International*. https://doi.org/10.1111/j.1365-246X.2006.03191.x

Tesauro, M., Kaban, M. K., Mooney, W. D., & Cloetingh, S. (2014). Tectonophysics NACr14 : A 3D model for the crustal structure of the North American Continent. *Tectonophysics*, *631*, 65–86. https://doi.org/10.1016/j.tecto.2014.04.016

Tesoniero, A., Auer, L., Boschi, L., & Cammarano, F. (2015). Hydration of marginal basins and compositional variations within the continental lithospheric mantle inferred from a new global model of shear and compressional velocity. *Journal of Geophysical Research: Solid Earth*, *120*(11), 7789–7813.

Thomas, M. D., Sharpton, V. L., & Grieve, R. A. F. (1987). Gravity patterns and Precambrian structure in the North American central plains. *Geology*, *15*(6), 489–492.

Thompson, D. A., Helffrich, G., Bastow, I. D., Kendall, J.-M., Wookey, J., Eaton, D. W., & Snyder, D. B. (2011). Implications of a simple mantle transition zone beneath cratonic North America. *Earth and Planetary Science Letters*, *312*(1), 28–36.

Thurner, S., Margolis, R., Levander, A., & Niu, F. (2015). PdS receiver function evidence for crustal scale thrusting , relic subduction , and mafic underplating in the Trans-Hudson Orogen and Yavapai province. *Earth and Planetary Science Letters*, *426*, 13–22. https://doi.org/10.1016/j.epsl.2015.06.007

Thybo, H., & Artemieva, I. M. (2013). Moho and magmatic underplating in continental lithosphere. *Tectonophysics*, *609*, 605–619.

Torsvik, T. H., Burke, K., Steinberger, B., Webb, S. J., & Ashwal, L. D. (2010). Diamonds sampled by plumes from the core-mantle boundary. *Nature*, *466*(7304), 352–355.

Trabant, C., Hutko, A. R., Bahavar, M., Karstens, R., Ahern, T., & Aster, R. (2012). Data products at the IRIS DMC: Stepping stones for research and other applications. *Seismological Research Letters*, *83*(5), 846–854.

Tromp, J., Tape, C., & Liu, Q. (2005). Seismic tomography, adjoint methods, time reversal and banana-doughnut kernels. *Geophysical Journal International*, *160*(1), 195–216. https://doi.org/10.1111/j.1365-246X.2004.02453.x

Tsai, V. C. (2009). On establishing the accuracy of noise tomography travel-time measurements in a realistic medium. *Geophysical Journal International*, *178*(3), 1555–1564.

Van Der Hilst, R. D., & Kárason, H. (1999). Compositional heterogeneity in the bottom 1000 kilometers of earth's mantle: Toward a hybrid convection model. *Science*. https://doi.org/10.1126/science.283.5409.1885

Van Der Lee, S., & Frederiksen, A. (2005). Surface wave tomography applied to the North American upper mantle. *Seismic Earth: Array Analysis of Broadband Seismograms*, 67–80.

Van Der Meer, D. G., Spakman, W., Van Hinsbergen, D. J. J., Amaru, M. L., & Torsvik, T. H. (2010). Towards absolute plate motions constrained by lower-mantle slab remnants. *Nature Geoscience*, *3*(1), 36.

Van Hinsbergen, D. J. J., Lippert, P. C., Dupont-Nivet, G., McQuarrie, N., Doubrovine, P. V, Spakman, W., & Torsvik, T. H. (2012). Greater India Basin hypothesis and a two-stage Cenozoic collision between India and Asia. *Proceedings of the National Academy of Sciences*, *109*(20), 7659–7664.

VanDecar, J. C., & Crosson, R. S. (1990). Determination of teleseismic relative phase arrival times using multi-channel cross-correlation and least squares. *Bulletin of the Seismological Society of America*, *80*(1), 150–169.

vanderVelden, A. J., & Cook, F. A. (1996). Structure and tectonic development of the southern Rocky Mountain trench. *Tectonics*, *15*(3), 517–544.

Villeneuve, M. E., Ross, G. M., Thériault, R. J., Miles, W., Parrish, R. R., & Broome, J. (1993). *Tectonic subdivision and U-Pb geochronology of the crystalline basement of the Alberta Basin, Western Canada*. *Geological Survey of Canada, Bulletin 447*. Ottawa.

Vinnik, L. P. (1977). Detection of waves converted from P to SV in the mantle. *Physics of the Earth and Planetary Interiors*. https://doi.org/10.1016/0031-9201(77)90008-5

Wang, R., Gu, Y. J., Schultz, R., & Chen, Y. (2018). Faults and non-double-couple components for induced earthquakes. *Geophysical Research Letters*.

Wang, R., Gu, Y. J., Schultz, R., Kim, A., & Atkinson, G. (2016). Source analysis of a potential hydraulic-fracturing-induced earthquake near Fox Creek, Alberta. *Geophysical Research Letters*.

Wang, R., Gu, Y. J., Schultz, R., Zhang, M., & Kim, A. (2017). Source characteristics and geological implications of the January 2016 induced earthquake swarm near Crooked Lake, Alberta. *Geophysical Journal International*, *210*(2), 979–988.

Wang, X., Chen, L., Ai, Y., Xu, T., Jiang, M., Ling, Y., & Gao, Y. (2018). Crustal structure and deformation beneath eastern and northeastern Tibet revealed by P-wave receiver functions. *Earth and Planetary Science Letters*, *497*, 69–79.

Wang, Y., Fan, W., Peng, T., Zhang, H., & Guo, F. (2005). Nature of the Mesozoic lithospheric mantle and tectonic decoupling beneath the Dabie Orogen, Central China: Evidence from 40 Ar/39 Ar geochronology, elemental and Sr–Nd–Pb isotopic compositions of early Cretaceous mafic igneous rocks. *Chemical Geology*, *220*(3), 165–189.

Ward, K. M., Porter, R. C., Zandt, G., Beck, S. L., Wagner, L. S., Minaya, E., & Tavera, H. (2013). Ambient noise tomography across the Central Andes. *Geophysical Journal International*, *194*(3), 1559–1573.

Webb, S. C. (1998). Broadband seismology and noise under the ocean. *Reviews of Geophysics*. https://doi.org/10.1029/97RG02287

Welford, J. K., & Clowes, R. M. (2006). Three-dimensional seismic reflection investigation of the upper crustal Winagami sill complex of northwestern Alberta, Canada. *Geophysical Journal International*, *166*(1), 155–169. https://doi.org/10.1111/j.1365-246X.2006.02805.x

Weller, O. M., & St-Onge, M. R. (2017). Record of modern-style plate tectonics in the Palaeoproterozoic Trans-Hudson orogen. *Nature Geoscience*, *10*(4), 305.

Whitmeyer, S. J., & Karlstrom, K. E. (2007). Tectonic model for the Proterozoic growth of North America. *Geosphere*, *3*(4), 220–259.

Wright, G. N., McMechan, M. E., & Potter, D. E. G. (1994). Structure and architecture of the Western Canada sedimentary basin. *Geological Atlas of the Western Canada Sedimentary Basin*, 25–40. Retrieved from http://www.ags.gov.ab.ca/publications/wcsb_atlas/a_ch03/ch_03.html

Wu, L., Gu, Y. J., Chen, Y., & Liang, H. (2018). Shear wave splitting discloses two episodes of collision-related convergence in western North America. *Journal of Geophysical Research-Solid Earth*.

Yang, Y., & Ritzwoller, M. H. (2008). Characteristics of ambient seismic noise as a source for surface wave tomography. *Geochemistry, Geophysics, Geosystems*. https://doi.org/10.1029/2007GC001814

Yang, Y., Ritzwoller, M. H., Levshin, A. L., & Shapiro, N. M. (2007). Ambient noise Rayleigh wave tomography across Europe. *Geophysical Journal International*, *168*(1), 259–274.

Yeck, W. L., Sheehan, A. F., & Schulte-Pelkum, V. (2013). Sequential h-κ stacking to obtain accurate crustal thicknesses beneath sedimentary basins. *Bulletin of the Seismological Society of America*. https://doi.org/10.1785/0120120290

Yilmaz, O. (2013). *Seismic data analysis Processing, In version, and Interpretation of Seismic Data*. Society of exploration geophysicists. https://doi.org/10.1002/9781118542392.fmatter

Youssof, M., Thybo, H., Artemieva, I. M., & Levander, A. (2015). Upper mantle structure beneath southern African cratons from seismic finite-frequency P-and S-body wave tomography. *Earth and Planetary Science Letters*, *420*, 174–186.

Yuan, H., French, S., Cupillard, P., & Romanowicz, B. (2014). Lithospheric expression of geological units in central and eastern North America from full waveform tomography. *Earth and Planetary Science Letters*, *402*, 176–186.

Yuan, H., & Romanowicz, B. (2010). Lithospheric layering in the North American craton. *Nature*, *466*(7310), 1063–1068.

Yuan, X., Ni, J., Kind, R., Mechie, J., & Sandvol, E. (1997). Lithospheric and upper mantle structure of southern Tibet from a seismological passive source experiment. *JOURNAL OF GEOPHYSICAL RESEARCH*. https://doi.org/10.1029/97JB02379

Zandt, G., & Ammon, C. J. (1995). Continental crust composition constrained by measurements of crustal Poisson's ratio. *Nature*, *374*(6518), 152.

Zhu, L., & Kanamori, H. (2000). Moho depth variation in southern California from teleseismic receiver functions. *Journal of Geophysical Research: Solid Earth*, *105*(B2), 2969–2980.